STUDY OF ELECTRONIC STRUCTURE OF CLUSTERS AND DISORDERED SOLIDS

A THESIS SUBMITTED TO THE

CENTRAL DEPARTMENT OF PHYSICS

INSTITUTE OF SCIENCE AND TECHNOLOGY
TRIBHUVAN UNIVERSITY
KATHMANDU, NEPAL

FOR THE AWARD OF
DOCTOR OF PHILOSOPHY
IN PHYSICS

BY

GOPI CHANDRA KAPHLE

April, 2014

DECLARATION

Thesis entitled **"Study of electronic structure of clusters and disordered solids"** which is being submitted to the Central Department of Physics, Institute of Science and Technology(IOST), Tribhuvan University, Nepal for the award of the degree of Doctor of Philosophy, is a research work carried out by me under the joint supervision of Associate Prof. Dr. Narayan Prasad Adhikari of Tribhuvan University and Prof. Dr. Abhijit Mookerjee of S. N. Bose National Center for Basic Sciences, Kolkata, India. This research is original and has not been submitted earlier in part or full in this or any other form to any university or institute, here or elsewhere, for the award of any degree.

Gopi Chandra Kaphle
Research Scholar
Central Department of Phyics,
Tribhuvan University,
Kathmandu, Nepal

Date:

RECOMMENDATION

This is to recommend that **Mr. Gopi Chandra Kaphle** has carried out research entitled **"Study of electronic structure of clusters and disordered solids"** for the award of Doctor of Philosophy (Ph. D.) in **Physics** under our supervision. To our knowledge, this work has not been submitted for any other degree.

He has fulfilled all the requirements laid down by the Institute of Science and Technology (IOST), Tribhuvan University, Kirtipur for the submission of the thesis for the award of Ph. D. degree.

(Dr. Abhijit Mookerjee)
Professor,
Materials Science Department,
S. N. Bose National Centre For Basic Sciences,
JD Block, Sector III, Salt Lake City,
Kolkata 700 098, India

(Dr. Narayan Prasad Adhikari)
Associate Professor,
Central Department of Physics,
Tribhuvan University,
Kirtipur, Kathmandu, Nepal

Date :

Date:

LETTER OF APPROVAL

On the recommendation of Professor Dr. Abhijit Mookerjee of S.N. Bose National Centre For Basic Sciences, Kolkata, India and Associate Professor Dr. Narayan Prasad Adhikari of Central Department of Physics, Tribhuvan University, Kirtipur, Kathmandu, Nepal, this Ph. D. thesis submitted by **Mr. Gopi Chandra Kaphle**, entitled **"Study of electronic structure of clusters and disordered solids"** is forwarded by Central Department Research Committee(CDRC) to the Dean, Institute of Science and Technology(IOST), Tribhuvan University(T.U.).

Dr. Binil Aryal
Professor,
Head,
Central Department Of Physics,
Tribhuvan University,
Kirtipur, Kathmandu, Nepal

Date:

To my Grandmothers and Mother

who are no more .....

ACKNOWLEDGMENTS

"The ending of one point is exactly the beginning of other new."

—Unknown

At this stage, I am about to cross the one ford which was tough and shows many paths to go in different directions in the journey of research. Actually, it was tough so it helps to develop me a confidence, strengthen my analytical power and provides me a kind of sprit. During this journey I faced many ups and downs and by taking the help of many people I finally come at this point, so this is the time to give thank to all. Thanks.

First of all I would like to express my sincere appreciation to my supervisors Emeritus Professor Dr. Abhijit Mookerjee of S. N. Bose National Center For Basic Sciences, Kolkata, India and Associate Professor Dr. Narayan Prasad Adhikari of Tribhuvan University, Kirtipur, Kathmandu, Nepal for their patience, Scientific guidance, support, friendship as well as parent-ship throughout of my research work.

I am thankful to Institute of Science and Technology, Tribhuvan Univesity, Kirtipur, Kathmandu, Nepal and Central Department of Physics, Tribhuvan University, Kirtipur Kathmandu, Nepal for providing me a chance to do my research work.

I would like to thank Prof. Dr. Binil Aryal, Head of Central Department of Physics and Prof. Dr. Lok Narayan Jha, Ex-head of Central Department of Physics, Tribhuvan University, Kirtipur Kathmandu, Nepal.

I would like to thank Prof. Dr. Sitaram Prasad Byahut of CDP, Kirtipur, Kathmandu, Nepal who suggested me to join the group of AM and NA and his suggestion turned my life towards the fields of research. I am thankful to all the Professors, all the staffs of central department of physics T U who helped me according to their level without which my thesis work would not be of present shape.

I am thankful to my senior Dr. Shreemoyee Ganguly and Dr. Rudra Banerjee who helped me to introduce computational dealing with disordered alloys. At the same time I would like to thank Dr. Soumendu Datta, Faculty fellow of S. N. Bose National Center for Basic Sciences, Kolkata, India who had introduced me to the field of clusters and nanophysics.

It is my great pleasure to thank my group members Prashant Singh, Rajeev Chauhan, A. P. Jena and Tanumoy Ghosh. They helped me all the times in all respects. Actually I never forget precise moments spent with them in SNBNCBS. I also want to thank my group members Nurapati Pantha, Saran lamichhane and M.Sc.thesis students who always supported and listened me without feeling bored at any time.

I would like to thank my friends Bandan, Azaj, Rishi, Victor and shubhajit who made me my stay pleasant in hostel as well as outside in SNBNCBS.

I do not want to miss this opportunity to thank all the staff of library, all the staff of computer centers, all the staffs of Security, Canteen and Student mesh of SNBNCBS for their help according to their level.

Finally, I would like thank Abdul Salam International Center For Theoretical Physics (ICTP) for providing fellowship under the project NET-56 through Third World Academy of Science (TWAS). I also would like to thank S. N. Bose National Center For Basic Sciences especially for Advanced Research Material Unit for providing computational facility and hospitality.

The last but not the least I would like to thank my parents and family members for their supports and encouragements. Special thank goes to Muna, Bishrut, Bishrant and Bibhuti who always makes me fresh and energetics.

Gopi Chandra Kaphle
Central Department of Phyics,
Tribhuvan University,
Kirtipur, Kathmandu, Nepal

ABSTRACT

We have carried out the first-principles calculation of Pd_n (n = 2-19) clusters with plane augmented wave (PAW) based Density Functional Theory (DFT) using the Perdew, Burke, Ernzerhof (PBE) exchange correlation functional implemented in Vienna *ab-initio* Simulation Package (VASP) to understand the structural evolution, electronic and magnetic properties of the clusters. Our findings show that the highly symmetric structures like Icosahedral, Buckle Bi-planner, Cube-Octahedral and Hexagonal closed pack do not represent the minimum energy configurations for all the clusters. Present calculations show that the enhanced stabilities for clusters size (n) = 2, 8, 13 and 18 indicating that pristine Pd_n clusters follow the magic number effect. The highest occupied molecular orbital (HOMO)-Lowest unoccupied molecular orbital (LUMO) gap is higher for these highly stable clusters in comparison to their neighbors. Interestingly, even though bulk structure of Palladium is nonmagnetic, some of the finite size clusters possess significant magnetic moment. The highest value of magnetic moment is found to be $6.57\mu_B$ for n = 13 in Icosahedral structure. To get further insight into the effect of Mn and Mn_2 doping on magnetic properties of Pd_n clusters, calculations have been carried out to study the magnetic properties of $Pd_{(n-1)}Mn$ and $Pd_{(n-2)}Mn_2$ for n = 2-13. For $Pd_{(n-1)}Mn$, the cluster of size (n) = 4, 7, 10 and 12 are more stable than their neighbors and magnetic moments for all the clusters increase due to Mn doping. The highest magnetic moments $9.64\mu_B$ is for $Pd_{12}Mn$ clusters. In case of $Pd_{(n-2)}Mn_2$, the clusters of sizes n= 3, 7, 9 are more stable than their neighbors. The magnetic moments enhance due to Mn_2 doping on $Pd_{(n-2)}Mn_2$ except for $Pd_{11}Mn_2$ clusters. It may be due to the fact that in $Pd_{11}Mn_2$ cluster the spin of two Mn atoms align antiparallel. To perform adsorption and dissociation properties of hydrogen and nitrogen molecules on Ta_n and Nb_n (n = 2-7) clusters, we have carried out structural stability, charge transfer, chemisorption energy as well as HOMO-LUMO gap. Our findings show that Ta_n and Nb_n clusters favor the dissociation of both hydrogen and nitrogen except TaH_2 and NbH_2. This indicates that Ta_n and Nb_n clusters can be used as catalyst for the dissociation of hydrogen and nitrogen molecules which is necessary for the synthesis of ammonia. Present result agrees well with results of Yadav and Mookerjee for the case of Ta_nH_2 for $n \geq 4$. It is also found that Ta_n and Nb_n clusters bind nitrogen more strongly than hydrogen. It it mainly due to the fact that binding of nitrogen with triple bond which requires large amount of force to break the bond than single bonded hydrogen atom. It is also concluded that Ta_n and Nb_n nano-structures may be used for the hydrogen storage materials. This will be the important task for future generation.

We have performed density functional based *ab-initio* calculations through VASP to carry out the stability and magnetic properties of ZnO nanosystems with different morphologies like nanosheet, nanotube and fullerene type structures in pristine form. Our findings show that nanosheet favors most energetic than nanotube and fullerene like structures. All the morphologies in elemental(ZnO) form do not bear any magnetic properties. Further to get insight into the magnetic properties after doping of TM elements (Mn, Fe, Co, Ni, Cu) in pristine system, we perform near and far dop case in all the systems. Present study showed that ZnO:Mn always favors the near dop AFM alignment in all three morphologies. In case of ZnO:X (X=Fe, Co, Ni), the AFM alignment favors for sheet and this alignment changes while moving sheet to fullerene like

structure. Our findings also show that there is lack FM alignment in ZnO:X (X = Mn, Co) indicating that these are not suitable candidate for spintronics applications at low temperature. Such properties agrees well with the previously reported data for bulk. This trends found to be changed while we are moving from tube to fullerene-like structures. To analyze the band gap properties, we used both PBE (GGA) and HSE06 version of hybrid functionals through VASP. We found there is no change in magnetic moments after the inclusion of Heyd-Scuseria- Ernzerhof (HSE). After the inclusion of HSE we found that Ni and Cu doped ZnO sheet show blue shift where as Mn, Fe and Co dope ZnO sheet show blue shift. Further ZnO:Ni tube shows blue shift with band gap 3.98 eV. We found red shift for all cases in ZnO doped TM fullerene like structures.

We have discussed electronic and magnetic properties of disordered NiMn experimentally as well as theoretically. For the theoretical work, we used self consistent ASR code and performed calculation on different concentrations of $Ni_{1-x}Mn_x$ with 15%, 20%, 25%. 30%, 35% and 30% of Mn by atom. For that we used lattice parameters 3.572 A^0, 3.583A^0, 3.595A^0, 3.615A^0, 3.654A^0 and 3.670A^0 coming through XRD analysis for increasing concentrations. It is observed that our theoretical and experimental phase diagram exactly matched with phase diagram of Montecarlo calculations. Further we used spin dynamics code to get more insight in to the spin glass behavior. From the present study we found that $Ni_{75}Mn_{25}$ shows anomalously slow relaxations which is one of the signature of spin glass phase. Further we studied the electronic and magnetic behavior of disordered Pt-Mn, Pd-Mn and Ni-Mn alloys. For this we used non-collinear version of TB-LMTO-ASR for the electronic and magnetic properties as well as linear muffin-tin orbital green function (LMTOGF) based on CPA code for the exchange pair energy interactions. We found SG behaviors in all the three systems. The magnetic phase diagrams of Pd-Mn and Pt-Mn are found to be more or less same kinds. In case of Pd-Mn SG phase stretches from 0.0 to 0.17 atomic concentration of Mn with tri-critical point around 200K and around 7% atomic concentration of Mn. Similarly, in Pt-Mn SG phase stretches from 0 to 0.2 atomic concentration of Mn with tri-critical points around 150K and 10% of Mn concentration. For Ni-Mn, the phase diagram is different from Pd-Mn and Pt-Mn on which random ferromagnet and anti-ferromagnet flanking either side (both Mn as impurity or Ni). The spin-glass phase stretches from 0.1 to 0.3 atomic concentration of Mn. The Ni-Mn phase diagram qualitatively agrees with experiment.

Keywords: Transition metal clusters, Nanosystems, Magnetic phase diagram, Augmented space recursion technique, Disordered alloys.

LIST OF ABBREVIATIONS

AFM : Anti-ferromagnetic
ASR : Augmented Space Recursion
AE : All Electron
ASF : Augumented Space Formalism
APW : Augumented Plane Wave
ASA : Atomic Sphere Approximation
BBP : Buckled Bi-Planner
B. E. : Binding Energy
B. L. : Bond length
BOA : Born-Oppenheimer Approximation
CNT : Carbon Nanotube
CPA : Coherent Potential Approximation
DFT : Density Functional Theory
DOS : Density of states
DMS : Dilute Magnetic Semiconductor
ECM : Embedded Cluster Method
eV : Electron volt
EPE : Effective Pair Energy
EA : Electron Affinity
FCC : Face centred Cubic
FM : Ferromagnetic
GGA : Generalized Gradient Approximation
GPM : Generalized Perturbation Method
GKS : Generalized Kohn-Sham
GF : Green Function
HF : Hartree-Fock
H.K : Hohenberg - Kohn
HOMO : Highest Occupied Molecular Orbital
HSE : Heyd-Scuseria- Ernzerhof
ICTP : Abdul Salam International Center For Theoretical Physics
IP : Ionization Potential
KKR : Korringa-Kohn-Rostocker
K. E. : Kinetic Energy
LUMO : Lowest Occupied Molecular Orbital
LDA : Local Density Approximation

LLG : Landau-Lifshitz-Gilbert
LAPW : Linear Augmented Plane Wave
LCAO : Linear Combination of Atomic Orbital
MCP : Multicritical Point
MSRO : Magnetic short range Order
MT : Muffin-tin
NN : Nearest Neighbour
OPW : Orthogonalised Plane wave
PAW : Projector Augmented Wave
PDOS : Projected density of states
PM : Paramagnetic
RKKY : Ruderman-Kittel-Kasuya-Yoshida
RDM : Reduced Density Matrix
SP : Slater Pauling
SNBNCBS : Satyendra Narayan Bose National Center for Basic Sciences
SG : Spin Glass
SQUID : Superconducting quantum interference device
SIC : Self-interaction-corrected
SCF : Self Consistent Field
TM : Transition Metal
TMOs : Transition metal oxides
TMC : Transition Metal Cluster
TWAS : Third World Academy of Science
TBLMTO : Tight Binding Linear Muffin-tin Orbital
T. U. : Tribhuvan University
VASP : Vienna *Ab-initio* Simulation Package
XRD : X-ray Diffraction
ZFC : Zero Field cooled

LIST OF TABLES

LIST OF FIGURES

TABLE OF CONTENTS

CHAPTER 3

CHAPTER 4

CHAPTER 1

INTRODUCTION

The study of clusters has a great deal of attention from the era of Rayleigh who investigated reason of proper color of strain glass (Rayleigh, 1892) which is due to scattering of light by small metal particles (clusters) embedded in glass. Later his followers (Mie, 1908), (Kreibig, 1970) used electrodynamics treatments to study the scattering of light by small clusters, which is relevant even today. The research in metal clusters has developed and advanced considerably in last two decades. Still many fundamental problems, like problems related to geometry (structural), electronic and magnetic properties of clusters remains unsolved. Metal clusters provide a convenient and relatively inexpensive tool for studying the properties of finite fermion systems with increasing size from atomic to mesoscopic dimensions and hopefully soon to the macroscopic domain as well. It is interesting from the fundamental point of view to study the evolution of physical properties like structural, electronic and magnetic properties moving from atom to clusters and clusters to the bulk solids. The observation of (Pedersen, *et al.* , 1991) on super-cell structure in alkali clusters with up to three thousand atoms represents a milestone in this development.

The structural and electronic properties of transition metal clusters offer important information regarding the fundamental aspect of catalysis, optical, magnetic and chemical properties of clusters (Nigam, *et al.* , 2007). The stable geometry is of the great interest because it's structural character drastically changed even slight change in size of clusters. Study of structure also help to find out the growth pattern (evolution) while moving from clusters to bulk which is important from the application point of view. The stable structure also provides the information of magnetic moments for examples, the magnetic behavior of 3d impurities in palladium clusters as a host offers formation of giant magnetic moments (Oswald, *et al.* , 1986). The study of stable structure, electronic and magnetic properties are of great interest for clusters as well as bulk systems.

The variation of structural, electronic, magnetic and other properties of transition metal(TM) doped on pristine clusters as well as the evolutions of size dependent TM doped on pristine clusters of TM atoms also of great important in various branch of

sciences as well as fundamental point of view (Brack, 1995). Although 3d, 4d and 5d have unfilled localized d- states, 3d transition metals are only known to form a magnetic solids. This feature can be attributed to strong localization of valence electron for 3d metals (Cox, *et al.* , 1994). This also indicate the importance of study of TM doped pristine clusters which is one of the theme of present study. Similarly adsorption and dissociation of hydrogen and nitrogen molecules on TM clusters is important to synthesize the ammonia which is one of the most useful fertilizer in the world as well as possible use of such clusters in hydrogen storage problem (Yadav & Mookerjee, 2010).

The study of II-VI transition metal oxide semiconducting materials have attracted much interest owing to their potential application in the field of spintronics, light emitting diodes, laser diodes, sensing devices and optical applications. One of these ZnO has become recent focus. It is due to use of novel applications in electronic magnetic and optical properties which facilitate the creation of multi functionality integrated devices. The use of ZnO also has a great interest because one can prepare nanosheet, nanotube, fullerene like structure from it for the use of them in above mentioned applications (Huang, *et al.* , 2010). The origin of magnetism in TM doped ZnO (like Mn, Fe, Co, Ni and Cu as a substitutional dop in Zn site) still are of great dispute which also make interest to study such systems. The study of variation of magnetic moments at different morphologies like nano-sheet, nano-tube and fullerene like structures are also of great interest due to above facts. In ordered to evaluate the electronic and magnetic properties we used density functional theory and hybrid functional Heyd-Scuseria-Ernzerhof (HSE) theory through Vianna *Ab-initio* Simulation Package (VASP) code.

The study of disordered alloys are of great interest because there is drastic change in magnetic behavior with atomic concentration of magnetic elements like spin glass. It is also important to know the application of it (spin glass) in physics, mathematics, medical as well as certain aspect of biological evolution (Chowdhury & Mookerjee, 1984). The study of bulk and disordered alloys like Pd-Mn, Pt-Mn and Ni-Mn are also important because of their use in shape memory alloys, spintronics, electromagnetic applications and advanced study of it also used to study the complex biological systems like brain. For this purpose we used Tight Binding Linear Muffin-tin Orbital Augmented Space Recursion(TB-LMTO-ASR) Code which is explained more detail in section (4.6).

Based on the above fact we categorized the systems in three categories and we focused our study towards these categories.

- Transition metal clusters and doping effect.

- Elemental and doped TM oxide.

- Disordered binary solids.

The overview of these systems are described in following sections.

1.1 Overview of transition metal clusters and Nanosystems

Owing to the importance of study of clusters and nanosystems, we focus our attention to study the meaning of clusters, structural growth patterns, electronic and magnetics properties of pristine transition metal clusters and the doping effect on it. The adsorption and dissociation of hydrogen and nitrogen also discussed. Further we focus our attention to discuss magnetic properties of the nanosystem in different morphologies (nanosheet, nanoube and fullerene like structures) of pristine ZnO and TM doped on these systems. We used VASP code to deal with pristine clusters, heterogeneous clusters and nanosystems. The overview of these are explained within this section as follows.

1.1.1 Transition metal clusters and doping effect

The word clusters means collection of a few to millions (2.0-10^6) of atoms or molecules bonded together and forms particular shape and size. Clusters of varying sizes can be generated using a variety of techniques such as sputtering, chemical vapor deposition, laser vaporization, supersonic molecular beam etc. (de Heer, 1995). Clusters lie somewhere between an atom and the bulk, forming a bridge between the atomic scale and the bulk scale (Brack, 1995). Therefore, clusters bridge the gap between the microscopic and the macroscopic worlds. The study of physical and chemical properties of clusters provide a useful laboratory for investigating the structure of materials and explain how its properties evolve with size. Presently we are dealing with the clusters of magnetic materials. Magnetic clusters and nano-particles are interesting not only because of their possible technological applications but also because in these systems we can systematically study the effect on magnetism with diminishing size and dimension. The clusters are interesting because finite size effect can lead to quite different structural, electronic, magnetic and other properties moving from molecules to bulk (Henry, 1998). The another interesting fact about the clusters is that their properties are not only size dependent even small change in single atom clusters properties change drastically in small size clusters. It is therefore important to study the evolution of clusters properties as it is built up atom by atom.

In transition metal clusters, the study of incomplete d-shells and localized d-shell electrons are more interesting in comparison to clusters with sp-shells whose properties are largely affected by delocalized sp-orbitals. The studies done on clusters and solids to

calculate different properties showing intrinsic difference between atomic and bulk nature. Magnetism in transition metal (TM) clusters is one of fundamental issue to be addressed at the atomic level. The magnetic properties of nano particles depending on size, composition and local atomic environment show variety of intriguing phenomena. The deflection experiment of Stern-Gerlach (SG) type is commonly used by experimentalists to study magnetism of free transition-metal clusters in molecular beams (Xu, *et al.* , 2005), (Knicklbein, 2004). Due to such intriguing properties of clusters, we have focused the present work mainly in following kinds.

- At first we study the characteristics of pristine Pd_n (n=2-19) clusters. We study the evolution of structural growth pattern. This is done through energy minimization process using Vieanna *ab-initio* Simulation Package (VASP). The electronic and magnetic properties of pristine Pd clusters are explained on the basis of HOMO-LUMO gap, Charge transformation as well as s, p and d hybridization.

- Second one is the structural evolution, origin of magnetism etc. after doping mono and bi-atoms of Mn in finite size clusters of palladium atoms(n$\leq$ 13). We try to find out the possibility of formation of devices applicable to spintronics, optical purposes and chemical catalysts. We observed that behavior of non magnetic bulk Pd has quite different in clusters. It shows drastic change in electronic and magnetic properties of system in pristine Pd clusters. The magnetic properties found to be enhanced after doping mono- and bi-atom of Mn on Pd_n clusters.

- Third, we are analyzing adsorption and dissociation of hydrogen and nitrogen by Ta_n and Nb_n clusters (n=2-7). The interaction of hydrogen and nitrogen molecules on the transition metal(TM) clusters is of considerable interest in the field of science and technology (Alonso, 2000), (Bertolus, *et al.* , 2001). The interest in hydrogen interaction properties of isolated metal nanoparticles is due to their relevance in hydrogen storage and catalysts. Most of the work on hydrogen storage based on adsorption and dissociation of hydrogen molecules by large surface area of metal nanoparticles. Similarly the efficient activation of nitrogen is a long standing issue in the heterogeneous catalytic process for the synthesis of ammonia. Transition metal clusters have been considered as a possible candidates for such catalysts. In this work we shall study the structural effect after doping hydrogen and nitrogen molecules on pristine clusters Nb and Ta atoms. We also try to find out the answer of the questions whether Nb and Ta act as catalyst for the reaction which requires dissociation of H_2 and N_2 for the synthesis of ammonia as well as whether these clusters can be used as a hydrogen storage purpose or not.

1.1.2 Elemental and doped transition metal-oxide

There is great interest and challenges to work on the transition metal nano-oxide (Josheph, 2011). It is due to their diverse and tunable magnetic and catalytic properties. ZnO and TM doped ZnO are important in technological application in catalytic, electrical, optoelectronic and quantum devices (Ozgur, *et al.* , 2005). It is direct and wide band gap semiconductor with large band gap around 3.37 eV (Josheph, 2011). Large numbers of nano structures like nanoparticles, nanorods, nanotubes and nanowires have been synthesized and used successfully in optical devices (Lany & Zunger, 2007), (Murugadoss, 2012). Zinc-oxide based low dimensional materials have aroused a great scientific interest due to their promising applications in above mentioned fields. ZnO nanoclusters are used in variety of biological(catalytic) process from photosynthesis to bacterially mediated organic matter decompositions (Guo.*et al.* , 2012), (Park, *et al.* , 2012). The prerequisite is to engineer the size of band gap and to engineer the magnetic effect. Though there are large number of experiments and theory (as mentioned above) in ZnO and ZnO doped materials but some of the problems within this system has yet to be resolved for examples, low doping elements solubility, deviation from the stereochemistry and optical energetic configurations. All of these characteristics also explain the disadvantages of semiconducting devices.

Similarly semiconductors with dilute magnetic impurities (DMS)(Sato, *et al.* , 2010) have opened up a possibility of manipulating the spin degree of freedom of electrons through interaction between the local moments of the doped magnetic ions and the spins of the charge carriers of the host semiconductors. Here, we purposed to study the reduced dimension band gap engineering after doping some TM elements like Mn, Fe, Co, Ni and Cu and enhancement of magnetic behavior on ZnO clusters in the form of monolayer(nanosheet), nano-tube and fullerene like structures to resolved the above mentioned problems and stands new issue related to this fields. We have chosen different morphologies of 48 atoms due to availability of computational facility.

All the clusters calculations are done using the first-principles calculation technique on which the properties of all the materials are predicted starting from the quantum mechanics. Many standard quantum chemistry techniques are used to calculate the electronic structure of TM clusters. But they have limited to small number of clusters due to computational load as well as difficulty in the treatment of d-electrons effects in TM clusters. In order to reduce such deficiency for TM, we generally use pseudo-potential and density functional theory (DFT). Pseudo-potential theory allows us to focus on the chemically active valence electrons by replacing the strong all electron(AE) atomic potential with weak spin polarized, which effectively reproduces the effect of core electrons

on the valence state. DFT replaces the many body wave function representation of the system which is present in standard quantum chemistry approaches, by the set of non interacting electronic wave-functions having same charge density as the original system. The basis sets that are used for expanding one electron wave-functions are plane waves. The extensive testing is needed for basis set like Gaussian atomic like functions but the plane wave methods have the advantage that only one parameter (the wavelength of the highest Fourier components used in the expansion) need to be refined to control the convergence. Plane wave requires a periodic boundary condition so the care should be taken to reproduce the vacuum during the study of non periodic systems, such as clusters to reduce the spurious interaction between replicate images of the system. The spin polarized and nonmagnetic DFT calculation were conducting using VASP with PBE exchange correlation functional and projected augmented wave pseudo potentials at required cutoff energy for all the calculations.

Many ground state properties such as crystal structure, lattice constant, crystal anharmonicity are studied by DFT with PBE exchange correlation functional with good agreement with experimental results(Jollet, *et al.* , 2009). It fails to describe important properties of materials with correlated orbitals like band gap of semiconductors which is underestimated by DFT due to self-interaction error. Furthermore systems such as high temperature superconductors, heavy fermions materials, TM oxides and 3d itinerant magnets i.e. for the system in which the fermi level falls into the region of narrow energy bands. Local density approximation(LDA) or Generalized gradient approximation(GGA) are usually can't describe accurately (Jollet, *et al.* , 2009). Schottky barriers formed at metal insulator interfaces are also underestimated. This failure is generally attributed due to the fact that the exchange and correlation energy is too crudely treated in the frame of the LDA or GGA approximations. To overcome this difficulty several methods have been proposed like LDA+U, Self-interaction-corrected(SIC) and new types of exchange correlation functionals like B3LYP, PBE0, HSE03 etc, (Becke, 1993), (Perdew *et al.* , 1996),(Henderson, 2008). We use HSE (Heyd-Scuseria-Ernzerhof) hybrid functional technique which is also available in VASP. This is mainly due to less computer time consuming as well as results are comparable or better than other at least in case of transition-metal monoxides. Another advantage is that it has no system dependent parameter. In this technique, a screened Coulomb potential is used in the HF energy. This is accomplished by splitting the Coulomb operator into short-range (SR) and long-range(LR). The Heyd-Scuseria-Ernzerhof (HSE) density functional retains only short-range Fock exchange and preserves the accuracy of PBE0 while avoiding the cost and pathologies of long-range Fock exchange. Unlike in traditional Kohn-Sham theory, hybrid functional generate nonlocal potentials, which is described by a general-

ized Kohn-Sham (GKS) theory. Ideally, an exact GKS functional can produce both a highest occupied molecular orbital (HOMO) and a lowest unoccupied molecular orbital (LUMO) that have orbital energies equivalent to the negative ionization potential(IP) and electron affinity(EA) respectively. In short, HSE and other short-range Fock exchange functionals are accurate for band gaps of TM oxide semiconductors (Park, 2011). We used it for the band gap estimation purposes, details of it is explained in consequent chapter.

1.2 Overview of disordered binary alloys

In solid state physics, we encounter large number of systems which have a lack of translational symmetry and periodicity, like clusters, surfaces, amorphous and random(disordered) alloys. We basically, focused on the binary disordered alloys in the present work. The symbolic representation of binary alloys are $A_{(x)}B_{(1-x)}$ where A and B are the constituent elements which forms alloys and x is the atomic percentage of A. It is difficult to distinguish the alloys whether they are ordered or disordered through general view. Alloys are said to be ordered or disordered according to the lattice structure and value of x as shown in Fig.(1.1). For example a simple cubic structure concentration of A should have a nx where n is integer with $1 < x \leq 7$ and x is equal to 12.5%. This is the necessary but not sufficient conditions for order phase. The disordered phase is possible even for all those concentrations depending on the ordering energy of alloys. The simple figures showing order and disorder structures are in Fig.(1.1).

As shown in Fig.(1.1) (Bottom) disorder in solids are categorized into two main classes : Compositional and structural. Our concern is only on the substitutional disordered which lies under the compositional type. The compositional type of disorder ness are also of two types: Substitutional and Topological(Interstitial) disordered. In substitutional disorder, underlying lattice are found to be remains unchanged, only the lattice sites are randomly occupied by different species of atoms ; where as in topological disorder the underlying lattice itself is found to be randomly distorted. In many situations both types of disorder may become relevant. In this thesis we shall address only particular class of substitutionally disorder magnetic solids viz. a spin glasses. These are the magnetic systems exhibiting both quenched(frozen) disordered and frustration. So far as the nature of the exchange interaction is concerned, SG systems which we used should follow the Ruderman-Kittel-Kasuya-Yoshida (RKKY) oscillation (Chowdhury & Mookerjee, 1984).

To deal such kinds of disordered systems, configuration averaging of physical quantities is most important as well as difficult. This difficulty is overcome by introducing mean-field

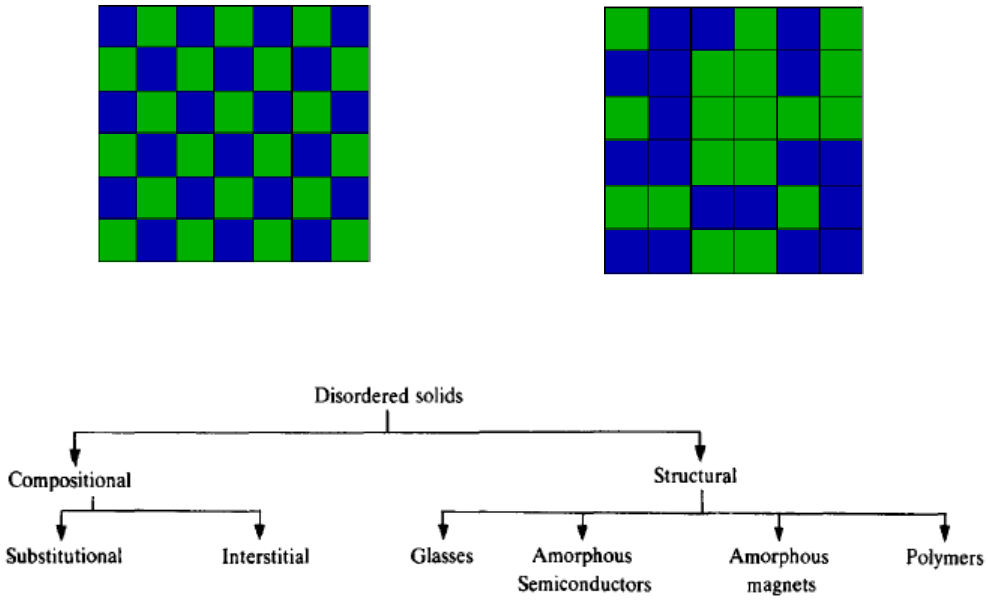

Figure 1.1: *(Top) Order and disordered structure and (Bottom) different kinds of disordered ness in solids.*

theories (Ehrenreich & Schwartz, 1982), (Faulker, 1982), (Prasad, 1995). In these approaches, the disordered system is replaced by a lattice periodic effective medium, with effective atoms occupying lattice sites. The coherent potential approximation (CPA) is one of the most successful technique to evaluate the configuration averaging (Soven, 1970). It is single-site mean field approximation. It cannot accurately take into account of local correlations leading to clustering or short-ranged order. It also can't deal with disorder in the off-diagonal part of the Hamiltonian that arise, for example, when there is a large difference in the band widths of the constituents. This indicates the need of other tool. With the realization of the need to beyond the CPA, several attempts have been reported. Among them Traveling cluster approximation and augmented space formalism(ASF) (Mookerjee, 1973) are the only approaches which have been proved to be analytic, while preserving the conservation laws and sum rules. The ASF is originally developed in the tight binding frame work provides self-consistent cluster coherent potential approximation (ScfCPA) in which one can go beyond CPA in the systematic way. The ASF, therefore, is a generalization of the CPA. We can introduce such approximations that short-ranged correlations are included and the essential properties like positive definite spectral densities and, in cases of homogeneous disorder, lattice translation symmetry of averaged quantities are all preserved. ASF is one of alternatives suggested for CPA because it goes beyond standard mean-field approximations to consider randomness not only at a site but also in its near neighborhood.

In this thesis we have projected both ASF and CPA in our calculations.To study the ordering effects in disordered alloys, we shall use the generalized perturbation method (GPM) (Turchi, *et al.* , 1988). The expansion coefficients are small energy differences of large energies. We have chosen the Lichtenstein formula
(Lichtenstein, *et al.* , 1987), (Antropov *et al.* , 1999) to accurately obtain such small energy differences. The GPM mapped our problem on the Ising model for doing magnetic phase analysis of disordered systems under consideration. We used Tight Binding Linear Muffin-tin Orbital Augmented Space Recursion(TB-LMTO-ASR) and its non-collinear version to deal with non-collinear magnetism in binary alloys like Pt-Mn, Pd-Mn and Ni-Mn. The exchange interaction energy which shows the RKKY oscillations, is calculated using Tight Binding Linear Muffin-tin Orbital Green Functions(TB-LMTO-GF) code which works under the frame work of CPA technique.

1.3 Main objectives of the present study

The main aim of the present thesis is to study the structural, electronic and magnetic properties of TM clusters and doping effect including nanosystems (with and without doping in reduced dimensions) and disorder binary solids. In order to deal the clusters we are using the density functional theory with PAW potential through Vienna *Ab-initio* Simulation Package (VASP). We used Heyd-Scuseria- Ernzerhof (HSE) hybrid functional to calculate accurate band gap of ZnO nano systems at different morphologies which is also available in VASP. The tight binding linear muffin tin potential augmented space recursion (TB-LMTO-ASR) code is used while dealing with collinear as well as non collinear systems. We used linear muffin-tin orbital green function(LMTOGF) and spin-dynamics codes to deal with the pair exchange interactions and spin relaxation respectively. The main objectives of this thesis are summarized as follows.

(I) The large number of theoretical as well as experimental work has been done in atomic as well as molecular form of transition metal clusters(TMC). It is mainly due to the variety of potential and technological uses of TMC as well as fundamental point of view. TMC are also used as a catalyst in many industrial and important chemical process. They are also extensively used as sensing device, magnetic storage materials, spintronics etc.. Pd clusters also serves as a catalyst in many heterogeneous catalytic systems. There are many conflicting remarks from both experimental as well as theoretical studies regarding the magnetic moments and stable shape of 13-atoms clusters. Some previous works reported that Mn, Fe, Co enhance the magnetic moments of Pd clusters due to FM coupling and $Pd_{12}Mn$ carries moments $11\mu_B$ which was icosahedral in structure whereas some other reported that Buckle bi-planner structure has

more energetically favorable than icosahedral structure. So motivation of this work is divided into two folds: one, to have a fresh look at body of often contradictory results by carrying out the systematic study to remove this uncertainties and second, to understand the influence of Mn impurities on the electronic and magnetic properties on the structure of host Pd clusters. The main objectives of the study will be analysis of structural, electronic and magnetic properties of Pd_n clusters (N=2-19) and effect of mono and bi-dop of Mn atom Pd_n clusters ($n \leq 13$). We specially focused on structural properties, density of states and magnetic properties of different isomers of Pd_{13}, $Pd_{12}Mn$ and $Pd_{11}Mn_2$ in some more details. We also try to find out the origin of magnetism within the systems under study.

(II) The interaction of hydrogen and nitrogen molecules on the TMC are of considerable interests. The interest in hydrogen interaction properties of isolated nanoparticles is due to their relevance in hydrogen storage and catalysts where as the interest in nitrogen due to its use in heterogeneous catalytic process for the synthesis of Ammonia which is one of the most consumable fertilizer in the world. Large number of experimental and theoretical work has been performed in past in the particular area related to interaction of hydrogen and nitrogen molecules with various TM clusters. These are related to geometrical structure, stability and reactivity of clusters but there is lack of the systematic study on adsorption and dissociation of hydrogen or nitrogen molecules on small Ta_n and Nb_n clusters (n = 2-7). With the motivation of previous works, we summarize the objectives as follows.

A. To study the structural and electronic properties of small Ta_n and Nb_n clusters (2-7) in pristine form as well as after doping H_2 and N_2 molecules over n = 1-7.

B. To study the possible charge transformation and chemisorption energy and test the stability after calculating the HOMO-LUMO gap.

C. Finally, we will analyze the adsorptive and dissociative properties of hydrogen and nitrogen molecules on Nb_n and Ta_n clusters (1-7). We also try to find out the answer of questions whether Nb_n and Ta_n clusters (2-7) can acts as catalysts for the reaction which requires dissociation of hydrogen as well as nitrogen molecules for the synthesis of Ammonia. We also try to find out the answer whether such clusters can also be used as hydrogen storage purpose or not.

(III) The study of grapheme like monolayers, tube and fullerene like structures of some transition metal oxides like ZnO at different morphologies in reduced dimension and possibility of their uses after doping TM elements, has been of great attraction, in the fundamental and application point of view. For doping purpose we used Mn, Fe, Co,

Ni and Cu. The main aim in this work will be to analyze the magnetic and band gap properties using DFT through VASP. We try to implement hybrid functional HSE06 for the study of band gap variation after doping TM elements. We also analyze the possible use of systems in non electronics, optoelectronics and spintronics applications.

(IV) The study of magnetism in Ni-rich $Ni_{1-x}Mn_x$ disordered alloys are of the great interest. The interest mainly due to results coming from heat treatment methodology which reported that it is difficult to make homo-phase Ni-Mn alloys and there exit ferromagnetic ordered on Ni_3Mn regions. Similarly Kouvel and Graham showed that the coexistence of ferromagnetism and anti-ferromagnetism coming from competing pair exchange interactions between the components at low temperatures in disordered $Ni_{1-x}Mn_x$ alloys with x = 20%, 25% and 30%, through hysteresis loop and torque. They reported the magnetic phase diagram in the composition range $23 \leq x \leq 27$. They observed, below the multicritical point (MCP) of x = 23.9 and T = $102K$, a double transition from a paramagnetic to a ferromagnetic state at T_C followed by a spin-glass (SG) like state at $T_{fg} < T_C$ with a re-entrant character. Above x = 23.9 they found a paramagnetic to a normal SG state at T_g. Hence, with the motivation of these we intend to do the experimental as well as theoretical work on these system around the MCP. So the objectives of this work are as follows.

A. To prepare the sample ranging from 15 -37% of Mn in $Ni_{1-x}Mn_x$. Then experimentally determine the magnetic properties specially around the MCP (at x = 25%) which has to be FM to AFM and around x = 37% there may be AFM to PM transitions. This can be analyze with study of susceptibility with and without using field.

B. To compare the experimental results with theoretical phase diagram which has to be analyzed using mean-field approximation.

C. To calculate the aging behavior and anomalously slow relaxation of magnetization in the composition range and compare with experimentally observed spin-glass behavior. In short, comparison and analysis of phase diagram observed from experiments, ASR technique and spin dynamics code are the main objectives of this study.

(V) The analysis of electronic and magnetic properties of disordered alloys using non-collinear formalism of TB-LMTO- ASR code is of great interest. It is because this technique can address non-collinear magnetism and the effects of spin-orbit coupling. In addition it can accurately handle disorder and disorder induced inhomogeneities like short-ranged ordering, clustering and local lattice distortions due to large size differences of the constituents. The test calculations have already done using this

technique for 50-50% Pt-Mn as well. Some experimental data are available for low concentration of Mn in case of $Pd_{1-x}Mn_x$ and $Pt_{1-x}Mn_x$ with short range AFM and long range FM coupling between magnetic moments. Based on these data various Montecarlo techniques faithfully reproduce the experimental phase diagram for $x < 0.15$. So with the base of above, we also intend to find out the electronic as well as magnetic properties for Pd-Mn, Pt-Mn and Ni-Mn. Hence the objectives of this part of work will be as follows.

A. To find out the stable structure with the application of non-collinear form of TB-LMTO-ASR technique.

B. Try to find out the origin of long range FM and short range AFM coupling on system under study with the composition range.

C. To study the electronic and magnetic properties of ordered as well as disordered alloys through different codes and mean-field analysis of the systems under study and analysis of phase diagram for the spin glass behavior of these systems.

1.4 Organization of the thesis

The thesis has been organized as follows:

(I) In **Chapter 1**, we introduce and discuss the objectives of the present study by taking the base of which we focus our study to systems, which also provides the motivation for dealing the particular systems.

(II) In **Chapter 2**, we introduce some previous literature and related work to support our works to reach the main goal and fulfill the objectives. This chapter will be named as literature review.

(III) **Chapter 3**, deals with detailed theoretical framework of electronic structure calculations carried out in this thesis and this also provides the necessary material used as a tools in the present work.

(IV) **Chapter 4** is divided into 5 sections on which we present and discuss the main findings of the present study. **Section 4.1** deals with the structural, electronic and magnetic properties of pristine Pd_n clusters for n=19 and Mono and bi-doped of Mn atom on Pd_n ($n \leq 13$). The structural evolution, analysis of electronic and magnetic properties are also explained within this section. In **Section 4.2**, we describe the results of adsorption and dissociation of nitrogen and hydrogen molecules by Ta_n and Nb_n (n=1-7) clusters. We have also tested this kinds of properties in Palladium (Pd_n)

and Platinum (Pt_n) (n=2-7) clusters(not included in this thesis). Here, we present the results of doping effect of hydrogen and nitrogen molecules on most stable conformer of clusters under study up to (n=1-7) from the possibilities of different isomers. The study of ZnO in reduced dimensions (nano-sheet, nanotube and fullerene) and doping effects are of great interest because of their uses in various fields like spintronics, optoelectronics, sensing devices etc.. We used 3d TM elements(Mn, Fe, Co, Ni and Cu) for doping purpose ($\approx$ 0-10 at.%). The results related to it is described in **Section 4.3**. **Section 4.4** contains the results carried out from the theoretical study of formation of moments and calculated the density of states and exchange interactions at various concentration of Ni rich Ni-Mn alloys and it also includes the results from the experiment, reverse Montecarlo technique and spin-dynamics codes. In **Section 4.5** we present the results related to electronic and magnetic properties of disordered alloys like Pd-Mn, Pt-Mn and Ni-Mn at various concentrations. The DOS of different configurations is calculated using non collinear form of LMTO-ASR Code. The exchange interaction at various concentration is carried out using TBLMTO-CPA code. The phase diagram showing the spin glass behavior, using mean field approximations is also presented in this section.

(V) The conclusions of the present work and some recommendations for further improvement of the work are presented in the **Chapter 5**.

(VI) The summary of the present work and future plan for further study are discussed in **Chapter 6**.

Finally the references and appendixes are listed at the end of thesis.

CHAPTER 2

LITERATURE REVIEW

This chapter contains the literature review of present study. The previous work which motivated us to do present works are described in section wise as follows,

2.1 Review of structural, electronic and magnetic properties of Pd_n, $Pd_{n-1}Mn$ and $Pd_{n-2}Mn_2$ clusters

Atomic and molecular clusters have a wide variety of potential and actual technological uses (Bansman, *et al.*, 2005). A large body of research exists on clusters. Technologically, transition metal clusters (TMC) serve as catalysts in many industrial and important chemical processes (Kumar, 2006). They are also used extensively in sensing devices, magnetic storage material and constitute important components in nanomaterials for diverse applications. TMC exhibit wide variety of geometric isomers and shapes (Kumar & Kawazoe, 2002). The physico-chemical properties of these clusters critically depend upon their size and shapes dictated by their atomic arrangements. So understanding the evolution of properties of clusters with size is necessary to design and development of novel materials (Aguilera-Granja, *et al.*, 2002), (Walter, *et al.*, 2002)].

Pd clusters serve as excellent catalysts in many heterogeneous catalytic systems. They exhibit interesting magnetic properties and show promise for essential application as supported metal catalysts. The magnetic properties of these catalysts are determined by their electronic structures and ultimately by their atomic arrangement. From earlier studies, it is known that even a 6% increment in the lattice constant can cause magnetism to appear in the system (Moruzzi & Marcus, 1989). In general, as size decreases, by the Stoner argument, magnetic moment approaches the atomic value in a magnetic material. This is usually higher than in the bulk.

The Pd atom is nonmagnetic with a closed shell electronic configuration, $4d^{10}5s^0$. In the small clusters, interaction between Pd atoms involves s, p, d hybridization, which leads to the depletion of $4d$ electrons and hence give rise to local magnetic moments. There

are many conflicting remarks from both experimental and theoretical studies regarding the magnetic moments of small size Pd clusters.

Stern-Garlach experiment suggested that there was no net magnetic moment in Pd clusters, whereas photoemission studies proposed that in smaller clusters, with less than 15 atoms, there was a finite magnetic moment. One of the experimental study (Shinhora, *et al.*, 2003) reported net magnetic moments found even in the larger size Pd clusters. From theoretical studies, (Moseler, *et al.*, 2002) reported that all small clusters Pd_n (n = 2-7 and 13) exhibit a finite magnetic moment. Rhodium also shows magnetism in clusters (Aguilera-Granja, *et al.*, 2002). Similar arguments have been made by (Kumar & Kawazoe, 2002), (Lee, *et al.*, 1998) and (Zhan, *et al.*, 2008). (Reddy, *et al.*, 1999) and (Fulschek, *et al.*, 2005) performed a calculation of the electronic structure of a 13-atom clusters of $4d$ group elements using local spin density approximation and reported that an icosahedron isomer of Pd_{13} has a stable structure with large magnetic moment. (Nigam, *et al.*, 2007) and (Jing, *et al.*, 2006) studied the geometrical, electrical and magnetic properties of Pd clusters doped with other transition metals. They reported that Mn, Fe and Co enhance the magnetic moments of Pd clusters due to ferromagnetic coupling and $Pd_{12}Mn$ carries magnetic moment about $11\mu_B$. (Chang & Chou, 2004) reported that new types of structures called Buckled bi-planer (BPP) with C_{2v} symmetry have lower energy than that of icosahedral and cub-octahedral clusters. They claimed that buckle bi-planner (BBP) is the lowest energy structure and this trend is followed by all transition elements with more than half fulfilled d-shells.

The various conflicting results obtain from different experiments and theories (Rogan, *et al.*, 2008), (Blonski & Hafner, 2011). This indicates that some work still have to be done a fresh look at the body of, often contradictory results by carrying out a systematic study and remove such uncertainties. These uncertainties is mainly due to the influence of Mn impurities on the electronic, atomic and magnetic structure of host Pd clusters. In present work we study, in particular, the structure, density of states and magnetic properties of different isomers of Pd_n (n = 2-19) and doping effect mono- and bi dop of Mn atoms on Pd_n (n=$\leq$ 13)clusters.

2.2 Review of Adsorption and Dissociation of Nitrogen and Hydrogen molecules on Tantalum and Niobium clusters

The interaction of hydrogen and nitrogen molecules doped on the transition metal(TM) clusters are attracted much intention in modern technology and fundamental point of view. The interest in hydrogen interaction properties of isolated metal nanoparticles is

due to their relevance in hydrogen storage and catalysts (Forrando, *et al.*, 2006) and other sensing devices (Alonso, 2000).

Most of the work on hydrogen storage based on adsorption and dissociation of hydrogen molecules by large surface area of metal nanoparticles. Similarly the efficient activation of nitrogen is a long standing issue in the heterogeneous catalytic process for the synthesis of ammonia. Transition metal clusters have been considered as a possible candidates for such catalysts. This is one of the motivation for the study of activation of hydrogen and nitrogen on Tantalum and Niobium clusters.

Actually ammonia is almost exclusive nitrogen source for living organism fertilizers and other artificial chemicals. The large amounts of ammonia about 10^8 tons per year is produced from Haber-Bosch process for ammonia synthesis by the use of di-nitrogen based heterogeneous catalytic reaction. The catalysis for the nitrogen fixation in biological systems are nitrogenous enzymes, which also produced same amount (like ammonia) per year. Similarly hydrogen is considered as the ideal candidate as an energy carrier for both mobile and stationary applications (Henwood & Carey, 2007). It is mainly due to its abundances, easy synthesis, potential for implementation in a carbon-free emission cycle and high efficiency.

Large number of experimental and theoretical work have been performed in past related to interaction of hydrogen and nitrogen with various TM clusters. These are related to electronic structure, stable geometry and reactivity of the clusters. (Yin, *et al.*, 2004) studied that group VIII metals or metal carbides/nitrides are suitable catalysts for the decomposition of ammonia. They especially coated that Ru clusters on different supports such as Al, Si, Mg, Carbon nanotube (CNT) are mostly active as a catalyst. However due to the restricted availability and high price of Ru researchers seek new alternatives elements like Nb,Ta, Pd, Pt etc.(Zhang, 2005). (Jiang, *et al.*, 2005) studied about the Ta clusters and observed that dissociative chemisorption of H_2 and N_2 is size selective for the bare metal clusters as well as cluster monoxide and mono-carbide. The study of Fe, Co and Nb have shown sharp variation in reactivity as a function of clusters size. (Yadav & Mookerjee, 2010) studied the adsorption and dissociation of nitrogen on tantalum clusters and they concluded that Ta can be used as a catalyst for the dissociation of nitrogen for synthesis of Ammonia.

In the present work, we study the structural and electronic properties of small Nb_n and Ta_n (n = 2-7) clusters before and after doping hydrogen and nitrogen molecules. We used stable geometry for the calculation of possible charge transformation and chemisorption energy. The stability will be analyzed by the characteristic feature of binding energy and HOMO-LUMO gap. The calculation of charge transformation,

chemisorption energy also help to know the stability of clusters. The majority of industrial catalysts consist of metal and metal compounds particles dispersed on an appropriate support. The catalysts provide the effective opportunities for separation of reaction product and catalysis. This indicate the huge application of hydrogen and nitrogen activation on metal clusters. So we intends to tackle this problem.

2.3 Review of Electronic and Magnetic properties of different morphologies of 3d transition metal doped ZnO

The study of ZnO and transition metal doped on it, has one of the exiting and interesting topic to the scientific community. It is due to the fact that dilute magnetic semiconductors(DMSCs) has special novelty on which both charge and spin of electrons can be used for spintronics devices (Gu, *et al.*, 2012). Different morphologies (Liao, *et al.*, 2005), (Wang, 2004), (Gardeniers, *et al.*, 1998) have different kinds of applications. ZnO is wide band gap semiconductor with novel magnetic, piezoelectric, electro optics and electromechanical properties (Ohno, 1998). The ferromagnetic induced by doped transition metals render ZnO with multifunctional characteristic. Large number of experimental as well as theoretical work has been performed related to induced FM in ZnO. (Sato & Yosida, 2000) studied the properties of n-type ZnO doped with 3d TM ions. A ferromagnetic state with T_c of around $2000K$ is predicted to favorable for V, Cr, Fe, Co and Ni while Mn-doped ZnO is predicted to be AFM. Some research groups,(Jung, *et al.*, 2002), (Norton, *et al.*, 2003) also reported the FM behavior in TM at or above room temperature. Other group (Fukumura, *et al.*, 2001), in contrast reported AFM, spin glass behavior and paramagnetism in TM doped ZnO. However, there is strong debate about the mechanism responsible for the origin. This is the main motivation to study of TM doped ZnO.

Similarly, some other group (Gopal & Spaldin, 2006), (Maiti, *et al.*, 2007) reported that some semiconductors like ZnO doped with magnetic ions are diluted(DMS) and the magnetic ions substituted cation site of host semiconductor are coupled by free carriers resulting ferromagnetism. They reported that ferromagnetic coupling is sometimes favorable for single-type substitutional transition-metal ions within the LSDA. But the nature of magnetic interactions changes when correlations on the transition-metal ion are treated within the more realistic LSDA+U method, often disfavoring the ferromagnetic state. This is another motivation to study of TM doped in pristine ZnO to use LSDA and hybrid functional (HSE06).

There are large number of experimental (Thota *et al.*, 2006), (Liao, *et al.*, 2005) as well

as theoretical (Lee & Chang, 2004) reports related to TM doped ZnO. However there is lack of the systematic study in different morphologies. Present work deals with the study of TM doped ZnO at different morphologies and try to find out the origin of magnetism within systems.

2.4 Review of Magnetic ordering in Ni-rich NiMn alloys around the multi-critical point

An early work, (Hahn & Kneller, 1958) carried out magnetic studies on Ni-Mn alloys as a function of heat treatment. They found that in spite of quenching from well above the ordering temperature, there exists small ferromagnetically ordered Ni_3Mn regions of about 20 A^0 in diameter in a matrix of the disordered material. This made the preparation of homo-phase Ni-Mn alloys a difficult task. Soon after, (Kouvel & Graham, 1959) established the coexistence of ferromagnetism and anti-ferromagnetism coming from competing pair exchange interactions between the components at low temperatures in disordered $Ni_{100-x}Mn_x$ alloys with x = 20, 25, and 30, through hysteresis loop and torque measurements.

(Kouvel, *et al.*, 1987) reported the magnetic phase diagram in the composition range $23 \leq x \leq 27$. They observed below the multicritical point (MCP) of x = 23.9 and T = $102K$, a double transition from a paramagnetic to a ferromagnetic state at T_C followed by a spin-glass (SG) like state at $T_{fg} < T_C$ with a re-entrant character. Above x = 23.9 they found a paramagnetic to a normal SG state at T_g.

(Aitken, *et al.*, 1982) found the MCP to be above x = 26. This difference could arise from the difference in atomic short-range order in the two works. (Hauser & Bernardini, 1984) studied sputtered films of $Ni_{(100-x)}Mn_x$ alloys and their bulk counterparts. They observed paramagnetic to spin-glass transition through ac susceptibility, $\chi(\omega)$ measured at 10 kHz and 4 Oe ac field. Bulk samples with x = 22, 27 and 31 gave T_g of 40, 78, $73K$ (much lower than 110 K found by (Aitken, *et al.*, 1982) and the Curie-Weiss plot ($\frac{1}{\chi}$ vs T for x = 27 gave a Neel temperature $\theta = 125K$ and n_{eff} of 2.5 μ_B which lies in between 0.3 and 3.2 μ_B found from neutron scattering experiments. It also gave a displaced hysteresis loop. Ferromagnetism disappeared at x = 27 since χ fell abruptly to 0.767×10^3 from 14.7×10^3 for x = 22 where $T_C \approx 290K$ and $T_g \approx 40K$. They concluded that the presence of ferromagnetism below x = 26 is independent of preparation conditions, induction, melted or quenched bulk alloys or sputtered films. However, the magnetic parameters such as T_C, T_g and $\chi(T)$ varied considerably. Needless to say that a more detailed magnetic phase diagram of this interesting system is certainly necessary, especially away

from the multicritical composition.

In the present case we are dealing with magnetism of $Ni_{1-x}Mn_x$ disordered systems with increasing atomic percentage of Mn ranges from $x = 15 - 37\%$ of Mn for both experimental as well as theoretical purpose. This is one of the classical examples of disordered system with competitive interactions and analyzed spin glass behavior around the MCP.

2.5 Review of Spin Glass behavior of disordered Pd-Mn, Pt-Mn and Ni-Mn alloys: non collinear version of TB-LMTO-ASR

The non collinear version of TB-LMTO-ASR technique is designed for the study of electronic structure of disordered alloys. This technique can address non-collinear magnetism and effects of spin-orbit coupling. It also can accurately handle disorder and disorder induced inhomogeneities like short-ranged ordering, clustering and local lattice distortions due to large size differences of the constituents (Bergman, *et al.*, 2006), (Ganguly, *et al.*, 2011). The technique first generalized the density functional approximation to take into account the possibility of non-collinear spin arrangements. It then went on to combine the tight-binding linear muffin-tin orbitals method (TB-LMTO) (Andersen & Jepsen, 1984), the recursion method (Haydock, *et al.*, 1972), (Haydock, *et al.*, 1975) and the augmented space method (AS) (Mookerjee, 1973). This is the main motivation of present work on which we intend to use that methodology to study, from a first-principles viewpoint, how lattice structure, composition and substitutional disorder influence the electronic structure and magnetic behavior of Mn based alloys. In many disordered alloys with closed packed lattice configurations, magnetic structures can become quite complex. In Mn based disordered alloys neutron diffraction experiments have often suggested complex magnetic alignments, e.g. in alloys like FeMn, PtMn, Mn_3Pt and Mn_3Rh. It has been suggested that this is possibly due to the presence of almost half-filled Mn $3d$ orbitals. In addition, interplay between atomic arrangement and disorder may introduce frustration effects.

A large body of experimental investigations has been carried out on Pt-rich$Pt_{1-x}Mn_x$. These include resistivity (Kastner, *et al.*, 1978), (Sarkissian & Taylor, 1974) measurement, magnetization and susceptibility (Tholence & Wasserman, 1977) and specific heat (Nieuwenhuys, *et al.*, 1973), (Sacli, *et al.*, 1974), (Kimishima, *et al.*, 1977). $Pt_{1-x}Mn_x$ alloys with $x < 0.02$ appear to have Kondo like behaviour. In the composition range $0.02 \leq x \leq 0.05$ $Pt_{1-x}Mn_x$ exhibits a pure spin-glass like behaviour with a strong

preference towards anti-ferromagnetic ordering. From this composition range to about $x = 0.10$, the alloy still shows spin-glass like behaviour, but now there is evidence of clusters forming and a cluster-glass picture seems more appropriate.

Above the percolation limit at $x \leq 0.15$, although the interaction is overwhelmingly anti-ferromagnetic, there is speculation that there is evidence of an additional ferromagnetic interaction of 'unknown type and origin' (Wasserman, 1982). There have been suggestions that precipitation of ferromagnetic Pt_3Mn phase in the disordered $Pt_{1-x}Mn_x$ matrix, arising from the preparation process may be responsible. However, (Wasserman, 1982) reports that in their samples with $x = 0.15$ X-ray scattering showed no signs of additional diffraction lines of Pt_3Mn. They detected changes in magnetic behaviour after annealing. The author suggests that perhaps during the alloy formation process finite clusters of Pt_3Mn were precipitated in the disordered matrix. In the Mn rich compositions, the ordered inter-metallic compound 50-50 Pt-Mn has a $L1_0$ structure. A small tetragonal distortion with $c/a \simeq 0.92$ lowers the total energy and stabilizes the compound. It exhibits collinear anti-ferromagnetism of the Mn atoms only (Sakuma, 2000). The Pt atoms carry negligible magnetic moment. The Néel temperature is rather high $\approx 1000K$ (Kren, *et al.*, 1968).

Experimental data is available on $Pd_{1-x}Mn_x$ for $x < 0.15$. These include measurements on magnetization and resistance (Coles, *et al.*, 1975), (Senoussi, *et al.*, 1980), specific heat (Boerstoel *et al.*, 1972), neutron scattering (De Pater, *et al.*, 1975), (Tsunoda, *et al.*1997) and a.c. susceptibility (Mulder *et al.*, 1981). Almost all experiments were for low concentrations of Mn and focus on the ferromagnetic phase that allegedly appears at low temperatures and very low concentrations of Mn. To try to understand this (Nieuwenhuys and Verbeek, 1977) proposed a short-ranged anti-ferromagnetic and a longer ranged ferromagnetic coupling between the magnetic moments. Based on this model there has been several Monte-Carlo studies (Gonzales & Parra, 1995),(Parra & Gonzales, 1992), (Kato & Saita, 2011) which faithfully reproduce the experimental phase diagram for x<0.15. However, there has been a lack of first-principles theories on this alloy system and certainly no work for those alloys with higher concentration of Mn. This is one of the motivation to perform calculation and will be one of the contributions of this work.

Magnetism in $Ni_{1-x}Mn_x$ alloys provide a classic example of a system with competing interactions. The study of (Kouvel, *et al.*, 1987) on disordered $Ni_{1-x}Mn_x$ reported a double transition below the multi-critical point (MCP) of $x = 0.239$ and $T = 102K$, from a paramagnetic to a ferromagnetic state at T_C followed by a spin-glass(SG)-like state at $T_{fg} < T_C$ with a re-entrant character and from a paramagnetic to a normal SG

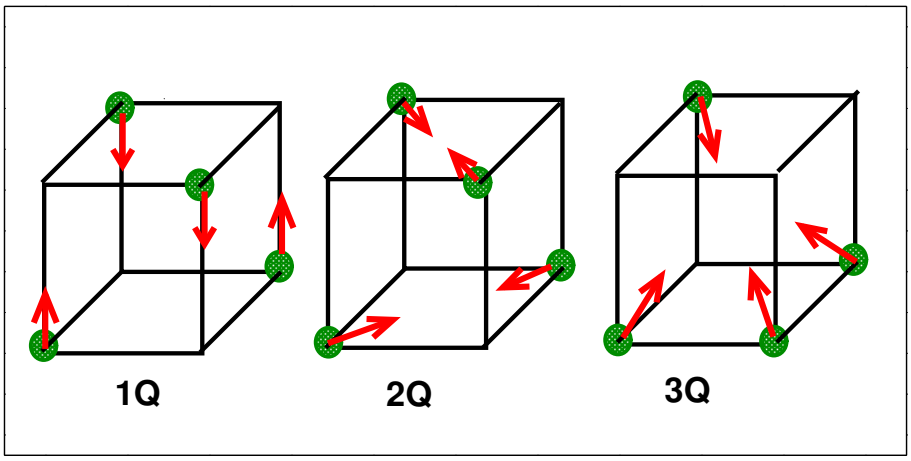

Figure 2.1: *(Color Online) The collinear 1Q and non-collinear 2Q and 3Q magnetic structures on the magnetic primitive lattice in a fcc structure.*

state at T_g above $x = 0.239$ (MCP).

The ordered 50-50 compounds have been studied earlier, first principles theoretical works on the disordered phase are conspicuous by their absence. In the disordered alloy, in contrast with the $L1_0$ ordered arrangement, the Mn and Pt atoms do not sit in parallel planes. The lattice structure is strictly face-centered cubic with both the corner and face-centre positions being occupied randomly with either Mn or Pt atoms with equal probability. The collinear magnetic arrangement on this face-centered lattice is shown in the left panel in Fig.(2.1). The arrangement which is found in the Pt rich compositions is the 1Q arrangement where the intra-layer alignment is collinear ferromagnetic while the inter-layer alignment is anti-ferromagnetic. Two other possible non-collinear arrangements are shown in the middle and right panels of Fig.(2.1). For the 2Q structure the moments lie in planes in twos and point towards each other. Finally the 3Q structure is quite similar to the 2Q with the difference that spins are raised in the lower plane and dipped in the upper plane so that now they all point towards the cube centre.

If we choose the positive c-axis as the global axis of quantization (z-axis) and represent the unit vector along the magnetic moment by $\vec{e}_{\vec{R}} = (\theta_{\vec{R}}, \phi_{\vec{R}})$, and if we label the position of the two sites on the bottom x-y plane as $\vec{R}_1, \vec{R}_2$ and those on the top x-y plane as $\vec{R}_3, \vec{R}_4$. Table 2.1 describes the spherical angles for the three structures.

Table 2.1: *Structural details of the three anti-ferromagnetic phases. Angles are given in units of* π

	$\vec{R}_1$		$\vec{R}_2$		$\vec{R}_3$		$\vec{R}_4$	
	θ	ϕ	θ	ϕ	θ	ϕ	θ	ϕ
1Q	0	0	0	0	1	0	1	0
2Q	0.50	0.25	0.50	1.25	0.50	0.75	0.50	1.75
3Q	0.304	0.25	0.304	1.25	0.304	0.75	0.304	1.75

Hence, with the above mentioned motivation we shall study Mn based alloys one of whose components is non-magnetic in the pristine state, like Pt-Mn and Pd-Mn and contrast their behaviour with another alloy one of whose components is ferromagnetic like Ni-Mn.

CHAPTER 3

MATERIALS AND METHODS

3.1 Introduction

A solid contains large number of electrons and nuclei in mutual interaction and dynamics of these particles in general can not be considered separately. We assume that nuclei are fixed in a given configuration(i.e. equilibrium configuration), so that we can focus on a electronic problem. Among the approaches to the many-electron system, we consider the historic(but always actual) Hartee-Fock theory. We will then discuss aspect beyond the one electron approximation, in particular the density functional theory(DFT) which has been very successful for the ground-state properties of solids. Here, firstly we describe about the electronic properties of many electron system and then focus next to the electronic band structure calculations. The Coherent Potential Approximation(CPA) and necessity of ASR, the process of calculating the pair energies and mapping of it to the Ising model used in the present work are also described. This is the basis of the present study to electronic and magnetic properties of the clusters as well as binary alloys.

3.2 The many-body Schrödinger equation

The Schrödinger equation is the conventional point to begin description of many-electron systems. For stationary state problems the Schrödinger equation for the system of many electron and nuclei in mutual interaction can be expressed as:

$$\hat{H}|\psi>= i\hbar\frac{\partial|\psi>}{\partial t} = E|\psi> \tag{3.1}$$

where $\hat{H}$ represents the Hamiltonian of an N-electron system and can be written as (Hartree units are used throughout)

$$\hat{H} = -\sum_{I=1}^{N_c}\frac{\nabla_I^2}{2M_I} - \sum_{i=1}^{N}\frac{\nabla_i^2}{2m} + \frac{1}{2}\sum_{i,j}\frac{1}{r_{ij}} + V_{eI}(\{\mathbf{r}_i\},\{\mathbf{R}_I\}) + V_{II}(\{\mathbf{R}_I\}) \tag{3.2}$$

In short notation it can be expressed as,

$$\hat{H} = \hat{T_N} + \hat{T_e} + \hat{V_{int}} + \hat{V_{ext}} + \hat{V_{II}} \tag{3.3}$$

such that,

$\hat{T_N} = -\sum_{I=1}^{N_c} \frac{\nabla_I^2}{2M_I}$	K. E of nuclei (the I^{th} ion core having a mass M_I)
$\hat{T_e} = -\sum_{i=1}^{N} \frac{\nabla_i^2}{2m}$	K. E.of electrons(the i^{th} valence electron with mass m)
$\hat{V_{int}} = \frac{1}{2}\sum_{i,j} \frac{1}{\lvert r_i - r_j \rvert}$	Electron-electron interaction energy
$\hat{V_{ext}} = -\frac{1}{2}\sum_{i,I} \frac{Z_I e^2}{\lvert r_i - R_I \rvert}$	Ion-electron interaction energy
$\hat{V_{II}} = \frac{1}{2}\sum_{I,J} \frac{1}{\lvert R_I - R_J \rvert}$	Ion-Ion interaction energy

Hence the terms V_{II} and V_{eI} are the Coulomb interactions between the ion-ion and between the electrons and ions. r_{ij} is the distance between the i^{th} and the j^{th} electron. The terms $\hat{V_{ext}}$ makes the term inseparable. The energy terms related to the spin and magnetic moments of the particles in the interaction are omitted. The analytical solution of this equation is tedious and almost impossible for larger systems though the mathematical solution of it for single atom and very small molecules are available. In order to solve this equation analytically some reasonable and well controlled approximation has to be made so that we can able to handle most of the systems. Some of the important approximations are explained as follows.

3.2.1 Born-Oppenheimer Approximation

The equation(3.2) is complex and crucial to solve because it deals with a large number of interacting ions and electrons which have very different masses. The first step towards the simplification of the above equation is the Born-Oppenheimer approximation(BOA) (Born & Oppenheimer, 1927). As we know, ions are much heavier than electrons ($\frac{m_e}{M_I} \approx (1/1836)$ for H atom), they move much slower compared to electrons and the electrons respond instantaneously to any ionic motion. In essence the electronic and the ionic degrees of freedom can be decoupled and the electronic properties can be calculated by assuming that the ions are fixed to a particular configuration. Following this approximation, the kinetic energy of ions can be neglected and the ion-ion interaction [last term of equation(4.2)] is assumed to be constant i.e. frozen core approximation. The constant term is called Madelung energy and is calculated classically. So under BOA approximation, the many-body Hamiltonian for a system of N interacting electrons moving in the field of fixed ion cores can be expressed as,

$$\hat{H} = -\sum_{i=1}^{N} \frac{\nabla_i^2}{2m} - \frac{1}{2}\sum_{i,I} \frac{1}{|R_I - r_{ij}|} + \sum_{i>j} \frac{1}{|r_i - r_j|} \tag{3.4}$$

The wave function may then be written in a separable form $\chi(\{\mathbf{R}_I\})\psi(\{\mathbf{r}_i\}|\{\mathbf{R}_I\})$. Thus, the Schrödinger equation for the electrons (for a given position of the ion cores $\mathbf{R_I}$) can be written as:

$$\left[-\sum_{i=1}^{N}\frac{\nabla_i^2}{2m}+V_{eI}(\{\mathbf{r}_i\}|\{\mathbf{R}_I\})+\frac{1}{2}\sum_{i,j}\frac{1}{r_{ij}}\right]\psi(\{\mathbf{r}_i\}|\{\mathbf{R}_I\})=E_e(\{\mathbf{R}_I\})\psi(\{\mathbf{r}_i\}|\{\mathbf{R}_I\}) \quad (3.5)$$

3.3 Single -Particle Approximation

The total energy of the system is a sum of electron and ion-core energies. The problem in trying to solve the equation (3.5) is the number of variables involved on it. This issue has been brilliantly put forward by Hartree :"The tabulation of one variable requires a page, of two variables a volume, and of three variables a library; but the full specification of a single wave function of neutral Fe is a function of seventy eight variables. It would be rather crude to restrict to ten the number of values at which to tabulate this function, but even so, full tabulation of it would require 10^{78} entries and even if this number could be reduced somewhat from considerations of symmetry, there would still not be enough atoms in the whole solar system to provide the material for printing such a table". Thus the interpretation of the solution is a 'difficult' problem. We quote Feynman "The trouble with quantum mechanics is not only in solving the equations, but in understanding what the solutions mean". Attempts to solve these problems due to the immensely large number of variables and lack of easy interpretation has led to the development of newer and advanced approaches. Efforts have been put, therefore, to develop an effective single-particle picture, in which the system of interacting electrons can be mapped into a system of non-interacting quantum mechanical particles that approximates the behavior of original system. Two distinct approaches have been put forward in this direction: wave function approach and density functional theory.

3.4 Wave function Approach

3.4.1 Hartree's Approximation

As we mentioned earlier, equation (3.2) is too difficult to solve numerically for even a few electrons. It's main difficulty lies behind the electron-electron Coulombic interactions that tie all the variables together. The Hartree method (Hartee, (1928) is one of the first approximations that tried to deal with these complexities; it ignores the antisymmetric characteristic of the all electron wave functions. According to this theory the many-body wave function can be expressed as a product of independent single-electron functions

$\phi_i(r_i)$. The wave function of the system will be of the form,

$$\psi_H(r_1, r_2\ , ...,\ r_n) = \phi_1(r_1)\phi_2(r_2).....\phi_n(r_n) \tag{3.6}$$

The total energy will be of the form,

$$H\psi(r_1, r_2, \cdots ...., r_n) = E\psi(r_1, r_2, \cdots ....., r_n)$$

$$\begin{aligned} E &= \langle\psi|H|\psi\rangle = \int d^3r_1 \int d^3r_2..... \int d^3r_n(\phi_1^*\phi_2^*.....\phi_n^* H\phi_1\phi_2.....\phi_n) \\ &= \sum_{i=1}^{n} \int d^3r\phi_i^*(r) \left\{-\frac{\nabla^2}{2} + V_{ext}(r)\right\} \phi_i(r) \\ &+ \sum_{ij, i\neq j} \int d^3(r) \int d^3(r')\phi_i^*(r)\phi_i(r)\frac{1}{|r-r'|}\phi_j^*(r')\phi_j(r') \end{aligned}$$

The single electron wave function $\phi_i(r)$ can be obtained by minimizing the total energy subjecting to normalization condition,

$$I = \int \phi_i^*\phi_i dr = 1$$

By variation method, wave function $\psi_i(r)$ and total energy E satisfy,

$$\delta\frac{\langle\psi|H|\psi\rangle}{\langle\psi|\psi\rangle} = 0 \tag{3.7}$$

$$\begin{aligned} &\delta(E - \lambda I) \\ &= \int d^3(r)\delta\phi_i^*(r) \left\{\left(-\frac{\nabla^2}{2} + V_{ext}\right)\psi_i + \left(\int d^3(r')\frac{1}{|r-r'|}\sum_{j\neq i}\phi_i^*(r')\phi_i(r')\right)\phi_i - \lambda\phi_i\right\} \\ &+ \int d^3r\delta\phi_i(r) \left\{\left(-\frac{\nabla^2}{2} + V_{ext}\right)\phi_i^* + \left(\int d^3(r')\frac{e^2}{|r-r'|}\sum_{j\neq i}\phi_j(r')\phi_i^*(r')\right)\psi_i^* - \lambda\phi_i^*\right\} \\ &= 0 \end{aligned}$$

Now the equation of Hamiltonian in terms of $\phi_i(r)$ can be written as,

$$\left(-\frac{\nabla^2}{2} + V_{(ext)} + \int d^3r'\frac{1}{(|r-r'|)}\sum_{j\neq i}\phi_j^*(r')\phi_j(r')\right) = \lambda\phi_i(r) \tag{3.8}$$

or,

$$\left(-\frac{\nabla^2}{2} + V_{(ext)} + V_{sc}\right)\phi_i = \varepsilon_i\phi_i(i = 1, 2, 3, ...n, \lambda \to \varepsilon_i) \tag{3.9}$$

where,

$$\begin{aligned} V_{(sc)} &= V_H \\ &= \int d^3r'\frac{1}{(|r-r'|)}\sum_{j\neq i}\phi_j^*(r')\phi_j(r') \\ &= \int d^3r'\frac{1}{(|r-r'|)}n_i(r')n_i(r') \\ &= \sum_{j\neq i}|\phi_j^*(r')|^2 \end{aligned}$$

Equation (3.9) is called the Hartee's equation which can be solved self-consistently, so it is also called self consistent field approximation. This is the equation that the single particle wave function for the ith electron has to satisfy. It is an eigenvalue equation for a single electron moving in the Coulomb potential of the nucleus plus a potential due to all the other electrons. The potential due to the other electrons depends on the charge density $|\phi_{(r_j)}|^2$. This charge density is only known after the above equations has been solved for each i. The self-consistent field approximation is an iterative procedure for solving the above set of equations. A trial function is used to calculate the initial charge density. New single particle wave functions are found by numerically solving the above equations. These wave functions now yield new charge densities, which in turn yield new wave functions. The procedure is repeated until the single particle wave functions ϕ_i and the single particle energies ϵ_i do no longer change, i.e. until self consistency is reached.

The Hartree approximation is a straightforward task to calculate the variational lowest energy. However, the Hartree wave function has a very important shortcoming, which is that it fails to satisfy anti-symmetry, which states that a fermion wave-function changes sign under odd permutations of the electronic variables. This approximation can only take into account the electron-electron Coulomb repulsion in a mean-field way, but it neglects the exchange and correlation properties completely. In order to satisfy the anti-symmetry condition and to include the exchange and corelation part a more sophisticated form than that of the Hartree wave function is required.

3.4.2 Hartree-Fock Approximation

Hartree Fock theory, introduce by (Fock, 1930), is one of the simplest approximate theories for solving the many-body Hamiltonian. This approximation includes the anti-symmetric character of electronic wave function in terms of single Slater (Slater, 1937) determinant of N spin-orbitals as,

$$\psi_{HF} = \frac{1}{\sqrt{N!}} \begin{vmatrix} \phi_1(r_1, s_1) & \phi_2(r_1, s_2) & \cdots & \phi_n(r_1, s_n) \\ \phi_2(r_2, s_1) & \phi_2(r_2, s_2) & \cdots & \phi_n(r_n, s_n) \\ \vdots & \vdots & & \vdots \\ \phi_n(r_n, s_1) & \phi_n(r_n, s_2) & \cdots & \phi_n(r_n, s_n) \end{vmatrix} \tag{3.10}$$

Now the Hamiltonian in the form of $\phi_i(r)$ can be expressed as,

$$\left(-\frac{\nabla^2}{2} + V_{ext}\right) + \int d^3r' \frac{1}{(|r - r'|)} \sum_{j \neq i} \phi_j^*(r')\phi_j(r')\phi_i(r) - \sum_{j \neq i} \phi_j^*(r')\phi_i(r')\phi_j(r)\delta_{s_i s_j} = \varepsilon_i \phi_i(r) \tag{3.11}$$

Where the exchange potential can be expressed as,

$$V_x = -\sum_{j \neq i} \frac{1}{|r - r'|} \phi_j^*(r')\phi_i(r')\phi_j(r) = \varepsilon_i \phi_i(r)$$

This indicates that the screening potential includes both Hartree and exchange terms, The equation of Hartree-Fock approximation will be,

$$\left(-\frac{\nabla^2}{2} + V_{(ext)} + V_{sc}\right)\phi_i = \varepsilon_i \phi_i$$

$$V_{sc} = V_H + V_x$$

The left hand side of the equation (3.11) consists of four terms. The first and second are the kinetic energy contribution and the electron-ion potential. The third term or Hartree term, is the simply electrostatic potential arising from the charge distribution of N electrons. As written, the term includes an unphysical self-interaction of electrons when $j = i$. This term is canceled in the fourth, or exchange term. The exchange term results from our inclusion of the Pauli principle and the assumed determinantal form of the wave function. The effect of exchange is for electrons of like-spin to avoid each other. Each electron of a given spin is consequently surrounded by an "exchange hole", a small volume around the electron which like-spin electron avoid. V_x is difficult to derive in practice because it is non-local and related to the interaction between all electrons in the system. In agreement with the variational principle, the Hartree-Fock energy E^0_{HF} is higher than the exact ground state energy E^0_{exact} of the many body system and the difference $E^0_{exact} - E^0_{HF}$ is called the correlation energy. Hartree-Fock(HF) Approximation does not include the electron correlation part to the multi-electron wave function, which plays an important role in the electronic structure and binding of many solids.

In spite of the importance and achievements of the Hartree-Fock approximation, corrections beyond it are often considered due to the fact that a single determinantal state, even with the best possible orbitals, remains in general a rather poor representation of the complicated ground state wave function of a many-body system. This leads to the development of density functional theory.

3.5 Density Functional Theory(DFT)

The density functional theory(DFT) is an alternative approach based on the reduction to lower dimensions. For more than past four decades density functional theory has been the dominant method for the quantum mechanical simulation of periodic systems. It has been adopted by quantum chemists and is now very widely used for the simulation

of energy surfaces in molecules. Although the electronic wave function for the N electron system is a function of 3N variables, the expectation value $\langle\Psi|\hat{A}|\Psi\rangle$ can be calculated through other derived quantities that depend on less number of variables, if $\hat{A}$ is a sum of one- or two-particle operators, as is the case for the Hamiltonian. Thus, for the ion-core electron potential energy consisting of one-particle terms, one has :

$$\begin{aligned}&\int \Psi^*(\mathbf{r}_1,\mathbf{r}_2,...,\mathbf{r}_N)\sum_i v_{eI}(\mathbf{r}_i|\{\mathbf{R}_I\})\Psi(\mathbf{r}_1,\mathbf{r}_2,...\mathbf{r}_N)d\mathbf{r}_1 d\mathbf{r}_2...d\mathbf{r}_N \\ &= N\int d\mathbf{r}\ v_{eI}(\mathbf{r}|\{\mathbf{R}_I\})\int \Psi^*(\mathbf{r},\mathbf{r}_2,...,\mathbf{r}_N)\Psi(\mathbf{r},\mathbf{r}_2,...\mathbf{r}_N)d\mathbf{r}d\mathbf{r}_2...d\mathbf{r}_N \end{aligned} \tag{3.12}$$

All electrons are identical, so we choose any of the variables and rename it $\mathbf{r}$ and renumber the rest $\mathbf{r}_2, \mathbf{r}_3 \ldots \mathbf{r}_N$. Hence the result

$$V_{eI} = \langle\Psi|\sum_i v_{eI}(\mathbf{r}_i|\{\mathbf{R}_I\})|\Psi\rangle = \int d\mathbf{r}\ v_{eI}(\mathbf{r}|\{\mathbf{R}_I\})\rho(\mathbf{r}) \tag{3.13}$$

valid for any single-particle multiplicative operator, where the single-particle density is defined as

$$\rho(\mathbf{r}) = N\int \Psi^*(\mathbf{r},\mathbf{r}_2,...,\mathbf{r}_N)\Psi(\mathbf{r},\mathbf{r}_2,...\mathbf{r}_N)\ d\mathbf{r}_2 d\mathbf{r}_3...d\mathbf{r}_N \tag{3.14}$$

Similarly, for two-particle multiplicative operators such as the electron-electron repulsion, one can write

$$V_{ee} = \langle\Psi|\frac{1}{2}\sum_{i,j}\frac{1}{\mathbf{r}_{ij}}|\Psi\rangle = \frac{1}{2}\int d\mathbf{r}_1 d\mathbf{r}_2\ \Gamma_2(\mathbf{r}_1,\mathbf{r}_2)/\mathbf{r}_{12} \tag{3.15}$$

where the two-particle density, which gives the joint probability of finding an electron at $\mathbf{r}_1$ and an electron at $\mathbf{r}_2$, is defined as

$$\Gamma_2(\mathbf{r}_1,\mathbf{r}_2) = \frac{N(N-1)}{2}\int \Psi^*(\mathbf{r}_1,\mathbf{r}_2,...,\mathbf{r}_N)\Psi(\mathbf{r}_1,\mathbf{r}_2,...\mathbf{r}_N)d\mathbf{r}_3...d\mathbf{r}_N \tag{3.16}$$

The functional Γ_2 is often referred to as the pair density.

The reduced density functions can also be expressed as the expectation values of the corresponding density operators, viz.

$$\rho(\mathbf{r}) = \langle\Psi|\sum_i \delta(\mathbf{r}-\mathbf{r}_i)|\Psi\rangle \tag{3.17}$$

Thus we can write

$$\Gamma_2(\mathbf{r}_1,\mathbf{r}_2) = \langle\Psi|\sum_{i\neq j}\sum \delta(\mathbf{r}_1-\mathbf{r}_i)\delta(\mathbf{r}_2-\mathbf{r}_j)|\Psi\rangle \tag{3.18}$$

For the kinetic energy term which involves differential operators, one can write

$$\begin{aligned} T &= -\langle\Psi|\sum_i \frac{\nabla_i^2}{2m_i})|\Psi\rangle \\ &= -\frac{1}{2}N\int \Psi^*(\mathbf{r}_1,\mathbf{r}_2,...,\mathbf{r}_N)\,\nabla_1^2\,\Psi(\mathbf{r}_1,\mathbf{r}_2,...\mathbf{r}_N)\;d\mathbf{r}_1 d\mathbf{r}_2...d\mathbf{r}_N \\ &= -\frac{1}{2}N\int \left[\frac{\nabla_1^2}{2m_1}\Psi^*(\mathbf{r}_1,\mathbf{r}_2,...,\mathbf{r}_N)\Psi(\mathbf{r}_1,\mathbf{r}_2,...\mathbf{r}_N)\right]_{r_1=r_1'} d\mathbf{r}_1 d\mathbf{r}_2...d\mathbf{r}_N \\ &= -\frac{1}{2}\int d\mathbf{r}_1\;\left[\frac{\nabla_1^2}{2m_1}\gamma(\mathbf{r}_1;\mathbf{r}_1')\right]_{r_1=r_1'} \end{aligned} \tag{3.19}$$

with the first-order reduced density matrix defined as

$$\gamma(\mathbf{r}_1;\mathbf{r}_1') = N\int \Psi^*(\mathbf{r}_1',\mathbf{r}_2,...,\mathbf{r}_N)\Psi(\mathbf{r}_1,\mathbf{r}_2,...\mathbf{r}_N)d\mathbf{r}_2 d\mathbf{r}_3...d\mathbf{r}_N \tag{3.20}$$

Clearly, the following relationships among the reduced density functions and matrices hold good.

$$\begin{aligned} \rho(\mathbf{r}_1) = \gamma(\mathbf{r}_1,\mathbf{r}_1) \quad ; \quad \Gamma_2(\mathbf{r}_1,\mathbf{r}_2) = \Gamma_2(\mathbf{r}_1,\mathbf{r}_2;\mathbf{r}_1,\mathbf{r}_2) \\ \int \rho(\mathbf{r}_1)d\mathbf{r}_1 = N \quad ; \quad \int \Gamma_2(\mathbf{r}_1,\mathbf{r}_2)d\mathbf{r}_1 d\mathbf{r}_2 = N(N-1) \\ \gamma(\mathbf{r}_1;\mathbf{r}_1') = \gamma^*(\mathbf{r}_1';\mathbf{r}_1) \quad ; \quad \rho(\mathbf{r}_1) = \frac{1}{N-1}\int \Gamma_2(\mathbf{r}_1;\mathbf{r}_2)d\mathbf{r}_2 \end{aligned} \tag{3.21}$$

For spin-polarized situation one has to include the spin dependence, such that,

$$\begin{aligned} \rho(x) \equiv \rho(\mathbf{r}\;s) \quad ; \quad \int dx \rightarrow \sum_s \int d\mathbf{r} \quad ; \quad \rho(\mathbf{r}) = \sum_s\;\rho(x)ds \\ \rho(\mathbf{r}) = \rho_\uparrow(\mathbf{r}) + \rho_\downarrow(\mathbf{r}) \qquad s(\mathbf{r}) = \rho_\uparrow(\mathbf{r}) - \rho_\downarrow(\mathbf{r}) \end{aligned} \tag{3.22}$$

The total energy can thus be expressed in terms of the reduced density matrices (RDM) as

$$E[\rho,\gamma,\Gamma_2] = T[\gamma(\mathbf{r}_1;\mathbf{r}_1')] + V_{eI}[\rho(\mathbf{r})] + V_{ee}[\Gamma_2(\mathbf{r}_1,\mathbf{r}_2)] + V_{II} \tag{3.23}$$

where V_{II} is the ion-core - ion-core interaction energy. This leads to the possibility of developing the quantum mechanics of many-electron systems in reduced space in terms of the RDM's bypassing the wave function. One of the important requirement is the possibility of direct determination of RDM by minimizing the energy with respect to the RDM's for which the effect of the Pauli exclusion principle has to be built-in into the RDM's. The existence of an antisymmetric ψ from which the RDM's can be obtained has to be guaranteed.

This is so called N-representability problem which has to be solved by imposing necessary and sufficient conditions on $\gamma_1(\mathbf{r}_1;\mathbf{r}_1^{'})$ and $\Gamma_2(\mathbf{r}_1,\mathbf{r}_2)$, which are unfortunately not yet known. The N-representability conditions on $\rho(\mathbf{r})$ are however known and are very simple, viz.

$$\int \rho(\mathbf{r})d\mathbf{r} = N; \qquad \rho(\mathbf{r}) \geq 0. \tag{3.24}$$

This makes the single-particle density (simplest reduced quantity) a promising candidate for the formulation of quantum mechanics in reduced space. Some of the many advantages for the electron density $\rho(\mathbf{r})$ to be the basic variable are :

(a) it is a function in 3D space in which we live and perceive,

(b) it is simpler to tabulate and plot,

(c) it provides a better visualization and

(d) it is an experimental observable, thus enabling one to compare the results of theoretical calculations directly with experiments.

Now we must resolve the frequently raised question that whether it is possible to develop a quantum theory in terms of density alone bypassing the wave function, for which one has to ensure if (a) the density contains sufficient information (b) calculation of the properties and the energy is possible from the density alone (c) it is possible to develop a method for the direct calculation of density. To resolve such problem many people have been explored a leading theory for the possibility of a density description of many-electron systems, so called density functional theory (DFT). Although the first DFT, viz. the Thomas Fermi method has existed since 1927, the birth of modern DFT has been come in to action through the formal proof of a theorem by Hohenberg and Kohn.

3.5.1 Hohenberg-Kohn Theorem

The Hohenberg-Kohn Theorem (Hohenberg, 1964) establishes the density as the basic variable. This theorem states that the ground-state density $\rho(\mathbf{r})$ of a bound system of interacting electrons in an external potential $v(\mathbf{r})$ determines this potential uniquely (up to an uninteresting additive term).

Consider the ground states of two N-electron systems characterized by the two external potentials (differing by more than an additive constants) $v_1(\mathbf{r})$ and $v_2(\mathbf{r})$ with corresponding Hamiltonian:

$$H_1 = T + U + \sum_i v_1(r_i) \quad ; \quad H_2 = T + U + \sum_i v_2(r_i)$$

where

$$T = -\frac{1}{2}\sum_i^N \nabla_i^2 \quad \text{and} \quad U = \frac{1}{2}\sum_{i\neq j} \frac{1}{|\mathbf{r}_i - \mathbf{r}_j|}$$

with the corresponding Schrödinger equation, $H_1\psi_1 = E_1\psi_1; H_2\psi_2 = E_2\psi_2$ and we assume that the two wave functions ψ_1 and ψ_2 yield the same density as,

$$\rho(\mathbf{r}) = N \int \psi^*_{1|2}(\mathbf{r}, \mathbf{r}_2, ..., \mathbf{r}_N)\psi_{1|2}(\mathbf{r}, \mathbf{r}_2, ...\mathbf{r}_N)\; d\mathbf{r}_2 d\mathbf{r}_3 ... d\mathbf{r}_N \tag{3.25}$$

Now,

$$\begin{aligned} E_1 &= \langle\Psi_1|H_1|\Psi_1\rangle \;\leq\; \langle\Psi_2|H_1|\Psi_2\rangle \\ &\leq \langle\Psi_2|H_2|\Psi_2\rangle + \langle\Psi_2|H_1 - H_2|\Psi_2\rangle \\ &\leq E_2 + \int dr\rho(r)[v_1(\mathbf{r}) - v_2(\mathbf{r})]. \end{aligned} \tag{3.26}$$

Now, similarly one could show that,

$$E_2 \leq E_1 + \int dr\rho(r)[v_2(\mathbf{r}) - v_1(\mathbf{r})]. \tag{3.27}$$

Summation of the above two inequalities leads to the contradiction

$$E_1 + E_2 \leq E_2 + E_1 \tag{3.28}$$

Hence the assumption of identical density arising from the two different external potentials is wrong. Thus a given $\rho(r)$ can only correspond to only one $v(\mathbf{r})$. If $v(\mathbf{r})$ is fixed, the Hamiltonian and hence the wave functions are also fixed by density $\rho(\mathbf{r})$. Since the wave function is a functional of density, the energy functional $E_v[\rho]$ for a given ion-core - electron potential $v_{eI}(\mathbf{r})$ is a unique functional of density. It can also be directly proved that this energy functional assumes a minimum value for the true density.

The Hohenberg-Kohn(HK) theorem has the far reaching consequences that requires a simple elaborations. A most important consequence is the formulation of the variational principle concerning to the ground state density of the system. Following the H-K theorem, the energy functional can be expressed in the form as,

$$E^{(HK)}[\rho(r); v_{ext}] = T[\rho(r)] + V_{ee}[\rho(r)] + \int v_{ext}(r)\rho(r)dr \tag{3.29}$$

The energy functional $E^{(HK)}[\rho(r); v_{ext}]$, which exists and is unique, is minimal at the exact ground state density and it's minimum gives the exact ground state energy of the

many-body electron system. The functional $F[\rho] = T[\rho(r)] + V_{ee}[\rho(r)]$ is called universal i.e. it doesn't depend on v_{ext}, which is not known explicitly and must be approximated appropriately.

From above description it can be said that HK theorem gives a one-to-one correspondence between $\rho_{(r)}$ and ψ_0, the ground state wave function. However it has following few limitations, like

(a) There is restriction to determine ψ_0 for a given ρ_0,

(b) It is not applicable to degenerate state.

This formulation also has an another problem that the density ρ_r was V-representable; though almost all problems in condensed matter physics can be formulated via this type of density, it is not the general one. (Levy, 1979) and (Lieb, 1982) introduced an alternative definition of the Hohenberg-Kohn theorems in their series of papers. This is a two step minimization, where we have to deal only the space of trial wave functions instead of searching the full N-particle Hilbert space for the trial density, which ultimately gives the density $\rho_0(r)$.

3.5.2 Kohn-Sham Equation

Kohn-Sham equations (Kohn & Sham, 1965) are obtained by minimizing the energy functional (3.29) with respect to $\rho(r)$. The minimization of $E_v[\rho]$ subject to the constraint of normalized density, as given by equation (3.24), leads to the Euler equation for the direct calculation of density, viz.

$$\delta[E_v[\rho] - \mu \int \rho(\mathbf{r}) d\mathbf{r} - N] = 0$$
$$\frac{\partial E}{\partial \rho} - \mu = 0 \Rightarrow \mu = \frac{\partial E}{\partial \rho} = v(\mathbf{r}) + \frac{\partial F}{\partial \rho}. \tag{3.30}$$

The important part of the problem is to obtain an expression for the energy functional in terms of density, the general form of it will be

$$E_v[\rho] = \int v_{eI}(\mathbf{r}) \rho(\mathbf{r}) d\mathbf{r} + F[\rho] \tag{3.31}$$

where $F[\rho]$ is a universal functional of density. The comparison of the energy functional in terms of the RDM's gives,

$$E_v[\rho, \gamma, \Gamma_2] = T[\gamma] + \int v_{eI}(\mathbf{r}) \rho(\mathbf{r}) d\mathbf{r} + \frac{1}{2} \int \int \frac{\Gamma_2(\mathbf{r}_1, \mathbf{r}_2)}{\mathbf{r_{12}}} d\mathbf{r}_1 d\mathbf{r}_2 \tag{3.32}$$

and using the decomposition we have

$$\Gamma_2(\mathbf{r}_1, \mathbf{r}_2) = \rho(\mathbf{r}_1)\rho(\mathbf{r}_2)[1 - f(\mathbf{r}_1, \mathbf{r}_2)] \tag{3.33}$$

where $f(\mathbf{r}_1, \mathbf{r}_2)$ is the correlation function. We can separate out from the electron-electron repulsion term from it. The classical electrostatic contribution can be written as,

$$E_{Hartree}[\rho] = \frac{1}{2}\int\int \frac{\rho(\mathbf{r}_1)\rho(\mathbf{r}_2)}{\mathbf{r}_{12}} d\mathbf{r}_1 d\mathbf{r}_2 \tag{3.34}$$

The exact kinetic energy functional $T[\rho]$ is usually replaced by the kinetic energy of a system of non-interacting particles $T_s[\rho]$ and the contribution from the electron-electron interaction energy other than the classical electrostatic contribution and the difference $T[\rho] - T_s[\rho]$ constitute what is known as the exchange-correlation (xc) energy functional $E_{xc}[\rho]$. Thus, one can write

$$E_v[\rho] = \int v(\mathbf{r})\rho(\mathbf{r})d(\mathbf{r}) + E_{Hartree}[\rho] + T_s[\rho] + E_{xc}[\rho]. \tag{3.35}$$

Thus E_{xc} is simply the sum of the error made in treating the electrons classically and in the error made in using a non-interacting kinetic energy. We note at this point that the nomenclature in general use and also used in the present context, exchange-correlation (xc) energy functional is quite misleading as stated above the E_{xc} contains an element of the kinetic energy and is not the sum of the exchange and correlation energies.

There are three major problems in evaluating the functional $E_v[\rho]$: (i) evaluation of the correct ground state charge density $\rho(r)$, for that we need a method of self-consistently (ii) evaluation of $T_s[\rho]$ with given $\rho(r)$ only cannot be done straightforwardly as there is no information on wave functions and (iii) the functional $E_{xc}[\rho]$ remains unknown and must therefore be represented in some simple and sufficiently accurate form. The scheme for obtaining the non-interacting kinetic energy functional $T_s[\rho]$ for a certain $\rho(\mathbf{r})$ is through the solution of the one-particle Schrödinger equations

$$\left[-\frac{1}{2}\bigtriangledown^2 + \lambda(\mathbf{r})\right]\ \psi_i = \epsilon_i\psi_i \tag{3.36}$$

for a suitably chosen $\lambda(\mathbf{r})$ such that the resulting orbitals yield the density as

$$\rho(\mathbf{r}) = \sum_i |\psi_i|^2 \tag{3.37}$$

and then evaluating the functional as

$$T_s[\rho] = \sum_i \epsilon_i - \int dr\lambda(\mathbf{r})\rho(\mathbf{r}). \tag{3.38}$$

The energy functional that is to be minimized for determining the correct equilibrium density is then given by

$$E_v[\rho] = \sum_i \epsilon_i - \int dr\lambda(\mathbf{r})\rho(\mathbf{r}) + \int v_{eI}(\mathbf{r})\rho(\mathbf{r})d(\mathbf{r}) + E_{Hartree}[\rho] + E_{xc}[\rho] \tag{3.39}$$

which leads to the variational condition

$$\partial E_v[\rho] = 0 = \sum_i \delta\epsilon_i - \int d\mathbf{r}\delta\lambda(\mathbf{r})\rho(\mathbf{r}) + \int \delta\rho(\mathbf{r})[-\lambda(\mathbf{r}) + v_{eI}(\mathbf{r}) + \tag{3.40}$$

$$\frac{\partial E_{Hartree}}{\partial\rho(\mathbf{r})} + \frac{\partial E_{xc}}{\partial\rho(\mathbf{r})} \tag{3.41}$$

Considering the expression for ϵ_i,

$$\epsilon_i = -\langle\Psi_i|\frac{1}{2}\bigtriangledown_i^2|\Psi_i\rangle + \langle\Psi_i|\lambda(\mathbf{r})|\Psi_i\rangle \tag{3.42}$$

we get,

$$\begin{aligned}\delta\epsilon_i &= \langle\delta\Psi_i|\frac{1}{2}\bigtriangledown_i^2|\Psi_i\rangle + \langle\delta\Psi_i|\lambda(\mathbf{r})|\Psi_i\rangle + c.c. + c.c. + \langle\Psi_i|\delta\lambda(\mathbf{r})|\Psi_i\rangle \\ &= \epsilon_i\delta\langle\Psi_i|\Psi_i\rangle(=0) + \langle\Psi_i|\delta\lambda(\mathbf{r})|\Psi_i\rangle \end{aligned} \tag{3.43}$$

and hence the result:

$$\sum\delta\epsilon_i = \int dr\rho(\mathbf{r})\delta\lambda(\mathbf{r}) \tag{3.44}$$

which in combination with the variational condition leads to the result

$$\delta E_v[\rho] = 0 = \int dr\delta\rho(\mathbf{r})[-\lambda(\mathbf{r}) + v_{eI}(\mathbf{r}) + \frac{\partial E_{Hartree}}{\partial\rho(\mathbf{r})} + \frac{\partial E_{xc}}{\partial\rho(\mathbf{r})}] \tag{3.45}$$

Since the variation of $\delta\rho(\mathbf{r})$ is arbitrary, the bracketed quantity must be zero and hence we have

$$\lambda(\mathbf{r}) = v_{eI}(\mathbf{r}) + \frac{\partial E_{Hartree}}{\partial\rho(\mathbf{r})} + \frac{\partial E_{xc}}{\partial\rho(\mathbf{r})} \tag{3.46}$$

This clearly shows that if one chooses $\lambda(\mathbf{r})$ given by this expression, the single particle Schrödinger equation leads to the correct density for the system. This provides the basis for the Kohn-Sham (K-S) density functional scheme which involves solution of a set of N nonlinear integro-differential equations:

$$[-\tfrac{1}{2}\bigtriangledown^2 + v_{eff}(\mathbf{r};\rho)]\psi_i = \epsilon_i\psi_i$$

with the effective potential given by

$$v_{eff}(\mathbf{r}) = v_{eI}(\mathbf{r}) + \int \frac{\rho(\mathbf{r}')}{|\mathbf{r}-\mathbf{r}'|}d\mathbf{r}' + \frac{\delta E_{xc}}{\delta\rho(\mathbf{r})} = \phi(\mathbf{r}) + \frac{\delta E_{xc}}{\delta\rho(\mathbf{r})} \tag{3.47}$$

where, $\bigtriangledown^2\phi = 4\pi\rho(\mathbf{r})$ and the density is calculated as

$$E_v[\rho] = \sum_i \epsilon_i - \frac{1}{2}\int\int \frac{\rho(\mathbf{r})\rho(\mathbf{r}')}{|\mathbf{r}-\mathbf{r}'|}drdr' + E_{xc}[\rho] - \int d\mathbf{r}\rho(\mathbf{r})\frac{\partial E_{xc}}{\partial\rho(\mathbf{r})} \tag{3.48}$$

for spin-polarized situations, incorporating the spin-components of the density as well we have,

$$E_v[\rho_\alpha,\rho_\beta] = T_s + \int v(\mathbf{r})\rho(\mathbf{r})d(\mathbf{r}) + E_{Hartree}[\rho] + T_s[\rho] + E_{xc}[\rho_\alpha,\rho_\beta]. \tag{3.49}$$

and the Kohn-Sham equation under the spin-polarized situation becomes

$$[-\frac{1}{2}\bigtriangledown^2 + v_{eff}(\mathbf{r};\rho_\sigma)]\psi_{k\sigma} = \epsilon_{k\sigma}\psi_{k\sigma} \tag{3.50}$$

with an effective potential given by

$$v_{eff,\sigma}(\mathbf{r}) = v(\mathbf{r}) + \int \frac{\rho(\mathbf{r}')}{|\mathbf{r}-\mathbf{r}'|}d\mathbf{r}' + \frac{\delta E_{xc}[\rho_\alpha,\rho_\beta]}{\delta\rho_\sigma(\mathbf{r})} \tag{3.51}$$

The corresponding density is given by

$$\rho(\mathbf{r}) = \textstyle\sum_i |\psi_{k\sigma}|^2$$

This set of non-linear equations (the Kohn-Sham equations) describe the behavior of non-interacting "electrons" in an effective local potential. For the exact functional, and thus exact local potential, the "orbitals" yield the exact ground state density and corresponding energy. The Kohn-Sham approach gives an exact correspondence of the density and ground state energy of a system consisting of non-interacting Fermions and the "real" many body system described by the Schrödinger equation. The correspondence of the charge density and energy of the many-body and the non-interacting system is only exact if the exact functional is known. In this sense Kohn-Sham density functional theory is an empirical methodology - we do not know (and have no way of systematically approaching) the exact functional. The functional what we discuss is universal - it does not depend on the materials being studied. In principle, We try to solve the Schrödinger equation exactly and determine the energy functional and its associated potential. This, of course, involves a greater effort than a direct solution for

the energy. We need good approximations (theory) which has the ability to determine the exact properties of the universal functional, modifications over it and used for wide range of materials to evaluate $E_{xc}[\rho]$.

3.6 Exchange-Corelation Functional

As discussed previously, there are three major difficulties in evaluating the functional $E_v[\rho]$ i.e. evaluation of charge density $\rho(r)$, $T_s(\rho)$ and $E_{xc}[\rho]$. The charge density is calculated through self consistent solution of equation(4.35) and hence the $T_s(\rho)$ but the crux of the problem is to solve third difficulty i.e. the exact form of $E_{xc}[\rho]$. This is still unknown and it's a great challenge in DFT. It is to be noted that this exchange-correlation energy contains (i) kinetic correlation energy, which is the difference in the kinetic energy functional between the real and the non-interacting system,(ii) the exchange energy, which arises from the requirement of antisymmetric nature of fermions, (iii) Coulombic correlation energy, which arises from the inter-electronic repulsion and (iv) a self-interaction correction. Large number of approximations have been suggested to estimate the $E_{xc}[\rho]$ but most important and successful approximations in predicting most of the material properties are briefly discussed in the following section.

3.6.1 The Local density approximation(LDA)

The generation of approximations for E_{xc} has lead to a large and still rapidly expanding field of research. There are now many different flavors of functional available which are more or less appropriate for any particular study. In the early days practical implementations of density functional theory was dominated by one particular system for which near exact results could be obtained - the homogeneous electron gas. In this system the electronic charge density (ρ) is uniform due to a constant external potential faced by the electrons. Thomas and Fermi studied the homogeneous electron gas in the early twentieth century (Fermi,1928). The orbitals of the system are, by symmetry, plane waves.

If the electron-electron interaction is approximated by the classical Hartree potential (that is exchange and correlation effects are neglected) then the total energy functional can be readily computed. Under these conditions the dependence of the kinetic and exchange energy on the density of the electrons can be extracted and expressed in terms of a local functions of density. This suggests that in the inhomogeneous system we might approximate the functional as an integral over a local function of the charge density. Using the kinetic and exchange energy densities of the non-interacting homogeneous

electron gas leads to;

$$T[\rho] = 2.87 \int \rho^{\frac{5}{3}}(\mathbf{r}) d\mathbf{r} \tag{3.52}$$

and

$$E_x[\rho] = 0.74 \int \rho^{\frac{4}{3}}(\mathbf{r}) d\mathbf{r} \tag{3.53}$$

These results are highly suggestive of a representation for E_{xc} in an inhomogeneous system. The local exchange correlation energy per electron might be approximated as a simple function of the local charge density (say, $\epsilon_{xc}^{LDA}(\rho)$). That is, an approximation of the form;

$$E_{xc}^{LDA}[\rho] = \int \rho(\mathbf{r}) \epsilon_{xc}^{LDA}(\rho(\mathbf{r})) d\mathbf{r} \tag{3.54}$$

An obvious choice is then to take $\epsilon_{xc}^{LDA}(\rho)$ to be the exchange and correlation energy density of the uniform electron gas of density ρ. This is the *local density approximation (LDA)*. Within the LDA, $\epsilon_{xc}^{LDA}(\rho)$ is a function of only the local value of the density. It can be separated into exchange and correlation contributions;

$$\epsilon_{xc}^{LDA}(\rho) = \epsilon_{x}^{LDA}(\rho) + \epsilon_{c}^{LDA}(\rho) \tag{3.55}$$

The Dirac form can be used for E_x^{LDA};

$$\epsilon_{x}^{LDA}(\rho) = -C\rho^{\frac{1}{3}} \tag{3.56}$$

Where C, is arbitrary constant. This functional form is widely applicable in the homogeneous electron gas. The functional form for the correlation energy density, ϵ_c^{LDA}, is unknown and has been simulated for the homogeneous electron gas in numerical quantum Monte Carlo calculations which yield essentially exact results (Ceperley & Alder, 1980). It is a remarkably noteworthy fact that the LDA works as well as it does in the reduction of the energy functional to a simple local function of the density. This is mainly due to the fact that in LDA there are very significant errors in the exchange and correlation energies but, as the exchange energy is generally underestimated and the correlation energy overestimated, these errors tend to cancel. This cancellation of errors is the most successful parts of LDA.

Further insight into the behavior of functional can be obtained by examining how well they approximate Γ_2 - the probability of finding an electron at $\mathbf{r}_1$ and an electron at $\mathbf{r}_2$. LDA seems to make a very poor approximation of Γ_2. At this moment, we are faced with the question- how can the LDA produce such reasonable energetics if the functional Γ_2 is so poorly described by it? The answer is based on the structure of the Coulomb

operator. We remember from equation (3.15) that the electron-electron interaction can be written as;

$$V_{ee} = \frac{1}{2}\int d\mathbf{r}_1 d\mathbf{r}_2 \Gamma_2(\mathbf{r}_1, \mathbf{r}_2)/\mathbf{r}_{12} \tag{3.57}$$

From this it seems a poor approximation to Γ_2 leads to a poor estimate of the electron-electron interaction. However, the Coulomb operator depends only on the magnitude of the separation of $\mathbf{r}_1$ and $\mathbf{r}_2$, $\mathbf{r}_{12}$. We can re-write V_{ee} as ::

$$\begin{aligned} V_{ee} &= \frac{1}{2}\int d\mathbf{r}_1 d\mathbf{r}_{12} \Gamma_2(\mathbf{r}_1, \mathbf{r}_1 + \mathbf{r}_{12})/\mathbf{r}_{12} \\ &= \frac{1}{2}\int_0^\infty 4\pi|\mathbf{r}_{12}|^2 \left[\frac{\int \Gamma_2(\mathbf{r_1}, \mathbf{r_1} + \mathbf{r_{12}})}{\mathbf{r}_{12}} \frac{d\Omega_{r_{12}}}{4\pi}\right] dr_{12} \end{aligned} \tag{3.58}$$

Thus the electron-electron interaction depends only on the spherical average of the pair density - P($\mathbf{r}_{12}$);

$$P(\mathbf{r_{12}}) = \int \mathbf{\Gamma_2}(\mathbf{r_1}, \mathbf{r_1} + \mathbf{r_{12}}) \mathbf{dr_1} \frac{\mathbf{d\Omega_{r_{12}}}}{\mathbf{4}\pi} \tag{3.59}$$

The LDA makes a reasonable approximation to this spherically averaged pair density. This explains the success of the LDA.

Thus, we can conclude that the remarkable performance of the LDA is a consequence of its reasonable description of the spherically averaged pair density along with the tendency for errors in the exchange energy density to be canceled by errors in the correlation energy density.

3.6.2 The Generalized Gradient Approximation (GGA)

In the generalized gradient approximation (GGA), the exchange-correlation functional E_{xc} depends on the density and its derivative as,

$$E_{xc}^{GGA}[\rho] = \int \rho(\mathbf{r}) \epsilon_{xc}^{GGA}(\rho(\mathbf{r}), |\bigtriangledown \rho(\mathbf{r})|) d\mathbf{r} \tag{3.60}$$

Now one can use the GGA functional by (Perdew & Wang, 1992), Perdew, Burke and Ernzerhof (PBE) (Perdew, *et al.*, 1996) and Becke's formula
(Becke, 1988) for the exchange part combined with Perdew's formula (Perdew, 1986) for correlation. The GGA improves significantly on the LDA's description of the binding energy of molecules. The exchange energy of spin polarized case can be constructed with the help of the non polarized case as,

$$E_{xc}^{G}GA[\rho\uparrow, \rho\downarrow \rho\uparrow] = \int dr f(\rho\uparrow, \rho\downarrow, \nabla\rho\uparrow, \nabla\rho\downarrow) \tag{3.61}$$

$$E_{xc}^{GGA-PBE}[\rho\uparrow, \rho\downarrow \rho\uparrow] = \int dr \rho \epsilon_x(\rho) F_{xc}(r_s, \xi, s) \tag{3.62}$$

Where $\rho(r) = \rho\uparrow + \rho\downarrow$, $\rho(r) = \rho\uparrow$ and $\rho\downarrow$ are the density of electrons with majority and minority spin. $\xi = \frac{\rho\uparrow - \rho\downarrow}{\rho}$ is the local polarization. We used GGA in PBE form of functional for all the calculations in this thesis.

3.7 Hybrid Functional

The LDA or GGA applied in the frame work of density-functional theory(DFT) solve most of the problems related to materials. It fails to describe important properties of materials with correlated orbitals. In Particular, structural parameters and atomic positions agree with experimental values typically within 3% and mechanical properties such as elastic constants are reproduced within 5% errors in most cases
(Park, *et al.*, 2011). This level of accuracy is particularly impressive given that exchange-correlation energies of electrons are greatly simplified in (semi)local functionals. Again, there is one critical drawback found in (semi)local functional for the energy gap, which is severely underestimated by $30 - 40\%$. This is because DFT is based on the ground state formalism and the energy gap is essentially an excited-state property. The energy-gap underestimation in the conventional DFT limits it's application in several places. For example, the position of defect levels with respect to band edges inevitably suffer from the error in the band-gap. In addition, Schottky barriers formed at metal-insulator interfaces are also underestimated (Jeon *et al.*2006).
This failure is generally attributed to the fact that the exchange and correlation energy is too crudely treated in the frame of the LDA or GGA approximations. To overcome these difficulties, several methods have been proposed in the literature (Anisimov, *et al.*, 1991), (Anisimov *et al.*, 1997), (Jollet, *et al.*, 2009). A first attempt is the LDA+U method. It leads to an orbital-dependent potential for the orbitals that are supposed to be localized, which corrects an aspect of the failure of the LDA approximation. Although it is possible to calculate the Hubbard parameter U, it is in practice considered as a parameter. The LDA+U method is a static approximation of the more general dynamical mean-field theory that treats on site interactions. This method is very promising, but for the moment, one need also to use a U parameter and the calculations are very time consuming. Another attempt is the self-interaction-corrected SIC. LDA that removes the self-interactions of orbitals supposed to be localized. Interesting results have been obtained with this method but plane-wave implementations are scarce and the calculations are also very time consuming. Due to above reasons and difficulties we choose hybrid functional present in the VASP code.

A lot of work has also been devoted to new exchange correlation functional, and among them, hybrid functional which combine Hartree-Fock (HF) exact exchange functional with LDA or GGA functional. These functional have shown to be very accurate for molecules, transition metal monoxides (TMOs) and the adsorption of carbon monoxide on d-metal surfaces (Marsman, *et al.*, 2008). The short descriptions of them are as follows.

3.7.1 PBE0

The PBE0 Hybrid functional is one of the successful approximation, which is constructed by mixing 25% of HartreeFock exchange to 75% of the well known PBE exchange (Ernzerhof & Scuseria, 1999), (Ernzerhof, *et al.*, 1996). The electronic correlation is represented by the corresponding part of the PBE density functional. Thus the resulting exchangecorrelation energy expression takes the following simple form:

$$E_{xc}^{PBE0} = \frac{1}{4}E_X^{HF} + \frac{3}{4}E_X^{PBE} + E_C^{HF} \tag{3.63}$$

where E_X^{PBE} and E_CPBE denote the PBE exchange and correlation energies, respectively. The $1:3$ mixing ratio of HartreeFock to PBE exchange is based on a conceptual model devised by Ernzerhof and co-workers (Perdew, *et al.*, 1996). Hybrid functionals based on their work are often called parameter free or non-empirical, since the amount of HartreeFock exchange to be admixed is not determined by a fit to experimental data.

3.7.2 HSE

Depending on the decay of the HartreeFock exchange interactions with distance, the evaluation of E_X^{HF} may be computationally very demanding. The decay is highly system dependent and may range from a few to hundreds of Angstroms. To avoid the calculation of expensive integrals over slowly decaying exchange interactions, (Heyd, *et al.*,2006) proposed to replace the long-range part of the HartreeFock exchange in the PBE0 HF/DFT hybrid by a corresponding density functional counterpart. The resulting expression for the exchange correlation energy (HSE03) is given by

$$E_{xc}^{HSE03} = \frac{1}{4}E_X^{HF,SR,\mu} + \frac{3}{4}E_X^{PBE,SR,\mu} + E_X^{PBE,LR,\mu} + E_C^{PBE} \tag{3.64}$$

where (SR) and (LR) denote the short-range and long-range parts of the respective exchange interactions (HF or PBE exchange). The separation of the exchange interactions into short-range and long-range parts is accomplished through a decomposition of the Coulomb kernel as,

$$\frac{1}{r} = S_\mu(r) + L_\mu(r) = \frac{erfc(\mu r)}{r} + \frac{erfc(\mu r)}{r} \tag{3.65}$$

where $r = |r - r'|$ and μ is the parameter that defines the range separation. μ is related to a characteristic distance, $(\frac{2}{\mu})$, at which the short-range interactions become negligible. Thus $E_X^{HF,SR,\mu}$ is given by equation (4.63), provided one replaces the Coulomb kernel by $S_\mu(r)$. The short-range and long-range parts of the PBE exchange energy are derived using the same decomposition as in equation (3.65). Empirically, it was shown that the optimum range-separation parameter μ is between 0.2 and 0.3 A^{-1}. Consequently, the HSE03 functional is a semi-empirical functional. In general, one finds that the results using HSE03 are very similar to those obtained using the PBE0. If we choose screening parameter μ as 0.2 A^{-1} we called it so called HSE06.

3.7.3 B3LYP

The B3LYP functional follows the formal structure of the hybrid functional proposed by (Becke, 1993). The exchange energy is given by

$$E_X^{B3LYP} = 0.8E_X^{LDA} + 0.2E_X^{HF} + 0.72\Delta E_X^{B88} \tag{3.66}$$

where E_X^{LDA} and ΔE_X^{B88} are the LDA exchange and the gradient corrections to the Becke exchange, respectively. The B3LYP correlation energy is defined as

$$E_C^{B3LYP} = 0.19E_C^{VWN3} + 0.81E_C^{LYP} \tag{3.67}$$

where E_C^{VWN3} and E_C^{LYP} denote the correlation energy from the Vosko-Wilk-Nusair III and the Lee-Yang-Parr correlation functional (Lee, *et al.*, 1988) respectively. The B3LYP functional is a semi-empirical functional. The coefficients in equations (3.66) and (3.67) are determined by a least square fit to atomization energies, electron and proton affinities and the ionization potentials of the atomic species and molecules in Poples G2 test set.

In the present calculation, we used PBE and HSE types of functional which yields the results very close and comparable to the experimental results.

3.8 General Band structures Methods

In order to solve the single-particle Kohn-Sham and to obtain the eigenvalues (band structure) and eigenfunction, a number of methods have been introduced. These methods are based on either k-space approach or real space approach and are applicable to both finite systems such as molecules or clusters as well as extended systems such as disordered solids. The most important methods frequently used in condensed mater physics are, localized muffin-tin orbital method or LCAO, Plane wave methods and

Atomic sphere methods. Out of them we used last two method in this thesis. The plane wave method is used for the calculation of clusters, which is based on k-space approach and fixed energy based basis set i.e. Plane wave. The atomic sphere method is used to deal with disordered binary solids which is based on real space approach and based on partial wave like basis set.

3.8.1 Basis set

Basis set is an important factor for the band structure calculation, whether we follow the k-space approach or real-space approach. There are various types of basis sets reported and we have to choose an appropriate basis set to expand the single-particle wave-functions. Depending on the choice of basis functions, different schemes, therefore, can be broadly grouped into two categories: (i) methods using energy independent basis sets or fixed basis sets, like tight binding method using linear combination of atomic orbitals (LCAO) type basis (Slater & Koster,1954), orthogonalized plane wave (OPW) method within a pseudo-potential scheme using plane waves orthogonalized to core states as the basis set and (ii) methods using energy dependent basis set, like cellular method (Philips & Kleinman, 1959), augmented plane wave (APW) method (Loucks, 1967) and the Korringa-Kohn-Rostocker (KKR) Greens function method (Korringa, 1994), which use partial waves as basis set. In the methods of fixed basis set, by standard variational techniques one obtains a set of linear eigenvalue equations given by

$$(H - \epsilon O).b = 0 \tag{3.68}$$

in terms of the Hamiltonian H and overlap matrix O to determine the eigenvalues ϵ and the expansion coefficients b. Most of the fixed basis set uses pseudo-potential for the electron-ion interaction, where localized core states are got rid of by replacing the strong crystalline potential by a weak pseudo-potential, while giving faithful determination of the valence and conduction bands. Pseudo-potential in conjunction with plane wave basis has become one of the most versatile and efficient approaches for calculating electronic properties. Methods of partial waves, on the other hand, result in a secular equation of the form,

$$M(\epsilon).b = 0 \tag{3.69}$$

In contrast to equation (3.68) which is a polynomial in ϵ, the equation(4.68) has a complicated non-linear energy dependence. We have no a priori idea how many roots we expect, nor whether all roots are physically permissible. The partial wave methods though complicated to solve, do have advantages. Firstly, they provide solutions of arbitrary accuracy for a muffin-tin potential and for closed packed systems, this makes

them far more accurate than the traditional fixed basis methods. Secondly, the information about the potential enters only via a few functions of energy. However as already stated, it has the disadvantage of being computationally heavy, the eigen energy ϵ_j must be found individually by tracing the roots of the determinant of M as a function of ϵ. To overcome this, Andersen first proposed a unified approach for linear methods (Andersen, 1975) such as linear augmented plane wave (LAPW) and linear muffin-tin orbital (LMTO) methods which are the linearized versions of APW and KKR methods, respectively. These methods therefore lead to secular equations like (3.68) rather than (3.69) and combine the desirable features of the fixed basis and partial wave methods. In this thesis, we use pseudo-potential method along with plane wave basis, as implemented in the Vienna ab initio simulation package (VASP) (Kresse & Hafner, 1993, 1996), to study finite sized clusters. Being finite sized objects, cluster calculations have been done using super-cell technique and structural optimization is performed using conjugate gradient or quasi-Newtonian dynamics. For disordered binary system we used TB-LMTO-ASR approach, on which we used LMTO self-consistent potential as inputs. Therefore, in the following two subsections, we discuss the pseudo-potential method and LMTO method in greater details.

3.8.2 Pseudo-potentials and Plane waves

Plane wave basis are orthonormal and energy independent. They convert the Kohn-Sham equation to a simple matrix eigenvalue problem for the expansion coefficients. Moreover, plane waves are atom and atomic position independent. In such calculations, the single electron wave function is expanded using plane wave basis $\exp(i\mathbf{G}.\mathbf{r})$, where the candidate G's are the reciprocal vectors of the unit cell used. The most important advantage of plane wave basis is its ability to perform the exact variational calculation based on a discrete numerical grid, i.e., instead of doing actual real space integrations, we can do a summation over a real space grid, the results are exactly the same.

The plane wave calculations require that the wave function be described by plane waves within a certain energy cut-off E_{cut}. In order to reduce E_{cut} to a reasonable value the wave function should be smooth. While it is often smooth at the chemically important bonding area, near the nuclei, the valence wave functions often have a lot of wiggles. These wiggles must exist so that the valence wave functions are orthogonal to the deep level core wave functions. Besides, it is difficult to describe those chemically-not-important core wave functions using plane wave basis. To overcome these difficulties, pseudo-potentials are developed. Basically, using a Pseudo-potentials, the core states will no longer exist, and the valence pseudo-wave functions become smooth near

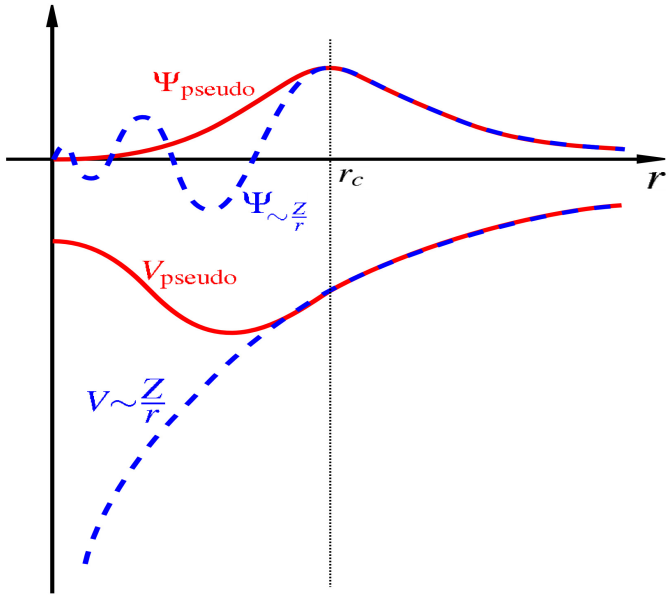

Figure 3.1: *The model of pseudo-potential*

the nuclei. Using this technique the unwanted singular behavior of the ionic potential at the lattice points can be removed. A good pseudo-potential wave function should be soft and transferable (Vanderbilt, 1985). A pseudo-potential is soft if it requires less number of plane waves. A pseudo-potential is transferable if it works considerably well in different environments. However, to have these good properties, it is necessary to have different pseudo-potentials for s, p and d states, i.e. the pseudo-potential is angular momentum dependent (non-local pseudo-potential).

3.8.3 Projector Augmented Wave

The drawback of the pseudo-potential method is that all information on the full wave function close to the nuclei is lost. This can influence the calculation of certain properties, such as hyperfine parameters and electric field gradients. Another problem is that one has no before hand knowledge of when the approximation yields reliable results.

A different approach is the augmented-plane-wave method(APW), in which space is divided into atom-centered augmented spheres inside which the wave functions are taken as some atom-like partial waves, and a bonding region outside the spheres, where some envelope functions are defined. The partial waves and envelope functions are then matched at the boundaries of the spheres. A more general approach is the projector augmented wave method (PAW) which is used in this thesis, which offers APW as a special case and the pseudo-potential method as a well defined approximation. The PAW method was first proposed by (Blöchl, 1994).

The projector augmented wave (PAW) method separates the Kohn-Sham wave functions, which displays rapid oscillations in some parts of space, and smooth behavior in other parts of space into auxiliary functions which are smooth everywhere and a contribution which contains rapid oscillations, but only contributes in certain, small, areas of space. Having separated the different types of waves they can be treated individually. Thus the Kohn-Sham total energy E can be separated into a part calculated on smooth functions $\tilde{E}$ and some atomic corrections ΔE^a, involving quantities localized around the nuclei only

$$E = \tilde{E} + \sum_a \Delta E^a \tag{3.70}$$

where the smooth part $\tilde{E}$ is the usual energy functional, but evaluated on the smooth functions $\tilde{\rho}$ instead of ρ and with the soft compensation charges $\tilde{Z}$ instead of nuclei charges $Z(\mathbf{r})$.

3.9 Linear Muffin-Tin Orbital Method

The tight binding linear muffin-tin orbital (TB-LMTO) method is a specific implementation of density functional theory within the local density approximation (LDA) (Skriver, 1984).[1]. In this method there is no shape approximation to the crystal potential, unlike methods based on the atomic-spheres approximation (ASA) where the potential is assumed to be spherically symmetric around each atom. For mathematical convenience the crystal is divided up into regions inside muffin-tin spheres, where Schrödinger equation is solved numerically, and an interstitial region. In all LMTO methods the wave functions in the interstitial region are Hankel functions. Each basis function consists of a numerical solution inside a muffin-tin sphere matched with value and slope to a Hankel function tail at the sphere boundary. The so-called multiple-kappa basis is composed of two or three sets of s, p, d, etc. LMTOs per atom. The extra variational degrees of freedom provided by this larger basis allow for an accurate treatment of the potential in the interstitial region. The first approximation in using atomic sphere method, is that the potential in the crystal has a local spherical symmetry and extremely flat at the interstitial region. This approximation is called atomic sphere approximation(ASA). The wave function at energy E can be written as

$$\psi_j(\mathbf{k}, \mathbf{r}) = \sum_{lm} b^{jk}_{Rlm} \psi_{Rl}(E, |\mathbf{r} - \mathbf{R}|) Y^m_l(\widehat{\mathbf{r} - \mathbf{R}}) \tag{3.71}$$

[1]The discussion of this part has been taken from the book *The LMTO method: muffin-tin orbitals and electronic structure* by H.L. Skriver

where b^{jk}_{Rlm} is the expansion coefficient of the partial wave, Y^m_l is a spherical harmonics, i^l is a phase factor which associates in spherical harmonics and ψ_{Rl} a solution of radial Schrödinger equation

$$\left[-\frac{d^2}{dr^2}+\frac{l(l+1)}{r^2}+v(\mathbf{r})-E\right]r\psi_l(E,\mathbf{r})=0 \tag{3.72}$$

The equation (3.72) is used for spherical harmonics (Condon & Shortley, 1935) gives Phase conventions. (Wigner & Seitz, 1934) suggested the spherically symmetric potential to extend until the boundary of atomic polyhedron. The wave functions in solid is then expressed as Bloch sum of equations

$$\psi_j(\mathbf{k},\mathbf{r})=\sum_R \mathbf{e}^{i\mathbf{k}\dot{\mathbf{R}}}\sum_{lm} b^{jk}_{lm}\delta(\mathbf{r}-\mathbf{R})\psi_l(E;|\mathbf{r}-\mathbf{R}|Y^m_l(\widehat{\mathbf{r}-\mathbf{R}}) \tag{3.73}$$

where δ inside atomic sphere is unity and zero outside. This cellular method is too tough for applying boundary conditions however it gave rise to KKR (named after Korringa, Kohn and Rostoker and LMTO) method and Wigner-Seitz rule of energy band. In Augmented Plane-wave(APW) of Slater, a muffin-tin(MT) sphere is inscribed in each atomic sphere. Inside the sphere, the potential is spherically symmetric and wave functions are expanded as Wigner-Seitz partial wave. Korringa and later Kohn and Rostoker expand the MT spheres similar to cellular and APW. The interstitial potential is flat and wave functions are expanded as phase shifted spherical wave. Boundary conditions are expressed as condition for self-consistent multiple scattering between the MT spheres. Later (Andersen, 1975) linearizes this method which is one of the most used method of solving the KS equation.

3.9.1 Korringa, Kohn and Rostoker Method

In the $KKR-ASA$, MT and interstitial region is divided into overlapping atomic spheres (ASs). The total volume of the ASs thus equals the total crystal volume. Any point r in the space is denoted by (r,R), where R is the index for th AS and $\mathbf{r}=(r,\hat{r})=(r,\theta,\phi)(r<R)$ is the vector denoting the position in each AS. Here R represents the radius of AS with azimuthal angle ϕ.

Starting point for KKR is an energy dependent orbital definded as

$$\chi_{lm}(E,\mathbf{r})=Y^m_l\begin{cases}\psi_l(E,r)+p_l(E)(\frac{r}{S}) & r<S\\ (\frac{S}{r})^{l+1} & r>S\end{cases} \tag{3.74}$$

where $\psi_l(E,r)$ is the solution of equation(3.74) and S is the radius of atomic sphere. This muffin-tin orbital(MTO) is regular, continuous and differentiable over all space.

The potential function $p_l(E,r)$ and normalization of $\psi_l(E,r)$ requires continuity and differentiability at the sphere boundary with the boundary conditions

$$p_l(E) = \frac{D_l(E)+l+1}{D_l(E)-1}, \tag{3.75}$$

$$Where,\ D_l(E) \ = \ \frac{S}{\psi_l(E,S)}\frac{\partial\psi_l(E,\mathbf{r})}{\partial r}|_{r=S} \tag{3.76}$$

is the logarithmic derivative function.

The tail of the orbital, $(\frac{S}{r})^{l+1}$ is the solution of Poisson's equation $\nabla^2 X = 0$, which has zero kinetic energy. So, the tail centered at $\mathbf{R}$ can be expanded around the origin in terms of spherical harmonics with shifted in phase, which yields,

$$\sum_{R\neq 0}\mathbf{e}^{i\mathbf{k}\dot{\mathbf{R}}}(\frac{S}{|\mathbf{r}-\mathbf{R}|})^{l+1}Y_l^m\widehat{(}\mathbf{r}-\mathbf{R}) = \sum_{l'm'}\frac{-1}{2(2l'+1}(\frac{r}{S})^{l'}Y_{l'}^{m'}(\hat{(}\mathbf{r})S^{\mathbf{k}}_{l'm',lm} \tag{3.77}$$

where $S^{\mathbf{k}}_{l'm',lm}$ is the canonical structure constant, converges inside the sphere of nearest neighbor.

The first term of MTO $Y_l^m(\hat{\mathbf{r}})\psi_l(E,\mathbf{r})$ is already a solution of eqation(3.72) and is the one-center expansion with origin at $\mathbf{r}$. For any other sphere, therefore, the term is

$$\sum_{lm} a^{j\mathbf{k}}_{lm}Y_l^m(\hat{\mathbf{r}})\psi_l(E,\mathbf{r}) \tag{3.78}$$

provided tails from all other sphere cancel the term

$$\sum_{lm} a^{j\mathbf{k}}_{lm}Y_l^m(\hat{\mathbf{r}})p_l(E)(\frac{r}{S})^l \tag{3.79}$$

where $a^{j\mathbf{k}}_{lm}$ is the expansion coefficient of MTO. From equation 3.77, the condition for this tail cancellation is

$$\sum_{lm}\left[P_l(E)\delta_{ll'}\delta_{mm'} - S^{\mathbf{k}}_{l'm',lm}\right]a^{j\mathbf{k}}_{lm} = 0 \tag{3.80}$$

where P_l is defined as

$$P_l(E) = 2(2l+1)\frac{D_l(E)+l+1}{D_l-1} \tag{3.81}$$

Solution of secular form of equation(3.80) gives eigenvectors $a^{j\mathbf{k}}_{lm}$ iff

$$det\left[P_l(E)\delta_{ll'}\delta_{mm'} - S^{\mathbf{k}}_{l'm',lm}\right] = 0 \tag{3.82}$$

This is the secular determinant of KKR-ASA approach.

3.9.2 Muffin-tin potential

The basic assumption of muffin-tin orbital is that in the neighborhood of an ion-core the potential seen by the electron in a solid is not very different from that of the atomic ion-core. This neighborhood is spherically symmetric with radius S centered at R. In the interstitial region the potential is flat, called muffin-tin potential(V_{MT}).

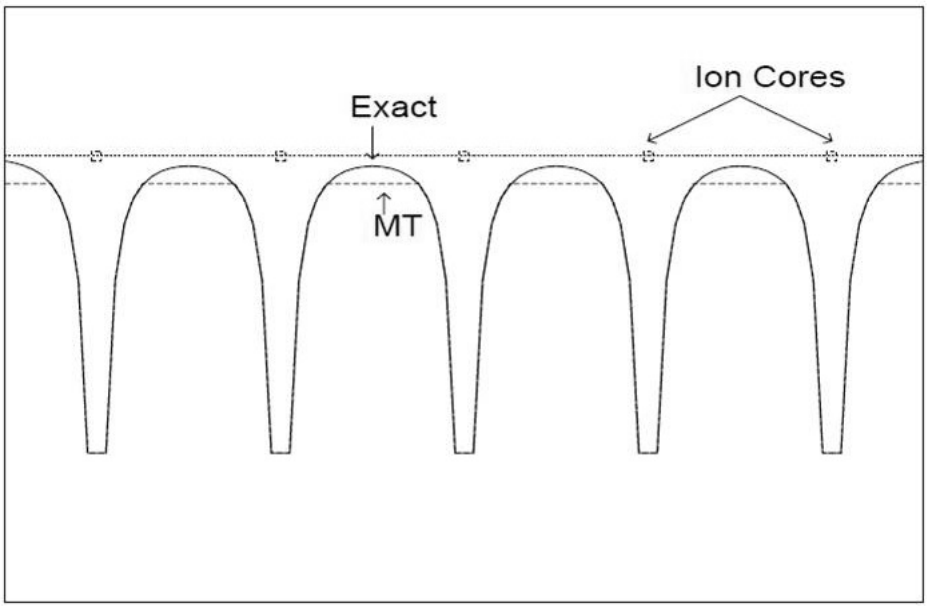

Figure 3.2: *Model of muffin-tin potential*

In muffin-tin potential is defined as

$$V_{MT}(\mathbf{r}-\mathbf{R}) = \begin{cases} \upsilon(|r-R|) - V_{MT} & r \leq S \\ 0 & r \geq S \end{cases} \tag{3.83}$$

is the muffin-tin potential where $\mathbf{R}$ and $\mathbf{r}$ are the positions of the ion-cores and electrons respectively. Thus Hamiltonian can be written as:

$$H = \nabla^2 + \sum_R V_{MT}(|\mathbf{r}-\mathbf{R}|) - \kappa^2 + E \tag{3.84}$$

where κ is the kinetic energy in the extended region, $\kappa^2 = E - V_{MT}$. Equation(3.72) has been solved numerically for radial solution $\psi_l(E,\mathbf{r})$ written in terms of Hankel and Bessel functions,

$$\psi_L(\epsilon,\kappa,\mathbf{r}) = Y_L(\hat{\mathbf{r}}) \begin{cases} \psi_l(\epsilon,\mathbf{r}) + \kappa cot(\eta_l(\epsilon)) j_l(\kappa r) & r \geq S \\ \kappa \eta_l(\kappa r) & r \leq S \end{cases} \tag{3.85}$$

with MT basis set

$$\chi_L^{MTO}(\epsilon,\kappa,\mathbf{r}) = Y_L(\hat{\mathbf{r}}) \begin{cases} \psi_l(\epsilon,\mathbf{r}) + \kappa cot(\eta_l(\epsilon)) j_l(\kappa r) & r \leq S \\ \kappa \eta_l(\kappa r) & r \geq S \end{cases} \tag{3.86}$$

where S is the muffin-tin sphere radius. j_l and n_l are the spherical Bessel function is defined as

$$j_l(\kappa\mathbf{r}) \rightarrow \begin{cases} \frac{(\kappa r)^l}{(2l+1)!} & \kappa r \rightarrow 0 \\ \frac{\sin(\kappa r + \frac{l\pi}{2})}{\kappa r} & r \rightarrow \infty \end{cases} \tag{3.87}$$

and spherical Neumann function is given by

$$\eta_l(\kappa\mathbf{r}) \rightarrow \begin{cases} -\frac{(2l-1)!}{(\kappa r)^{2l+1}} & \kappa r \rightarrow 0 \\ -\frac{\cos(\kappa r + \frac{l\pi}{2})}{\kappa r} & r \rightarrow \infty \end{cases} \tag{3.88}$$

which means j_l is regular both at origin and at ∞ , where n_l is regular at ∞ only and diverges at origin. This yields a bound state envelop function which is real and regular both inside (since $j_l(\kappa r)$ is regular at origin) and outside (since $n_l(\kappa r)$ is regular at infinity) the sphere. The inclusion of $j_l(\kappa r)$ in the single particle basis set includes the effect of neighbors so that the minimal basis set is capable of describing the full system. Anderson's method of linearization (Andersen & Kasowski, (1971), (Andersen & Jepsen, 1984) shows that the basis can be written as

$$\chi_{RL}^{\alpha} = \phi_{RL}(\mathbf{r_R}) + \sum \dot{\phi}_{R'L'}^{\alpha}(\mathbf{r'_R}) h_{R'L',RL}^{\alpha} \tag{3.89}$$

where $\dot{\phi}_{R'L'}^{\alpha}(\mathbf{r'_R})$ is linear combination of ϕ and $\dot{\phi}$ and given by

$$\dot{\phi}_{R'L'}^{\alpha} = \dot{\phi}_{R'L'}^{\alpha} + \phi_{R'L'} o_{R'L'}^{\alpha} \tag{3.90}$$

here, $o_{R'L'}^{\alpha}$ is overlap matrix and Hamiltonian matrix h^{α} are defined as,

$$h^{\alpha} = C^{\alpha} - \epsilon_{\nu} + (\nabla^{\alpha})^{1/2} S^{\alpha} (\nabla^{\alpha})^{1/2}. \tag{3.91}$$

where C^{α} and ∇^{α} are the diagonal potential matrices (parameters) defined as

$$C^{\alpha} = \epsilon_{\nu} - \frac{P^{\alpha(\epsilon_{\nu})}}{\dot{P}^{\alpha}(\epsilon_{\nu})}, (\nabla^{\alpha})^{1/2} \frac{1}{\dot{P}^{\alpha}(\epsilon_{\nu})} \tag{3.92}$$

These are called band center and band width respectively. Each set of α is also characterized by screening parameters. The numerical value of site independent constants are firstly calculated by Andersen and Jepsen. These are as,

$$\alpha = \left\{ \begin{array}{lll} 0.3458 & l=0 & (s) \\ 0.0530 & l=1 & (p) \\ 0.0107 & l=2 & (d) \end{array} \right\}. \tag{3.93}$$

LMTO, together with this screening parameters are called tight-binding (TB)-LMTO sets. Also, for the self consistency to achieve, a correction term, named combined correction is attached. The corresponding (corrected) Hamiltonian is given by

$$H^{\alpha} = C^{\alpha} + (\nabla^{\alpha})^{1/2} S^{\alpha} (\nabla^{\alpha})^{1/2} - \left(\kappa^2 + v_0\right) \delta_{\kappa^2 h^{\alpha}} \tag{3.94}$$

3.10 The Recursion Technique.

Bloch's theorem (Ashcroft & Mermin, 1976) has rigid requirements of lattice translational symmetry. The implementation of it to systems with surfaces or/and randomness is very difficult. Our present work is based on real space vector recursion technique which is the generalized version of scalar recursion technique. Here, we will discuss the scalar recursion technique in brief. The real-space based scalar recursion method (introduced by (Haydoc *et al.*, 1972) (details given in (Mookerjee, 2003) is a very convenient approach for the determination of the eigen-solutions of matrices, especially those of very large rank and sparse character (i.e. with many matrix elements equal to zero). In the electronic calculation the recursion method has been originally introduced in connection with local basis representation of the electronic states in solids and expands solution to the Schrödinger equation in a sequence of increasingly delocalized functions. Considering $|0\}$ to be the orbital on which the solutions are to be projected, the recursion method uses the electronic Hamiltonian H to generate a sequence of orbitals $|1\}, |2\}, \ldots |n\}, \ldots$ which are the successively less-localized. These orbitals are related to one another by H according to the three-term recurrence relation,

$$H|n\} = \alpha_n|n\} + \beta_{n+1}|n+1\} + \beta_n|n-1\} \tag{3.95}$$

where $|-1\}$ is taken to be zero and the dependence of these orbitals on position, spin and other coordinates has not been considered. The projection of the solution onto $|0\}$, the projected density of states (PDOS), is the singular part of a solution to the above recurrence, namely the continued fraction,

$$G(E) = \cfrac{1}{E-\alpha_0-\cfrac{\beta_1^2}{z-\alpha_1-\cfrac{\beta_2^2}{z-\alpha_2-\cfrac{\beta_3^2}{z-\alpha_3-\cfrac{\beta_4^2}{\ddots}}}}} \tag{3.96}$$

Now, the parameters $\{\alpha_n, \beta_n\}$ need to be determined.

The construction of the three term recurrence relation and its solution as a continued fraction can be carried out either analytically or numerically; the only real difference being whether the parameters $\{\alpha_n, \beta_n\}$ can be expanded as functions of n.

In analytic, applications, the electronic states are mapped onto systems of orthogonal polynomials which satisfy the same recurrence as the Hamiltonian. When this happens, the PDOS is the weight distribution for the polynomials, and the eigenstates of the

Hamiltonian can be expanded in the polynomials. In such cases, the mathematical properties of the many known polynomial systems can be applied to physical problems. Otherwise, the $\{\alpha_n, \beta_n\}$ can be computed using some basis for the $\{n\}$.

In a numerical approach to recursion, the orbitals $\{n\}$ must be expanded in some basis which should be as similar to the recursion orbitals as possible. Though the recursion orbitals are not known beforehand, which is why the numerical approach is essential, still a good choice of basis helps a lot. The best basis is the one for which the Hamiltonian is most sparse, has most of the matrix elements zero. It is seen that this criterion is usually achieved by functions similar to the valence orbitals of atoms, not necessarily orthogonal, but decaying exponentially at large distances. Another essential requirement for the choice of basis is that it should be easy to calculate the matrix elements of the Hamiltonian. This is facilitated by the use of a two-center approximation (involving a two-center integral). The tight-binding approximation is such an approximation (Bullett,1980). It gives very simple parametrization of the Hamiltonian matrix elements for various orientations of the orbitals and atoms. The assumption behind tight-binding is that there are negligible contributions from the potential centered on one atom to Hamiltonian matrix elements for hopping from an orbital centered on a second atom to an orbital centered on a third atom. The *d*-electrons in transition metals are sufficiently localized for this approximation to work well, but fails quantitatively for less localized valence electrons such as the *s*- and *p*- electrons.

In the recursion approach Haydock devised a scheme to transform the basis in such a way that the Hamiltonian of the system has a tri-diagonal form. A new orthonormal basis set $|n\}$ in which the Hamiltonian is tri-diagonal is constructed by the three term recurrence formula mentioned earlier. The first recursion orbital $|0\}$, is assumed to have a normalization of unity, and is the one on which the states are to be projected. Thus this orbital plays a significant role in determining the specific physical property and the new state $|1\}$ takes the form as,

$$\beta_1|1\} = H|0\} - \alpha_0|0\} \tag{3.97}$$

The whole set of orthonormal states are generated by the following three term recurrence relation:

$$\beta_{n+1}|n+1\} = H|n\} - \alpha_n|n\} - \beta_n|n-1\} \tag{3.98}$$

α_n and β_n are the coefficients to orthogonalized $H|n\}$ to the preceding vectors $|n\}$, $|n-1\}$ and β_{n+1} is the coefficient to normalize $|n+1\}$ to unity. β_0 is assumed to be unity. In the new basis, the Hamiltonian matrix elements are,

$$\{n|H|n\} = \alpha_n \ ; \ \{n-1|H|n\} = \beta_n \text{ and } \{n|H|m\} = 0 \tag{3.99}$$

In this new representation, the Hamiltonian has the following tri-diagonal form,

$$\begin{pmatrix} \alpha_0 & \beta_1 & 0 & 0 & 0 & 0 & 0 \\ \beta_1 & \alpha_1 & \beta_2 & \ddots & 0 & 0 & 0 \\ 0 & \beta_2 & \alpha_2 & \beta_3 & \ddots & 0 & 0 \\ 0 & \ddots & \beta_3 & \alpha_3 & \beta_4 & \ddots & 0 \\ 0 & 0 & \ddots & \ddots & \ddots & \ddots & 0 \\ 0 & 0 & \ddots & \ddots & \ddots & \ddots & 0 \end{pmatrix} \tag{3.100}$$

The above transformation can be graphically represented as the transformation of a d-dimensional system to a semi-infinite linear chain. $\{\alpha_n\}$ and $\{\beta_n\}$ are represented as the on-site term and the coupling between two sites.

As we have discussed earlier, we can not apply Bloch's theorem for systems where the lattice symmetry breaks down,so we take recourse to an alternative approach to calculate the electronic properties instead of solving Schrodinger equation. In this approach, properties are extracted from the corresponding Green function of the system which is defined as the resolvent of the Hamiltonian :

$$G(z) = (zI - H)^{-1}$$

In the recursion method, we use the same approach and calculate the diagonal elements of the Green function which is directly related to the density of states, spectral functions, structure factors etc. and most of the material properties follow thereafter. The starting state of recursion is then :

$$|0\} = |R, \alpha\rangle$$

where R indicates the position of the R-th unit cell and α the Cartesian direction.

The diagonal element of the Green function by definition is,

$$G_{00}(E) = \{0|(EI - H)^{-1}|0\} = \frac{M_1(E)}{M_0(E)} = \frac{1}{G_1(E)}$$

where M_0 and M_1 are the determinant of the matrix $(EI - H)^{-1}$ (represented in the new basis $\{|n\}\}$) and the determinant of the matrix obtained from the original matrix by deleting the first row and column respectively.

By using Cauchy's expansion theorem we have,

$$\begin{aligned} M_n(E) &= (E - \alpha_n)M_{n+1} - \beta_{n+1}^2 M_{n+2} \\ G_{n+1} &= E - \alpha_n - \frac{\beta_{n+1}^2}{G_{n+2}} \end{aligned} \tag{3.101}$$

This suggests that it is possible to express the Green function as a continued fraction expansion characterized by a set of coefficients,

$$G_{00}(E) = \cfrac{1}{E - \alpha_0 - \cfrac{\beta_1^2}{E - \alpha_1 - \cfrac{\beta_2^2}{E - \alpha_2 - \cfrac{\beta_3^2}{E - \alpha_3 - \cfrac{\beta_4^2}{\ddots}}}}} \tag{3.102}$$

where the coefficients $\{\alpha_n\}$ and $\{\beta_n\}$ are the ones appearing in the tri-diagonal matrix H.

In any practical calculation we can go only up to a finite number of steps, consistent with our computational process. This limits the number of atoms that can be modeled, and also implies that one is always studying a finite system. The terminating continued fraction obtained in this process yields a number of isolated bound states, appropriate for a finite clusters. For most purpose this is an unphysical approximation to the problem under investigation and one needs to overcome these finite size effects by the embedding the clusters in an infinite medium. Mathematically a suitable terminator should be appended to the continued fraction so as to obtain a Green function with a branch cut, rather than a set of simple poles. Several terminators are available in the literature (Beer & Pettifor, 1984),(Luchini & Nex, 1987) which reflects the asymptotic properties of the continued fraction expansion of the Green function accurately. The advantage of such a termination procedure is that the approximate resolvent retains the analytic properties of the Green function, called the Herglotz properties which are as follows :

- All the singularities of G(z) lie on the real z-axis.
- $\Im$m [G(z)]>0 when $\Im$m (z)<0 and $\Im$m [G(z)]<0 when $\Im$m (z)>0.
- G(z)$\rightarrow$ $1/z$ when $\mathcal{R}$e(z)$\rightarrow$ ∞ along the real axis. Terminator preserves the first 2n-moments of the density of states exactly.

In case the coefficients converge, i.e. if $|\alpha_n - \alpha| \leq \epsilon$, $|\beta_n - \beta|] \leq \epsilon$ for $n \geq N$, we may replace $\{\alpha_n, \beta_n\}$ by $\{\alpha, \beta\}$. for all $n \geq N$. In that case the asymptotic part of the continued fraction may be analytically summed to obtain :

$$T(E) = (1/2)\left(E - \alpha - \sqrt{(E-\alpha)^2 - 4\beta^2}\right)$$

which gives a continuous spectrum $\alpha - 2\beta \leq E \leq \alpha + 2\beta$. The terminator coefficients are related to the band edges and widths so that a sensible criterion for the choice of these asymptotic coefficients is necessary, so as not to give arise to spurious structures

in our calculations. (Beer & Pettifor, 1984) suggested a sensible criterion : given a finite number of coefficients, we must choose $\{\alpha, \beta\}$ in such a way so as to give, for this set of coefficients, the minimum bandwidth consistent with no loss of spectral weight from the band.

3.11 Augmented Space Recursion

This section deals with the study of the configuration space, averaging procedure, mathematical form augmented space theorem in general and application of it to the binary systems are described systematically.

3.11.1 Configuration averaging in disordered systems

One of the crucial and vital task to deal with the disordered systems is taking averaging which plays an important role in quantum mechanics and statistical physics. At finite temperatures, different possible states of a canonical ensemble, for example, are occupied with Boltzmann probabilities and observable physical properties are averages over the ensembles. Similarly, when we wish to measure a given physical observable in a quantum system, the result of the measurement is spread over different possible states with probabilities given by squared amplitudes of the wave function projection onto those states. With the realization of the need to beyond the CPA, several attempts have been reported which are broadly classified into two categories:

(1) Non-self consistent clusters approach which assumed a clusters consisting of a central site and its shell of nearest neighbor(NN) embedded in an effective medium and
(2) Self-consistent cluster approach within which great deal of work has been done, mostly in tight binding models. Among them travailing cluster approximation(TCA) and augmented space formalism(ASF) (Mookerjee, 1973) are the only approaches which have been proved to be analytic, while preserving the conservation laws and sum rules. The ASF is originally developed in the tight binding frame work provides self-consistent cluster coherent potential approximation in which one can go beyond CPA in the systematic way (Mookerjee & Prasad, 1993). In this method, the effective medium is determined by the self consistency condition that the averaging scattering from all possible configurations of the real cluster embedded in the effective medium be zero. The following sections provides the more detail theoretical description about the augmented space theorem and its mathematical description which is applicable for binary alloys.

3.11.2 Mathematical description of the configuration space

The visualization of configuration space of a set of random variables is most essential to understand the augmented space theorem. This can be done by taking the example of Ising model. The model consists of set of spins σ_R arranged in a discreet lattice labeled by R. Each spin σ_R can have two possible states or configurations denoted as $|\uparrow_R\rangle$ and $|\downarrow_R\rangle$. The collection of all linear combination of these two states $a|\uparrow_R\rangle + b|\downarrow_R\rangle$ is called configuration space of σ_R. It is of rank two and is spanned by the states $|\uparrow_R\rangle$ and $|\downarrow_R\rangle$. Let us represent this space ϕ_R. The set of, say, N points then have 2^N possible configurations each of which can be written as sequence of m-up states and (N-m) down states. The ordering of this sequence is crucial, since different orderings corresponds to different configurations. The number (N-m) states is defined as cardinality of the configuration and the sequence C of sites $R_{i_1}, R_{i_2} \cdots R_{i_{N-m}}$. where the down states sit is called the cardinality sequence of the configuration. For example, take a particular configuration of 5 spins: $|\uparrow_1\downarrow_2\downarrow_3\uparrow_4\downarrow_5\rangle$. It has has a cardinality 3 and the cardinality sequence $\{2, 3, 5\}$. Another configuration $|\downarrow_1\uparrow_2\downarrow_3\downarrow_4\uparrow_5\rangle$ also has a cardinality 3, but its cardinality sequence is $\{1, 3, 4\}$. These two configurations are distinct from each other. Note that the cardinality sequence uniquely describes the configuration and is a very convenient way of labeling the different configurations $|C_k\rangle$ where $(k = 1, 2, 3, ...2^N)$ of the set of N spins. The configuration space Φ is of rank 2^N and can be written as a direct product of the configuration spaces of the individual spins.

$$\Phi = \Pi_R \bigotimes \phi_R$$

The generalization of these ideas when the spins can have $n > 2$ states is quite straight forward. The configuration of an individual spin can be labeled as $|k_R\rangle$. where $k_R = 1, 2, 3, ..., n$. The rank of ϕ_R is now n, the set of N spins has n^N configurations. The cardinality of the configuration of an individual spin can be defined as the particular k_R and cardinality sequence which uniquely describes a configuration of the set of N spins is the sequence $k_1, k_2, ...k_N$. if we now translate our idea from spins σ_R to the random variables ε_R of the Anderson model, we can immediately visualize the configuration space of the Hamiltonian variables ε_R. When these terms have a binary distribution, their configuration space is isomorphic to the one for collection of Ising spins. Let us now assume that the variable ε_R are independently distributed and the probability densities are given by $\rho(\varepsilon_R)$. We shall take into account only those probability densities which have finite moments to all orders.

Physically relevant densities almost all fall in this category. Since the probability densities are positive definite functions, we can always write them as spectral densities of a

positive definite operator which is formulate as follows:

$$\rho(\varepsilon_R) = (\frac{-1}{\pi})Im\langle\emptyset|((\varepsilon - R + iO)\mathbf{I} - \mathbf{M}_R)^{-1}|\emptyset\rangle = Img(\varepsilon_R + iO) \tag{3.103}$$

if $\rho(\varepsilon_R)$ has a binary distribution, taking the values 0 and 1 with probabilities x and $y = 1 - x$, then a representation of $\mathbf{M}$ is:

$$\begin{pmatrix} x & \sqrt{xy} \\ \sqrt{xy} & y \end{pmatrix}$$

We may interpret this in terms of the configuration space ϕ_R introduced earlier. The configuration space is spanned by the states $|0\rangle$ and $|1\rangle$, which are eigen-states of $\mathbf{M}_R$ with eigenvalues 0 and 1. This is rather similar to the description in quantum mechanics, where an observable taking a random set of values in associated with an operator whose eigenvalues are possible values observed and the states of the system in which the observable takes a particular value corresponds to the related eigenvalue.

The operator $\mathbf{M}_R$ in the configuration space ϕ_R will be associated with the random variable ε_R. The representation of $\mathbf{M}_R$, shown above, is in a different basis:

$$|\emptyset\rangle = \left(\sqrt{x}|0\rangle + \sqrt{y}|1\rangle)\right)$$

$$|R\rangle = \left(\sqrt{y}|0\rangle - \sqrt{x}|1\rangle)\right)$$

The reason for choosing this particular basis will become clear later. The state $|\emptyset\rangle$ will be called the average state of the system.

For the general probability distribution, we may always find the representation of operator $\mathbf{M}_R$ in similar basis by first expanding the probability density as a continued fraction.

$$g(\varepsilon_R) = -(1/\pi)\cfrac{1}{\varepsilon_R - a_0 - \cfrac{b_1^2}{\varepsilon_R - a_1 - \cfrac{b_2^2}{\ddots}}}$$

Here, $p(\varepsilon_R) = Img(\varepsilon_R)$.

Since $p(\varepsilon_R) = Img(\varepsilon_R)$ is a positive definite function with finite moments to all orders, $p(\varepsilon_R)$ can be expanded as a convergent continued fraction.
The required representation of the matrix M_i, is given by

$$\begin{pmatrix} a_0 & b_1 & 0 & 0 & \cdots \\ b_1 & a_1 & b_2 & 0 & \cdots \\ 0 & b_2 & a_2 & b_3 & \cdots \\ \cdots & \cdots & \cdots & \cdots & \cdots \end{pmatrix}$$

The average state is defined by $|\emptyset\rangle = \sum_k \sqrt{x_k}|k\rangle$ where k are the random values taken by ε_R with probabilities x_k. The other members of the countable basis $|n\rangle$, in which

the above representation of M_R is given, may be obtained recursively from the average state through:

$$|0\rangle = |\emptyset\rangle$$

$$b_1|1\rangle = M_R|0\rangle - a_0|0\rangle$$

$$b_n|n\rangle = M_R|n-1\rangle - a_{n-1}|n-1\rangle - b_{n-1}|n-2\rangle$$

.

3.11.3 The augmented space theorem

To explain the augmented space theorem, consider the average of a well-behaved function $f(\varepsilon_R)$ of ε_R.
From the definition

$$\ll f(\varepsilon_R) \gg = \int f(\varepsilon_R) p(\varepsilon_R) d\varepsilon_R$$

This equation may be rewritten as:

$$\ll f(\varepsilon_R) \gg = \oint f(z) g(z) dz$$

The integral is taken over a closed contour enclosing the singularities of $g(z)$ but not any of $f(z)$. In this case $f(z)$ is assumed as well-behaved, means it has no singularities in the neighborhood of a singularity of $g(z)$. We now expanded the function $g(z)$ in the basis of its eigen-states $|\mu\rangle$ of M_i. These may be either discrete or continuous.

This expansion can be written as a Stielje's integral in terms of the spectral density function $\rho(\mu)$ of M_i,

$$\ll f(\varepsilon_R) \gg = \int d\rho(\mu) \langle\emptyset|\mu\rangle [\oint f(z)(z-\mu)^{-1}] \langle\mu|\emptyset\rangle$$

$$= \langle\emptyset| [\int d\rho(\mu) |\mu\rangle f(\mu) \langle\mu|] \emptyset\rangle$$

The second line requires the function to be well behaved at infinity. The expression in the brackets on the right side of the bottom equation is, by definition, the operator $f(M_R)$. It is the same functional of $f(M_R)$ as $f(\varepsilon_R)$ was of (ε_R). For example, if $f(\varepsilon_R)$ is $(\varepsilon_R)^2$ then $f(M_R)$ is $(M_R)^2$.

This yields the central equation of the augmented space theorem:

$$\ll f(\varepsilon_R) \gg = \langle\emptyset| f(M_R) |\emptyset\rangle$$

The result is significant, since we have reduced the calculation of averages to one of obtaining a particular matrix element of an operator in the configuration space of the

variable. Since we have applied the theorem to a single variable alone, the power of the above theorem is not apparent. Let us now go back to the Anderson model, where we have a set of random variables ε_i which we have assumed to be independently distributed. The joint probability distribution is given by:

$$P(\varepsilon_{R_1}, \varepsilon_{R_2}. \cdots, , \varepsilon_{R_i}, \cdots) = \prod_i p\varepsilon_{R_i}$$

The generalization of above theorem to averages of functions of the set of random variables is straightforwards.

$$\ll f(\varepsilon_R) \gg = \langle \emptyset | \tilde{f}((\tilde{M}_R)) | \emptyset \rangle$$

All operators in the full configuration space Φ will be denoted by tilde variables. The operators $(\tilde{M}_R)$ are built up from the operators M_R as:

$$\tilde{M}_R = I \otimes I \otimes I \otimes \cdots M_R \otimes I \otimes \cdots \tag{3.104}$$

This is the augmented space theorem, proposed by (Mookerjee, 1973).

If we carry out the configuration averaging of, say, Green function element.

$$G_{RR}(z) = \langle R | (zI - H(\varepsilon_{R'})^{-1} | R \rangle$$

The theorem leads to:

$$\ll GRR(z) \gg = \langle \otimes \emptyset | (z\tilde{I} - H(\varepsilon_{R'}))^{-1} | R \otimes \emptyset \rangle \tag{3.105}$$

Where

$$\tilde{H} = \sum_R p_R \otimes \tilde{M}_R + \sum_R \sum_{R'} V_{RR'} T_{RR'} \otimes \tilde{I}$$

The power of the theorem now becomes apparent. The average is seen to be particular matrix elements of Green function of an augmented Hamiltonian. This is constructed out of the original random Hamiltonian by replacing the random variables by the corresponding configuration space operators built out of their probability distributions. This augmented Hamiltonian is operator in the augmented space $\psi = \mathcal{H} \otimes \Phi$ where $\mathcal{H}$ is the space spanned by the tight-binding basis and Φ the full configuration space.

3.11.4 Augmented space theorem for binary alloy

As discussed in previous section we can apply recursion method directly on the augmented space without carrying out any mean-field-like approximations. The starting point of the augmented space recursion is the most localized, sparse, tight binding

Hamiltonian, derived systematically from the LMTO-ASA theory and generalized to substitutionally disordered random binary alloys:

$$H^{\alpha}_{RL,R'L'} = \hat{C}_{RL}\delta_{RR'}\delta_{LL'} + \hat{\triangle}^{1/2}_{RL} S^{\alpha}_{RL,R'L'} \hat{\triangle}^{1/2}_{R'L'}$$

$$\begin{aligned} \hat{C}_{RL} &= C^{A}_{RL} n_R + C^{B}_{RL} 1 - n_R \\ \tilde{\triangle}^{1/2}_{RL} &= (\triangle^{A}_{RL})^{1/2} n_R + (\triangle^{B}_{RL})^{1/2} 1 - n_R \end{aligned}$$

Here R labels the lattice sites and L = (l m) are the orbital indices (for transition metals $l < 2$), C^{A}_{RL}, C^{B}_{RL} and $\triangle^{A}_{RL}$, $\triangle^{B}_{RL}$ are the potential parameters of the constituents A and B of the alloy. n_R are the local site occupation variables which randomly take values 1 and 0 according to whether the site is occupied by an A atom or not.

Hence, the Hamiltonian in the augmented space can be represented as,

$$\begin{aligned} \tilde{H} &= \textstyle\sum_{RL} (C^{B}_{RL} \tilde{I} + \delta C_{RL} \tilde{M}_R) \otimes \mathcal{P}_R \cdots \\ &+ \textstyle\sum_{RL} \sum_{R'L'} \left((\triangle^{B}_{RL})^{1/2} \tilde{I} + \delta\triangle_{RL} \tilde{M}_R \right) S^{\alpha}_{RL,R'L'} \\ &\times \left((\triangle^{B}_{R'L'})^{1/2} \tilde{I} + \delta\triangle_{R'L'} \tilde{M}_R \right) \otimes \mathcal{T}_{RR'} \end{aligned}$$

Where,

$$\delta C_{RL} = \left(C^{A}_{RL} - C^{B}_{RL} \right)$$

$$\delta\triangle_{RL} = \left((\triangle^{A}_{RL})^{1/2} - (\triangle^{B}_{RL})^{1/2} \right)$$

Other parameters have their usual meaning and $\tilde{I}$ is the identity operator defined in the augmented space, $\tilde{M}_R$ is given by:

$$\tilde{M}^{R} = x\mathcal{P}^{0}_{R} + y\mathcal{P}^{1}_{R} + \sqrt{xy}\left(\mathcal{T}^{01}_{R} + \mathcal{T}^{10}_{R} \right) \tag{3.106}$$

$\mathcal{P}^{10}_{R}$ and $\mathcal{T}^{10}_{R}$ are projection and transfer operators in the augmented space, where each site R is characterized by two states labeled 0 and 1, these are identified with up and down states of an Ising system.

The augmented Hamiltonian is an operator in a much enlarged space $\Phi = \mathcal{H} \otimes \prod \phi^{R}$ (the augmented space), where $\mathcal{H}$ is Hilbert space spanned by the countable basis set $|R\rangle$ (the real space). The enlarge Hamiltonian does not involve any random variables but incorporates within itself the full information about the random occupation variable. After the substitution of M_R the augmented Hamiltonian contains the following types of operators,

a) $\mathcal{P} \otimes \tilde{I}$ and $\mathcal{T}_{RR'} \otimes \tilde{I}$. These operators acting on vector in the augmented space changes only the real space label but keeps the configuration part unchanged.

b) $\mathcal{P} \otimes \mathcal{T}^{01}_{R}$,$\mathcal{P} \otimes \mathcal{T}^{01}_{R'}$, $\mathcal{T}_{RR'} \otimes \mathcal{T}^{01}_{R}$ and $\mathcal{T}_{RR'} \otimes \mathcal{T}^{01}_{R'}$. These operators acting on an augmented space vector may or may not change the real space label. In addition they may also

change the configuration at the site R or R' or both. This resembles a single spin-flip Ising operator in the configuration space.

c) $\mathcal{P} \otimes \mathcal{T}_R^{01} \otimes \mathcal{T}_{R'}^{01}$ and $\mathcal{T}_{RR'} \otimes \mathcal{T}_R^{01} \otimes \mathcal{T}_R^{01}$. These operators may change the real space label, as well as configuration either at site R or R' or both. This resembles a double spin-flip Ising operators in the configuration space. A basis $|m\rangle$ in the Hilbert space $\mathcal{H}$ is represented by column vector C_m with zeros every where except at the m-th position. The inner products are defined as,

$$\langle m|\rangle = C_m^{\mathcal{T}} C_n$$

$$\mathcal{P}_m C_P = \delta_{mp} C_p$$

$$\mathcal{T}_{mn} C_P = \delta_{np} C_m$$

In terms of the binary basis the sequence of position at which we have 1's C is called the cardinality sequence labels the basis. Thus a binary sequence $B[C]$ is representation of the member of the basis in the configuration space. The inner product between the basis member is then

$$(B[C], B[C']) = \delta(C.C')$$

We are using TBLMTO-ASR code(Banerjee & Mookerjee, 2010) for the calculation of electronic properties of binary alloys $Ni_{1-x}Mn_x$, $Pd_{1-x}Mn_x$, $Pt_{1-x}Mn_x$ with variation of concentration ranges from 1% Mn to 50% Mn.

3.12 Effective pair Exchange interactions

The derivation of the lowest configurational energy for a specified alloy system is essential to understand the onset of ordering in random alloys. Different models have been set up describing configurational energies in terms of effective multi-site interactions in particular EPE (Gonis, *et al.*, 1987). In EPE approach, one can do the analysis of alloy ordering tendencies and phase stability. Traditionally there have been two different approaches for obtaining the EPE. The first approach is to start with the electronic structure and total energy determinations of ordered super-structures of the alloy and to use these to invert the relationship between total energies and EPE to obtain the latter. This is the Connolly-Williams method (Connolly & Williams, 1983). The second approach is to start with the disordered phase, setup a perturbation in the form of concentration fluctuations associated with an ordered phase and study whether the alloy can sustain such a perturbation. This approach includes the Generalized Perturbation Method (GPM) (Ducastelle & Gautier, 1978), the embedded cluster method (ECM) and the concentration wave approach (Pokrovski & Khachaturyan, 1986). We shall follow

this second approach i.e. Generalized Perturbation Method (GPM) for the calculation of EPE.

3.12.1 Generalized Perturbation Method(GPM)

The Lichtenstein's formulation (Lichtenstein, *et al.*, 1987), (Jena, *et al.*, 2011) is used directly for the calculation of EPE. In this method we start from homogeneously disordered alloy A_xB_{1-x} at which each site occupied by either A or B types of atom with probabilities proportional to their concentration. We define local occupation variable $n(R_i)$ which randomly takes value 0 or 1 if the site R_i is occupied by A or by B with average $<< n(R_i) >>= x$. This perturbative approach expands the total internal energy of a particular configuration as,

$$E = V^{(0)} + \sum_{R_i} V^{(1)}_{R_i} \delta n(R_i) + \sum_{R_i} \sum_{R_j} V^{(2)}_{R_n} \delta n(R_i \delta n(R_j + ... \tag{3.107}$$

$$+ \sum_{R_i} \sum_{R_j} \sum_{R_k} V^{(3)}_{R_i,R_j,R_k} \delta n(R_i) \delta n(R_j) \delta n(R_k) + ... \tag{3.108}$$

where

(1) $R_n = R_i - Rj$ such that $i \neq j$

(2) $\delta n(R_i) = n(R_i) - x$ and $<< \delta n(R_i) >>= 0$

(3) If the configuration is homogeneously disordered then it follows, $<< E >>= E_{dis} = V^{(0)}$

(4) If $E^I(R_i)$ is the configuration averaged total energy of a configuration in which any arbitrary site labeled R_i is occupied by an atom of the type I and the other sites are randomly occupied then, $V^{(1)}_{R_i} = E^A_{R_i} - E^B_{R_i}$

(5) If $E^{IJ}(R_n)$ is the averaged total energy of another configuration in which the sites R_i and $R_i + R_n$ are occupied by atoms of the types I and J respectively and all other sites are randomly occupied, then $V^{(2)}_{R_n} = E^{AA}_{R_n} + E^{BB}_{R_n} - E^{AB}_{R_n} - E^{BA}_{R_n}$

The single-site energy $V^1(R_i)$ is unimportant for bulk ordered structures emerging from disorder. It is important for emergence of inhomogeneous disorder at surfaces and interfaces. The pair energies $V^2(R_n)$ dominantly govern the emergence of bulk ordering. The multi-site energies $E^3(R_i, R_j, R_k)$.... are usually too small to affect our conclusions qualitatively, except in cases of complex ordering. We shall ignore all such higher terms for the calculations pair interaction energies. This help us to find out the FM and AFM interactions which is one of the most important gradient of spin glass properties.

3.13 Spin Glass Phase

Spin-glass (SG) is one of the most interesting and complex systems in the study of condensed matter Physics. Experimental and theoretical researchers are mostly attracted towards SG because of its equally important as physics in other fields like computer science, Biology, Mathematics including future generation technology. A spin glass is a disordered magnet with frustrated interactions, augmented by stochastic positions of the spins (magnetic moments), whose low temperature state is frozen disordered one.

The theory of Spin glass was first systematically documented in seminal paper of (Edward & Anderson, 1975) showing that this phase is essentially due to the competitive interaction between ferro and antiferromagnetic ordering given by the Hamiltonian

$$H_J = -\sum_{<ij>} J_{ij}\sigma_i\sigma_j - h\sum_i \sigma_i \tag{3.109}$$

Where J_{ij} is called exchange interactions and takes the value positive or negative depending on ferromagnetic and anti-ferromagnetic interactions. Many theoretical as well as experimental works (Fischer & Hertz, 1993), (Mydosh, 1993), (Binder & Yong, 1986) have been carried out ever since, but due to complexity of the system, no one come to the single point to obtain an exact solution. However all theoretician come to the point that there are three main essential ingredient that build up the spin glass phenomena.

(1) a randomness in the interaction between sites

(2) Competitive interaction between Ferromagnetic and Anti-Ferromagnetic spins

(3) a competitions among interactions as to the preferred direction of spin(Frustration)

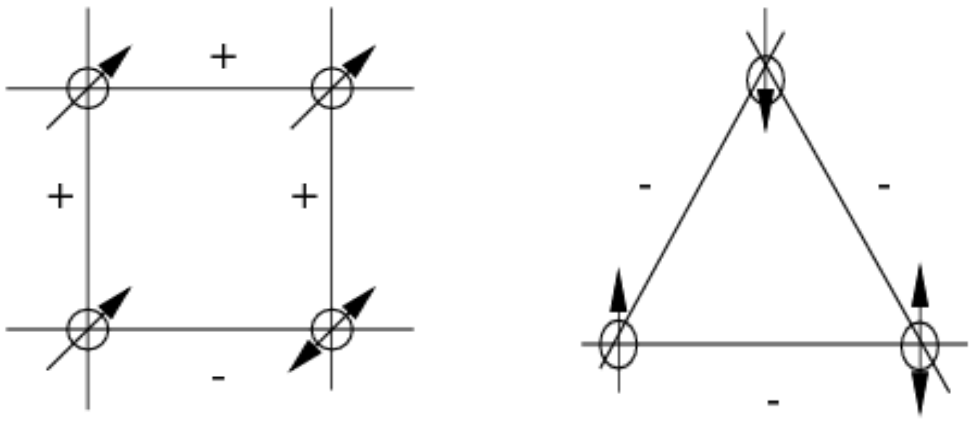

Figure 3.3: *(left) frustrated plaquette, (right) Frustrated AFM in triangle*

.

A randomness in the interaction between the sites arise in the class of impure metal spin glasses, amorphous alloys and rare earth combination (Chowdhury & Mookerjee, 1984). Such types of SG's have the strong interactions depends upon the distance between two impurities. This strong interaction is due to the Ruderman, Kittel, Kasuya and Yosida (RKKY) (Rudernam & Kittel, 1954), (Kasuya, 1956), (Yasida, 1957) coupling which takes the following expressions,

$$J(R) = 6\pi Z J^2 N[\frac{sin(2k_F R) - cos(2k_F R)}{(2k_f R)^3}] \tag{3.110}$$

where Z is the number of conduction electrons per atom, J the s-d exchange constant, N_{E_F} is the DOS at the fermi level. k_F fermi wave vector and R is the distance between two impurities. In this case moments of impurity transition metal polarize the conduction electron of host which leads to the RKKY coupling between moments.

Figure in (3.3) clearly explain the existence of frustration in system. Actually, the competition interactions (the long-range and short-range of sites) comes about from FM and AFM couplings. The comparable strength of these two will lead to frustrated states. This frustrated states result in complex physical properties like infinite numbers of ground states and existence of metastable states.

CHAPTER 4

RESULTS AND DISCUSSION

4.1 Introduction

In this chapter, we present and discuss the main findings of our work. We have studied the pristine clusters Pd_n (n=2-19), Pristine clusters with mono dop $Pd_{n-1}Mn$ and bi-dop $Pd_{n-2}Mn_2$ of Mn atoms. We replaced Mn_1 and Mn_2 on Pd_n (n=1-13) atoms substitutinally and focused our study up to the 13 atom clusters. We also study the adsorption and dissociation of hydrogen or nitrogen molecules on Ta_n and Nb_n (n=2-7) clusters. Further we study the transition metal doped ZnO in different morphologies (Nanosheet, Nanotube and Fullerene like structures). The Vienna *ab-initio* Simulation (VASP) code is used to study the structural, electronic and magnetic properties of clusters and nano-systems. In case of bulk we have focused our attention about the spin-glass behaviour of Pd-Mn, Pt-Mn and Ni-Mn. The TB-LMTO-ASR code is used to deal the disordered systems. The results and discussion of the present study are presented in the section wise for simplicity as follows.

4.2 Structural, electronic and magnetic properties of Pd_n, $Pd_{n-1}Mn$ and $Pd_{n-2}Mn_2$ clusters

In this section, we present the results and discussion obtained from the present calculations related to geometrical optimization, electronic properties and magnetic properties for pristine Pd_n(n=2-19) clusters. Further we have also discussed electronic and magnetic properties of mono and bi-doped Mn atoms on Pd_n(n $\leq$ 13) clusters separately. The binding energy (BE), dissociation energy, magnetic moment (MM), charge transformation and electronic properties etc. are analyzed to describe geometrical stability, doping effects and origin of magnetism. To begin it, we first study the pristine Pd_n(n=2-19) clusters which form the background of doping studies.

4.2.1 Structural growth pattern of Pd_n (n=2-19) clusters

We have used full structure optimization using VASP code on various isomers of pristine clusters. The difference in binding energies among the isomers are rather small so we present only optimized one. The optimized geometry with BE/atom and the magnetic moments are shown in Fig.(4.1) for Pd_n (n=2-19) clusters. For pristine Pd dimer (n=2), the bond length is found to be 2.48 $\mathring{A}$. This value of bond length exactly resembles with experimental value as well as previous works (Shen, *et al.*, 2008). The binding energies per atom is found to be 0.645 eV/atom which is around 7% less than experimental value (0.698 eV) (Yuewen, *et al.*, 2011). In Pd_3 the isosceles triangle is found to be stable than the distorted equilateral triangle which may be due to Jahn Teller's effects. The binding energy of Pd_3 is found to be equal to 1.26 eV/atom. This value agrees about 0.07 % of previous theoretical work (Futschek, *et al.*, 2005). The average bond length is calculated as 2.47$\mathring{A}$ which is also matching about 0.08% with results of previous works(2.49 $\mathring{A}$) (Rogan, *et al.*, 2005), (Sutton & Chen, 1990). Pd_4 shows highest binding energy in distorted tetrahedron structure. It's binding energy found to 1.49 eV/atom. The bond lengths do not vary more than 0.01 $\mathring{A}$ within the error bar of computational package VASP. The average bond length found to be 2.47 $\mathring{A}$. This value agrees with the previously reported value (2.49 $\mathring{A}$) by (Cleri & Rosato, 1993).

Similarly Pd_5, Pd_6 and Pd_7 grew with trigonal bi-pyramid, Octahedron and pentagonal bi-pyramid configurations respectively with increasing average bond length and binding energies. The bond lengths of these clusters also vary within the error bar of computational package. The Pd_2-Pd_7 are the base of all higher clusters with stable geometry, so called building blocks of stable geometry.

For Pd_8 to Pd_{12}, we derived the various isomers by removing atom one by one from 13 atoms clusters of cub-octahedron, hexagonal, Icosahedron and buckle bi-planner types. The higher clusters Pd_{14} to Pd_{19} are also derived by adding atom by atom on the top of these four isomers. The ground state geometries of Pd_8 to Pd_{19} are shown in Fig.(5.1)(g-u). Figs.(4.2) show the four different isomers of 13 atoms clusters by taking the base of which we derived most of the clusters and tested for the ground state geometry through optimization process. The properties of ground state geometry of Pd_8 to Pd_{19} are described as follows

In case of Pd_8, the lowest ground state energy structure is slightly deviated from bi-pyramid type and appears to be quite "irregular". The ground state configuration is distorted double octahedrons in one of the face. The binding energy per atom of Pd_8 found to be 1.99 eV/atom. This value agrees about 1% with previously reported data (Karabacak, *et al.*, 2002). The bond length is found to be 2.67$\mathring{A}$ which also agrees well

with Karabacak's results. The ground state structure of Pd_9 is regarded as half type icosahedron structure with average binding energies 2.08 eV/atom with bond length 2.70$\mathring{A}$. This agrees the results of Yuewen. In case of Pd_{10} icosahedral structure is found to be less stable than octahedral with two side capped. Fig.(5.1)(i) shows the two side caped octahedron structure of Pd_{10}. The geometrical pattern agrees well with previously reported findings (Cox, *et al.*, 1990), (Rogan, *et al.*, 2005). The BE and bond length are found to be 2.16 eV/atom and 2.71 $\mathring{A}$ respectively. Fig.(5.1)(j)shows the highest binding energy structure of Pd_{11} clusters. It is derived from cube-octahedron structure of 13-atom clusters after removing atom by atom and relaxing. The optimized geometry has average bond length 2.71 $\mathring{A}$ and binding energy 2.21 eV/atom. For Pd_{12} we tested cub-octahedron, hexagonal and Icosahedron with vacant center and buckle bi-planner types. We obtained cube-octahedron with vacant center as most stable than others isomers. It is observed that cube-octahedron with central vacant atom has 0.014 meV/atom has higher binding energy than icosahedron with vacant center. The optimized structure has BE 2.23 eV/atom. The majority of the bonds in the clusters ranges from 2.60 $\mathring{A}$-2.71 $\mathring{A}$ which is within the error bar of the computational package. The average bond length found to be 2.69 $\mathring{A}$ which agrees about 1% of the previously reported data(2.71$\mathring{A}$)(Luo, *et al.*, 2007).

Figs. (5.1)(l, m, n and o) represent the optimized geometry of Pd_{13} Icosahedral, Buckle bi-planer, Cub-octahedral and Hexagonal structures respectively. These stable geometries are of interest for researcher.

A typical icosahedral structure with binding energy 2.31 eV/atom is found to be the most stable geometry for Pd_{13} clusters which contradicts the result reported by (Chang & Chou, 2004). They reported Buckle bi-planner is most stable than icosahedral type. In the present work, we observed that typical icosahedral structure has 0.007 eV/atom less binding energy than buckle bi-planner structure. This is mainly due to fact that they choose different search procedure, which start from high symmetry structure, obtained by molecular dynamics at $300K$ and compare their energy at $0K$. Present result is also against the report of Piostrowski *et al.*(Blonski & Hafner, 2011) on which they predicted distorted hexagonal bilayer like(HBL) structure as a low lying structure. This discrepancy is mainly due to the fact that Piostrowski *et al.*used spin orbit coupling procedure to find out the ground state energy. However, our results are consistent with other theoretical works (Rey, *et al.*, 1993), (Garcia-Rojeda, *et al.*, 1994), (Efremenko & Sheintuch, 1998). The majority of the Pd-Pd bonds in the icosahedral Pd_{13} clusters fall within the range 2.72$\mathring{A}$-2.75$\mathring{A}$ which is within the error bar of the computational package. The average Pd -Pd bond length is found to be 2.73 A^0 which is close agreement with results of Lee (Lee, 1998).

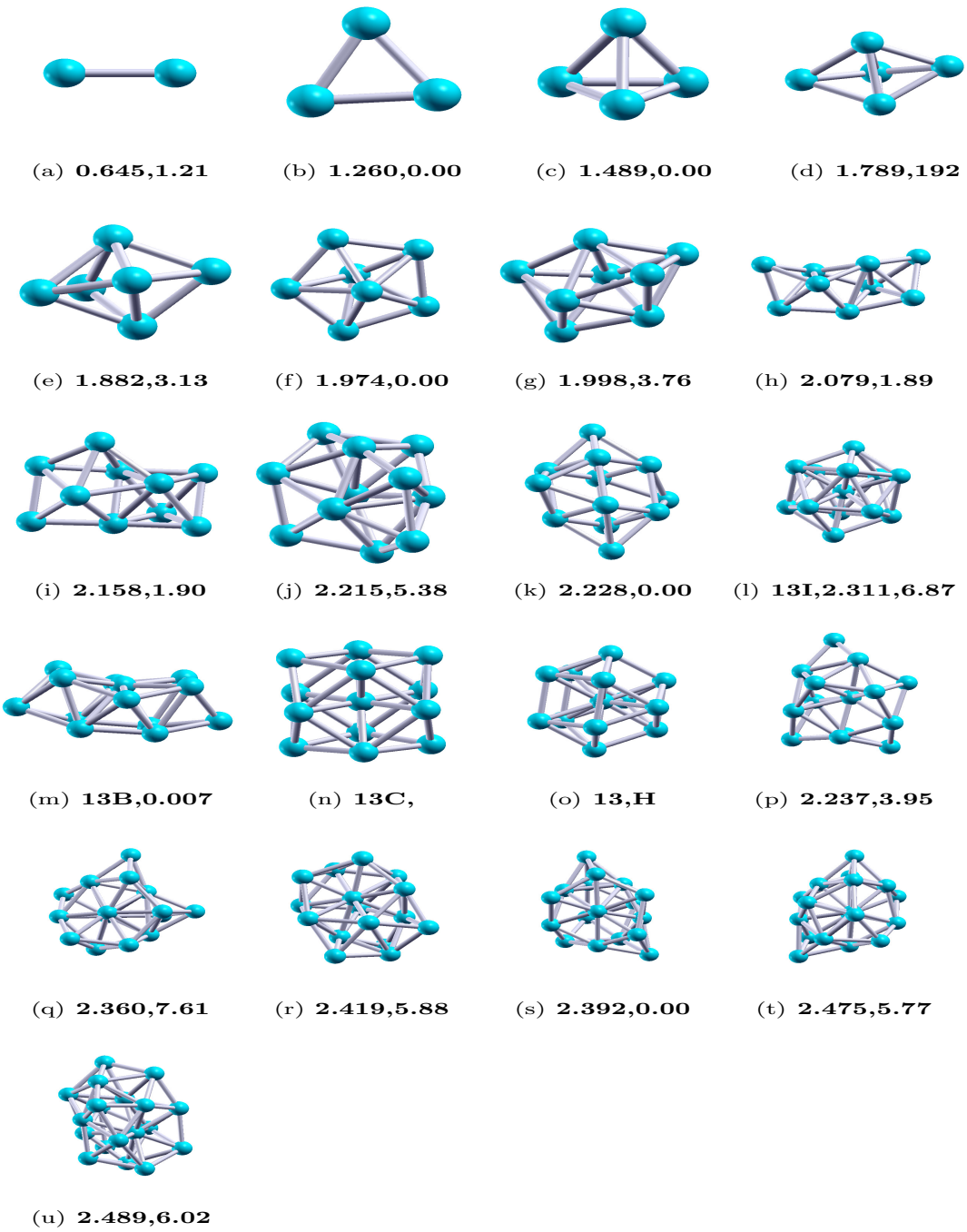

(a) **0.645,1.21** (b) **1.260,0.00** (c) **1.489,0.00** (d) **1.789,192**

(e) **1.882,3.13** (f) **1.974,0.00** (g) **1.998,3.76** (h) **2.079,1.89**

(i) **2.158,1.90** (j) **2.215,5.38** (k) **2.228,0.00** (l) **13I,2.311,6.87**

(m) **13B,0.007** (n) **13C,** (o) **13,H** (p) **2.237,3.95**

(q) **2.360,7.61** (r) **2.419,5.88** (s) **2.392,0.00** (t) **2.475,5.77**

(u) **2.489,6.02**

Figure 4.1: *Most stable geometries of* $Pd_n (n \leq 19)$ *clusters showing binding energy per atom and Magnetic moment.*

In case of Pd_{14} clusters, the pentagonal prismatic configuration with three atoms caped at prismatic side is found to be most stable geometry. It is derived from the icosahedral type structure. This geometry has BE 2.24 eV/atom. The ground state geometry of Pd_{15} clusters is a typical type of fcc -like structure with some atoms in the faces slightly out of plane. The binding energy of Pd_{15} is found to be 2.36 eV/atom.

Fig.(5.1)(r) shows the ground state geometry of Pd_{16}. It is obtained from cube-octahedral base type which contains an atom in the center and the remaining atoms form a shell around of it. The geometry agrees with the result of Karabacak. The BE Pd_{16} is found to be 2.42 eV/atom which is around 3% less than previously reported data. The difference in BE is due to the procedure adopted during the energy minimization scheme. The ground state of Pd_{17} is regarded as a distorted structure as obtained by (Rogan, *et al.*, 2005) due to Jahn teller's effect. In this case six atom-rings are distorted in two sides. It has a binding energy 2.392 eV/atom. Pd_{18} is also derived from icosahedral type of structure. The growth pattern is same as Pd_{17} clusters. The BE of Pd_{18} clusters is found to be 2.457 eV/atom and bond length 2.734 $\mathring{A}$. The ground state geometry of d_{19} clusters is obtained double icosahedral types of structure. It is one of the unique geometry formed by pentagonal bi-pyramid structures. The stable structure has binding energy 2.489 eV/atom.

Finally among the large number of low lying isomers of Pd-clusters, we observed four types of structural growth pattern via (i) fcc-like based (Pd_6, Pd_{15}. Pd_{17} etc.) (ii) octahedron based(Pd_8, Pd_{10}. Pd_{11}, Pd_{16} etc.) (iii) icosahedron base (Pd_9, Pd_{12}, Pd_{13}, Pd_{14}, Pd_{19} etc.) and (iv) buckle-bi-planner type (Mostly found in nearest stable structures). We take references of four structures to find out the optimized structures of 13 atoms clusters. From the calculations we found that icosahedral structure is found to be most stable for Pd_{13} clusters among other. The four structures which we used to derived lower and higher clusters in different isomers are shown in Fig.(4.2).

In short, we found no any special regular trends of structural growth pattern. Perhaps, the special trends will achieve as we move to higher clusters. We have also studied the effect of Mn_1 and Mn_2 doping on the equilibrium structure of Pd_n (n = 1$\leq$ 13) clusters which is described in following sections.

4.2.2 Structural Effects of Doping

In this section, we analyze the structural effect on pristine Pd_n (n$\leq$ 13) clusters up to a size of 13 atoms after doping mono- and bi-dop of Mn atom. We are using exactly the same methodology and parameters of Pd_n clusters as the later doping studies, so that a consistent picture emerges.

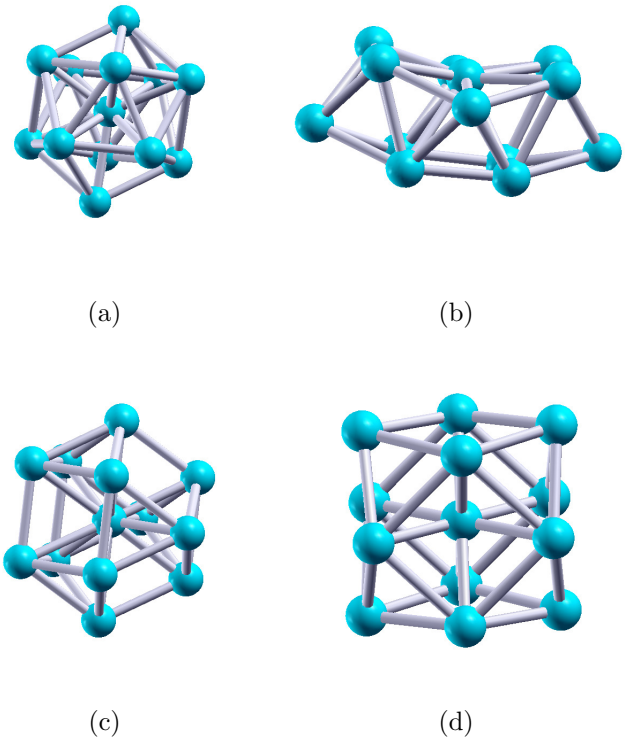

Figure 4.2: *The different isomers of Pd_{13} clusters by taking the base of which other lower and higher clusters are formed.*

As mentioned above, we first obtained the equilibrium structures of $Pd_n(n = 2 - 13)$ clusters. We doped Mn_1 on the $Pd_n(n = 1 \leq 13)$ clusters to get $Pd_{n-1}Mn_1(n = 2 \leq 13)$. We tested various isomers out of them most stable geometries are presented in Fig.(4.3). The binding energy and magnetic moments are presented at beneath the respective figures. Similarly, we doped Mn_2 on the $Pd_n(n = 1 \leq 13)$ clusters to get $Pd_{n-2}Mn_2(n = 2 \leq 13)$. The most stable conformers for $Pd_{n-2}Mn_2(n = 2 \leq 13)$ are listed in the Fig.(4.4). Further Fig.(4.4) contain BE and MM at the bottom of the each optimzed geometry. We have compared the ground state geometry of doped $Pd_{n-1}Mn_1(n = 2 \leq 13$ and $Pd_{n-2}Mn_2(n = 2 \leq 13$ with the pristine $Pd_n(n = 2 \leq 13$ clusters. The table 6.1 given in Appendix -I summarizes all the characteristics of pristine Pd_n (n = 2-19), $Pd_{n-1}Mn$ and $Pd_{n-2}Mn_2$ up to 13 atom size clusters. Our conclusions are described below :

(i) **n = 2**, the bond length of PdMn cluster has found to be 2.258 $\AA$, which agrees about 0.04 % with the result of (Yuewen, *et al.*, 2011) (2.268$\AA$). Pd-Mn bond length is about 10% less than Pd-Pd bond length of pristine Pd_2(2.478 $\AA$). This is consistent with the stronger binding between Pd and Mn, having BE 1.308 eV/atom as compared with BE of two Pd atoms (0.645 eV/atom).

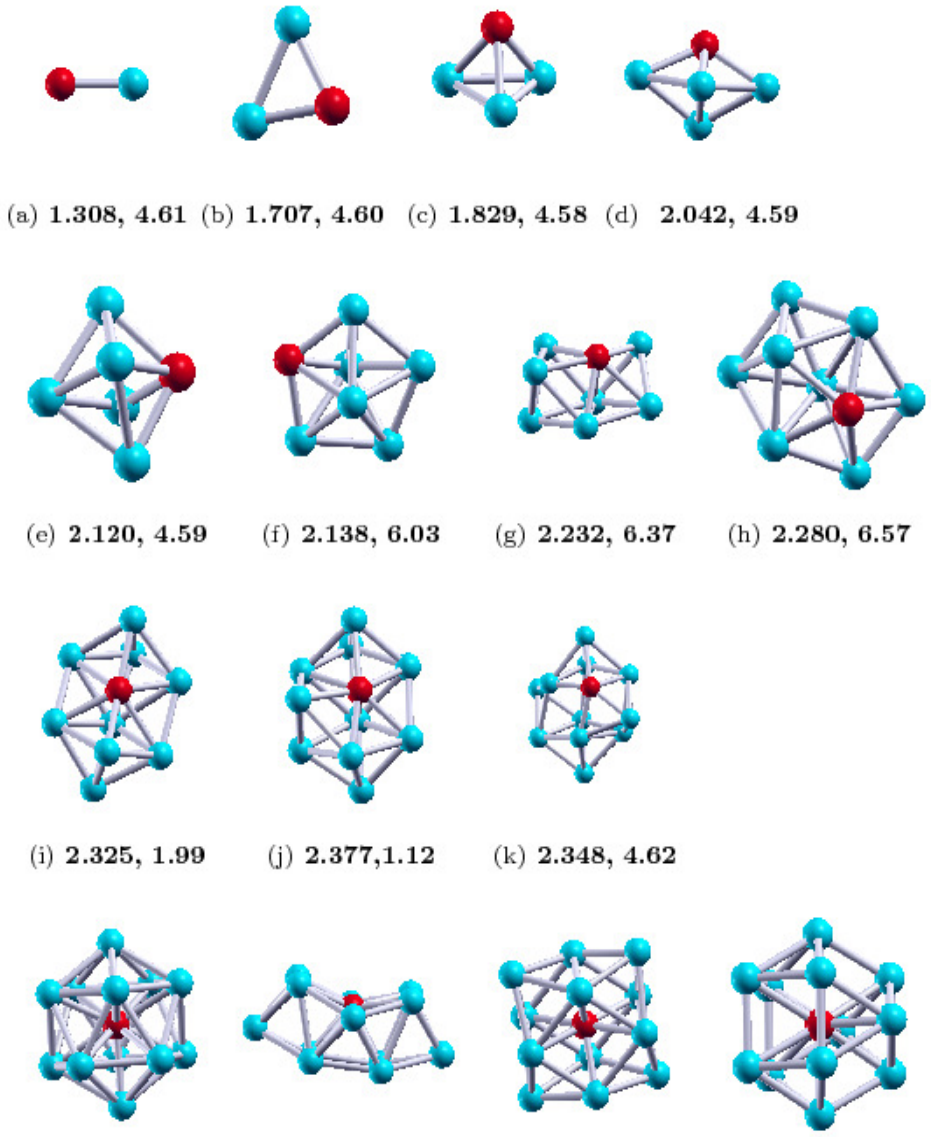

Figure 4.3: *Most stable geometries of* $Pd_{n-1}Mn(n = 2 \leq 13)$ *clusters showing binding energy per atom and magnetic moment (Red ball represents the Mn atom) and I, B, C and H represent Icosahedral, Buckle Bi-planner, Cube-octahedral and Hexagonal close-Packed structures respectively.*

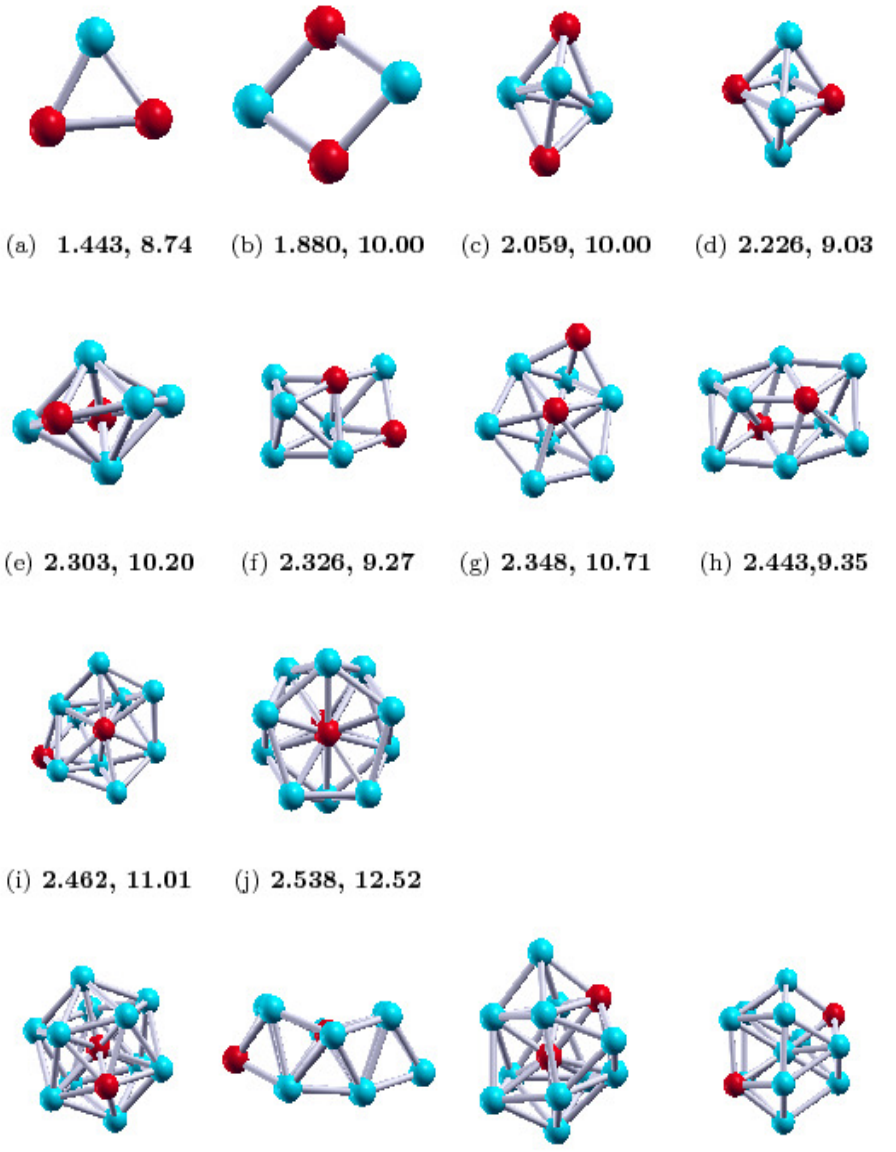

Figure 4.4: *Most stable geometries of* $Pd_{n-2}Mn_2 (n = 3 \leq 13)$ *clusters showing binding energy per atom and Magnetic moment (Red ball represents the Mn atom) and I, B, C and H represent Icosahedral, Buckle Bi-planner, Cube-octahedral and Hexagonal close-Packed structures respectively.*

(ii) **n = 3**, the stable structure for Pd_2Mn is isosceles triangle like Pd_3 from symmetry considerations with the binding energy 1.707 eV/atom. The Pd-Pd bond length is 2.46 $\mathring{A}$ while the Pd and Mn binds with bond length 2.35 $\mathring{A}$. This is also consistent with the stronger Pd-Mn bonding. The Fig.(4.4) shows the equilibrium configurations of $Pd_{n-2}Mn_2$ $n = 3 \leq 13$. From figure it is observed that the $PdMn_2$ clusters bind with average bond length 2.49$\mathring{A}$ where as average Pd-Mn bond length is 2.40 $\mathring{A}$ with BE 1.443 eV/atom. This is indicative of Pd-Mn bound more strongly in $PdMn_2$ than Pd_2Mn clusters which may be the effect of Mn-Mn bonding. In these cases the linear configuration is higher in energy and therefore unstable as in pristine Pd_3.

(iii) **n = 4**, the lowest energy stable structure for Pd_3Mn is a distorted tetrahedron. The average bond length of system is 2.47 $\mathring{A}$ while Pd-Pd bond lengths found to be 2.64 $\mathring{A}$ larger than Pd-Mn ones (2.42 $\mathring{A}$). It has the BE 1.829 eV/atom. For the Pd_2Mn_2 the planar rhombus with Mn atoms at two opposite ends found to be more stable than three dimensional isomer which has BE 1.880 eV/atom. This resembles the planar structures found in pristine Mn clusters.

(iv) **n = 5, 6 and 7**, the clusters of sizes 5-7 all found to be grow in bi-pyramidal configurations with increasing bond length and binding energies as in pristine Pd_n clusters shown in Figs.(4.3). In case of mono dop, Mn atom is directly bonded with four Pd atoms. For the bi-doped clusters both the Mn atoms bind with four Pd atoms of bi-pyramids configurations on opposite corners. The three dimensional structures win over those with planer geometry. As the size increases, the number of isomers also increases. The difference in binding energies among the isomers is rather small and when such clusters are formed at finite temperatures the other types of isomers may also be present. We have considered only the lowest energy configurations. We found that Mn substitution doping almost does not change the structure of the pristine palladium clusters, and the lowest-energy structure of $Pd_{n-1}Mn$ is still similar to that of the corresponding Pd_n clusters. This geometry agrees the pattern of previous calculation by Yuewen.

(v) **n = 8**, the lowest energy structures of Pd_7Mn and Pd_6Mn_2 are distorted bi-pyramid type. This is same as the geometry of the pristine case. The Pd_7Mn has binding energies 2.233 eV/atom with average bond length 2.67 $\mathring{A}$ and Pd_6Mn_2 has BE 2.326 eV/atom with average bond length 2.70 $\mathring{A}$. The geometry of most stable conformers for Pd_7Mn and Pd_6Mn_2 clusters resemble the pristine one with some distortions around the Mn sites (Yuewen, *et al.*, 2011).

(vi) **n = 9**, the structure of Pd_8Mn has characteristic icosahedral signature with binding

energies 2.280 eV/atom. This is the indication of starting of icosahedral geometry. Similarly Pd_7Mn_2 has distorted icosahedral types with distortion in Mn site, having BE 2.348 eV/atom. After distortion, geometry tends to emerge the shape of octahedral type. From the figures, it is seen that the geometry of Pd_8Mn and Pd_7Mn_2 are different from each other as well as from pristine Pd_9 clusters.

(vii) **n = 10**, the stable geometry of mono-doped Pd_9Mn is a square bi-pyramid with Mn at one of the square bases. It has a binding energy 2.325 eV/atom. Similarly bi-doped Pd_8Mn_2 is a double pentagon with the BE 2.443 eV/atom. These doped clusters resemble neither the pristine Pd cluster nor each other.

(viii) **n = 11**, For $Pd_{10}Mn$ structure with the highest binding energy (2.337 eV/atom) has icosahedral type while Pd_9Mn_2 bears a cube-octahedral signature with binding energy 2.462 eV/atom. These doped clusters are also resemble neither the pristine Pd_{11} cluster nor each other.

(ix) **n = 12**, for $Pd_{11}Mn$ and $Pd_{10}Mn_2$, we deal with two almost degenerate isomers : the cub-octahedron and the icosahedron with vacant centers. In case $Pd_{11}Mn$ the cub-octahedron with a vacant central atom found to be most stable one with BE 2.348 eV/atom which is 0.024 eV/atom higher binding energy than the icosahedral type. In case $Pd_{10}Mn$ the BE Of cub-octahedron with a vacant central atom has 2.538 eV/atom. This value is 0.015 eV/atom higher binding energy than the icosahedral geometry. The energy differences are within our error bar of calculations, so we cannot decide between these isomers with any confidence. Even then cube-octahedral pattern shows the stable one in both the cases. The pristine Pd_{12} shows the icosahedral geometry with vacant central atom as a stable one.

(x) **n = 13**, the icosahedral structures are found to be more stable than other isomers in both $Pd_{12}Mn$ and $Pd_{11}Mn_2$ clusters. The BE of $Pd_{12}Mn$ is found to be 2.505 eV/atom which is icosahedral structure. This stable geometry has 0.065 eV/atom higher binding energy as compared to the buckled bi-planner structure and 0.042 eV/atom higher BE than cube-octahedral structure. Our results are consistent with other theoretical works (Yuewen, *et al.*, 2011). Similarly, the BE of $Pd_{11}Mn_2$ is found to be 2.579 eV/atom which is icosahedral structure. The icosahedral structure has 0.018 eV/atom binding energy higher than nearest neighbour stable structure(cube-octahedral). We found that there is large difference between the strength of the Pd-Pd bond and the Pd-Mn bond within these systems.

We summarized all the characteristics of pristine Pd_n (n=2-19), $Pd_{n-1}Mn$ and $Pd_{n-2}Mn_2$ up to 13 atom size clusters with binding energies, energy differences, magnetic moments,

bond lengths, spin-gaps etc. in table (6.1) given in Appendix -I.

Doping of Mn_1 and Mn_2 atom on Pd clusters are expected to open up other channels where one can tailor the properties of clusters by varying the nature of doping. Large magnetic moments in Mn substitutional doped on Pd_n (n $\leq$ 13) clusters have been predicted (section 4.2.4). Bulk Pd alloyed with Mn undergo paramagnetic to ferromagnetic and also anti-ferromagnetic and spin-glass transitions in some regions of the composition-temperature phase diagram (Kaphle, *et al.*, 2012). The conditions after doping Mn_2 may differ in some cases due to opposite alignment of two Mn atoms. It would be rather interesting to know how mono (Mn_1) and bi-dop (Mn_2) of Mn atoms influence the stability and magnetic behavior of Pd clusters. We address these problems in the following sections.

4.2.3 Binding and Stability of Pd_n (n=2-19), $Pd_{n-1}Mn$ and $Pd_{n-2}Mn_2$ ($n \leq 13$) clusters

In this section we have focused our attention on the variation of binding energy with size of the clusters and stability of Pd_n(n=2-19) clusters. Further, we also discussed the variation of BE and effect of stability after doping Mn_1 and Mn_2 atom on pristine Pd_n (n=2-13). The definitions and computational details to calculate BE, dissociation energy,and second differences are explained in Appendix-I. Fig.(4.5) shows the binding energies, the first difference (dissociation energy), the second difference energies and spin-gap as a function of cluster sizes for Pd_n(n = 2-19). Fig.(4.5(a)) shows that the binding energy(BE) increases monotonically with the size of Pd-clusters and tending to reach towards the bulk behavior i.e towards the cohesive energy of bulk Pd solid (-3.89 eV/atom) (Rogan, *et al.*, 2008) which is the general properties of the clusters. The higher binding energy reflects the behavior of higher stability. We observed that Pd_{14}, Pd_{17} clusters are less stable than their neighbors.

In order to investigate the clear picture of stability of clusters we have to analyze the dissociation energy, second difference of energy and spin-gap. Fig.4.5(b and c) give the information of dissociation energy and second difference of Pd_n clusters. The peak of the dissociation energy represents the stability. From figure of dissociation energy it is seen that the pure Pd clusters show odd-even effect up to n=6. Above that, we found peaks at Pd_8, Pd_{10}, Pd_{13}, Pd_{15} and Pd_{18} indicating that Pd_8, Pd_{10}, Pd_{13}, Pd_{15} and Pd_{18} were more stable as compare to their neighbors. The second difference in BE of a particular clusters indicate its relative stability with respect to the neighboring size. The lowest peak in the second difference in the bonding energy represents the higher stability of

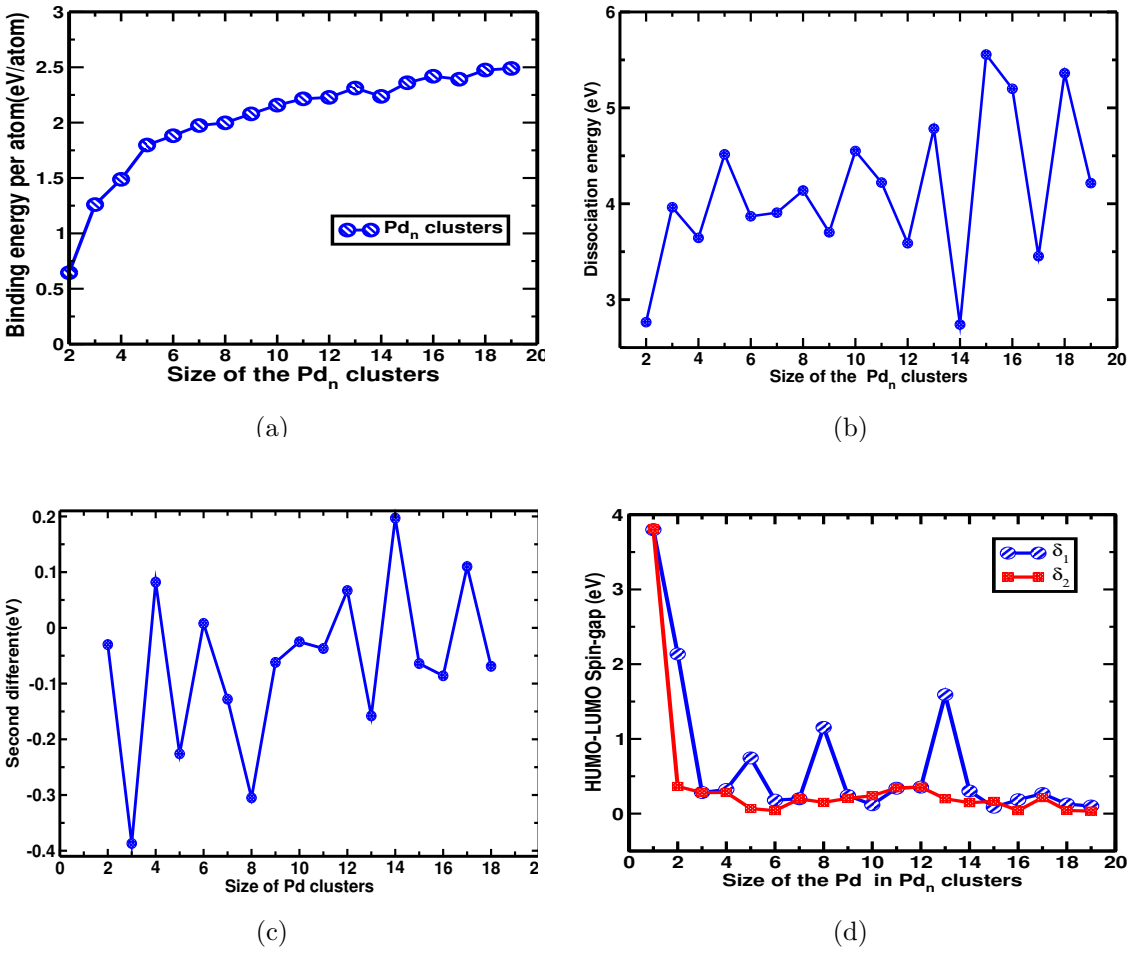

Figure 4.5: *Binding energy, dissociation energy, second differences and spin-gap of pristine Pd_n(n=2-19) clusters.*

corresponding clusters which in general is correlated with experimental mass spectral intensities rather than with binding energies. The Fig.4.5(c) reflects the corresponding stability (Rogan, *et al.*, 2005). In the series of Pd_n clusters, it also shows odd even effects up to n = 6. However Pd_8, Pd_{13}, Pd_{16} and Pd_{18} has lowest peaks indicating that Pd_8, Pd_{13} and Pd_{18} are the most stable.This trends clearly follows magic number 2, 8, 13, 18 etc. are most favorable geometrical structure and stable.

To verify the chemical stability of the clusters we have to analyze the spin gap. Spin-gap represents the energy required to move an infinitesimal amount of charge from HOMO of one spin channel to LUMO of other. The large HOMO-LUMO gap implies low chemical reactivity because it is energetically less favorable to add the electrons to higher lying LUMO or extract electrons from a low lying HOMO, thereby prohibiting the formation of a large clusters. The structure which has larger HOMO-LUMO gap is more stable and vice versa. Therefore, the magnitude of spin gap is a measure of chemical activeness of the clusters (Venkataramanan, *et al.*, 2010). The values of δ_1 and δ_2 are calculated using

the equation described in the Appendix-I. Fig.4.5(d) shows the spin-gap as a function of cluster size of pristine Pd_n (n=2-19) clusters. It is observed that the values of δ_1 and δ_2 are found to be positive for all the clusters. Some of the clusters show higher spin gap. These are attributed to quantum size effect. From figure, we have seen that Pd_2, Pd_5, Pd_8, Pd_{13} and Pd_{18} have larger spin-gap indicating that they are less reactive in comparison their neighbors. In short, it is seen that first difference, second difference and spin-gap energy follows the magic number Pd_2, Pd_8, Pd_{13} and Pd_{18} stability for the pristine Pd clusters.

Now, we focus our discussion on the BE and stability of mono and bi doped Mn atoms on pristine Pd clusters. We will discuss only up to the 13 atoms clusters as described in stable geometry. Fig.(4.6)(a) shows the variation of BE as a function of cluster size for Pd_n (n=2-13) $Pd_{n-1}Mn_1$ (n=2-13) and $Pd_{n-2}Mn_2$ (n=3-13). From the figure, It is found that BE increases with clusters size and follows the general trends of clusters as before. The $Pd_{n-2}Mn_2$ (n=3-13) clusters are found to be more stable than the $Pd_{n-1}Mn$(n=2-13). This indicates that enhancement of stability mainly comes from the doping of mono and bi atom of Mn on the Pd clusters.

From the study of dissociation energy and second difference energy from Fig.(4.6)(b and c), we found that Pd_2Mn, Pd_4Mn, Pd_7Mn and $Pd_{12}Mn$ peaks for $Pd_{n-1}Mn$(n=2-13) clusters indicating that they were more stable than their neighbors. Similarly more stable clusters in the bi-doped series were at Pd_2Mn_2, Pd_4Mn_2, Pd_8Mn_2 and $Pd_{10}Mn_2$.

The second difference in BE of a particular clusters indicate their relative stability with respect to their neighbors. The peak in the second difference in the bonding energy also represents the higher stability of corresponding clusters against breakup. From the second difference energy curve of $Pd_{n-1}Mn_1$ ($n = 2 \leq 13$), We found Pd_3Mn, Pd_6Mn, Pd_9Mn and $Pd_{11}Mn$ are more stable than their neighbour. We found first and second difference do not give the conclusive results about the stability, this is mainly due to strange behaviour of Mn atom doped on to the Pd clusters. To come into conclusions we have to analyze the spin-gap behavior. Spin-gap measures the energy required to move an infinitesimal amount of charge from HOMO of one spin channel to LUMO of the other. The the magnitude of spin gap also measures the chemical activeness of the clusters and hence the chemical stability of the clusters. Fig.4.7(a) shows the spin-gap for $Pd_{n-1}Mn_1$ ($n = 2 \leq 13$) clusters. From the figure, it is seen that $PdMn$, Pd_3Mn, Pd_5Mn, Pd_7Mn, $Pd_{10}Mn$ and $Pd_{12}Mn$ are more stable than their neighbour. This results some how supports the first energy difference. From the analysis first difference and spin-gap we conclude that n= 2, 6, 8 and 11 are more stable than their neighbour.

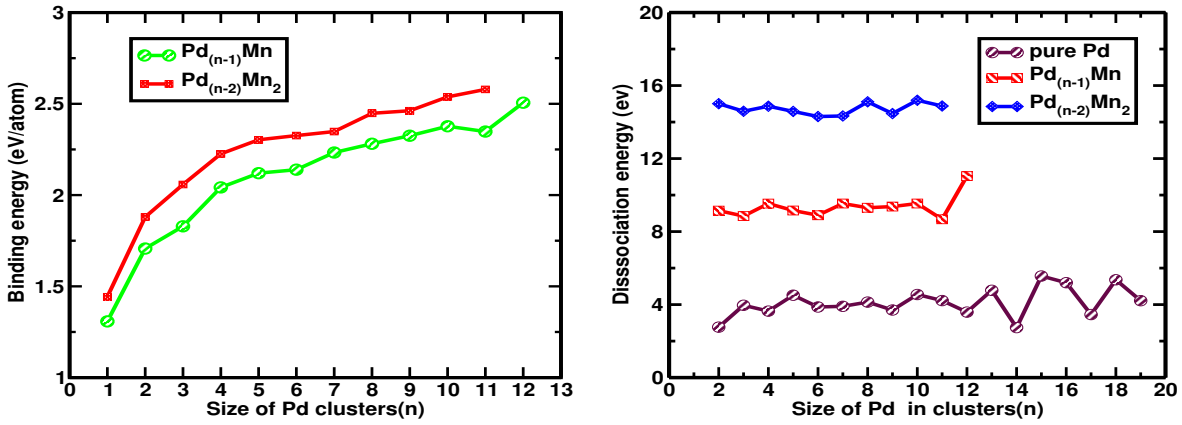

(a) (b)

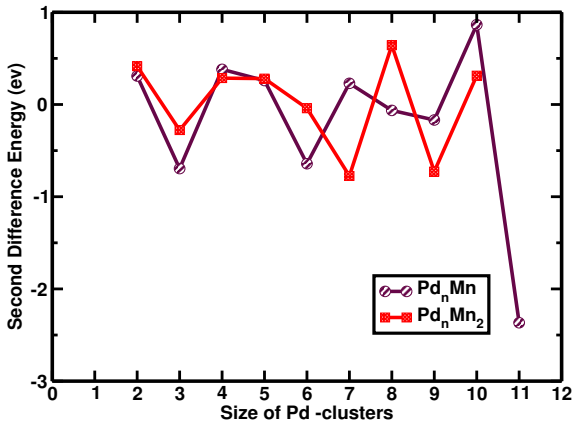

(c)

Figure 4.6: *(a) Binding energies (b) first energy differences of pristine Pd, mono- and bi-doped Mn on Pd clusters and (c) second energy differences after doping Mn_1 and Mn_2 on pristine clusters.*

Similarly, from the second difference energy curve of $Pd_{n-2}Mn_2$ $(n = 3 \leq 13)$ clusters we have seen that Pd_1Mn_2, Pd_5Mn_2 and Pd_7Mn_2 clusters are found to be more stable than their neighbour. This also does not provide the clear picture about stability. Fig.4.7(b) shows the spin-gap for $Pd_{n-2}Mn_2$ $(n = 3 \leq 13)$ clusters. From the figure, it is seen that $PdMn_2$, Pd_3Mn_2, Pd_5Mn_2, Pd_7Mn_2 and $Pd_{10}Mn_2$ are more stable than their neighbour. These results supports the second energy energy difference. The characteristics of spin-gap is given in table (7.1) of Appendix-I.

In short, From values of spin-gap, we found mono-doped clusters have higher spin gap than the pristine or bi-doped clusters. This clearly indicates that $Pd_{n-1}Mn_1$ $(n = 2 \leq 13)$ is more stable than $Pd_{n-2}Mn_2$ $(n = 3 \leq 13)$

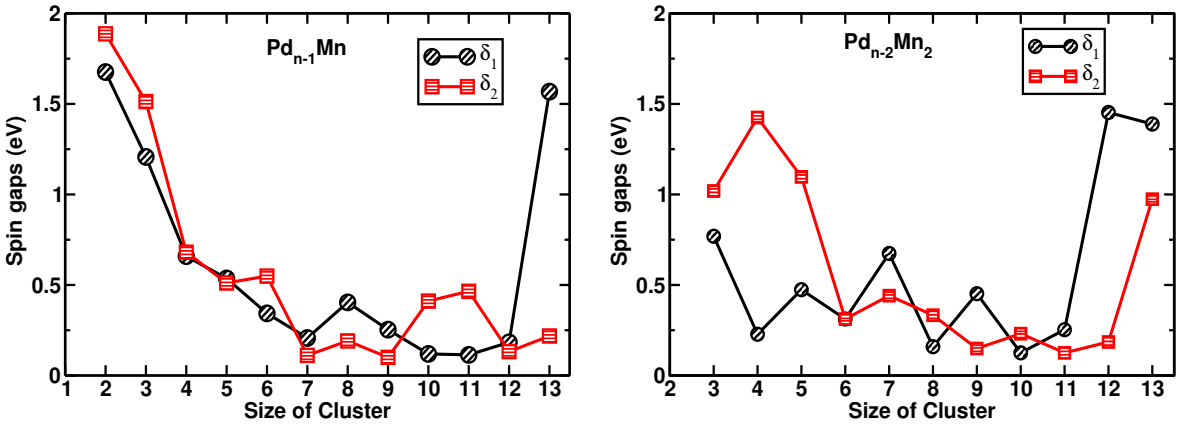

(a) (b)

Figure 4.7: *(a) Spin-gaps (in eV) for* $Pd_{n-1}Mn_1$ $(n = 2 \leq 13)$ *and (b)* $Pd_{n-2}Mn_2$ $(n = 3 \leq 13)$*clusters.*

4.2.4 Magnetic Properties

It is well understood that small sized Pd clusters show the magnetic behavior as contrast to the non-magnetic behavior of pure bulk Pd (Luo, *et al.*, 2007). The actual origin of such a magnetic properties exhibited by such clusters are still unclear. To know the origin of magnetism, we tested variation of bond length with size of the clusters.

Fig.(4.8)(a) shows variation of Pd-Pd and Pd-Mn bond length as a function of clusters size. We observed that there is no special trends of variation of Pd-Pd and Pd-Mn bond length with respect to the cluster size. So it is difficult to relate MM and variation of bond length. Fig.(4.8(b)) displays the variation of magnetic moment of Pd_n clusters in the unit of Bohr's magnetrons, of optimized lowest energy configurations of Pd_n. The average magnetic moments of Pd in Pd_n clusters found to be more or less step like behavior and varies irregularly with the size of Pd clusters. In case of Pd_{13} clusters, we found $0.52\mu_B$/atom which is around 10% higher than previously reported data (Lee, (1998).

Fig.(4.8 (c) and (d)) show the variation of average magnetic moment of Pd and Mn separately, of optimized lowest energy configurations of pristine and mono- and bi-doped Pd clusters. In case of $Pd_{n-1}Mn$ clusters, there is a slight decrease in magnetic moment of Pd and Mn up to cluster size 6, but nearly same magnetic moment of Pd for n = 7, 8 and 9, whereas one sees high magnetic moment of Mn at n = 7. This may be due to different rates of charge transfer from Mn to Pd. This is mainly due to their different electro-negativities (1.55 for Mn and 2.20 for Pd). Total magnetic moment of mono-

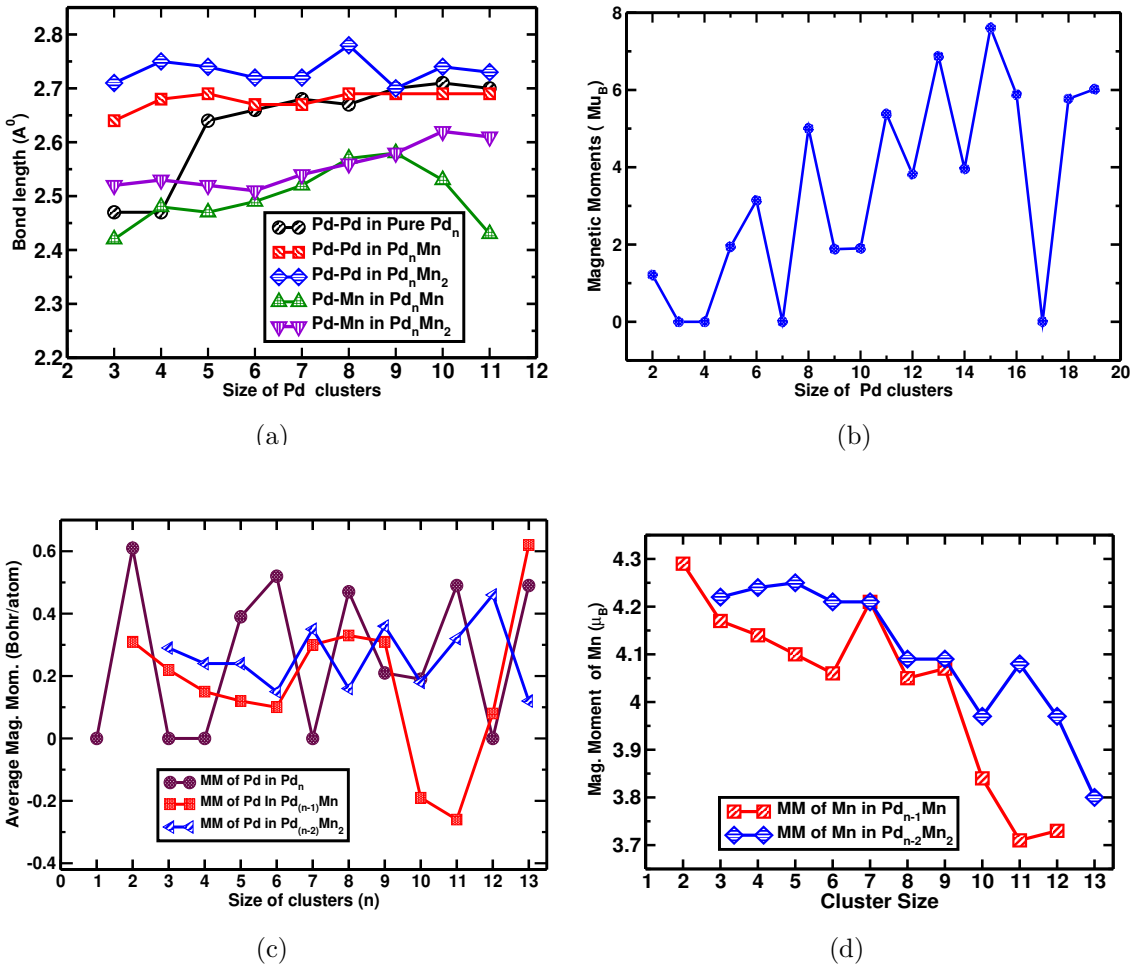

Figure 4.8: *(a) Average bond-lengths (b) Magnetic moment of pristine Pd_n clusters (c) Magnetic moment/atom of Pd on pristine and doped clusters and (d) Magnetic moments of Mn on mono- and bi-doped Mn on pristine Pd_n clusters.*

doped clusters are found to be ranges from 4.58-9.64μ_B. The magnetic moment of stable icosahedral $Pd_{12}Mn$ clusters is found to be 9.64μ_B. Present result agrees well with the conclusions of (Knickelbein, 2004). Knickelbein reported that due to hybridization and interstitial contribution, the actual magnetic moment of Mn atoms in $Pd_{n-1}Mn$ clusters is smaller than expected by Hund's rules, but much larger than that of Mn_n clusters with similar size, which is only in the range $(0.4 - 1.7)\mu_B/atom$ for n = 5-19.

In case of $Pd_{n-2}Mn_2$ clusters we found even-odd variation in magnetic moments for n $\geq$ 11. The magnetic moments for $Pd_{10}Mn_2$ is found to be very high(12.52μ_B) this may be due to alignment of two Mn in same direction. This case is just reverse in $Pd_{11}Mn_2$ at this case icosahedral structure is found to be most stable having less magnetic moment (2.00μ_B)). The less in MM is due to the anti-ferromagnetic alignment of two different Mn atoms sit at different sites as shown in Fig.(4.10(d)).

Fig.(4.9(a) and (b)) show total magnetic moment for $Pd_{n-1}Mn$ and $Pd_{n-2}Mn_2$ clusters

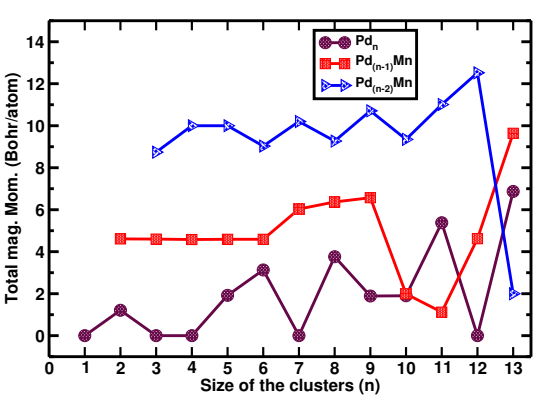

(a)

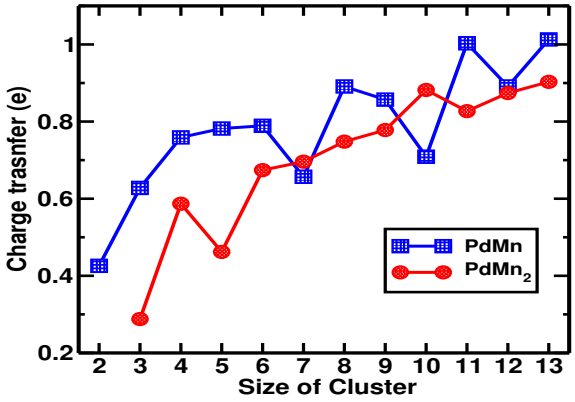

(b)

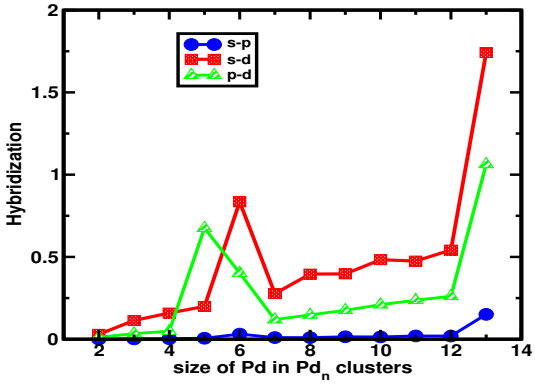

(c)

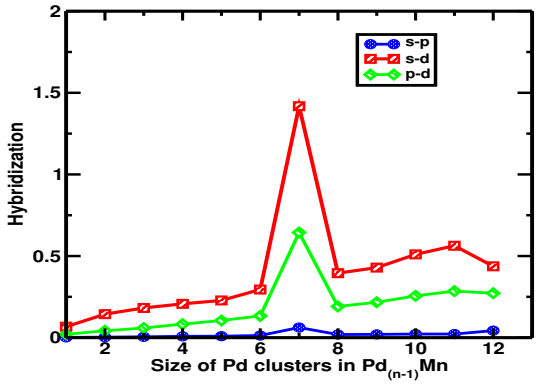

(d)

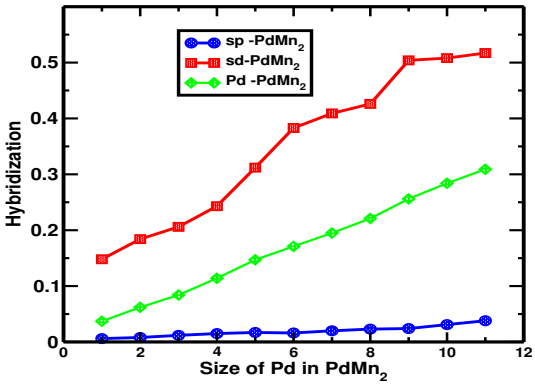

(e)

Figure 4.9: *(a)Total magnetic moment of $Pd_{n-1}Mn$ and $Pd_{n-2}Mn_2$ clusters (b) Charge transformation on mono- and bi-doped of Mn on Pd clusters (c) Hybridization in pristine Pd clusters (d) Hybridization in $Pd_{n-1}Mn_1$ and (e) Hybridization in $Pd_{n-2}Mn_2$ clusters.*

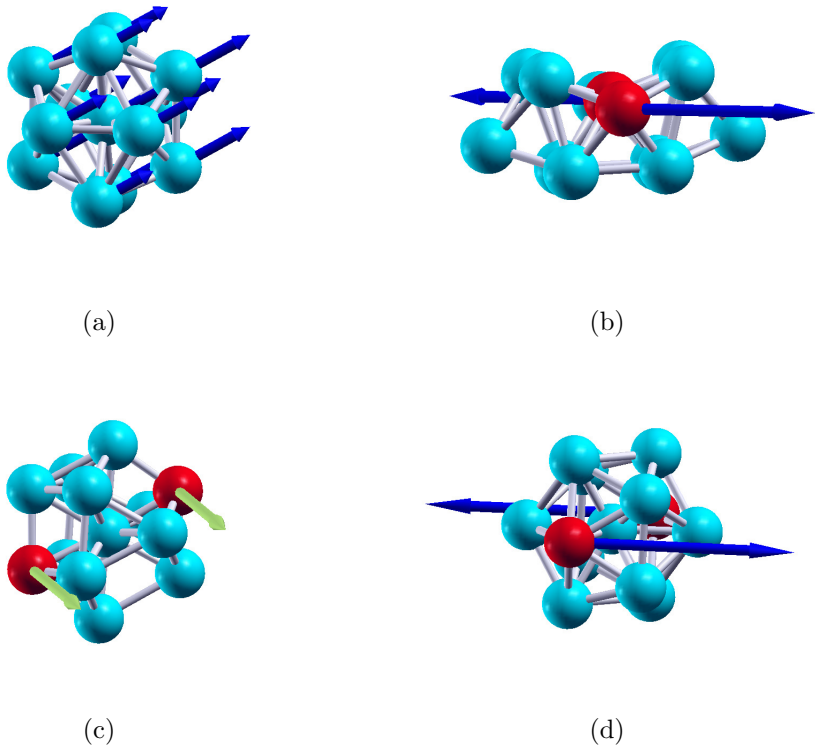

Figure 4.10: *Magnetic moments (a) on Pd in the icosahedral pristine Pd cluster (b) on Mn in the BBP $Pd_{11}Mn_2$ cluster (ferrimagnetic), (c) on Mn in fcc based $Pd_{11}Mn_2$ (ferromagnetic) and (d) on Mn in icosahedral $Pd_{11}Mn_2$ (antiferromagnetic)(Red ball represents the Mn atom).*

and charge transformation from Mn. It is seen from the figure that the charge transformation in $Pd_{n-1}Mn$ increases except for Pd_6Mn, Pd_9Mn, $Pd_{11}Mn$. Similarly rate of transformation of charge found to be followed the increasing trends in Pd_nMn_2 except for Pd_3Mn_2, Pd_9Mn_2. This indicates that as charge transformation increases the MM of Mn for $Pd_{n-1}Mn$ and $Pd_{n-2}Mn_2$ are found to be decreases.

Fig.(4.9(c),(d) and (e)) represents the hybridization for pristine Pd_n, $Pd_{n-1}Mn$ and $Pd_{n-2}Mn_2$ clusters. Longer bond lengths lead to lower hybridization giving higher moments according to the Stoner type argument. But this trend are not strictly followed by pristine clusters of sizes 6, 7, 8, 10 and 11 atoms.

Fig.(4.9(c)) shows that $s-d$ hybridization dominates the overall properties of Pd_n pristine clusters. In this case Pd_5 clusters show the contributions of p-d hybridization also and produces the local magnetic moments $1.92\mu_B$. Similarly in case of Pd_6 which has a magnetic moments $3.92\mu_B$ and follows the trends dominating s-d hybridization. The maximum magnetic moment is shown at 13-atoms icosahedral structure which is the most stable in this series. As we have discussed earlier, the shorter bond lengths of Pd_5 create strong hybridization between the localized d states and p state and hence produce smaller magnetic moment. Whereas for Pd_6, there is significant $s-d$ hybridization offset

by large transitions between up and down spin PDOS which creates its rather larger magnetic moment. The magnetic moments of Pd_7 is zero where as Pd_8 reaches to $5.1\mu_B$. Similarly Pd_9 and Pd_10 magnetic moments are found to be 2.08 μ_B and 2.16 μ_B respectively. This indicates that MM is very sensitive to clusters geometry. We found that MM of Pd_{12} is small(3.92 μ_B) where as Pd_{13} has highest MM (6.87 μ_B). The highest MM is due to alignment of all spins in particular directions as in Fig.(4.10(a)) and due to their high symmetries and low mean coordination. The trends of lowest energy structures of Pd_n clusters and variation trend of the magnetic moment with the cluster size of the present work is similar to that of previously reported trends (Kumar, 2006), (Rogan, *et al.*, 2008).

Fig.(4.9(d)(e)) show the $s-p$, $p-d$ and $s-d$ hybridization for $Pd_{n-1}Mn_1$ and $Pd_{n-1}Mn_1$ clusters. It is found that there is notable $s-d$ and $p-d$ hybridization which produces large transitions between spin up and down states. Together with sufficient bond lengths, it is likely to produce the large magnetic moments. The relatively smaller bond lengths between Pd-Pd and Pd-Mn in $Pd_{10}Mn$ and $Pd_{11}Mn$ leads to anti-ferromagnetic alignment between Pd and Mn decreasing the total moments. In the case of $Pd_{12}Mn$, the bond length leads to ferro alignment between Pd and Mn and hence produce larger total moment. Similarly, In the bi-doped clusters we can not totally neglect the $p-d$ contributions. This is due to the unusual magnetic behavior of Mn_2 molecules. The magnetic moments for n=6, 10, 8 and 13 are found to be less magnetic moments. This is due to the anti-ferromagnetic alignment of two Mn atom sitting in different sites.

The bond lengths between Pd-Pd and Pd-Mn of respective clusters cause the s and d states to split leading depletion of 4d states through s-p-d hybridization, giving rise to large magnetic moments. Smaller bond lengths create strong d-d interactions and Pd and Mn moments align anti-ferromagnetically. In the icosahedral clusters of $Pd_{11}Mn_2$ the two Mn moments also align anti-ferromagnetically as shown in Fig.4.10(d) so as to produce less magnetic moments.

4.2.5 Projected DOS

The knowledge of s, p and d-projected density of states is required to understand the exact magnetic behavior of the clusters. Since the magnetic moment of Pd_n cluster is highest for n = 13 and most stable geometry, we present and discuss the projected density of states(PDOS) and total density of states (TDOS) of icosahedral structures for pristine, mono-doped and bi-doped of 13 atoms clusters. The Fig.(4.11), Fig.(4.12(a,b)) and Fig.(4.12(c,d)) display the TDOS and PDOS of Pd_{13} cluster, $Pd_{12}Mn$ and $Pd_{11}Mn_2$ clusters respectively. From Fig.(4.11), we found that the d-projected DOS, exchange

split with s, plays an dominant role in producing magnetism in Pd_{13} clusters. There is negligible contribution from p-projected DOS and an even smaller contribution from s-PDOS. This is consistent with the physical picture that incomplete d-shell electrons should be mainly responsible for the magnetism of TM clusters. It is seen that, as discussed on pure Pd_{13} clusters, the d states of both Pd host atoms and doping Mn atoms in $Pd_{n-1}Mn$ and $Pd_{n-2}Mn_2$ clusters play dominant role in the determination of total magnetic moment. The contribution of s states is found to be negligibly small. In case of $Pd_{n-1}Mn$ the Mn atom tends to be coupled ferromagnetically where as two Mn atoms tends to be coupled antiferromagnetically in case of $Pd_{n-2}Mn_2$. This make the difference in spin up and down peak of $Pd_{n-1}Mn$ and $Pd_{n-2}Mn_2$.

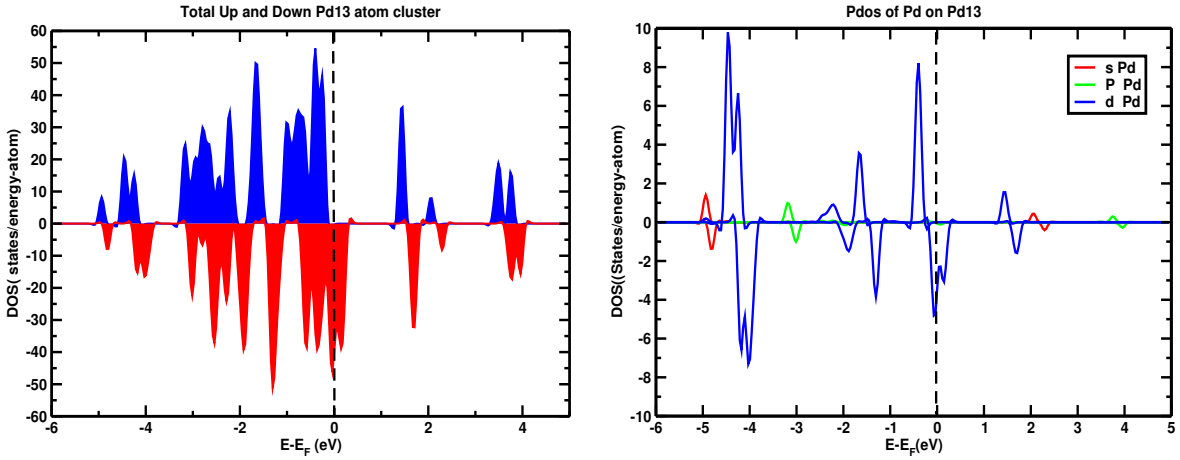

Figure 4.11: *Total DOS and Spin-orbital projected PDOS for pristine Pd_{13} clusters. .*

4.3 Adsorption and dissociation of N_2 and H_2 molecules on tantalum and niobium clusters

In this section, we present our findings about the stability, adsorption and dissociation of pristine Ta_n and Nb_n(n=2-7) clusters. Further we have doped hydrogen and nitrogen molecules on Ta_n and Nb_n(n=2-7) clusters. The main reason of taking n = 7 clusters is that these are the building blocks of higher clusters (Karabacak, *et al.*, 2002). The information whatever found from these also reflect for higher clusters. We tested doping effect using single atom as well as molecular form for searching the optimize structures. In ordered to deal the problem, we used DFT and plane wave basis set through the code given in VASP. The formula used for the calculation and procedure are explained in Appendix-I. The variation of binding energy, chemisorption energy, charge transformation and HOMO-LUMO gap with the clusters size have been explained.

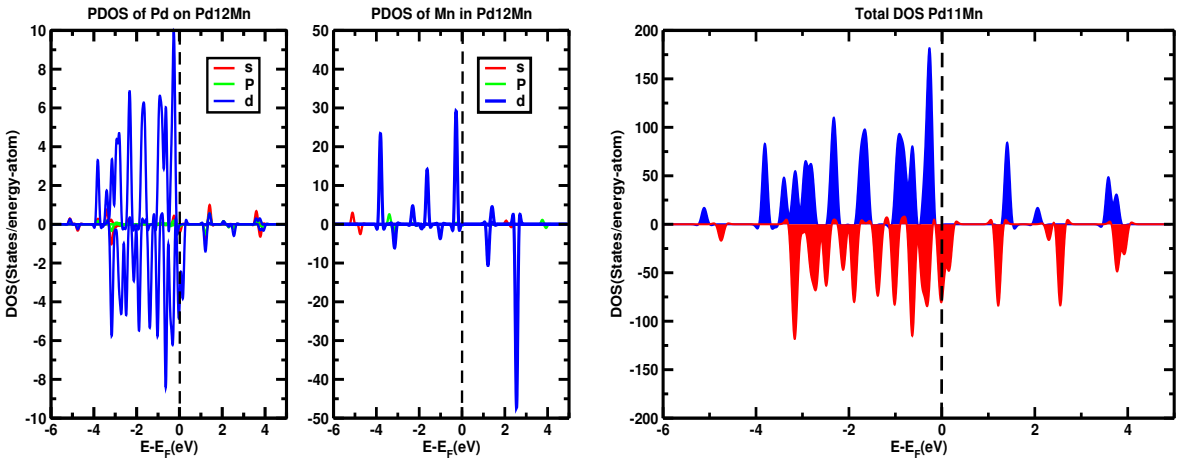

(a) (b)

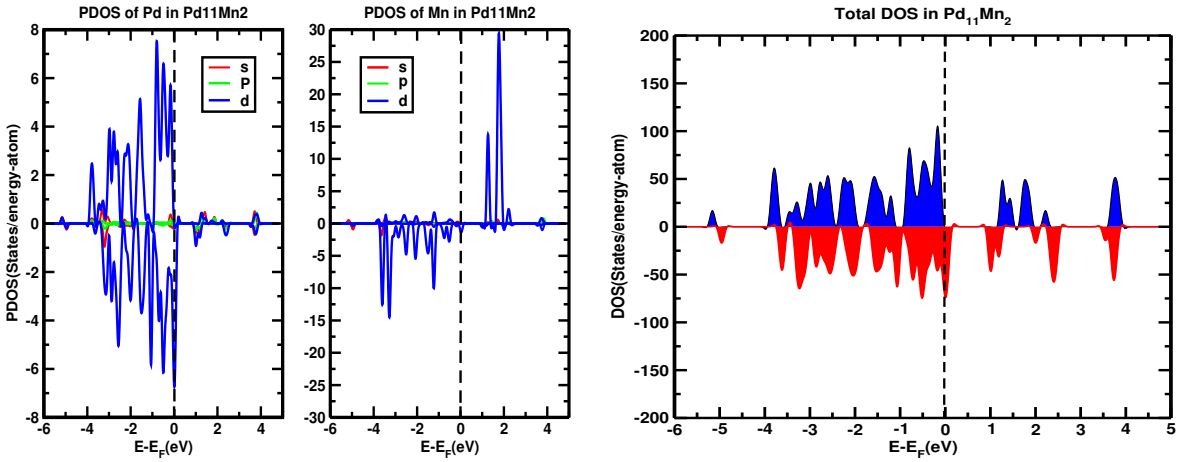

(c) (d)

Figure 4.12: *(a) Spin-orbital projected DOS (b) Total DOS for $Pd_{12}Mn$ and (c) Spin-orbital projected DOS (d) Total DOS for $Pd_{11}Mn_2$.*

4.3.1 Geometry of pristine Ta_n and Nb_n (n=2-7) clusters

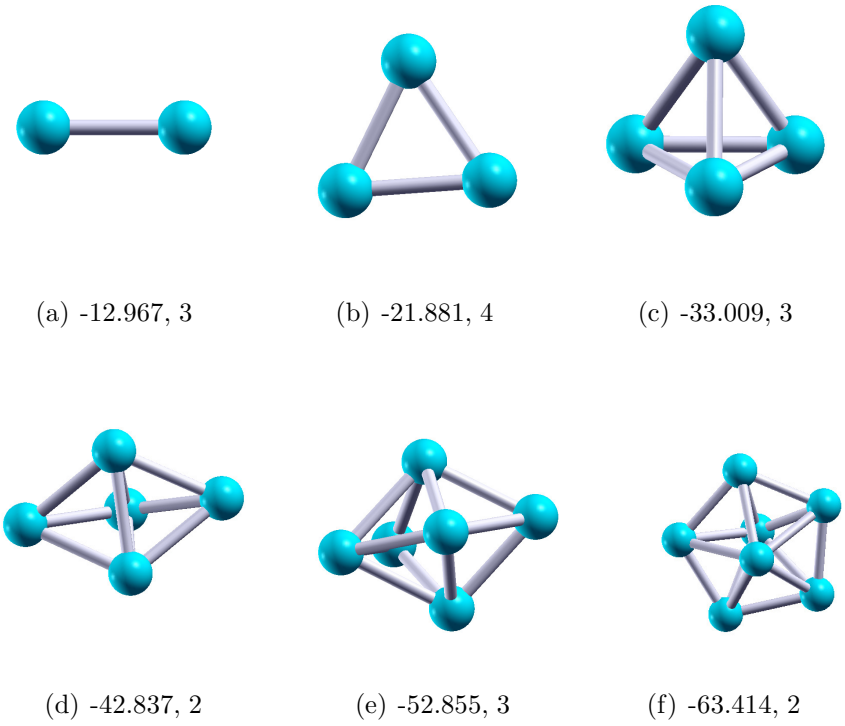

(a) -12.967, 3 (b) -21.881, 4 (c) -33.009, 3

(d) -42.837, 2 (e) -52.855, 3 (f) -63.414, 2

Figure 4.13: *Most stable geometries of Ta_n (n=2-7) clusters. The optimized energies(eV) and spin multiplicity are given beneath the stable geometry.*

From the energy values of the individual Ta and Nb atoms and their clusters, we have estimated the BE of the clusters of n = 2-7. Similarly, we have estimated the average bond length, spin gap etc. The optimized geometry for small Ta_n and Nb_n clusters with n = 2-7 are shown in Figs.(4.13) and (4.14) respectively. These are the base of our doping structures. We tried different isomers. We presented only the most stable configurations for Ta_n clusters with optimized energy (eV) and spin multiplicity. In case of Nb_n(n = 2-7), we presented most stable and nearest neighbour optimized geometry with optimized energy (eV) and spin multiplicity. The binding energy(BE), magnetic moment, Spin-gap and average bond length for the most stable geometry of Ta_n and Nb_n (n = 2-7)clusters have been presented in tables (4.1) and (4.2) respectively.

To confirm the validity of code, we performed the analysis with dimers. From table (4.1), the BE of Ta-Ta found to be 3.016 eV/atom which is higher than experimental results(2.01 ± 0.5) eV/atom (Morse, 1986) and less than the calculated result of Karolewski (3.49 eV/atom). The bond length of Ta dimer found to be $2.21A^o$ agrees about 0.9% with experiment (2.23 $\AA$) (Shun-Ping, *et al.*, 2011), (Sun *et al.*, 2010). Similarly, the binding energy of Nb-Nb dimers found to be 2.293 eV/atom which lies within the error bar of experimental results(2.5 ± 0.2) (Karolewski, 2001). The calculate bond length

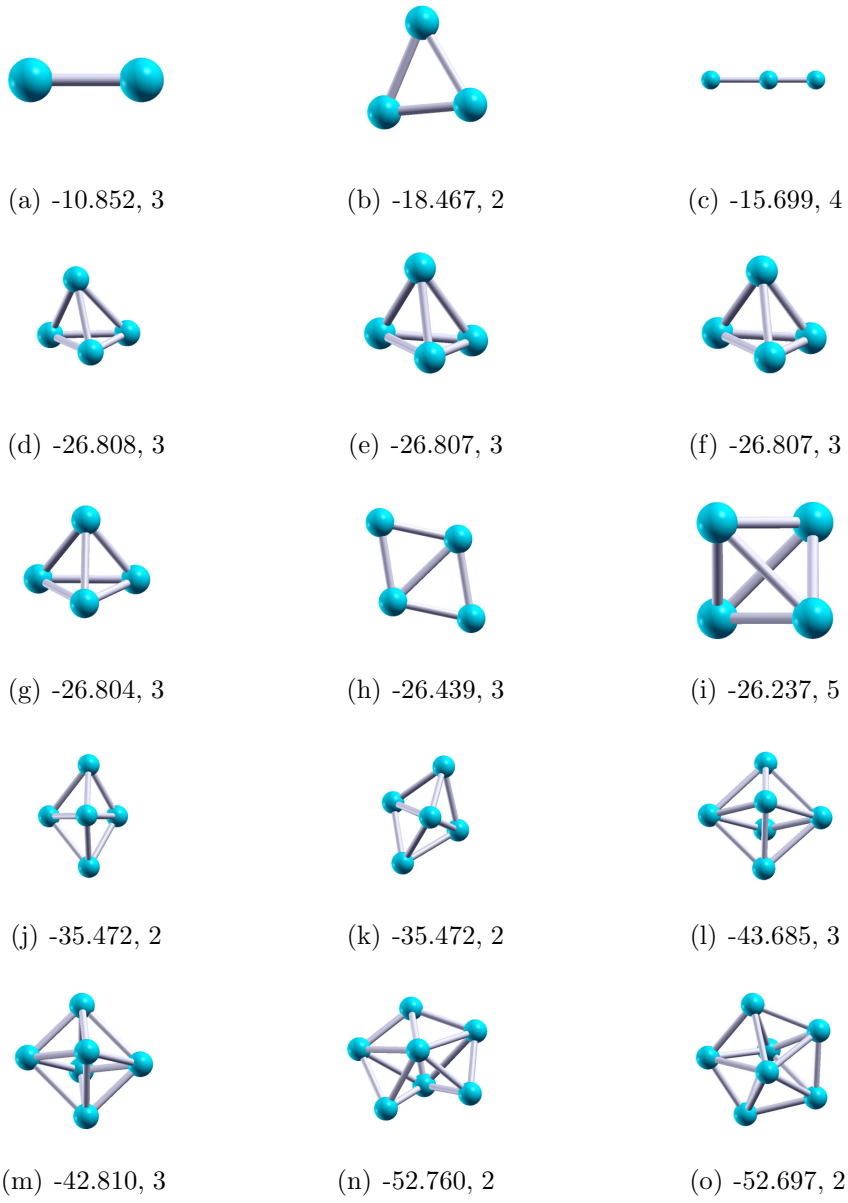

(a) -10.852, 3 (b) -18.467, 2 (c) -15.699, 4

(d) -26.808, 3 (e) -26.807, 3 (f) -26.807, 3

(g) -26.804, 3 (h) -26.439, 3 (i) -26.237, 5

(j) -35.472, 2 (k) -35.472, 2 (l) -43.685, 3

(m) -42.810, 3 (n) -52.760, 2 (o) -52.697, 2

Figure 4.14: *Most stable geometries of Nb_n (n=2-7) clusters with optimized energy and spin multiplicity.*

Table 4.1: *Calculated Binding energy, Magnetic Moment, Spin Gap for the geometry of most stable Ta_n Clusters*

Clusters size	Binding Energy (eV)	Magnetic moment (μ_B)	spin-gap		Average bond length
			δ_1(eV)	δ_2(eV)	$\mathring{A}$
Ta_2	3.016	1.670	0.823	0.646	2.210
Ta_3	3.826	2.320	0.513	0.571	2.393
Ta_4	4.785	0.000	0.939	0.939	2.512
Ta_5	5.100	0.965	0.385	0.494	2.505
Ta_6	5.342	1.590	0.537	0.885	2.677
Ta_7	5.592	1.023	0.294	0.235	2.556

Table 4.2: *Calculated Binding energy, Magnetic Moment, Spin Gap for the geometry of most stable Nb_n Clusters.*

Clusters size	Binding Energy (eV)	Magnetic moment (μ_B)	spin-gap		Average bond length
			δ_1(eV)	δ_2(eV)	$\mathring{A}$
Nb_2	2.293	1.543	1.483	0.745	2.119
Nb_3	3.022	0.783	0.843	0.577	2.377
Nb_4	3.568	1.111	0.574	0.718	2.564
Nb_5	3.961	0.851	0.635	0.399	2.594
Nb_6	4.147	1.672	0.343	0.890	2.680
Nb_7	4.394	0.887	0.582	0.221	2.643

for Nb dimer from the present calculation (2.11 $\mathring{A}$) agrees within 1.4% with the experimental values i.e. 2.08 $\mathring{A}$ (Jules & Lombardi, 2003). We have also calculated the equilibrium structure and hence BE and bond length of H_2 and N_2. From the present calculation, the BE of H_2 is found to be 2.236 eV/atom which agrees within 1.7% to the experimental result (Cabria, *et al.*, 2006). The bond length of H_2 is estimated to be 0.74 $\mathring{A}$ which exactly agrees with previous experimental results of (Cabria, *et al.*, 2006). The BE of N_2 found to be 5.18 eV/atom agrees within 5% within experimental results (4.90 eV/atom) and the bond length 1.36 $\mathring{A}$ which is about 6% less than experimental results 1.45 $\mathring{A}$ of Cabria *et al.*. From the study of these geometries, we observed that Nb and Ta both favors the same kinds of geometrical growth pattern.

The main aim of the present study is to analyze the structural effect of doping and adsorption or/and dissociation of hydrogen molecule(H_2) and nitrogen molecule (N_2)

on Ta_n and Nb_n (n = 1-7) clusters which have been explained in following section.

4.3.2 Structural effect on Ta_n (n=2-7) clusters after doping H_2 and N_2

We have investigated the change in structures of Ta_n for (n = 1-7) after doping H_2 and N_2 using DFT through VASP. We also studied adsorption or/and dissociation of hydrogen and nitrogen on Ta_n (n = 1-7) clusters. We optimized ground state geometry of pristine Ta_n for (n=1-7) clusters after doping hydrogen and nitrogen in various ways. Out of several isomers most stable geometries are shown in Fig.(4.15-4.18). The optimization energy and spin multiplicity are associated beneath the respective figures.

n = 1, Figs.(4.15(a) and (b)) represent the stable structures of TaH_2. Fig.(4.15)(a) is linear where as Fig.(4.15)(b) is isosceles triangle. The BE of ground state geometry of TaH_2 is 1.845 ev/atom (optimized energy -11.225 eV). The bond length of Ta-H estimated to be 1.732$\mathring{A}$ and spin multiplicity 2. It is observed that by doping H_2 on Ta the bond length of H-H increased by 0.074$\mathring{A}$(0.81 $\mathring{A}$) against the free H_2(0.74$\mathring{A}$) (Kim, *et al.*, 2010). The next nearest conformer (Fig.(4.15)(a)) of TaH_2 has optimized energy O.104 eV higher than ground state which has spin multiplicity 2. The $\angle(H-Ta-H)$ found to be 65.04^0. The H-H distance increased by 0.08 $\mathring{A}$ (1.82 $\mathring{A}$) against the free H_2 Similarly, Figs. (4.17(a),(b), (c),(d)) represent the stable structures of TaN_2. The ground state geometry is linear at which nitrogen molecule found to be adsorbed molecularly. The bond length of N-N is increased by o.03$\mathring{A}$ (1.17$\mathring{A}$) against the free N_2 (1.14$\mathring{A}$) (Limpijumnong, *et al.*, 2005). The BE of TaN_2 found to be 4.07 ev/atom (optimized energy -21.952 eV) with Ta-N bond length $1.803A^o$. The second and third conformer has $\angle(N-Ta-N)$ 64.72^0 and 50.52^0 with N-N separation 1.54$\mathring{A}$ and 1.23$\mathring{A}$ respectively. In short, both H_2 and N_2 molecules found to be adsorbed molecularly on Ta and linear structure is found to be most stable conformer.

n = 2, in case of Ta dimer with two H atoms, a squared shaped structure with cyclically positions of Ta and H atoms are found to be stable geometry. Similar kinds of structure found as stable in case of two nitrogen atoms doped on Ta dimer.

In case of Ta_2H_2, the ground state (Fig.(4.15)(c)) geometry has BE 2.865 eV/atom (optimized energy -20.620 eV) with Ta-Ta and Ta-H bond length 2.205$\mathring{A}$ and 1.86$\mathring{A}$ respectively. The $\angle(H-Ta-Ta)$ is found to be equal to 53.246^0 and $\angle(H-Ta-H)$ was 106.72^o. Two H atoms are at the corners separated by 2.982$\mathring{A}$ indicating that it favors dissociative properties. Fig.(4.15)(c) has a spin multiplicity 3. The next stable structure (Fig.(4.15)(d)) has spin multiplicity 1 on which each atom bounds to single Ta almost perpendicular form. The optimized energy of this structure found to be 0.237 eV more than ground state. In case of Ta_2N_2, Ta-Ta and Ta-N bond length are found to

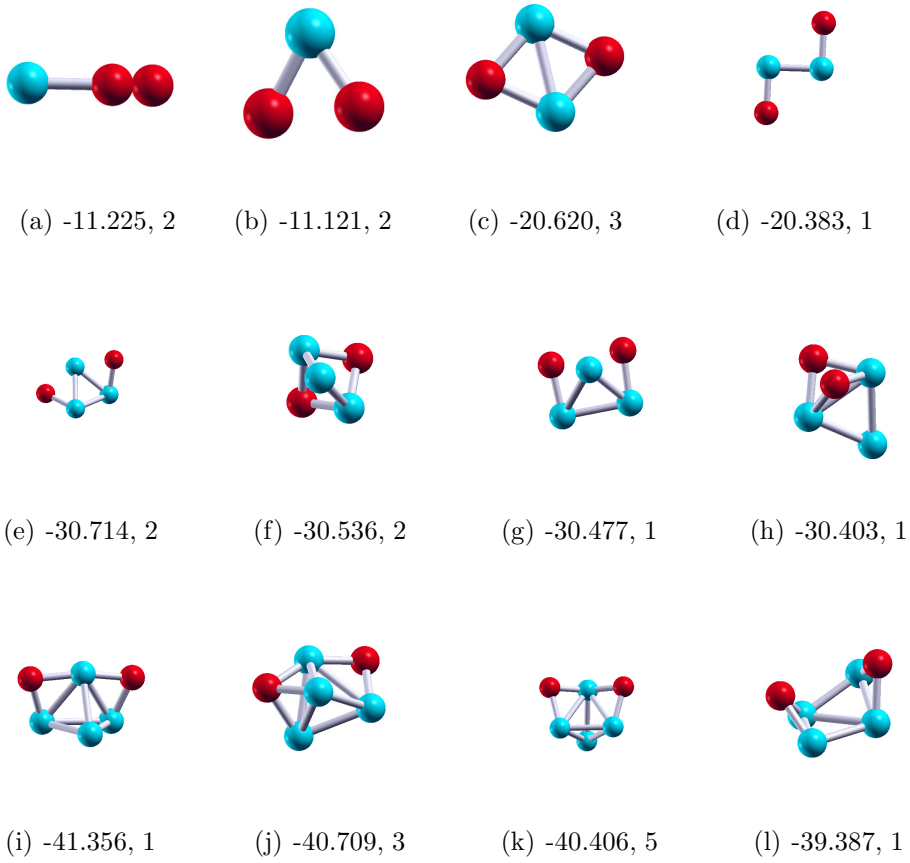

(a) -11.225, 2 (b) -11.121, 2 (c) -20.620, 3 (d) -20.383, 1

(e) -30.714, 2 (f) -30.536, 2 (g) -30.477, 1 (h) -30.403, 1

(i) -41.356, 1 (j) -40.709, 3 (k) -40.406, 5 (l) -39.387, 1

Figure 4.15: *Most stable geometries of Ta_nH_2 (n=1-4) clusters showing total energies(eV) and spin multiplicity of optimized figures (Red ball represents the H atom).*

be 2.701$\mathring{A}$ and 1.87$\mathring{A}$ respectively with $\angle(N-Ta-N) = 87.760^0$. Two N atoms are at the different corners of a squared shaped structure separated as 2.586$\mathring{A}$ indicating that it also favors dissociative properties. This has spin multiplicity 1. The ground state geometry has much large BE 5.182 eV/atom. This indicate that Ta-Ta dimer binds nitrogen atoms more strongly than hydrogen atoms. From above we can say that both hydrogen and nitrogen adsorbed dissociatively on Ta_2 clusters but spin multiplicity of pristine (3) get change.

n = 3, Fig.(4.13(b)) shows the ground state geometry of Ta_3 trimer which is isosceles triangle such that geometry having equal sides are separated by 2.393$\mathring{A}$ and other has (2.67$\mathring{A}$). This has a spin multiplicity 4. Present geometry the resembles with results of previous work (Yadav & Mookerjee, 2010). Fig.(4.15(e)) shows the most favorable geometry of (Ta_3H_2) on which one H atom lying in the plane of the three Ta atoms and another H atom is out of plane and situated at the bridging site of two Ta atoms. The average Ta-Ta and Ta-H bond lengths are found to be 2.373$\mathring{A}$ and 1.874$\mathring{A}$ respectively. Two H atom separated with each other by 3.826$\mathring{A}$. This indicates that hydrogen molecules tends to dissociate by Ta_3 trimer It has BE 3.618 eV/atom with the spin multiplicity 2. The nearest conformer has optimized energy 0.178 eV higher than ground states which also shows dissociation of hydrogen molecules after relaxation with the same spin multiplicity(2). Third and fourth conformers also shows the dissociation of hydrogen molecules but spin multiplicity found to be changes from 2 to 1. Similar nature of geometry has found after doping two N atoms in Ta_3. Figs.(4.17(i, j, k, l)) show the optimized geometry for (Ta_3N_2). The ground state geometry of (Ta_3N_2) has BE 5.334 eV/atom. The separation of Ta-Ta and Ta-N found to be 2.545$\mathring{A}$ and 1.906$\mathring{A}$ respectively. It has spin multiplicity 2. In the ground state geometry two N atoms sit at the bridging site of two Ta atoms (separated by 3.203$\mathring{A}$) indicating that nitrogen molecules also show dissociative behavior. The second conformer has 0.068 eV energy higher than ground state with the same spin multiplicity. The third and fourth conformers show the nitrogen adsorbed in molecular form but these conformers has higher optimized energies than dissociate ones.

n = 4, Fig.(4.13(c)) shows the ground state structure for Ta_4 which is tetrahedron shape with BE 4.785 eV/atom having spin multiplicity 3. The average Ta-Ta distance is found to be 2.512$\mathring{A}$. Fig.(4.15(j-l)) show the favorable geometries of Ta_4H_2. Fig.(4.15(j)) is the ground state geometry of Ta_4H_2 which has BE 4.211 eV/atom with spin multiplicity 1(singlet state). In the ground state geometry one H atom lying in the plane of four Ta atom and another atom out of plane and situated at the bridging site of two Ta atoms(separated each other by 3.961$\mathring{A}$). This means hydrogen molecule found to be dissociate. The average bond length of Ta-Ta and Ta-H are found to be equal to 2.46$\mathring{A}$

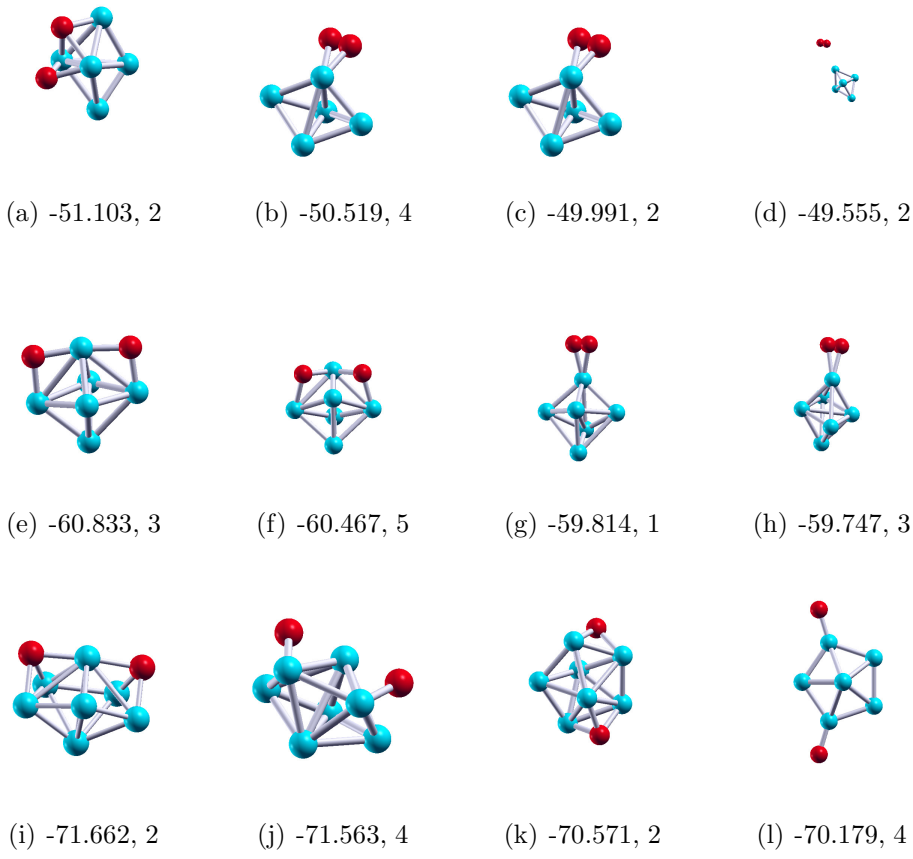

(a) -51.103, 2 (b) -50.519, 4 (c) -49.991, 2 (d) -49.555, 2

(e) -60.833, 3 (f) -60.467, 5 (g) -59.814, 1 (h) -59.747, 3

(i) -71.662, 2 (j) -71.563, 4 (k) -70.571, 2 (l) -70.179, 4

Figure 4.16: *Most stable geometries of Ta_nH_2 (n=5-7) clusters showing total energies(eV) and spin multiplicity of optimized figures (Red ball represents the H atom).*

and 1.954$\mathring{A}$ respectively. The hydrogen molecule also found to be dissociate on other conformers. Similarly, Fig.(4.17(m-p)) show the favorable structure for Ta_4N_2. In the ground state geometry two nitrogen atoms are found to adsorbed on the bridging sites of two different Ta atoms. This shows that nitrogen molecule (separated by 4.426$\mathring{A}$) found to be dissociate after doping on Ta_4 cluster. The spin multiplicity 3 of pure Ta_4 tetrahedron remains unchanged after doping two nitrogen atoms. The BE of Ta_4N_2 is found to be 5.644 eV/atom. The average Ta-Ta and Ta-N bond length are found to be 2.65 $\mathring{A}$ and 1.88$\mathring{A}$ respectively. Present results agrees well with the previously calculated data(Yadav & Mookerjee, 2010). The conformers on which nitrogen molecules are found to be adsorbed in molecular form are less stable. These have higher optimized energy than the ground state as in Fig.(4.17(o-p)). These have optimized energies 3.987 eV and 4.017 eV higher than ground state geometry respectively.

n = 5, The stable structure of Ta_5 have bi-pyramid type having BE 5.100 eV/atom with Ta-Ta bond-lengths 2.505$\mathring{A}$ as in Fig(4.13(d)). Fig.(4.16(a-d)) present the stable configurations of Ta_5H_2. In the ground state geometry, Fig.(4.16(a)) of Ta_5H_2, Two H

(a) -21.952, 4 (b) -21.950, 2 (c) -21.616, 2 (d) -10.621, 4

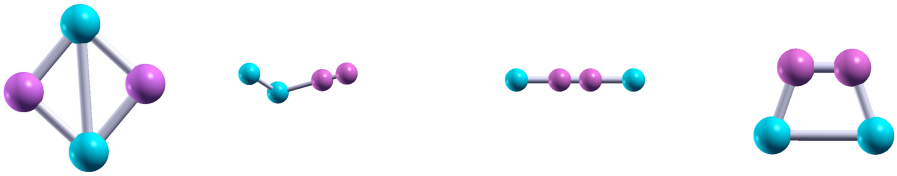

(e) -33.912, 1 (f) -30.406, 1 (g) -29.340, 1 (h) -29.340, 1

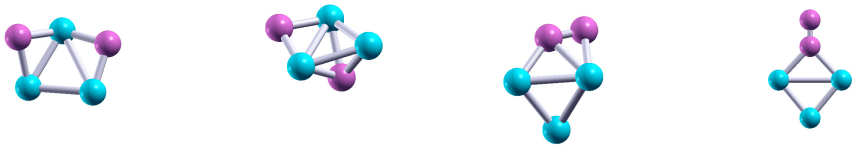

(i) -43.314, 2 (j) -43.246, 2 (k) -40.225, 2 (l) -39.011, 2

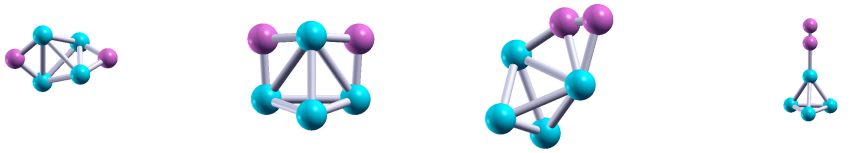

(m) -53.983, 3 (n) -53.635, 3 (o) -49.996, 5 (p) -49.966, 1

Figure 4.17: *Most stable geometries of Ta_nN_2 (n=1-4) clusters showing total energies(eV)and spin multiplicity of optimized figures (Violet color ball represents the N atom).*

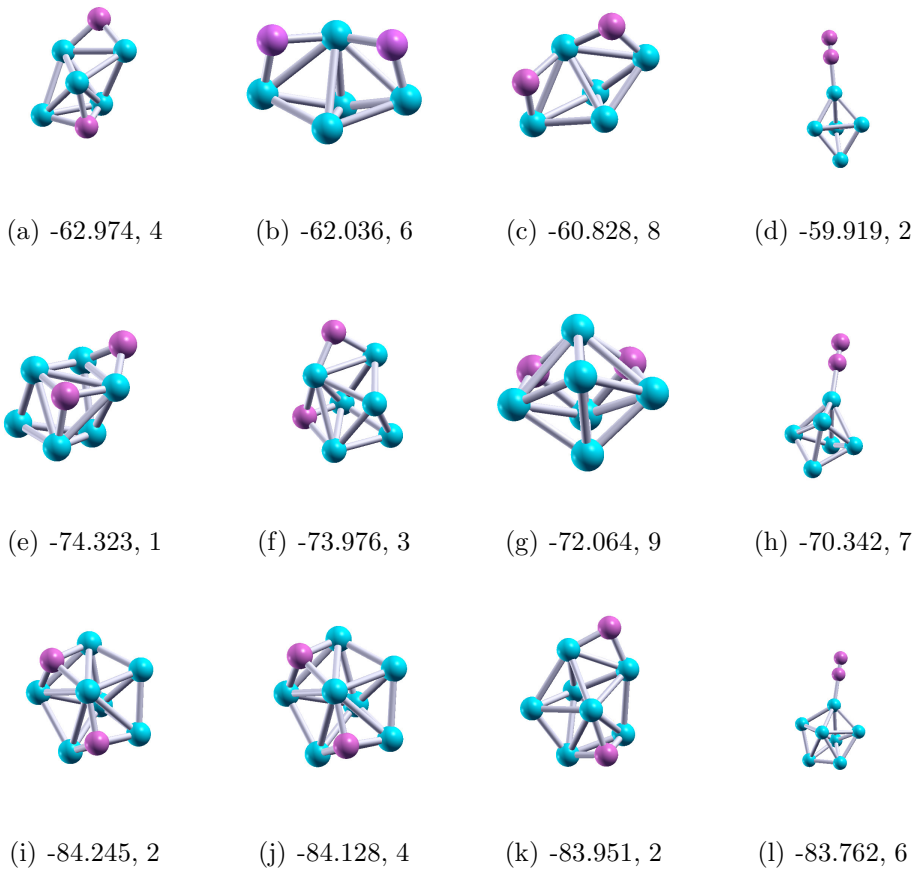

(a) -62.974, 4 (b) -62.036, 6 (c) -60.828, 8 (d) -59.919, 2

(e) -74.323, 1 (f) -73.976, 3 (g) -72.064, 9 (h) -70.342, 7

(i) -84.245, 2 (j) -84.128, 4 (k) -83.951, 2 (l) -83.762, 6

Figure 4.18: *Most stable geometries of Ta_nN_2 (n=5-7) clusters showing total energies(eV) and spin multiplicity of optimized figures (Violet color ball represents the N atom).*

atoms are separated by 2.248$\mathring{A}$, bridging from the side of pyramid structures with $\angle(H-Ta-H)$ 66.95$\mathring{A}$. In this case Ta-H bond length ranging from 2.943 $\mathring{A}$ to 1.964$\mathring{A}$. We have seen that hydrogen atoms dissociate after doping on Ta_5. It has spin multiplicity 2 which doesn't change with the spin multiplicity of pristine Ta_5. We have seen that other conformers show the adsorptive behaviour but they have higher optimized energy than ground state geometry as in Fig.(4.16(b-d)). The ground state geometry of Ta_5N_2 is slightly different from the usual one. In this system two N atom attached two opposite sides of bi-pyramid of Ta as in Fig.(4.18(a)) separated with length 4.568$\mathring{A}$. This bears the spin multiplicity 4 and binding energy 5.627 eV/atom, slightly higher than binding energy of pure Ta_5. This shows that nitrogen molecule found to be dissociate on Ta_5. From the figures it is seen that the geometry on which nitrogen molecule adsorbed in molecular form has 3.055 eV high optimized energy than ground state energy.

n = 6 and 7, Now Ta_6 and Ta_7 are found to be grown with bi-pyramid structures with average Ta-Ta bond-lengths 2.677$\mathring{A}$ and 2.556$\mathring{A}$ with spin multiplicity 3 and 2 respectively as in Fig.(4.13(e and f)). After doping H_2 two H atoms found to be bridging

Table 4.3: *Calculated binding energy, Chemisorption energy, Spin Multiplicity, Spin Gap and Bader charges for the geometry of most stable Ta_nH_2 clusters*

Cluster size	Binding Energy (eV)	Chem. Energy (eV)	Spin Multiplicity	spin-gap		Bader charge	
				δ_1(eV)	δ_2(eV)	$H_1(e)$	$H_2(e)$
Ta_1H_2	1.845	1.061	2.00	0.542	0.942	0.933	0.937
Ta_2H_2	2.865	0.956	1.00	1.667	1.229	0.785	0.777
Ta_3H_2	3.618	2.137	2.00	0.679	0.907	0.702	0.705
Ta_4H_2	4.211	1.651	1.00	0.782	0.781	0.692	0.672
Ta_5H_2	4.506	1.569	2.00	0.894	0.669	0.595	0.641
Ta_6H_2	4.726	1.309	3.00	0.356	0.708	0.807	0.757
Ta_7H_2	5.019	1.551	2.00	0.374	0.127	0.707	0.704

Table 4.4: *Calculated Chemisorption energy, Spin Multiplicity, Spin Gap and Bader charges for the geometry of most stable Ta_nN_2 clusters.*

Cluster size	Binding Energy (eV)	Chem. Energy (eV)	Spin Multiplicity	spin-gap		Bader Charge	
				δ_1(eV)	δ_2(eV)	$N_1(e)$	$N_2(e)$
Ta_1N_2	4.070	1.873	2.00	2.174	1.099	1.116	1.096
Ta_2N_2	5.182	4.336	1.00	0.563	0.563	1.068	1.063
Ta_3N_2	5.334	4.527	2.00	0.556	1.077	2.077	2.170
Ta_4N_2	5.644	4.361	1.000	0.945	0.673	2.169	2.171
Ta_5N_2	5.627	3.524	4.00	0.379	0.924	2.722	3.572
Ta_6N_2	5.909	4.856	1.00	0.596	0.596	2.478	2.166
Ta_7N_2	5.969	4.219	2.00	0.344	0.680	2.524	2.512

from the vertex of bi-pyramid in the most stable structures of Ta_6H_2 and Ta_7H_2 as in Fig.(4.16(e)) and Fig.(4.16(i)). This indicate that hydrogen molecules found to be dissociated on Ta_6 and Ta_7. The most stable conformer of Ta_6H_2 has binding energy 4.726 eV/atom with spin multiplicity 3 such that two H atoms separated as 3.933$\mathring{A}$. From the figure it is seen that the conformers on which H_2 adsorbed in molecular form have higher energies than ground state geometry. Similarly, the BE of ground state geometry of Ta_7H_2 found to be 5.019 eV/atom with spin multiplicity 2 such that two H atoms separated as 4.093$\mathring{A}$. It is found that hydrogen molecule also found to be dissociated by all the conformers having higher optimized energy than ground state geometry for Ta_7H_2. The stable structure of Ta_6N_2 is different from Ta_6H_2, in this system two N atoms attached at the opposite side of bi-pyramid of Ta_6 clusters and tends to make the square base with Ta-Ta bond-length 2.623$\mathring{A}$ and Ta-N bond length ranging from 2.913$\mathring{A}$ to 2.075$\mathring{A}$. This is the base of cub-octahedral structures. It has BE 5.909 eV/atom. This shows that nitrogen molecule found to be dissociate with N-N separation 3.497$\mathring{A}$ for most stable Ta_6N_2 clusters. The GS geometry of Ta_7N_2 has same kinds of configuration of Ta_7H_2 with spin multiplicity 2. This has a binding energy 5.969 eV/atom. In this system two N atoms separated as 3.688$\mathring{A}$. The average Ta-Ta and Ta-N bond lengths are found to be equal to 2.596$\mathring{A}$ and 2.012$\mathring{A}$ respectively. The conformer on which nitrogen molecule adsorbed molecularly on Ta_7N_2 have 0.483 eV higher optimized energy than ground state one shown in Fig.(4.16(f)).

4.3.3 Structural effect on Nb_n (n=2-7) clusters after doping H_2 and N_2

The optimized geometry of pristine Nb_n for (n=2-7) clusters shown in Fig.(4.14). The stable geometry after doping hydrogen and nitrogen on Nb_n for (n = 1-7) have been studied using the DFT through VASP code. We studied the adsorption or/and dissociation of hydrogen and nitrogen molecules on Nb_n (n = 2-7) clusters. To find out the exact conformer, we relaxed several isomers with different configurations and presented only the most stable and nearest to the most stable. The most stable geometries of Nb_nH_2 and Nb_nN2_2 for (n=1-7)are shown in Fig.(4.19-4.22). The optimized energy and spin multiplicity of most stable conformers are expressed beneath the respective figures. The structural effect of doping is explained as follows.

n = 1, the stable geometries of Nb atom doped with H_2 are shown in Fig.(4.19(a-d)). The ground state geometry of NbH_2 found to be adsorbed two hydrogen atom in molecular form which has a linear geometry with spin multiplicity 3. The bond length of H-H found to be enlarged and attends value (0.80 $\mathring{A}$) against the free H_2 (0.740 $\mathring{A}$) with Nb-H separation 1.776$\mathring{A}$. The next nearest conformer has spin multiplicity 6 which

has linear structure with Nb atom at middle and bears the spin multiplicity 4. It has a optimized energy 1.119 eV higher than ground state linear geometry. Figs. (4.21(a),(b), (c),(d)) represent the stable structures of NbN_2. The ground state geometry is linear at which nitrogen molecule found to be adsorbed molecularly. The separation of N-N found to be ($1.162\mathring{A}$) enlarged against the free N_2 ($1.14\mathring{A}$) (Limpijumnong, *et al.*, 2005). The bond length of Nb-N is found to be $1.699\mathring{A}$ with spin multiplicity 4. The spin multiplicity of second and third nearest conformers of NbN_2 are 6 and 2 respectively. These are in the meta stable states on which nitrogen bond lengths are found to be enlarged. In short, both H_2 and N_2 molecules found to be adsorbed molecularly on Nb and linear structure is found to be most stable conformer.

n = 2, In case of Nb_2H_2, a squared shaped structure with cyclically positions of Nb and H atoms are found to be stable geometry as in Fig.(4.19(e)). This has BE 2.613 eV/atom with spin multiplicity 2 different from pristine Nb_2 which has spin multiplicity 3. In such a case Nb-Nb and Nb-H are found to be $2.20\mathring{A}$ and $1.91\mathring{A}$ respectively. Two H atoms found in alternate corner (with H-H separation $2.660\mathring{A}$) indicating that hydrogen molecule favors the dissociative property on Nb_2. All others conformers given in Fig.(4.19(f-i)) are very close to the ground state energy but the fourth one is zigzag with spin multiplicity 3 having optimized energy 0.59 eV higher that GS. The geometry of nitrogen doped Nb_2 is not different from hydrogen doped. The stable conformers are given in Figs.(4.21(e-i)). The ground state geometry has BE 4.558 eV/atom. The Nb-Nb and Nb-N bond length is found to be $2.349\mathring{A}$ and $1.89\mathring{A}$ respectively. In this case position of two N atoms seems to be at alternate corner (with N-N separation $2.807A^o$) of squared shaped structure indicting that nitrogen completely dissociates on. The fourth conformer did not dissociate hydrogen whereas fifth was linear with two H-atoms at the middle of two Ta atoms. These all are in the metastable states.

n = 3, the isosceles triangle shown in Fig.(4.14(b)) is found to be most favorable geometry for pristine Nb_3 having BE 3.022 eV/atom with two equal sides of values $2.377\mathring{A}$ and spin multiplicity 2. Fig.(4.19(k-n)) represent the possible conformer having optimized energy closed to ground state. The most stable geometry of Nb_3H_2 (Fig.(4.19(k))) has the BE 3.045 eV/atom such that one H atom lying in the plane of the three Nb atoms and another H atom is out of plane and situated at two Nb atoms bridging together. The separation of H-H is found to be $3.967\mathring{A}$. There is no change in spin multiplicity after doping hydrogen atoms on Nb_3 clusters. The Nb-Nb and Nb-H bond length of GS geometry found to be 2.43 $\mathring{A}$ and $1.890\mathring{A}$ respectively. The third and fourth nearest stable structures has spin multiplicity 4 and 6 respectively. Similarly, fig.(4.21(j-o)) show the stable conformers of Nb_3N_2. The ground state geometry of the most stable conformer of Nb_3N_2 has same geometry as GS geometry of Nb_3H_2 with BE 4.637 eV/atom

having spin multiplicity 2. The bond length of Nb-Nb and Nb-N are found to be 2.67$\mathring{A}$ and 2.004$\mathring{A}$ respectively. The separation of N-N for most stable geometry is found to be 2.778$\mathring{A}$. Some of the conformers of Nb_3N_2 shown in Fig.(4.21(m-o)) are found to be adsorbed nitrogen in molecular form but these are less stable.

n = 4, Fig.(4.14(d)) represents the ground state structure for Nb_4. The ground state geometry has tetrahedron shape in the triplet state having BE 3.568 eV/atom with average Nb-Nb bond length 2.564 $\mathring{A}$. The ground state with two adsorbed H atoms in Nb_4H_2 are found to be in singlet state with the stable geometry at which one H atom lying in the plane of four Nb atoms and another atom out of plane and situated at the bridging site of two Nb such that H-H length is found to be 3.974$\mathring{A}$. This indicate that hydrogen molecule found to be dissociate. It has BE 3.504 eV/atom. The bond length of Nb-Nb and Nb-H are found to be 2.51$\mathring{A}$ and 1.916$\mathring{A}$ respectively. The geometrical structure of Nb_4N_2 is not different from Nb_4H_2, which has spin multiplicity 1. The two nitrogen in the ground state are adsorbed on the bridging sites of two different Nb atoms(with N-N separation 4.432$\mathring{A}$). The average bond length of Nb-Nb and Nb-N are found to be equal to 2.64$\mathring{A}$ and 1.89$\mathring{A}$ respectively. This indicates that both hydrogen and nitrogen are found to be adsorbed dissociatively.

n = 5, the GS geometry of Nb_5 have bi-pyramid type with Nb-Nb bond-lengths 2.594$\mathring{A}$ and spin multiplicity 2 as in Fig.(4.14(j)). The ground state geometry of Nb_5H_2 shown in Fig.(4.20(a)), Two H atoms (with H-H separation 2.837$\mathring{A}$) are bridging from the side of pyramid structures with $\angle(H - Nb - H)$ has 87.244$\mathring{A}$ and Nb-H bond length 2.082$\mathring{A}$ showing that hydrogen atoms dissociate. It has BE 3.718 eV/atom with spin multiplicity 2. Other conformers on which hydrogen found to be bound molecular form do not change the spin multiplicity, however bear higher optimization energy than ground state indicating that Nb_5H_2 clusters do not favor the adsorption of hydrogen. In case of Nb_5N_2 two N atom(with N-N separation 3.202$\mathring{A}$) attached two opposite sides of bi-pyramid of Nb as in Fig.(4.22(a)) which bears the spin multiplicity 2 and binding energy 4.897 eV/atom. This also shows the dissociative nature of nitrogen molecule. The bond length of Nb-Nb and Nb-N are found to be 2.594$\mathring{A}$ and 1.977$\mathring{A}$ respectively. In this stable structure $\angle(N - Nb - N)$ found to be 110.38^o with spin multiplicity 2. The conformer which shows the nitrogen adsorbed in molecular form Fig.(4.22(f)) has optimization energy 3.743 eV higher than ground state indicating that this system do not follow the adsorption of nitrogen molecule.

n = 6, Fig.(4.14(l)) shows the ground state geometry of Nb_6 which has the BE 4.147 eV/atom with average Nb-Nb bond length 2.680$\mathring{A}$. In case of Nb_6H_2, the ground state geometry shown in Fig.(4.20(g)) at which two different H atoms(with H-H separation

5.196$\mathring{A}$) attached on the vertex of bi-pyramid and bridging to nearest Nb atoms present at side of it. This indicate that it also favors dissociation of hydrogen molecule. The ground state geometry of Nb_6H_2 has binding energies 3.924 eV/atom and the spin multiplicity 1 . Similarly, in the ground state geometry of Nb_6N_2 two N atoms (with N-N separation 5.597$\mathring{A}$) found to be bridging in opposite sides and making a icosahedral types of structure as a stable geometry having spin multiplicity 1 with binding energy 4.936 eV/atom. The next nearest conformer has 0.201 eV higher optimized energy than GS which also has spin multiplicity 1. The conformer on which nitrogen molecule adsorbed, Fig.(4.22(l)) has 3.573 eV optimized energy higher than ground state.

n = 7 Fig.(4.14(l)) the ground state geometry of Nb_7 which has the BE 4.394 eV/atom with average Nb-Nb bond length 2.643$\mathring{A}$. In the most stable geometry of Nb_7H_2, we found two different H atoms (with H-H separation 4.011$\mathring{A}$) attached on the vertex of bi-pyramid and bridging to nearest Nb atoms. The BE of most stable structure Nb_7N_2, Fig.(4.22(m)) found to be 5.047 eV/atom with spin multiplicity 2. The next nearest conformer has 0.207 eV higher optimized energy than GS which has spin multiplicity 4. The conformer on which nitrogen molecule adsorbed, Fig.(4.22(p)) has 3.17 eV optimized energy higher than ground state. The N-N separation for most stable structure found to be 3.713$\mathring{A}$ with $\angle(Nb-N-Nb) = 96.485^o$.

From the above discussion, we found that Ta_n and Nb_n(n = 2-7) clusters dissociatively adsorbed the hydrogen as well as nitrogen molecules. These clusters can be used as a catalyst for the reaction of dissociation of H_2 and N_2 which is required for the synthesis of ammonia. This kind of effect also very useful for the hydrogen storage devices indicating that these clusters are also applicable for hydrogen storage application and catalyst for the production of hydrogen which has a great importance for future fuel.

4.3.4 Binding energy, Chemisorption energy and Stability

The calculated data of binding energy, chemisorption energy, spin-gap etc.for the pristine clusters Ta_n, Nb_n(n=2-7) and hydrogen and nitrogen doped clusters Ta_nH_2, Ta_nN_2, Nb_nH_2 and Nb_nN_2 are listed in the tables 4.1, 4.2,4.3, 4.4, 4.5, 4.6 respectively. The plot of variation binding energy as a function of cluster size for the case of Ta_nH_2, Ta_nN_2, Nb_nH_2 and Nb_nN_2 are shown in Figs.(4.23(a)(b)). From the Fig.(4.23(a)), it is seen that as cluster size increases the binding energy increases. The BE of Ta_3N_2, Ta_5N_2 are found be lower than their neighbour indicating that nitrogen molecules bounds loosely Ta_3 and Ta_5 clusters. Similarly, Fig.(4.23(b) shows that the BE of Nb_nH_2 increases monotonically with clusters size. For the case of Nb_nN_2, we found that BE abruptly increases as we moved from NbN_2 to Nb_2N_2 beyond that increases slightly. This shows

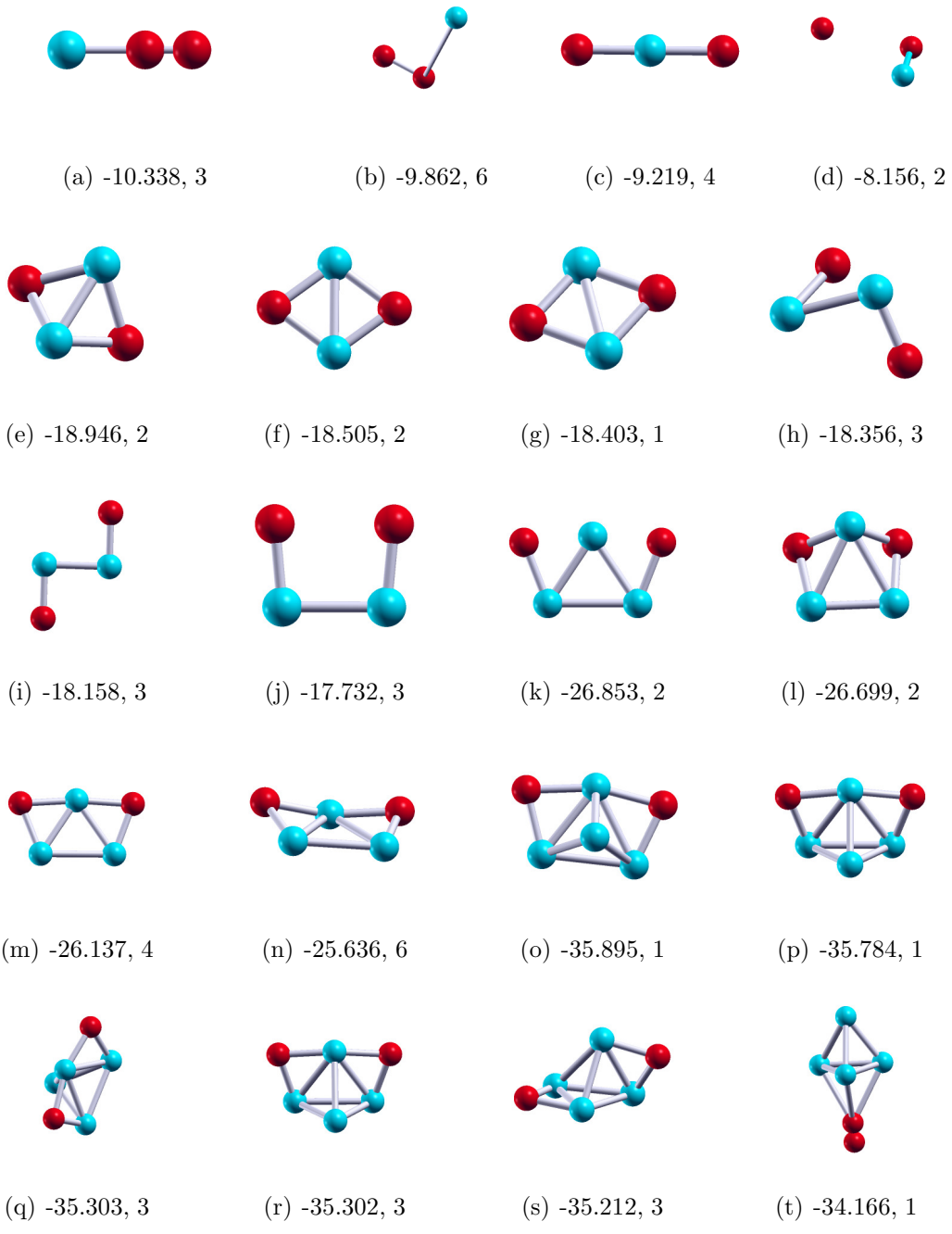

(a) -10.338, 3 (b) -9.862, 6 (c) -9.219, 4 (d) -8.156, 2

(e) -18.946, 2 (f) -18.505, 2 (g) -18.403, 1 (h) -18.356, 3

(i) -18.158, 3 (j) -17.732, 3 (k) -26.853, 2 (l) -26.699, 2

(m) -26.137, 4 (n) -25.636, 6 (o) -35.895, 1 (p) -35.784, 1

(q) -35.303, 3 (r) -35.302, 3 (s) -35.212, 3 (t) -34.166, 1

Figure 4.19: *Most stable geometries of Nb_nH_2 (n = 1-4) clusters showing total energies(eV) and spin multiplicity of optimized figures (Red ball represents the H atom).*

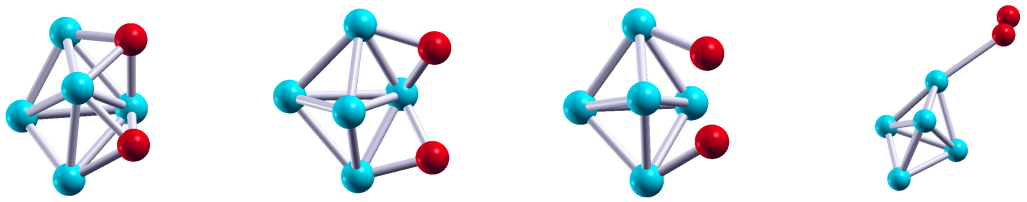

(a) -43.919, 2 (b) -43.696, 2 (c) -43.239, 4 (d) -42.192, 2

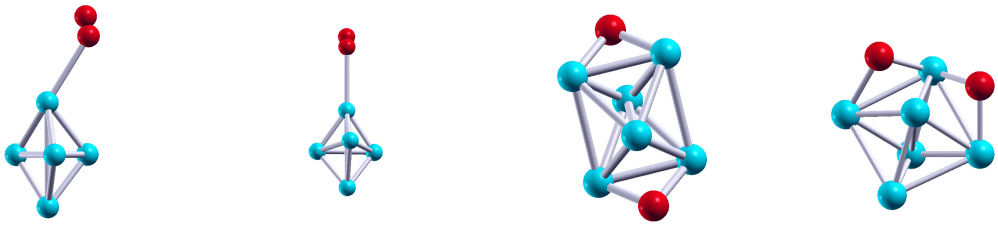

(e) -42.191, 2 (f) -42.190, 2 (g) -52.419, 1 (h) -51.921, 5

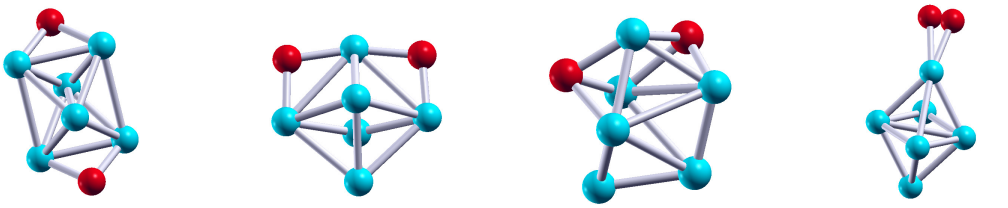

(i) -51.902, 3 (j) -51.795, 5 (k) -51.776, 3 (l) -50.698, 5

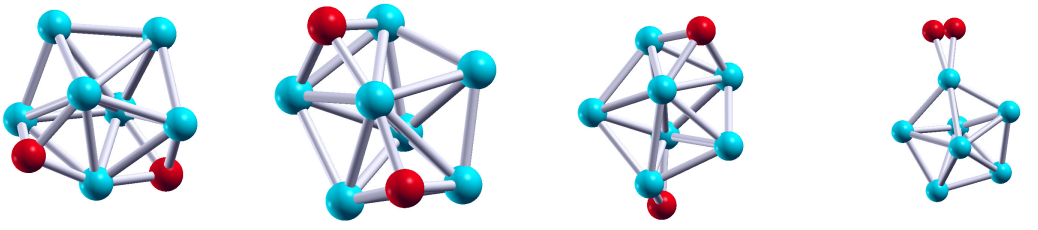

(m) -61.497, 2 (n) -61.449, 2 (o) -61.149, 4 (p) -60.089, 2

Figure 4.20: *Most stable geometries of Nb_nH_2 (n = 5-7) clusters showing total energies(eV) and spin multiplicity of optimized figures (Red ball represents the H atom).*

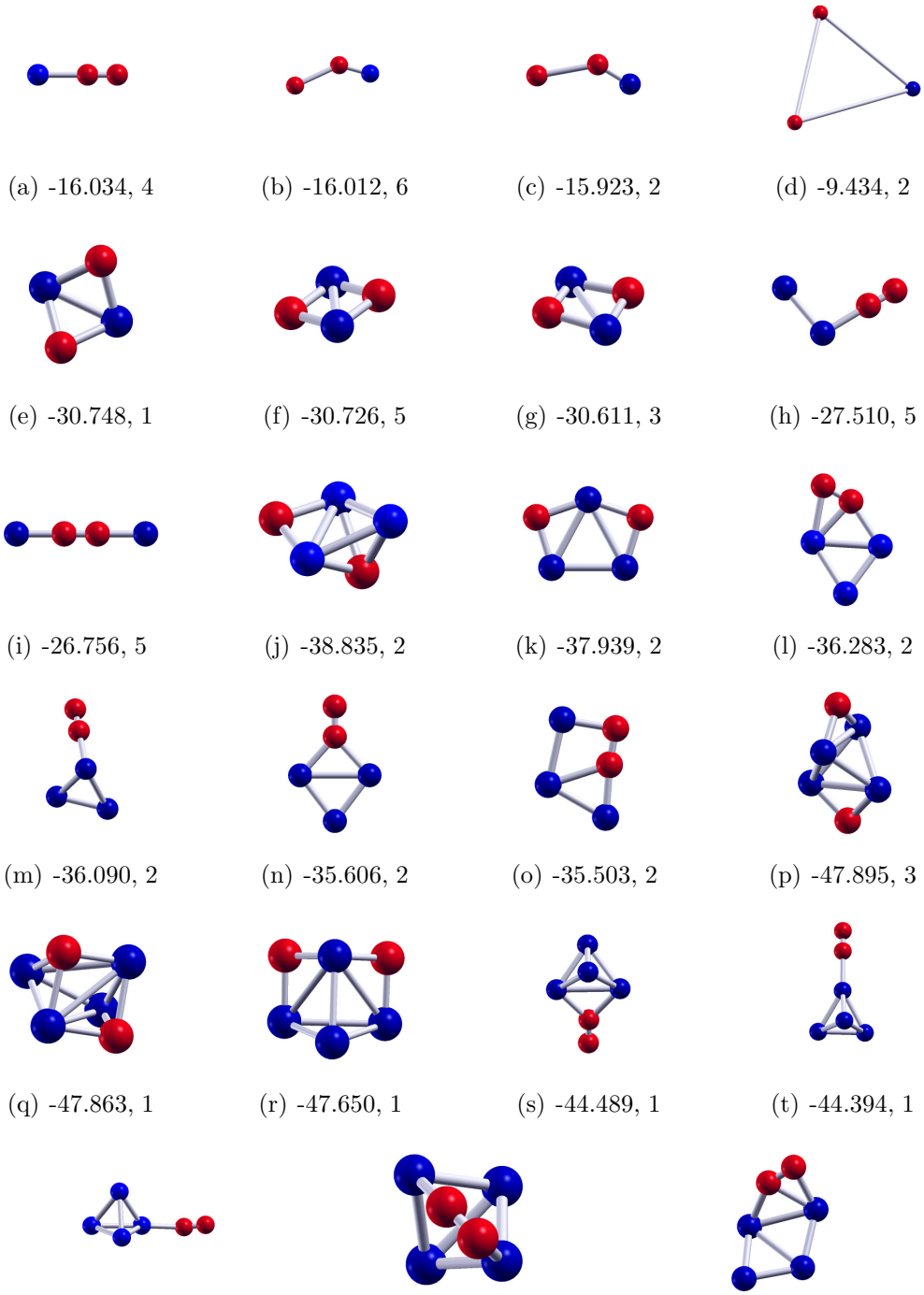

(a) -16.034, 4 (b) -16.012, 6 (c) -15.923, 2 (d) -9.434, 2

(e) -30.748, 1 (f) -30.726, 5 (g) -30.611, 3 (h) -27.510, 5

(i) -26.756, 5 (j) -38.835, 2 (k) -37.939, 2 (l) -36.283, 2

(m) -36.090, 2 (n) -35.606, 2 (o) -35.503, 2 (p) -47.895, 3

(q) -47.863, 1 (r) -47.650, 1 (s) -44.489, 1 (t) -44.394, 1

(u) -44.382, 1 (v) -44.226, 5 (w) -44.049, 5

Figure 4.21: *Most stable geometries of* Nb_nN_2 *(n = 1-4) clusters showing total binding energies(eV)and spin multiplicity of optimized figures (Red ball represents the N atom).*

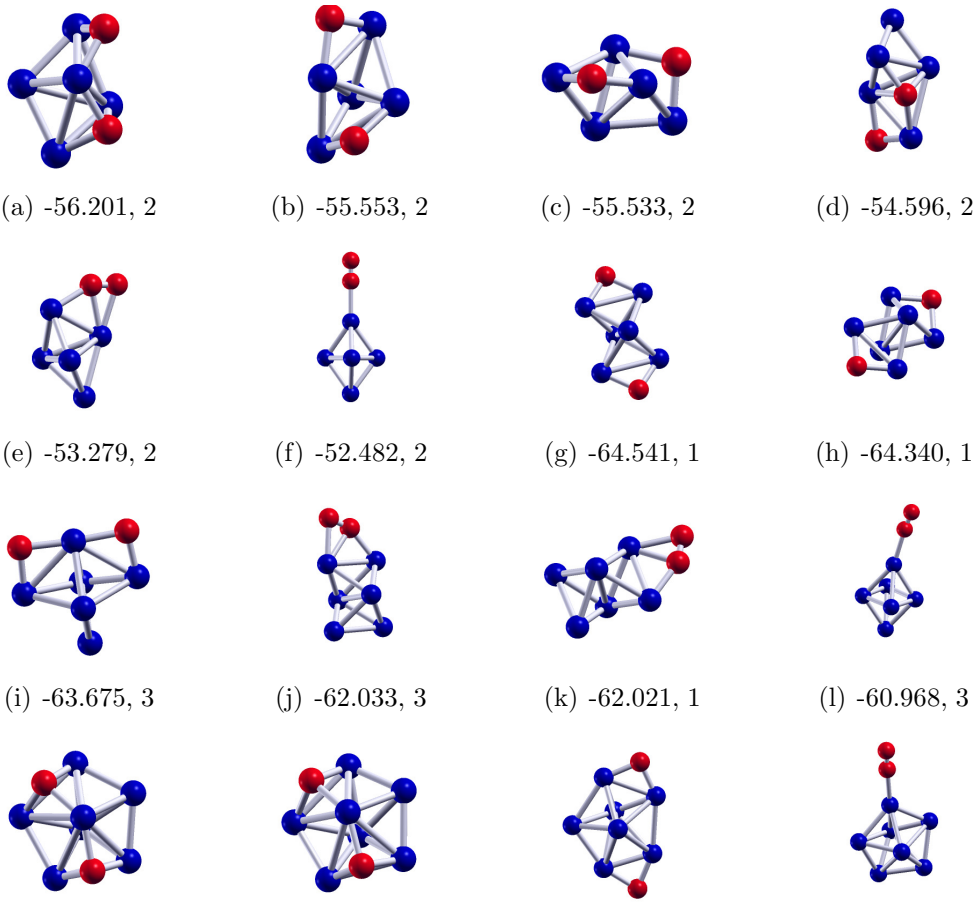

(a) -56.201, 2 (b) -55.553, 2 (c) -55.533, 2 (d) -54.596, 2

(e) -53.279, 2 (f) -52.482, 2 (g) -64.541, 1 (h) -64.340, 1

(i) -63.675, 3 (j) -62.033, 3 (k) -62.021, 1 (l) -60.968, 3

(m) -73.608, 2 (n) -73.401, 4 (o) -71.687, 2 (p) -70.438, 2

Figure 4.22: *Most stable geometries of Nb_nN_2 (n = 5-7) clusters showing total energies(eV)and spin multiplicity of optimized figures (Red ball represents the N atom).*

Table 4.5: *Calculated Binding energy, Chemisorption energy, Spin Multiplicity, Spin Gap and Bader charges for the geometry of most stable Nb_nH_2 clusters.*

Cluster size	Binding Energy (eV)	Chem. Energy (eV)	Spin Multiplicity	spin-gap		Bader charge	
				δ_1(eV)	δ_2(eV)	$H_1(e)$	$H_2(e)$
Nb_1H_2	1.501	0.031	6.000	2.145	8.617	1.006	-1.006
Nb_2H_2	2.613	1.397	1.000	1.013	1.013	0.437	0.421
Nb_3H_2	3.045	1.689	2.000	0.986	0.798	0.475	0.475
Nb_4H_2	3.504	2.282	1.000	0.847	0.847	0.475	0.471
Nb_5H_2	3.718	1.7499	3.000	1.276	0.395	0.453	0.460
Nb_6H_2	3.924	2.038	1.000	0.687	0.688	0.467	0.467
Nb_7H_2	4.149	2.104	2.000	0.629	0.622	0.514	0.504

Table 4.6: *Calculated Binding energy, Chemisorption energy, Spin Multiplicity, Spin Gap and Bader charges for the geometry of most stable Nb_nN_2 clusters.*

Cluster size	Binding Energy (eV)	Chem. Energy (eV)	Spin Multiplicity	spin-gap		Bader charge	
				δ_1(eV)	δ_2(eV)	$N_1(e)$	$N_2(e)$
Nb_1N_2	2.418	-3.111	6.000	0.346	3.014	0.054	0.921
Nb_2N_2	4.558	3.283	3.000	0.965	0.966	1.121	1.119
Nb_3N_2	4.637	3.755	2.000	0.922	0.553	1.146	1.192
Nb_4N_2	4.852	4.474	2.000	0.746	1.065	1.182	1.191
Nb_5N_2	4.897	4.111	2.000	0.606	0.600	1.189	1.305
Nb_6N_2	4.936	4.243	1.000	0.464	0.464	1.205	1.194
Nb_7N_2	5.047	4.298	2.000	0.389	0.501	1.352	1.345

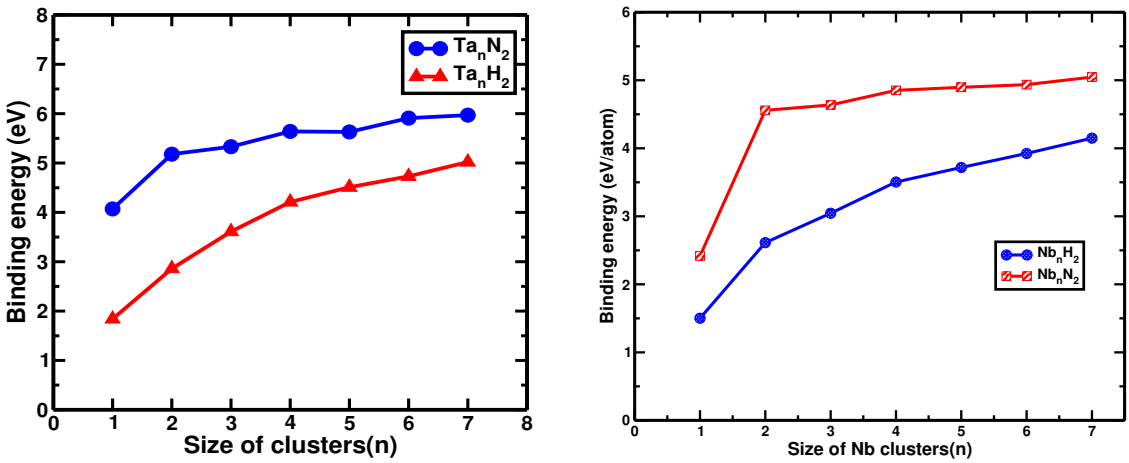

(a) (b)

Figure 4.23: *Binding energy analysis of Ta_n and Nb_n cluster with H_2 and N_2 doped respectively.*

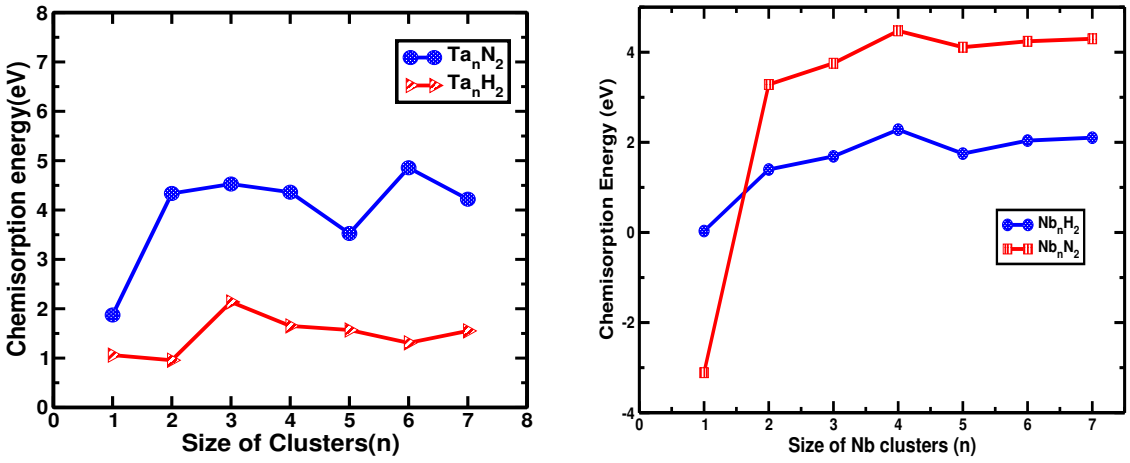

(a) (b)

Figure 4.24: *Chemisorption energy analysis of Ta_n and Nb_n cluster with doped H_2 and N_2 molecules respectively.*

that overall feature follows the general trends of clusters. Moreover, the binding energy of Ta_nN_2 and Nb_nN_2 are greater than Ta_nH_2 and Nb_nH_2 indicating that Ta and Nb clusters bind the nitrogen more strongly than hydrogen. So more energy is required to dissociate the nitrogen than hydrogen. This is mainly due to the binding of nitrogen with triple bond which requires large amount of force to break the bond than single bonded hydrogen atoms.

One of the important objective of the present study is to understand the chemical reactivity of hydrogen and nitrogen molecules on Ta_n and Nb_n clusters. Fig.(4.24(a)) displays the chemisorption energy with respect to the size of Ta clusters. In case of Ta_nH_2, chemisorption energy is nearly same in TaH_2 and Ta_2H_2 which is maximum at Ta_3H_2 after that chemisorption energy decreases up to Ta_6H_2. Chemisorption energy again increases in Ta_7H_2. This gives the idea that Ta_3H_2 clusters has highest chemisorption energy. From Fig.(4.24(a)), it can be said that chemisorption energy increases as we move from TaN_2 to Ta_2N_2. It remains constant up to Ta_4N_2. In Ta_5N_2, chemisorption energy is minimum. This indicates that Ta_5 cluster is less reactive with nitrogen. This energy increases for Ta_6N_2 and again decreases slightly in Ta_7N_2.

Similarly, Fig.(4.24(b)) shows the variation of chemisorption energy for hydrogen and nitrogen as a function of size of Nb clusters. In case of Nb_nH_2, the chemisorption energy abruptly as we move from NbN_2 to Nb_2N_2. It's value increases slightly up to Nb_4N_2. The chemisorption energy decreases on Nb_5H_2 after that goes on increasing in small ratio. This indicates that Nb_5N_2 is less reactive From above it is clear that hydrogen and nitrogen undergo the dissociative chemisorption on Nb and Ta clusters. Present

result agrees well with previously reported theoretical results of clusters and surfaces (Venkataramanan, *et al.*, 2010).

To get further insight into the nature of the interaction between Ta_n and Nb_n clusters with hydrogen or nitrogen, we have to analyze the bader charge distribution on the minimum energy conformers. Fig.(4.25(a)(b)) display the information of transformation of charge from Ta and Nb clusters to hydrogen and/or nitrogen molecules. From the Fig.(4.25(a)), it is seen that the transformation of charge decreases as size of Ta clusters in Ta_nH_2 increases from n=0 to n=4 and becomes minimum at Ta_5H_2. The charge transformation found to be increase in Ta_6H_2 where as again decreases slightly in Ta_6H_2. Similarly, In Ta_nN_2 , we found charge transformation increases when we move from TaN_2 to Ta_2N_2 then it becomes more or less constant up to Ta_4N_2. This is now abruptly decreases in the case of Ta_5N_2 due to the effect of which chemisorption energy also becomes less in this clusters as before. Further BE is also less for Ta_5N_2 than its neighbor. After that it increases at the same rate as before decreases to Ta_6N_2 and Ta_7N_2.This is the indication of less reactivity of Ta_5N_2 clusters in dissociation of nitrogen. Fig.(4.25(b)) gives the information of charge transformation on niobium clusters after doping nitrogen and hydrogen. It is seen that some of the charge transformed from second atom of hydrogen to Nb in case of NbH_2, where as first atom of H absorbed the large amount of charge from Nb. The transformation of charge for other clusters are in constant ratio. Similarly in the case of NbN_2, initially transformation of charge from Nb to nitrogen atoms are increased as we move from NbN_2 to Nb_2N_2. After that transformation of charge in second atom of nitrogen is slightly greater than first atom but more or less in constant ratio. Hence from the above discussion, it can be said that Ta and Nb clusters plays an important role to transfer the charge and dissociates the hydrogen as well as nitrogen molecules and hence enhance the chemisorption energy of clusters. Such kinds of effect may be used to alter the chemisorption properties of Ta and Nb nanoclusters for the hydrogen storage applications also.

Fig.(4.25(a)) represents the HOMO-LUMO gap of Ta_nH_2 and Ta_nN_2 (n=1-7) clusters which suggest the relative stability of the clusters with respect to their neighbors. In case of Ta_nH_2, Our findings show that Ta_2H_2 and Ta_5H_2 have higher HOMO-LUMO spin-gap than their neighbors. This indicates that Ta_2H_2 and Ta_5H_2 are most stable conformers than their neighbor. Due to the effect of which charge transformation also found to be minimum at Ta_5H_2. Similarly, in case of Ta_nN_2, the clusters TaN_2, Ta_3N_2 and Ta_5N_2 are found to be more stable than their neighboring clusters. Present results also supports the charge transformation and chemisorption for Ta_5N_2. The charge transformation and chemisorption for Ta_5N_2 both are minimum as the cluster is stable. Fig.(4.25(b)) represents the HOMO-LUMO gap of Nb_nH_2 and Nb_nN_2 (n=1-7) clusters.

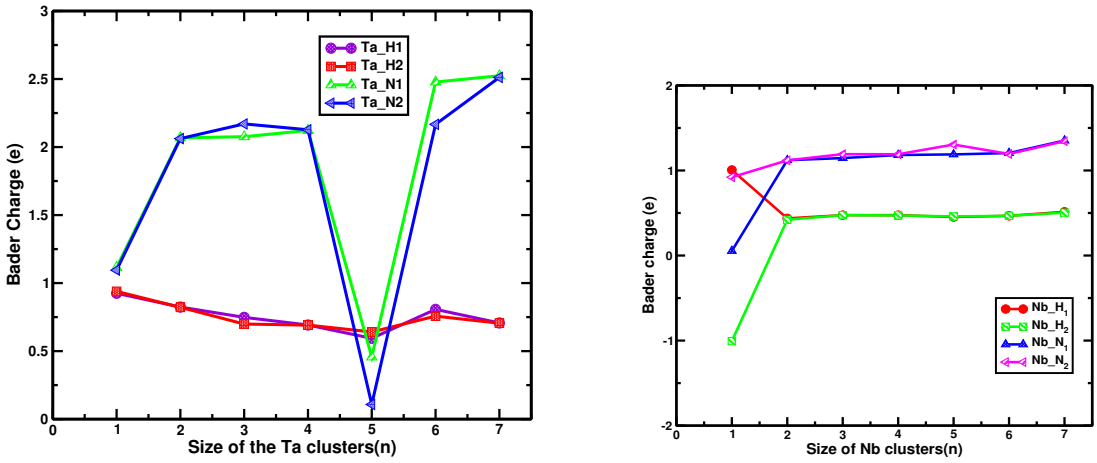

(a) (b)

Figure 4.25: *Bader charge analysis of Ta_n and Nb_n clusters after doping H_2 and N_2 molecules respectively.*

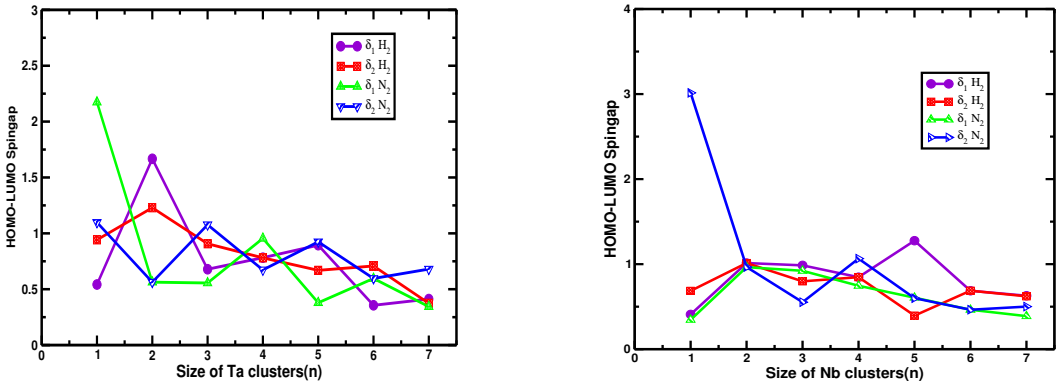

(a) (b)

Figure 4.26: *HOMO-LUMO spingap analysis of Ta_n and Nb_n clusters after doping H_2 and N_2 molecules respectively.*

In case of Nb_nH_2, Nb_2H_2 and Nb_5H_2 are found to be more stable than their neighbor. This also supports the bader charge distribution and chemisorption energy. In case of Nb_nN_2, NbN_2 and Nb_4N_2 are found to be most stable structures for nitrogen doped. This also support the chemisorption energy bader charge distribution which is found to be minimum on NbN_2.

Fig.(4.27) shows the charge density plot of Ta_2H_2, Ta_4H_2 and Ta_6H_2. This indicates that some amounts of charge is transferred from Ta to H which is accordance with the bader-charge plot but transformation rate is more or less constant. Same kinds of scenario is observed in Ta_2N_2, Ta_4N_2 and Ta_6N_2 as in Fig.(4.28). The amount of charge transferred from Ta to nitrogen atoms is larger than amount of charge transferred

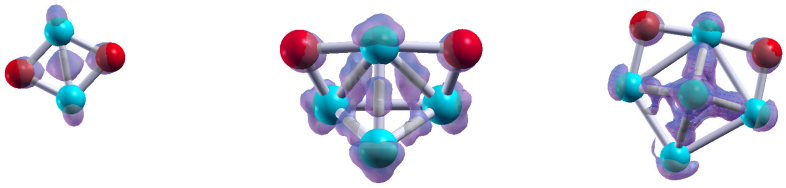

(a) (b) (c)

Figure 4.27: *Charge Density plot of Ta_2H_2, Ta_4H_2 and Ta_6H_2 respectively.*

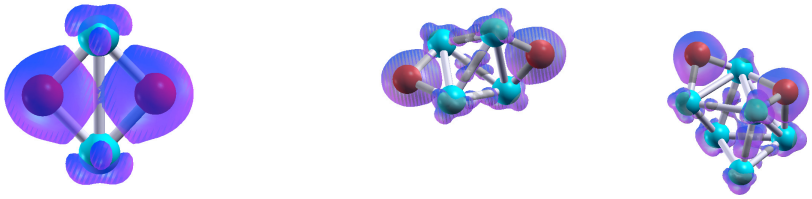

(a) (b) (c)

Figure 4.28: *Charge Density plot of Ta_2N_2, Ta_4N_2 and Ta_6N_2 respectively.*

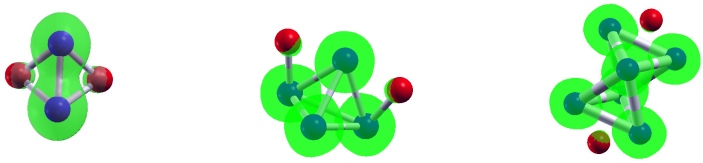

(a) (b) (c)

Figure 4.29: *Charge Density plot of Nb_2H_2, Nb_4H_2 and Nb_6H_2 respectively.*

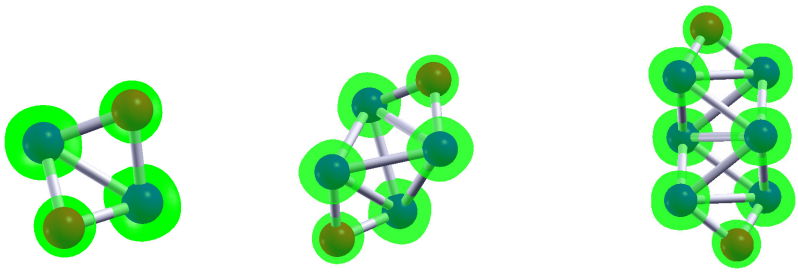

(a) (b) (c)

Figure 4.30: *Charge Density plot of Nb_2N_2, Nb_4N_2 and Nb_6N_2 respectively.*

through Ta to H atoms. This is clearly reflects from the charge distribution plot.

Fig.(4.29) and Fig.(4.30) show that very less amount of charge transferred from Nb to each H atoms but transformation ratio throughout the system Nb_2H_2, Nb_4H_2 and Nb_6H_2 are remaining constant which can be seen from the bader charge analysis plot. Similarly the ratio of transformation of charge from Nb to each N atoms are found to be constant in the clisters Nb_2N_2, Nb_4N_2 and Nb_6N_2 but greater than that transformation of charge from Nb to H atoms. This analysis also supports the results of badercharge analysis and chemisorption on the clusters.

In short hydrogen and nitrogen are found to be adsorbed in case of TaH_2, TaN_2, NbH_2 and NbN_2 respectively. The N-N and H-H bond length increases and suggest that hydrogen and nitrogen wants to dissociate but unable to do due to binding effect. We found higher clusters favor dissociative properties of hydrogen and nitrogen which is applicable for catalyst for synthesis of NH_3 and hydrogen storage applications.

4.4 Electronic and Magnetic properties of different morphologies of 3d transition metal doped ZnO

This section contains our main findings of pristine ZnO and doping effect of 3d Transition Metals(TM) (Mn, Fe, Co, Ni, Cu) on ZnO in different morphologies. The different morphologies considered in the present work are (i) ZnO nanosheet (ii) ZnO nanotube and (iii) ZnO fullerene like structure as shown in Fig.(4.31(a,b,c)). We used DFT based code for the calculation of optimization characters of all the system through VASP. The stability, magnetic properties and electronic properties have been described in section wise as follows. We actually try to find out the origin of magnetism and band gap within the reference systems.

4.4.1 Stability and energetics

To analyze the stability of three morphologies of pristine ZnO and TM doped on ZnO, we have carried out calculation of the exact ground state (GS) of pristine ZnO in three different morphologies. For it, we have taken 48 atoms as a reference atoms to construct different morphologies(nanosheet, nanotube and fullerene like structure). After that we have taken single substitutional TMs dop arrangement as in Fig.(4.31(d, e f)) and then near as well as far arrangements of bi-dop TM. The near and far dop arrangements are named according to the doping position of TM like (i)-TM-O-TM- as in Fig.(4.33(a, b, c)) and (ii)-TM-O-Zn-O-TM- as in Fig.(4.33(d, e, f)) respectively. We also analyzed whether FM coupling is more favorable or AFM coupling..

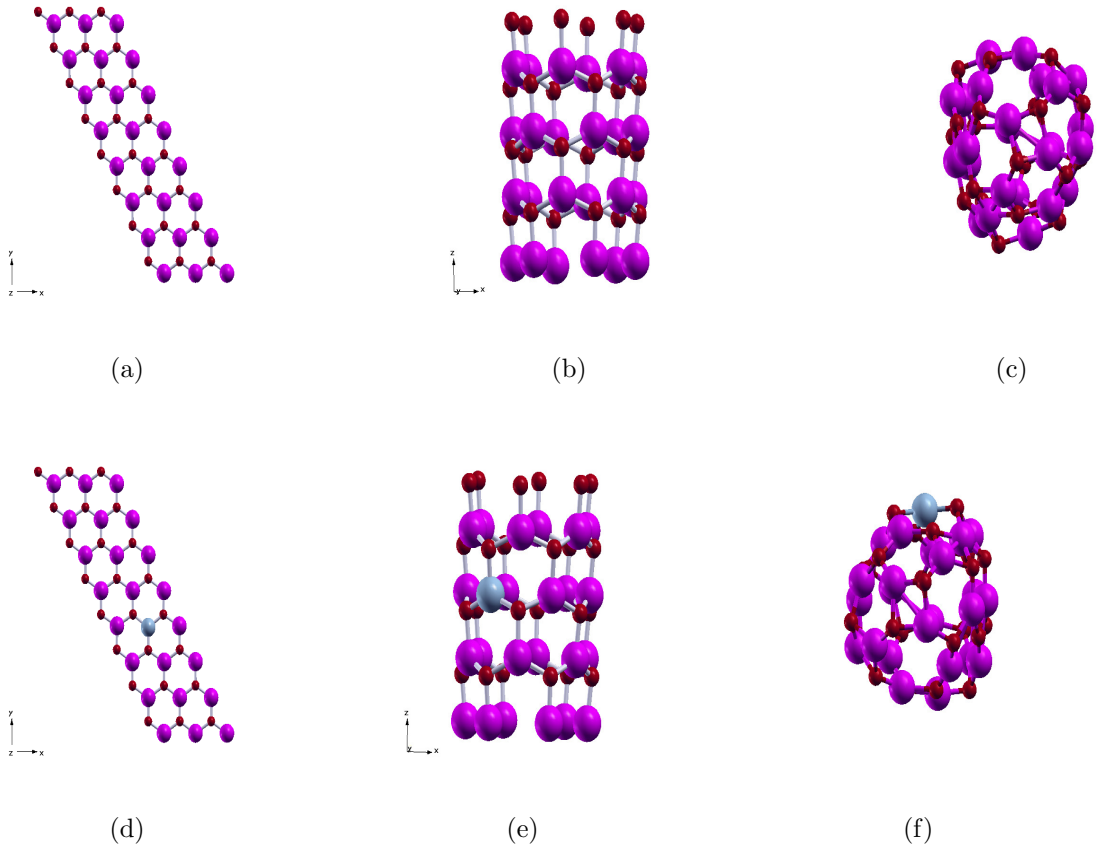

Figure 4.31: *Most stable geometries of Nanosheet, Nanotube and Fullerene in pristine (a),(b) and (c) and single Dop TM elements (d), (e) and (f) respectively, 48 atoms are taken as reference for each systems.*

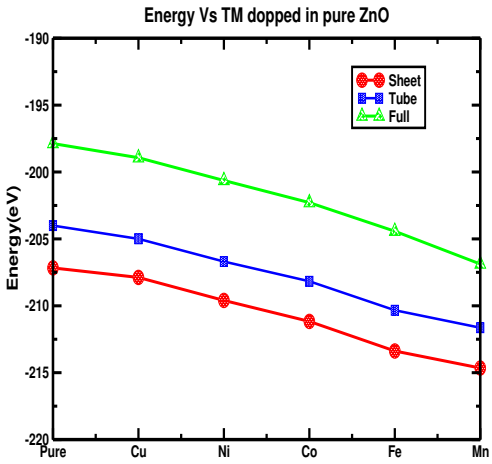

Figure 4.32: *The energetics of Nanosheet, Nanotube and Fullerene like structure in pristine and single Dop TM elements on ZnO.*

We have used DFT implemented in VASP to study the magnetic moments. From the Fig.(4.32), we observed that TM doped sheet is energetically most stable than other two morphologies where as fullerene like structure is energetically found to be least stable. Similarly the most stable geometry of the near and far doped TM (Mn,Fe, Co, Ni, Cu) are given in Fig. (4.33). Now in case of sheet, near-dop FM is favorable for Cu, Ni and Co bi-dop where as far-dop FM is stable in case of Fe and Mn. In case of Co, AFM-far dop is more favorable whereas all others favors the near-dop arrangements. In case of tube Fe and Mn favor the far dop FM and other Co, Cu and Ni favors the Near-dop FM. All the TM dop elements favors near dop in AFM case. Similarly in case of fullerene like structure, Mn and Co are found to be favored by near dop but Fe, Co and Cu are seemed to be favor of far-dop in both ferromagnetic and anti-ferromagnetic alignments as in Fig. (4.34). We have calculated energy differences between the near and far configurations. It is clear from the Fig.(4.34) that in case of sheet AFM couplings are favorable in all the system except Cu. It seems slight AFM in nature. In tube, condition is reverse means all are found to be stable in FM coupling except Mn on which AFM coupling is favorable. In case of fullerene like structure we observed Mn and Cu favor feeble AFM coupling and other Fe and Co are remains in favoring FM coupling. Ni also favors negligible amounts of AFM coupling behavior which is seen clearly in Fig. (4.35).

4.4.2 Magnetic Properties

The magnetic moment of pure $(ZnO)_2 4$ Nanosheet, nanotube and fullerene like structure are found to be zero (Ahmed, *et al.*, 2012), (Ozgur, *et al.*, 2005). Our interest is to investigate the magnetic properties of $(ZnO)_{24}$ Nanosheet, nanotube and fullerene like structures after doping TMs (Mn, Fe, Co, Ni, Cu). We first analyze effect of substitutional doping by single atom of TM. It is found that there is no change in magnetic moments of doped TM atoms except Mn in case of fullerene like structure as in Ftg.(4.34)(a). After that We relax all internal coordinates for near and far arrangements of the bi dop-TM atoms for both AFM and FM orderings.

We have calculated energy differences between the near and far configurations for both FM and AFM alignments using formula $\Delta E = E_{near} - E_{far}$. The negative energy difference indicates that the TM ions prefer to be in a near spatial configuration. Fig.(4.34)(b) shows the energy difference plot and our findings are explained as follows.

In case of sheet, Far-dop FM is found to be stable in Mn and Fe where as near-dop FM is favorable for Co, Ni and Cu bi-dop. Similarly, we found near dop AFM arrangement as most stable configuration in case of Mn, Fe, Ni and Cu. But AFM-far dop configuration is found to be more favorable for Co.

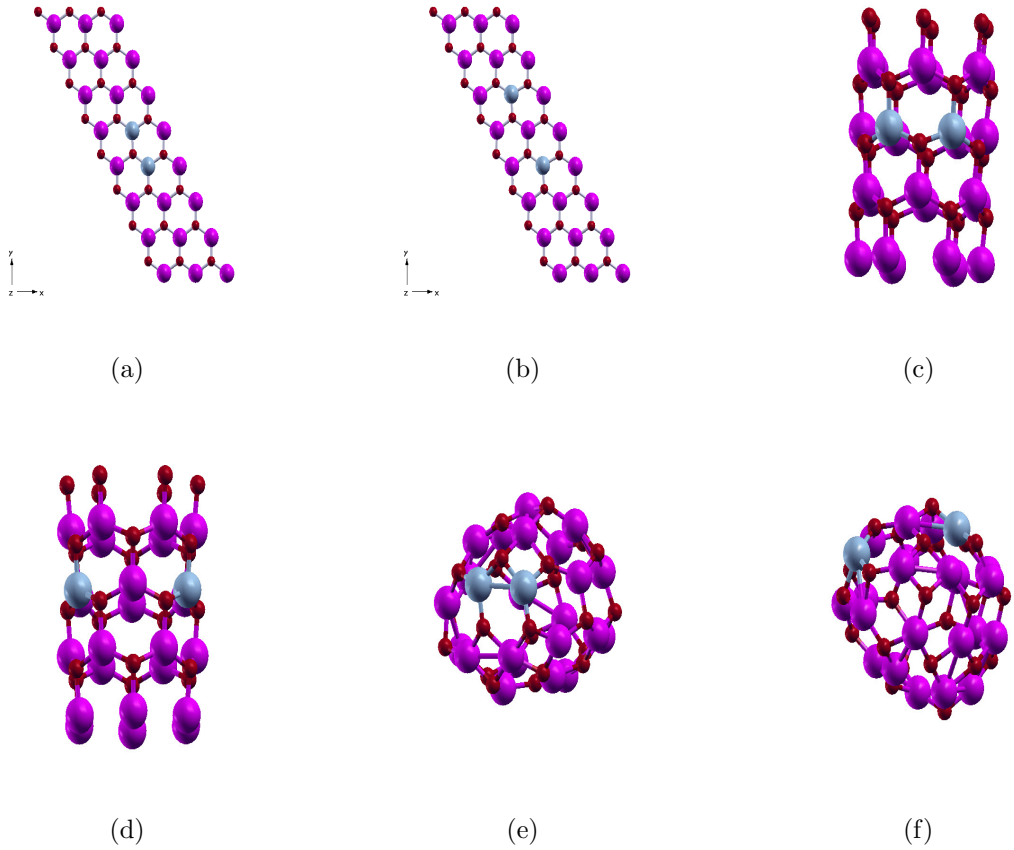

(a) (b) (c)

(d) (e) (f)

Figure 4.33: *Most stable geometries of Nanosheet, Nanotube and Fullerene like structure for near(a, b, c) and far (d, e, f) substitutinal bi-dop TM elements respectively (Dark red ball represents O atom, Cyan color ball represents TM dop elements and Magenta ball represents Zn atom).*

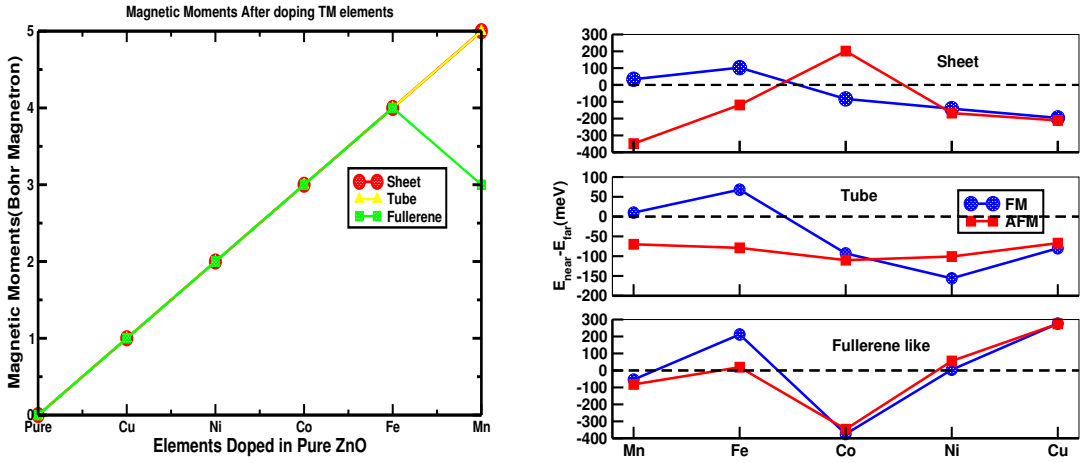

(a) (b)

Figure 4.34: *(a) Magnetic moments as a function of single substitutinal dop TMs (b) LSDA energy differences $\Delta E = E_{near} - E_{far}$ for substitutional TMs. The negative energy difference indicates that the TM ions prefer to be in a near spatial configuration.*

In case of tube, Fe and Mn favor the far dop FM where as Co, Cu and Ni favors the Near-dop FM. All the TM dop elements favors near dop in AFM case. Similarly, in case of fullerene like Mn and Co are found to be favored by near dop FM and AFM alignment but Fe, Co and Cu are seemed to be favor of far-dop in both ferromagnetic and anti-ferromagnetic alignments as in Fig. (4.34(b)). Further, we have estimated the energy differences between the most favorable FM and AFM alignment in different morphologies using $\Delta E = E_{AFM} - E_{FM}$ for substitutional TM ions. The negative energy difference indicates that the TM ions prefer to be in a AFM couplings. Fig. (4.35) shows the plot of most favorable alignment as a function of TM ions doped in different morphologies of ZnO. It is clear from the Fig. (4.35) that in case of sheet AFM couplings are favorable in all the system except Cu. It seems slight AFM in nature. In tube, condition is reverse. All are found to be stable in FM coupling except Mn on which AFM coupling is favorable.

Similarly, in case of fullerene like structure, we observed Mn and Cu favor feeble AFM coupling and other Fe and Co are remains in favoring FM coupling. Ni also favors negligible amounts of AFM coupling behavior. In short, We found the magnetic transition when we move from nanosheet to nanotube. Such behavior hs a very important for the application of spintronics devices, sensing devices, medical as well as technological appliances. In ordered to find out the exact origin of such favorable magnetic alignment we have to analyze the up and down density of states for most favorable configurations.

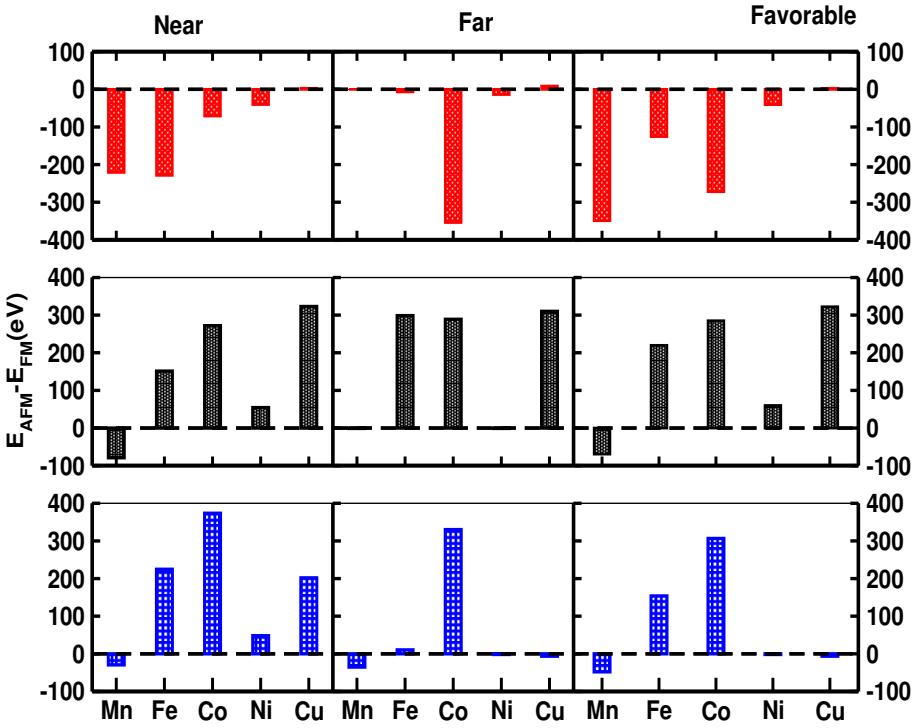

Figure 4.35: *LSDA AFM and FM differences $\Delta E = E_{AFM} - E_{FM}$ for substitutional TM ions. The negative energy difference indicates that the TM ions prefer to be in a AFM couplings (Red strip line represents for sheet, Black strip line for Tube and Blue strip shows for Fullerene-like structure.*

4.4.3 Electronic Properties

We present and discuss our findings regarding the density of states. We used PBE based DFT implemented in VASP to calculate the DOS. We first calculated the total density of states (TDOS) for pristine $(ZnO)_{24}$ and TMs doped ZnO in different morphologies. We also present the projected density of states(PDOS) of individual doped atom and analyze its interaction with Zn atoms and oxygen atoms.

Figs. (4.36-4.38) provides the TDOS and individual DOS of pristine and TM doped in nano-sheet, nano-tube and fullerene type structures respectively. From the figures, we see that the energy of TM 3d states relative to the top of valence band shift down in energy on moving right across the series (Mn, Fe, Co, Ni and Cu). The variation of the MM in 3d series reflect the decreasing in exchange splitting and the increase in the number of electrons. More detail analysis of individual bi-doped TM on ZnO for three different morphologies including TM-3d, Zn-3d and O-2d contributions are explained separately as follows.

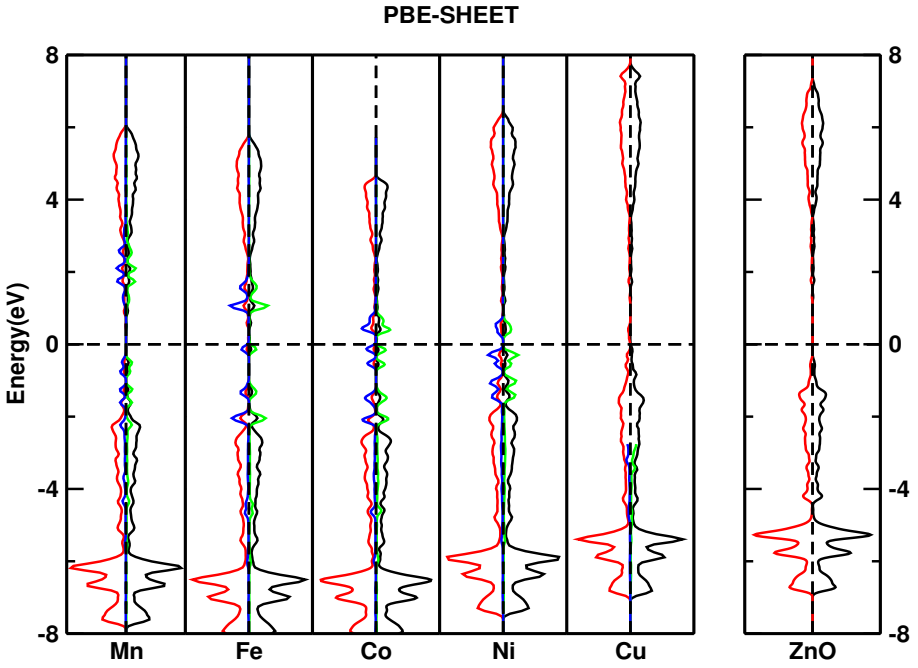

Figure 4.36: *DOS and PDOS of TM-doped ZnO with the TM atoms in the most favorable spatial configuration for sheet calculated within the LSDA. The blue-green lines show the TM d states and the regions covered by black-red lines show the total DOS. The right panel is the DOS for prestine ZnO.*

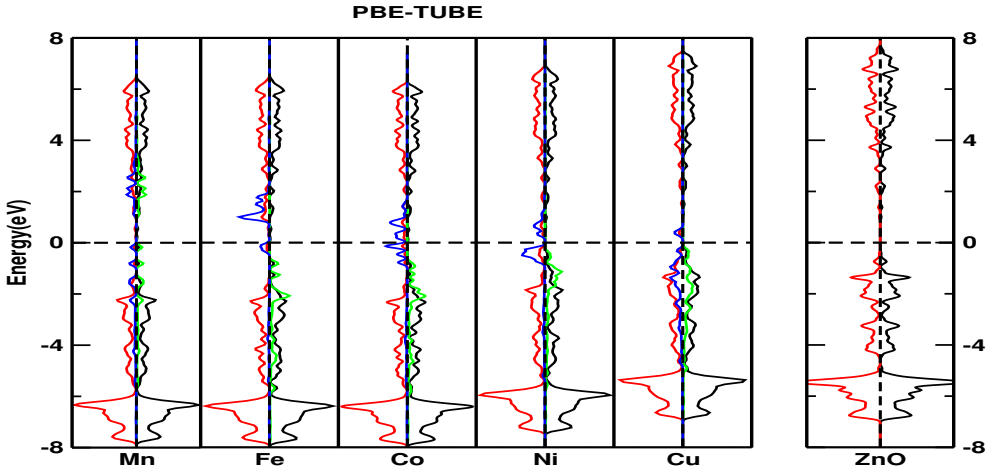

Figure 4.37: *DOS and PDOS of TM-doped ZnO with the TM atoms in the most favorable spatial configuration for tube calculated within the LSDA. The blue-green lines show the TM d states and the regions covered by black-red lines show the total DOS. The right panel is the DOS for pristine ZnO.*

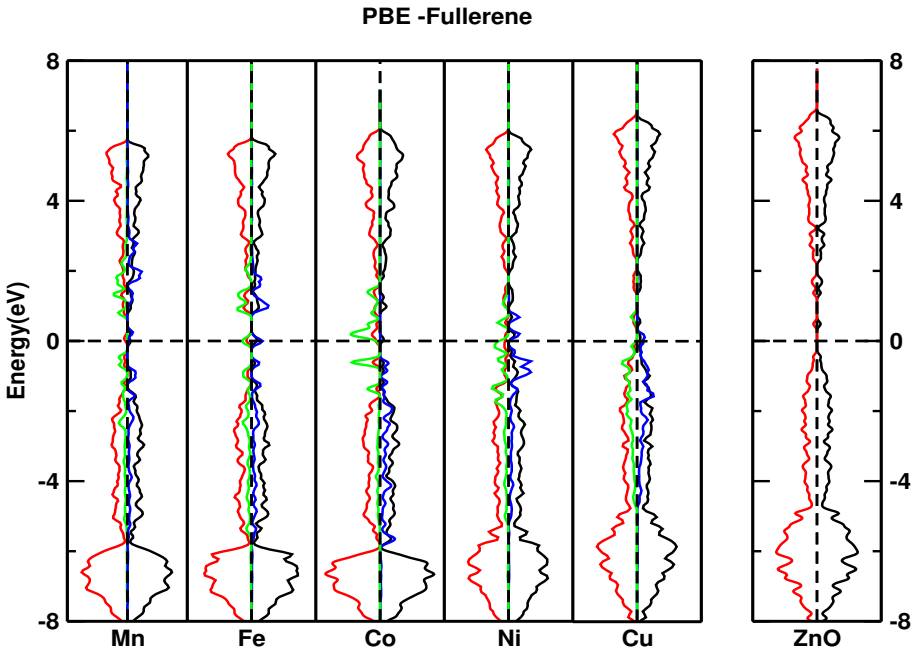

Figure 4.38: *DOS and PDOS of TM-doped ZnO with the TM atoms in the most favorable spatial configuration for fullerene-like structure calculated within the LSDA. The blue-green lines show the TM d states, and the regions covered by black-red lines show the total DOS. The right panel is the DOS for pristine ZnO.*

A. Electronic Properties of Mn doped ZnO

The pristine ZnO is nonmagnetic in nature due to its fulfilled 3d states of Zn ion but it becomes magnetic after doping TM atoms. Mn doped ZnO shows the strongest MM due to half filled d orbital. We here present the analysis of bi-dop Mn atom on pristine ZnO at different morphologies

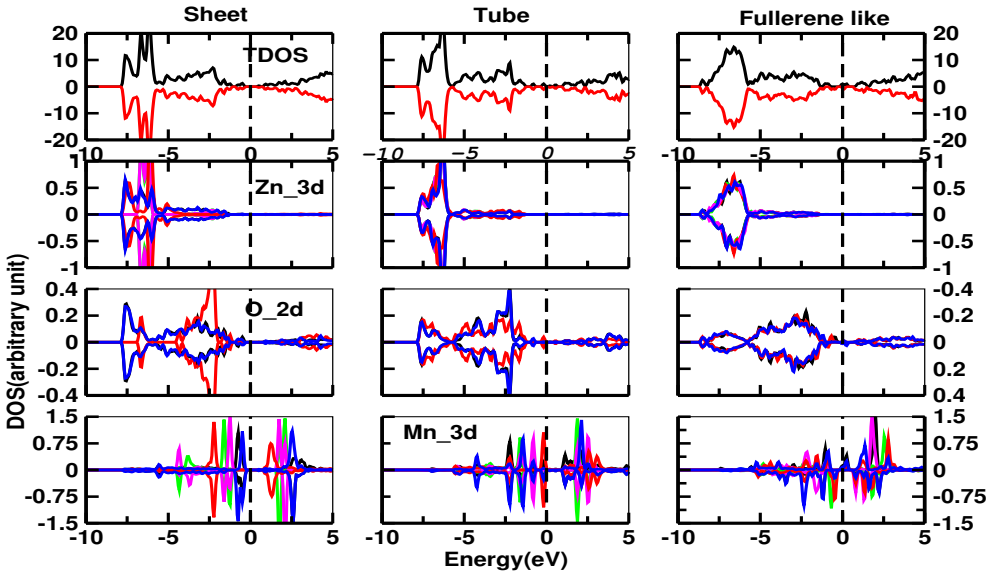

Figure 4.39: *DOS of most stable geometries of Mn in different morphologies with Zn-3d, O-2d and TM-3d respectively.*

Present calculations show that Mn doped ZnO favors AFM alignment(see Section 4.4.2). The previous work shows FM nature of Mn doped ZnO at room temperature in thin film (Dietl, *et al.*, 2000). However, the experimental result (Ghosh, *et al.*, 2004), $\geq 4\%$ of Mn doped ZnO thin film has posed challenge to the theoretical understanding of FM for such systems. This indicates that FM in Mn-doped system is not understood. It is because Mn in +2 valence state doesn't dop any carrier to the ZnO system. (Rao & Deepak, 2005) experimentally showed that Mn doped ZnO has lack of FM which clearly supports the present result. The MM appears in Mn doped ZnO nanotube is mainly due to hybridization between O_{2p} and Mn_{3d} states. It's MM depends upon bond length between (Zn-O) and between (Mn-O) as well as diameter of the tube. The anti-ferromagnetism also appears in fullerene like structure. The symmetrical distribution of spin up and down calculation also shows AFM alignment in bi-dop Mn. For the hydrogen storage purpose we need high surface to volume ratio of ZnO based nano-structure. Some experimental studies have been carried out for this purpose also. So far origin of AFM in nanosized structure is quite unknown till date

Total DOS between the up and down spin for ZnO is symmetrical indicating that ZnO

has no magnetism. The asymmetrical DOS between up and down spin channels near the fermi level suggest the magnetic properties. For bi-dop Mn the electron spin of up-spins is found to be same as down-spin(synetric distributions) at GS geometry suggested that Mn bi-dop favors AFM. This is against the previous results (Samanta, *et al.*, 2006) which shows FM nature. It is clear that Mn_{3d}, O_{2p} and Zn_{4s} partial DOS found to be symmetrical near the fermi level and strong AFM(or FM) coupling exits in Mn_{3d}, O_{2p} and Zn_{4s} electrons. There is noticeable change happens in the partial DOS of 4s state of Zn atom around the fermi level. Fermi level lies middle of the forbidden band. There is peak near the fermi level and impurity energy level is symmetrically broadened forming wider acceptor than pure ZnO The electron number of 3d states of Mn doped ZnO is less than pure ZnO. The reason is that the electrons in 3d states of Mn atoms has opposite spin. The impurity atoms keep close together and bound electron wave function of do-pant obviously overlapped at high concentration of doping. So that there is problem in electron sharing for 3d states of Mn and 2p states of O atom (Dai, *et al.*, 2013)

The splitting of d orbitals e_g and t_{2g} of Mn^{2+} 3d state is half filled, when atomic number of TM atom is before Mn, additional charge transfer causes increase in MM before Mn, additional charge decreases MM (half full filled) and hence the overall distribution of charge shows symmetric in nature. Prediction of Mn doped ZnO FM at room temperature is suitable application in spintronics. However GS nature of Mn doped ZnO is AFM. (Jung, *et al.*, 2002) found that spin glass behavior with strong AFM exchange coupling. First principles study of thin film predicts the coupling between Mn ions be AFM (Wang & Jena, 2004), same thing reported on bulk Mn doped ZnO as well. In case of Mn doped ZnO, AFM comes from the O_{2p}, Mn_{3d} and Zn_{4s} interactions. MM of single Mn($4.62\mu_B$) comes from spin polarized Oxygen atom and transition metal but bi-dop case it has zero MM due to equal and opposite alignments of up and down spins.

ZnO (II-IV) semiconductor is stable in wurtzite structure has wide band gap (3.37 eV). (Sharma, *et al.*, 2003) reported FM in Mn doped ZnO while (Tiwari, *et al.*, 2002) reported spin glass behavior. Experimental study finds no evidence of magnetic ordering down to $2K$ (Lawes, *et al.*, 2005), (Cheng & Chien, 2003). Mn in +2 valence state does not dope any carrier to the ZnO system and hence by first principle studies, must lead to anti-ferromagnetic ground state. The additional charge may transfer to the 3d states of each TM atom. The 3d orbit configuration t_{2g} and e_g in the Mn atoms are responsible for Mn 2+ ion to create AFM coupling in GS geometry.

B. Electronic Properties of Fe doped ZnO

Fe doped Zno also shows the anti-ferromagnetic in nature in sheet, generally in near dop case dominated. The Fe is found to be mixed Fe^{2+}/Fe^{3+} valence state with Fe^{2+} as the dominant state. Experimentally, it is observed as FM nature and this value increase up to 5% doping and decrease 7% to 10% of doping (Ahmed, *et al.*, 2012). Presently, we used below 10% TM dopant. If Fe is present in the substitution sites in a defect free ZnO crystal, the valence state of Fe will be 2+. However both EPR and Mossbauer results confirms the presence of uncoupled Fe^{3+} within sample giving rise to PM behaviors.

The moment per magnetic cation can be less due to several factors. Since the concentration of Fe is very close to the cationic percolation threshold, nearest neighbor antiferromagnetic interaction (super-exchange) between the Fe ions can lower the magnetic moment. Also, the presence of uncoupled Fe 3+ spins on the surface of the nanosheet may lower the magnetic moment. In case of other two morphologies we observed ferromagnetic behavior. The Fig.(4.40) shows the TDOS and PDOS for all the morphologies for bi dop of Fe in ZnO.

To investigate the actual reason for the observed ferromagnetism and value of magnetic moment per Fe, we have to know the results of EPR and FMR measurements and also the Mossbauer studies (Jung, *et al.*, 2002). Their reports confirm the presence of Fe^{3+}, if cationic vacancies (Zn for the present case) are present in the nearest neighborhood of Fe^{2+} in the substitutional cationic site, to neutralize the charge imbalance, the valence state of Fe can be converted to 3+. This can happen mostly on the surface of the nanosheet where the probability of transformation of charge within atoms near to Fe dop is more. The charge transformation near Fe, can promote Fe^{2+} into Fe^{3+} and also mediate the Fe^{2+} - Fe^{2+} exchange interaction. Since the TM doping percentage is slightly on the higher side towards cationic percolation threshold, Fe^{2+} - Fe^{3+} exchange, although being less in number in comparison to Fe^{2+} -Fe^{2+} interaction, may also be possible.

The characteristic feature of the DOS is the deep Fe derived states in the semiconducting gap of ZnO. These states are broadened due to hybridization with O-p states. The expected valence state of the substitutional Fe atom will be 2+ and it will be in the d^6 configuration. The Fe-d states get split into two fold degenerate e_g-levels and three fold degenerate t_{2g}-levels with the e_g levels being lower in energy. out of the available 6 electrons per Fe, four electrons are accommodated in the low lying e_g-level and the rest into the t_{2g}-levels in the non-spin polarized that the exchange splitting is much larger in comparison to the crystal field splitting and the system therefore favors a high spin configuration with the various levels serially filled up. Hence, the spin down

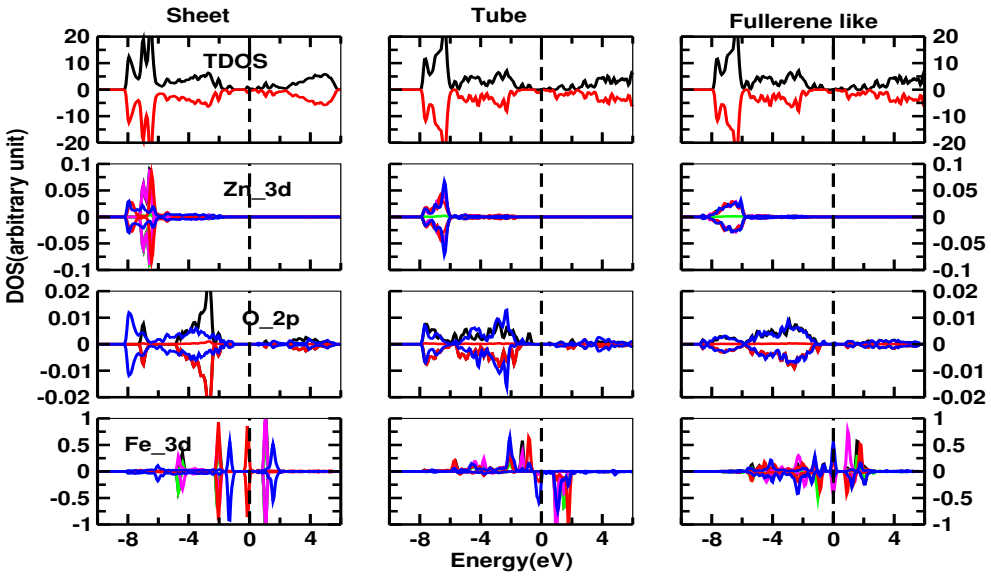

Figure 4.40: *DOS of most stable geometries of Fe in different morphologies with Zn-3d, O-2d and TM-3d respectively.*

channel completely filled while the spin up e_g level is half filled resulting in a net integral magnetic moment of 4 μ_B. This situation can be observed due to asymmetrical spin up and down spin near the fermi level for tube and fullerene. However, such a situation cannot stabilize ferromagnetism in the presence of Coulomb correlations. We have tried to understand the exact origin of ferromagnetism by knowing the exchange between 2^+ and 3^+ valence states. Same kind of situation is obtained through experiments by EPR and Mossbauer, indicating the presence of the dopant cation in both valence states 2^+ and 3^+.

C. Electronic properties of Co doped ZnO

Most of the experimental results (Sharma, *et al.*, 2003) show that among TM do-pants Co-doped ZnO systems are FM in thin film as well as bulk. The FM properties of Co are investigating using PAW and ultra-soft pseudo-potential based on DFT (Dai, *et al.*, 2013). Present study also favors AFM in sheet and FM in tube and fullerene structures. The FM comes from interaction of spin polarized oxygen-atoms, Zinc atoms and transition metal. MM are mostly contributed by spin-polarized oxygen-atom and TMs. The plot of TDOS and PDOS in different morphologies are shown in Fig.(4.41).

The spin-polarized calculations, when Co atoms are in short configuration, the ground state is found to be AFM state and lower than FM state by 0.068 eV per Co atom in sheet with Co-O distance ranges from 1.835 A^0 to 1.857A^0. For tube and fullerene like

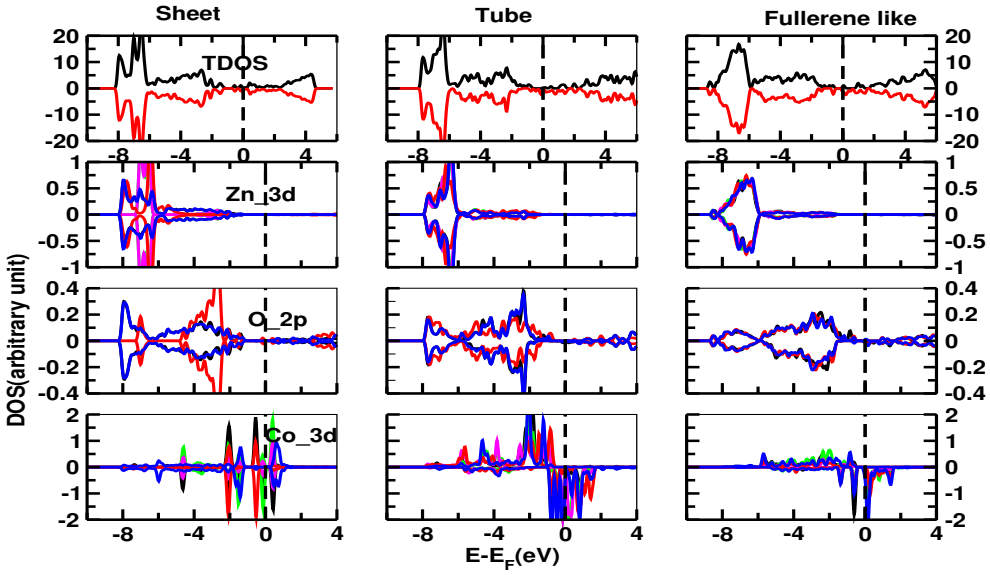

Figure 4.41: *DOS of most stable geometries of Co in different morphologies with Zn-3d, O-2d and TM-3d respectively.*

structure we observed FM states are more favorable than AFM having energies 0.301 eV and 0.306 eV per Co atom above its AFM state, respectively. When Co ions are in far configuration, PM state is predicted because of the negligible energy difference between AFM and FM states(0.021 eV). This indicates that magnetic coupling in ZnO:Co has a short range nature. The ground state of ZnO:Co is found to be AFM state in far configuration for sheet but FM ordering in short configuration. We also found FM nature in tube and fullerene like structures. The PBE shifts the valence-band maximum (VBM) to higher energy by overestimating the hybridization between Co 3d states and O 2p states. The partial DOS of ZnO:Co indicates that the ferromagnetism originates only from the hybridization between Co-3d and O-2p electrons in the vicinity of the Fermi level. The Zn-4s electrons do not contribute to the peak at the Fermi level. The additional charge may transfer to the 3d states of each TM atom. for both the systems.

D. Electronic properties of Ni doped ZnO

Fig.(4.41) shows the plot of TDOS and PDOS for most stable geometry of ZnO:Ni in three defined morphologies. In case of sheet ZnO:Ni, We found symmetrical distribution of up and down spins near the fermi level showing the anti-ferromagnetic behavior. The ZnO:Ni tube shows ferromagnetic nature. The origin of ferromagnetic properties in Ni doped ZnO has been explained by analyzing the coupling of Ni 3d levels. FM coupling between Ni atom is more stable . Results from the DOS show that O_{2p} hybridizes with Ni_{3d}, which results in electronic states spin polarization at the fermi energy. The fullerene structure nearly behaves FM in nature. The FM is due to additional charge

transfer to the 3d states of each Ni atom. The 3d orbit configuration in the symmetry of each TM atom is due to e_g and t_{2g} for Ni^{2+} ion. The total DOS of the ZnO:Ni NT to shift down to lower energy region. The asymmetric distribution of Ni_{3d} near the fermi level shows the Ferromagnetic behavior in case of tube and fullerene like structure.

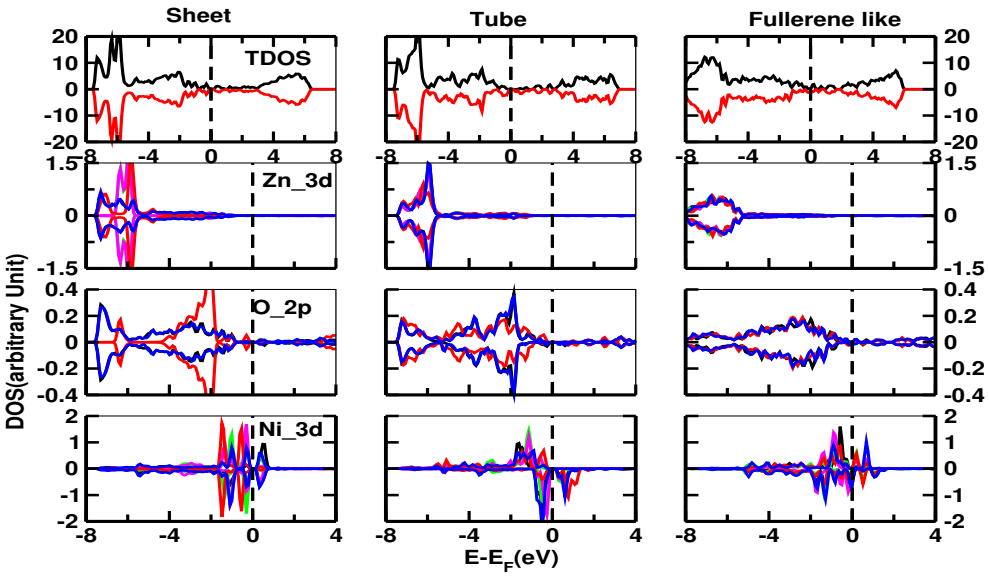

Figure 4.42: *DOS of most stable geometries of Ni in different morphologies with Zn-3d, O-2d and TM-3d respectively.*

E. Electronic properties of Cu doped ZnO

The plot of TDOS and PDOS for most stable geometry of ZnO:Co in three defined morphologies is shown in Fig.(4.42) shows From the plot, we found slight FM nature in Cu sheet and tube whereas slight AFM alignment in fullerene like geometry in the ground state. In fact, Copper (Cu) is non-magnetic in nature. In the case of ZnO:Cu de-localized holes induced by O_{2p} and Cu_{3d} hybridization are found to be very efficient to mediate the FM exchange interactions.

The FM interaction decreases as we decrease distance Cu-Cu indicating that far FM interaction is long range interaction in cu-doped ZnO systems. Cu pair in ZnO has an apparent clustering tendency for both FM and AFM states. The ground state of ZnO:Cu is FM ordering in configuration for sheet and tube and non-magnetic ordering in fullerene like structures which is consistent with previous study (Huang, *et al.*, 2008). We also note that the nearest neighbor coupling changes from being AFM to FM as we moved from fullerene to sheet. This is probably because the TM 3d states are split d ions into lower and upper t_{2g} states and the occupation of minority t_{2g} states due to enough 3d electrons which results in a transition from AFM to FM ordering. A net

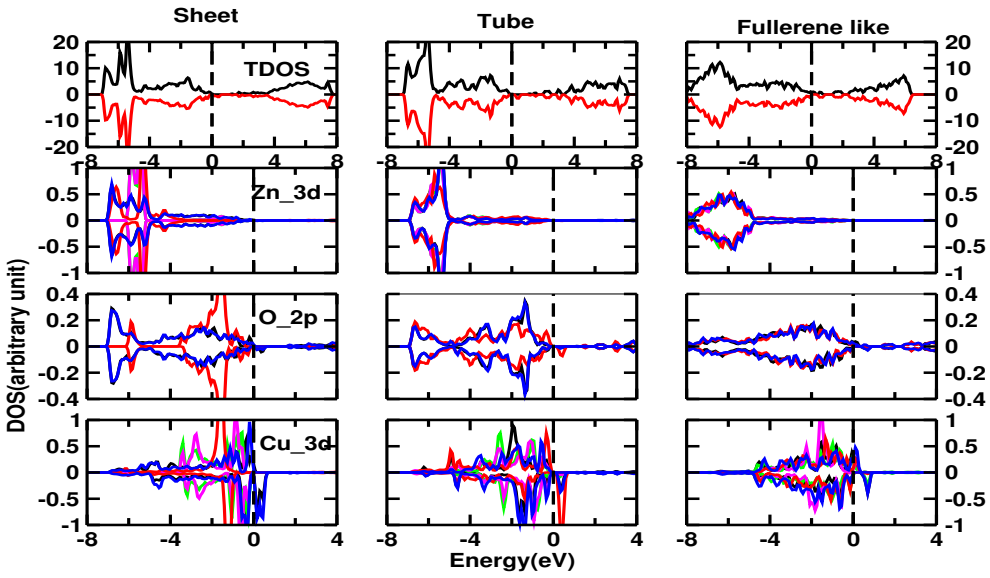

Figure 4.43: *DOS of most stable geometries of Cu in different morphologies with Zn-3d, O-2d and Cu-3d respectively.*

magnetic moment for Cu is found to be 1 μ_B per Cu. The electronic states near E_F are dominated by strong hybridization between O_{2p} and Cu 3d which implies that the Cu-O bond is quite covalent instead of purely ionic. We see no clustering tendency of the Cu atoms. Since there is no magnetic element in this compound, Cu-doped ZnO appears to be an unambiguous dilute magnetic semiconductor where ferromagnetic precipitate problems can be avoided The Cu-doped ZnO has a FM ground state in sheet agrees with the prediction by (Kim & Park, 2004). They used LDA linear maffin-tin orbital atomic sphere approximation (LMTO-ASA) method and obtained half-metallicity with magnetic moment of $0.81\mu_B$ per Cu atom. They also showed that the Cu magnetic moment increased to $1.85\mu_B$ after the inclusion of on-site Coulomb repulsion and spin-orbit coupling. In their report they reported that the possible Jahn-Teller JT distortion drives the system into a more stable insulating state, quenches the orbital moment and enhances the Cu spin magnetic moment to $0.99\mu_B$. In present case we found that the PBE calculation unable to deal a strong correlation effect of the Cu 3d states. Actually, there is no experimental evidence to support the strong correlation or any measurement.We suggest further calculation using HSE. The performance of the HSE treatment is still unknown. In the work of Sato and Katayama-Yoshida (Sato & Yosida, 2000) by the Korringa-Kohn-Rostoke(KKR) Green function method based on the LDA combined with the coherent potential approximation CPA. They reported no magnetic moment on Cu and concluded that Cu doped ZnO is nonmagnetic. This discrepancy of this results and present study is unknown. It is possible that their simulated doping level

(x=0.25) is too high so that the short-range AFM super exchange interaction becomes stronger and neutralizes the FM interaction. Since the origin of the FM in DMS's is still under debate, it is interesting to see how a different carrier density affects the strength of the magnetic interaction in Cu:ZnO. We considered the possibility of Cu clustering by varying the Cu-Cu distance.

4.4.4 Band gap Properties

In this section, we focused our attention to investigate the change in band gap after doping the transition elements in different morphologies.In ordered to solve the band gap problem, we used PBE in the frame work of density-functional theory (DFT) implemented in VASP. Further, we studied the band gap problem using hybrid function Heyd-Scuseria- Ernzerhof(HSE) (see section 3.7.2) as PBE underestimate the band gap. While implementing the HSE, we used data of optimized geometry from PBE calculation and then we implement HSE through VASP on the top of that relaxed structure giving only single iteration. We do so because of the computational cost. The variation of the band gap in PBE and HSE calculations for the different morphologies are listed in table (4.7) and Fig.(4.44). From the data, the band gap properties found to be changed drastically when we are moving from nanosheet to fullerene like structures of 48 atoms in PBE and HSE calculations. According to quantum confinement there should be increase in band gap as crystal size decreases. In our case the quantum confinement is exactly not applicable because tube and fullerene like structures are not exactly as a 1D or 2D as we aspect. Such study is very much useful for solar cells (Huynh, *et al.*, 2002), Optoelectronic (Klimov, *et al.*, 2000), catalysis (Ahmadi, *et al.*, 1996) as well as medical purposes (Huang, *et al.*, 2007).

Table 4.7: *Calculated Band gap energy for different Morphology for ZnO for PBE and HSE.*

System	PBE(eV)			HSE(eV)		
	Sheet	*Tube*	*Fullerene*	*Sheet*	*Tube*	*Fullerene*
$ZnO + pure$	1.753	1.429	0.933	3.385	2.995	2.218
$ZnO + Mn$	1.919	0.386	0.809	2.540	2.070	1.210
$ZnO + Fe$	0.677	0.272	0.475	1.960	1.937	1.510
$ZnO + Co$	0.153	0.259	0.136	2.810	2.680	0.278
$ZnO + Ni$	0.581	0.588	0.491	3.720	3.982	1.725
$ZnO + Cu$	0.417	0.557	0.437	3.420	2.841	2.020

We observed that band gap decreases when we are moving from nanosheet to fullerene type structures. Present result consistent with the data of previous work (Datta, *et*

al., 2012). In case of sheet, for PBE result the band gap of ZnO is found to be 1.753 eV/atom. The band gap of pristine ZnO sheet is found to be 3.385 eV which is (about 0.5%) greater than bulk ZnO (3.37 eV) (Joaheph & Venkateswaran, 2011). Similarly for ZnO tube and Fullerene like structures are found to be 2.995 eV and 2.215 eV. In nanosheet ZnO:Mn shows the blue shift in PBE calculations with a value of 1.92 eV with respect to pure ZnO (1.75 eV). This behavior agrees with previous trends(Wojcik, *et al.*, 2004), (Kane, *et al.*, 2005). This trends breaks in the application of HSE. After using HSE band gap of Zno:Mn becomes (2.54 eV) while pristine ZnO sheet has value (3.385 eV). In PBE, all other TM (Fe, Co, Ni and Cu) doped shows the red shift. However after using HSE Ni and Cu doped Zno shows blue shift with values 3.72 eV and 3.42 eV respectively. This red shift is mainly due to the s, p and d exchange interaction between the band electrons and the localized "d" electrons of the transition metals ion at cationic site (Kim & Park, 2004). In case of tube, band gap shows the red shift in PBE calculation whereas in HSE calculation ZnO:Ni shows the blue shift with band gap (3.98 eV). Similarly all shows red shift in fullerene like structures for both PBE and HSE.

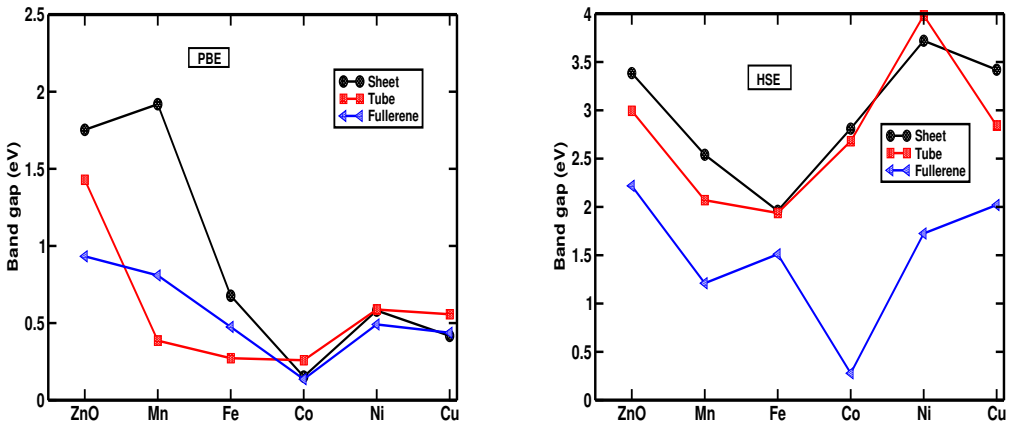

Figure 4.44: *Variation in band gap as a function of dopants in PBE (left) and HSE (right) functionals.*

In short, we found that the widening of the band gap is mainly due to blocking of low energy transition by the donor electrons occupying the states at the bottom of the conduction band which is known as Burstein-Moss effect. Similarly the decreasing of band gap due to displacement of charge from one atomic species to another in ZnO polar semiconductor and host atom becomes charged. These moving charged particles cause a displacement polarization, where an electron in the conduction band forms a clouds of positive charge and hole in the valence band forms a cloud of negative charge around of it. This particle and its charge cloud constitute a polaron which modifies the self energy and cause a downwards shift due to many-body interactions (Sernelius, *et*

al., 1988). From HSE calculations, we predict that ZnO based nanostructures and TM doped on it can be used for flat screen displays, field emmission sources, gas, chemical (Liao, *et al.*, 2005) and biological sensors and as ultraviolet light emitters and switches (Wang & Jena, 2004), (Sirbuly, *et al.*, 2005) etc. as well as some of other applications in piezoelectric (Gardeniers, *et al.*, 1998) and spintronics (Norton, *et al.*, 2003) devices.

4.5 Magnetic ordering in Ni-rich NiMn alloys around the multi-critical point

This section contains the magnetic behavior of Ni-rich NiMn alloys. For that we perform experiment over different six types of samples and compare their properties with theoretical calculation. We used TB-LMTO-ASR, TB-LMTO-GF and spin dynamics code to calculate the DOS, magnetic moments, and decay of magnetization. Further, we used Montecarlo calculation to analyze the magnetic phase diagram. The experimental results and theoretical results from the present work are explained as follows.

4.5.1 Experimental results of samples

In order to investigate the magnetic properties more detail experimentally as well as theoretically, We have chosen six samples of $Ni_{1-x}Mn_x$ with $x = 15 - 37$ at.% of Mn where it is expected to exhibit spin-glass behavior (Bolzoni, 2004). From the experiment of XRD, it is observed that $Ni_{1-x}Mn_x$ bears Fcc structures (Pal, *et al.*, 2012) throught of our sample of working range. The diffraction pattern is shown in Fig.(4.45(a)). Experimentally we have to analyze the transition temperatures, Magnetization saturation, Coercivity for different compositions are useful in assessing their application potentials, which are explain as follows.

We see from Fig.(4.45(b)) that for alloys with x = 15 and 20, ZFC and FC, M(T) curves show irreversibility in the low-temperature region. As T increases from $5K$, there is a bifurcation between ZFC and FC M(T) curves at T_{fg} indicating a transition from a re-entrant ferro SG-like state to a ferromagnetic state. In the intermediate temperature range, both ZFC and FC M(T) remain constant almost until T_C is reached. This is in contrast to the result of (Hahn & Kneller, 1958), for x = 23 and 23.5. At low temperatures, our alloys with x = 15 and 20 exhibit a reentrant/ferro spin-glass-like mixed phase having a spontaneous FM moment as well as glassy behavior below T_{fg} as seen from M(H) curves at 5 K in Fig. (4.46). The sample with x = 15 has $T_{fg} = 37K$ and $T_C = 310K$while the sample with x = 20 has $T_{fg} = 60K$ and $T_C = 270K$. This "reentrant" phase having a "mixed" character was predicted theoretically (Mookerjee,

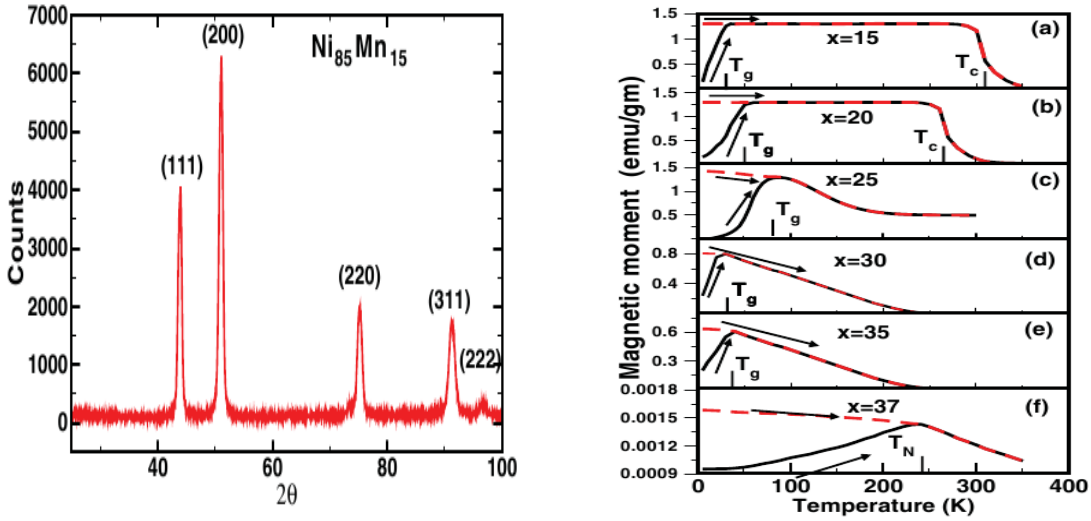

(a) (b)

Figure 4.45: *(a)XRD pattern of x=15, showing that $Ni_{1-x}Mn_x$ alloys formed FCC structures in all alloys ranges from $15 \geq x \geq 37$ and (b) Magnetization vs temperature curves for Ni-Mn alloys between 5 and 350 K on heating after ZFC (black/full line) and then again heating after FC (red/dashed line) in a magnetic field of 20 Oe using a SQUID magnetometer. In the composition range $15 \geq x \geq 20$. we note that in addition to the para-ferro transition at T_C, there is a glassy transition at $T_g < T_C$ with a bifurcation between ZFC and FC curves. In the composition range $25 < x < 37$ the figure shows only a glassy transition. For $x > 37$ we see only a para-antiferro transition at T_N.*

1980) long back and involves below T_{fg} a SG ordering of the spins transverse to the coexisting FM moments, while in the FM state above T_{fg} the transverse SG ordering is absent and only the FM alignment of the longitudinal spin components remains. It must be stressed here that this coexistence of FM and SG phase below T_{fg} is not a spatially segregated coexistence of infinite ferromagnetic clusters decoupled from finite clusters. The coexistence takes place over the whole sample. The FM ordering persists down to the lowest temperatures ($T << T_{fg}$. AuFe (Coles, *et al.*, 1978), (Verbeek & Mydosh, 1978) is the first system where the coexistence was observed just below the percolation threshold of 15 at.% Fe. $Fe_{80-x}Ni_xCr_{20}$ $(10 \leq x \leq 30)$ alloys,(Majumdar & Blanckenhagen, 1984) with a variation of Ni from 10-30 at.% at the cost of Fe with Cr remaining fixed, is another system, similar to the NiMn, which offered a unique opportunity of observing various magnetic phases such as ferromagnetic, mixed ferro-spin-glass, spin-glass, and anti-ferromagnetic (Moze, *et al.*, 1984).

We associate the lower temperature transition at T_{fg} for $x = 15$ and 20 and the single transition at the MCP for $x = 25$ with a spin-glass-like phase. The samples with x = 25, 30, 35, and 37 have only one type of transition which can be clearly seen from the

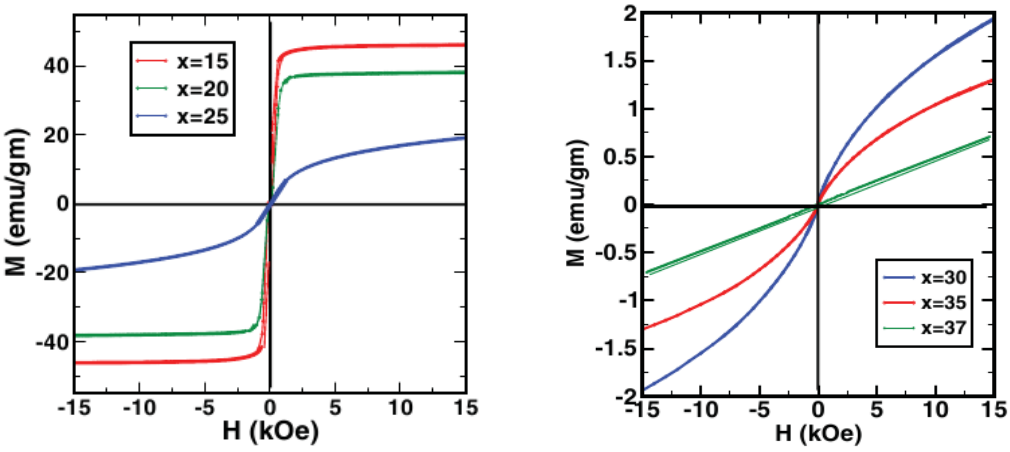

(a) (b)

Figure 4.46: *(a) Magnetization measured at low temperatures (5K) as a function of applied fields H. In the composition range $x < 25$ the hysteresis with saturation at high fields is characteristic of ferromagnetism. At the MCP ($x = 25$) the hysteresis curves do not saturate and resemble those for spin glasses.(b) For $15 < x < 37$ the hysteresis again is characteristic of spin glasses, until at $x > 37$ it becomes almost linear, indicating anti-ferromagnetism.*

steep rise in the M(T) curves [Figs.4.45{b} (c)-(f)] until a maximum is reached and then a clear knee indicating a paramagnetic to a spin-glass-like (PM-SG)/anti-ferromagnetic (AF) transition. T_g/T_{fg} for x = 25 is 100 K and T_g of x = 30 is $29K$. T =$40K$ for x = 35 may be a spin-glass freezing temperature or a Neel temperature (T_g/T_N whereas for x = 37, $237K$ is clearly the Neel temperature T_N, since the moment decreases abruptly at this concentration from 0.6 to 0.0016 emu/g as x changes from 35 to 37. For x = 30-37, the spin-glass-like/anti-ferromagnetic state goes directly to the paramagnetic one without passing through any intervening ferromagnetic phase.

Hysteresis loops were obtained for each sample after cooling in zero fields to $5K$ from above $T_C/T_{fg}/T_g/T_N$ and measured in fields up to $50kOe$ using the vibrating-sample magnetometer. In Fig.(4.46), we have plotted the magnetization of all six samples at $5K$ till $16kOe$. They show drastic changes with Mn content. For the samples with x = 15 and 20, $16kOe$ was sufficient for magnetic saturation. In the case of $x \leq 25$, the magnetization was still rising at the highest attainable field of 120 kOe, as shown in the set of Fig.(4.46(a)) for x = 25. The reentrant/ferro spin-glass-like mixed phases for x = 15, 20, and 25 have spontaneous FM moments below T_{fg}. When x increases beyond x = 25, the M(H) curves spread out. At x = 25 (Fig.(4.46(a)), we get hardly any magnetic saturation and this locates the critical point. The bell-shaped low-field region for x = 25 resembles those observed in spin glasses but the sample still retains a high susceptibility at low temperatures. For lower values of x, the M(H) curves saturate at fields $\approx 1kOe$ like those of ferromagnets but with the increase of x, the lack of saturation gradually

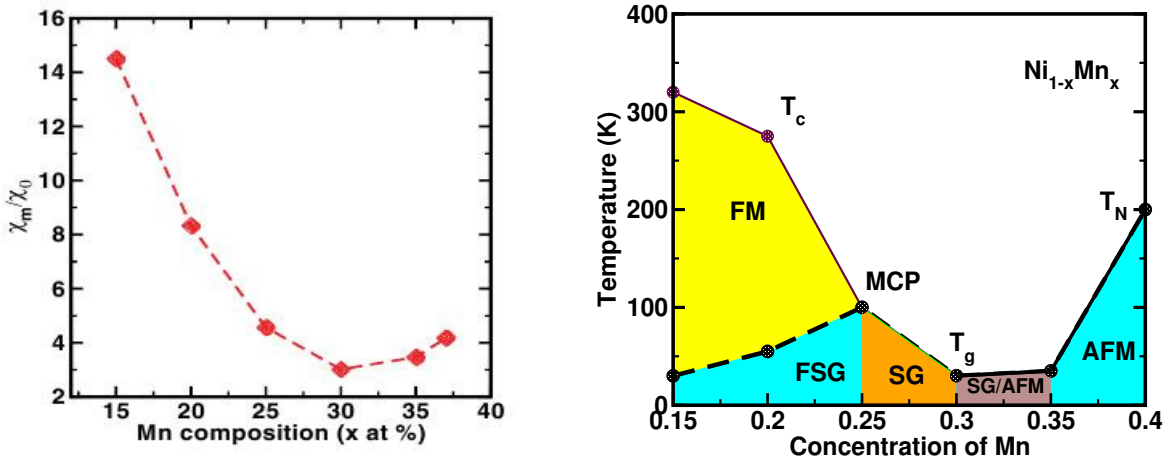

(a) (b)

Figure 4.47: *(a)χ_m/χ_0 vs Mn concentration (at.% Mn) in $Ni_{1-x}Mn_x$ alloys. At $x = 25$ (MCP) this ratio approaches the value ≈ 4.4 characteristic of spin glasses. The ratio increases either as ferro or antiferromagnetism sets (b) Experimental Magnetic phase diagram.*

becomes more evident and finally around x = 37 their curvature disappears and M(H) becomes almost linear implying antiferromagnetic character (Fig.(4.46(b)).

In Fig.4.47(a), the ratio χ^m/χ^0 versus Mn concentration (at.% of Mn) is plotted, where χ^m and χ^0 are the demagnetization corrected low-field susceptibilities (after zero-field cooling) at the maximum values and at $5K$ respectively. We find that the ratio value decreases with increasing x. It is as large as $\approx$ 15 for x = 15 indicating a long-range ferromagnetic order, while at x = 25, the ratio $\approx$ 4.4 which is typical of a canonical spin glass. It is interesting to note that subsequently the value of the ratio reaches a minimum around 35 at.% Mn and then it starts increasing indicating the onset of another long-range order (here anti-ferromagnetic).

Fig.(4.47(b)) shows the magnetic phase diagram of disordered $Ni_{1-x}Mn_x$ alloys showing ferromagnetic (FM), ferro-spinglass (FSG), conventional (canonical) spin-glass (SG), paramagnetic (PM), and anti-ferromagnetic (AFM) regions. The values of T_C, T_{fg}, T_g, and T_N are taken from Fig.(4.45) (H = $20Oe$). The lines joining the first three all meet at a point which is called the multicritical point (MCP; x = 25, T =$100K$). Beyond the MCP, at higher at.% of Mn, the spin-glass state directly goes to the paramagnetic state (up to 30 at.% Mn) or the anti-ferromagnetic state to the paramagnetic state (for 35 and 37 at.% Mn) with no intervening ferromagnetic phase. Beyond x = 25 till 30, T_g goes down; then at 35 there is a slight increase in the bifurcation temperature while M (Magnetization) gradually decreases all the way (from $\approx$ 1 to 0.6 emu/g). However, according to the neutron diffraction work (Moze, *et al.*, 1984) long-range anti-ferromagnetism does not set in for x = 30 but 35 at.% Mn is indeed antiferromagnetic but

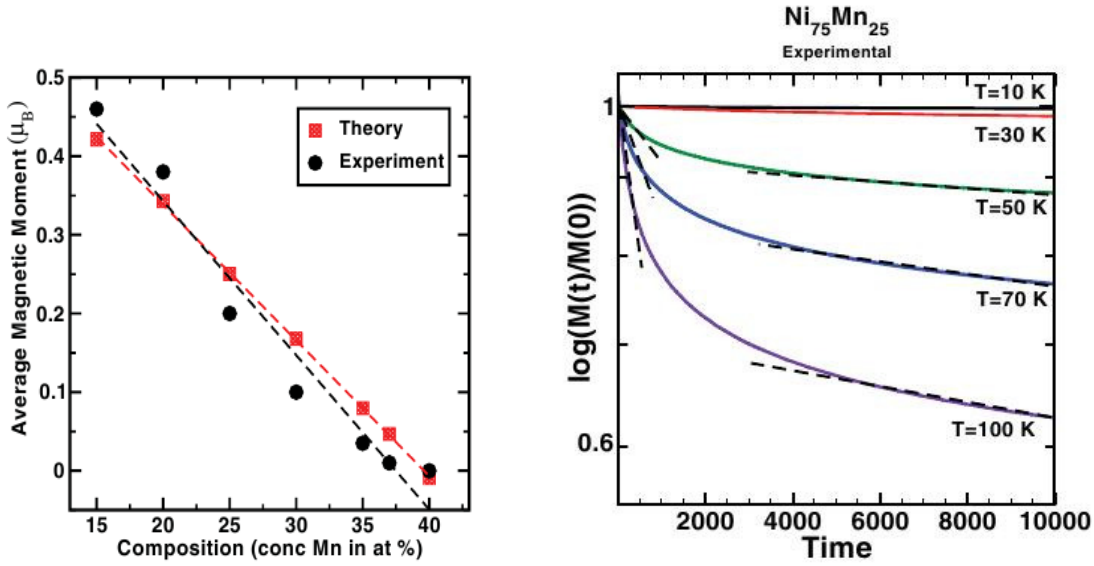

(a) (b)

Figure 4.48: *(a) Comparison of magnetic moments with change in (at.% of Mn) in* $Ni_{1-x}Mn_x$ *alloys. (b) Experimental study of time decay of magnetization at x=25 at different temperatures. The alloy magnetization shows anomalously slow relaxation as we approach and cross the glass-transition temperature below* $100K$*. Below* $100K$ *we can no longer fit data with exponential decay functions phase diagram.*

T_N could not be found because of the weak Bragg peak and the temperature-dependent diffuse scattering. For lower values of x, below the multicritical point, the samples pass through two phases, ferromagnetic (FM) and re-entrant spin-glass or ferro-spin-glass. In reentrent spin-glass (RSG or FSG) systems,with decreasing temperature one observes a paramagnetic-ferromagnetic transition at T_C. Then at a lower temperature T_{fg}, spin-glass-like properties show up. In the phase diagram , we get a critical concentration which is the point (x = 25) where T_C and T_{fg} (100 K) come together. We further note that the value of T_{fg} increases and T_C decreases with increasing x. The variation of T_g with Mn concentration is very interesting. Up to x = 30, it decreases linearly with increasing x, then we get T_N in place of T_g signifying AFM order which increases with Mn concentration. The boundary between the re entrant/ferro-spin-glass (FSG) and the canonical spin-glass (SG) phases is a vertical line which touches the multicritical point (x = 25).

The phase diagram that we obtained from magnetization data shows an interesting nature within concentration range ($15 \leq x \leq 25$) in which the system undergoes two magnetic transitions on lowering the temperature: from paramagnetism to ferromagnetism and from ferromagnetism to a spin-glass-like state. For ($25 \leq x \leq 35$) %, however, only paramagnetic to spin-glass-like transition is observed and x = 37 shows

only one transition but that is from anti-ferromagnetic to a spin-glass state. Since the magnetic properties of quenched Ni-Mn alloys depend strongly on composition around 25 at.% Mn, it is essential to ensure an accurate determination of composition. We also find that the lattice parameter increases monotonically with x and shows no anomaly as the magnetic state widely changes from a mixed FM-SG-like state to an AFM one. So, we have taken EDAX (energy dispersive x-ray analysis) of every sample and got satisfactory results. The variation of magnetic moments as a functions of Mn concentration from both experiment and theory is seen in Fig.(4.48(a))

Fig.(4.48(b)) shows the plot of the experimental time decay of normalized magnetization $ln[M(t)/M(0)]$ for $0 < t < 10,000s$ for $Ni_{75}Mn_{25}$ alloy at different temperatures. The magnetization shows anomalous slow relaxation as we approach and cross the glass-transition temperature. Around and below $70K$, although for long times ($> 6000s$) ln[M(t)/M(0)] can be fitted to a line; its slope is so small that anomalous slow (power law or logarithmic) decay is suggested.

4.5.2 Electronic structures and magnetic moment ordering

In order to understand the onset of magnetic ordering in random alloys, we proceeded in two steps. The formation of a magnetic moment within an atomic sphere was analyzed using the TB-LMTO-ASR, which is the reliable technique to deal with the disorder in the system and averaging over the disordered described else where in this thesis. This gives an itinerant electron picture where the moment is produced by an exchange splitting of the majority and minority spin projected densities of states. The spin PDOS for the composition range of $Ni_{1-x}Mn_x$ are shown in Fig.(4.49).

The ordering of moments carrying by atomic spheres is studied via derivation of the lowest configurational energy for a specified spin configuration. Models have been set up describing configurational energies in terms of effective multi-site interactions, in particular effective pair energies (EPE). We used Lichtenstein technique see section 3.12.1 directly for the calculation of effective pair exchanges. Using this technique we have calculated EPE on $(40 \times 40 \times 40)$ lattice. The EPE of Mn-Mn, Mn-Ni and Ni-Ni, shows the oscillatory behaviour with distance i.e. RKKY type oscillation and the nearest neighbor Mn-Mn EPE is found to be anti-ferromagnetic where as nature of EPE for Mn-Ni and Ni-Ni are ferromagnetic. This is a clear indication of strong frustration in the system. The $J_{Ni_Ni}(0)$ increases with increase of Ni concentration, consistent with the fact that Ni has very fragile magnetic moment and depends heavily on its surroundings. When Ni concentration is high, its more likely to be surrounded with more Ni atoms and the dominant $J_{Ni-Ni}(0)$ increases. On the other hand the dominant EPE for both

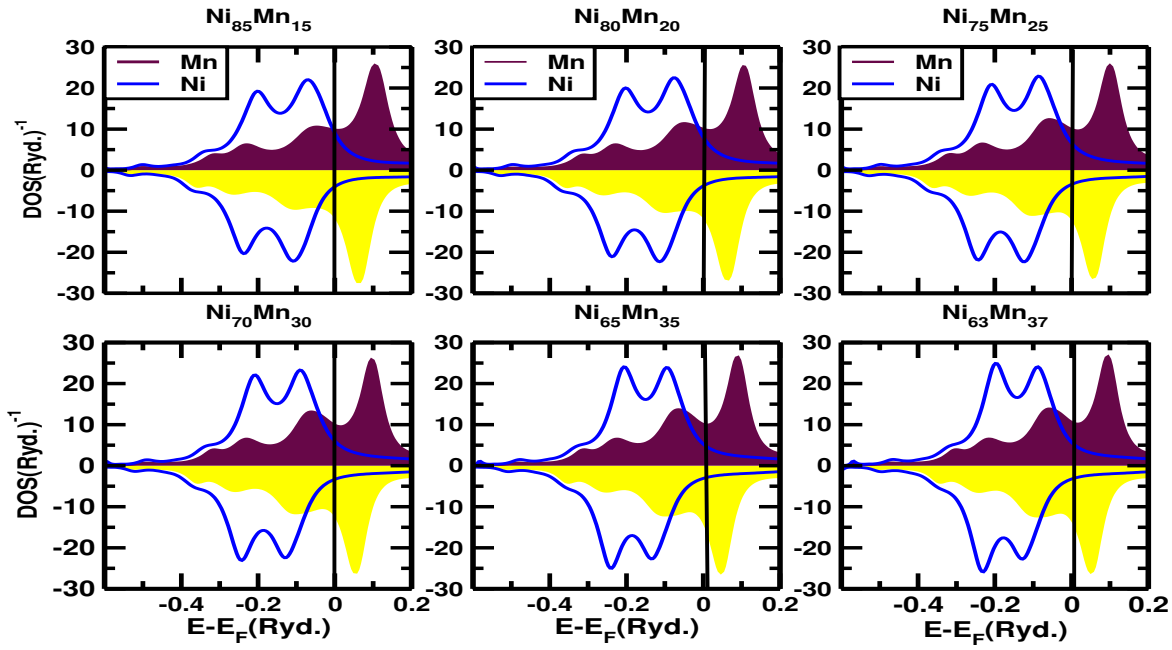

Figure 4.49: *PDOS of* $Ni_{1-x}Mn_x$ *at various concentration of Mn ranges from* $15 \geq x \geq 37$.

Mn-Mn and Mn-Ni decreases with increase of Ni concentration.as in Fig.4.50

4.5.3 Mean field analysis and Magnetic Relaxations

We are strictly following the Mookerjee and Roy approach(Mookerjee & Roy, 1983) for the mean field analysis. Such types of approach suggested earlier by various groups (Kaneyoshi, 1976), (Kaneyoshi, 1981), (Plefka, 1976) (Thouless, *et al.*, 1977), (Anderson, *et al.*, 1972). In this approach they mapped EPE with random Heisenberg model and studied the T = 0 phases and have shown that there exists a critical concentration x_C which separates the spin-glass from the ordered phases. We have also carried out a mean field calculation of critical temperature and obtained the magnetic phase diagram as in Fig. (4.51(a)) which is resemblance with the phase diagram suggested by experiment in Fig. (4.47(b)) as well as Montecarlo simulations as in fig. (4.51). If we compare this phase diagram with Fig.(4.46), we see that our mean-field-based calculation can qualitatively yield phase boundary as a function of Mn concentration with a ferromagnetic phase for $x < 15$, an anti-ferromagnetic phase for$x > 37$, with glassy phases in between. Of course, it grossly overestimates critical temperatures, which is not surprising for a simple mean-field calculation and the shape of the paramagnetic-spin-glass boundary is rather crudely reproduced. We also perform Montecarlo simulation and plot mean field phase diagram which also gives the information across a para-ferro transition. Comparing between Fig.(4.47) and Fig.(4.51), it can be said that the Monte

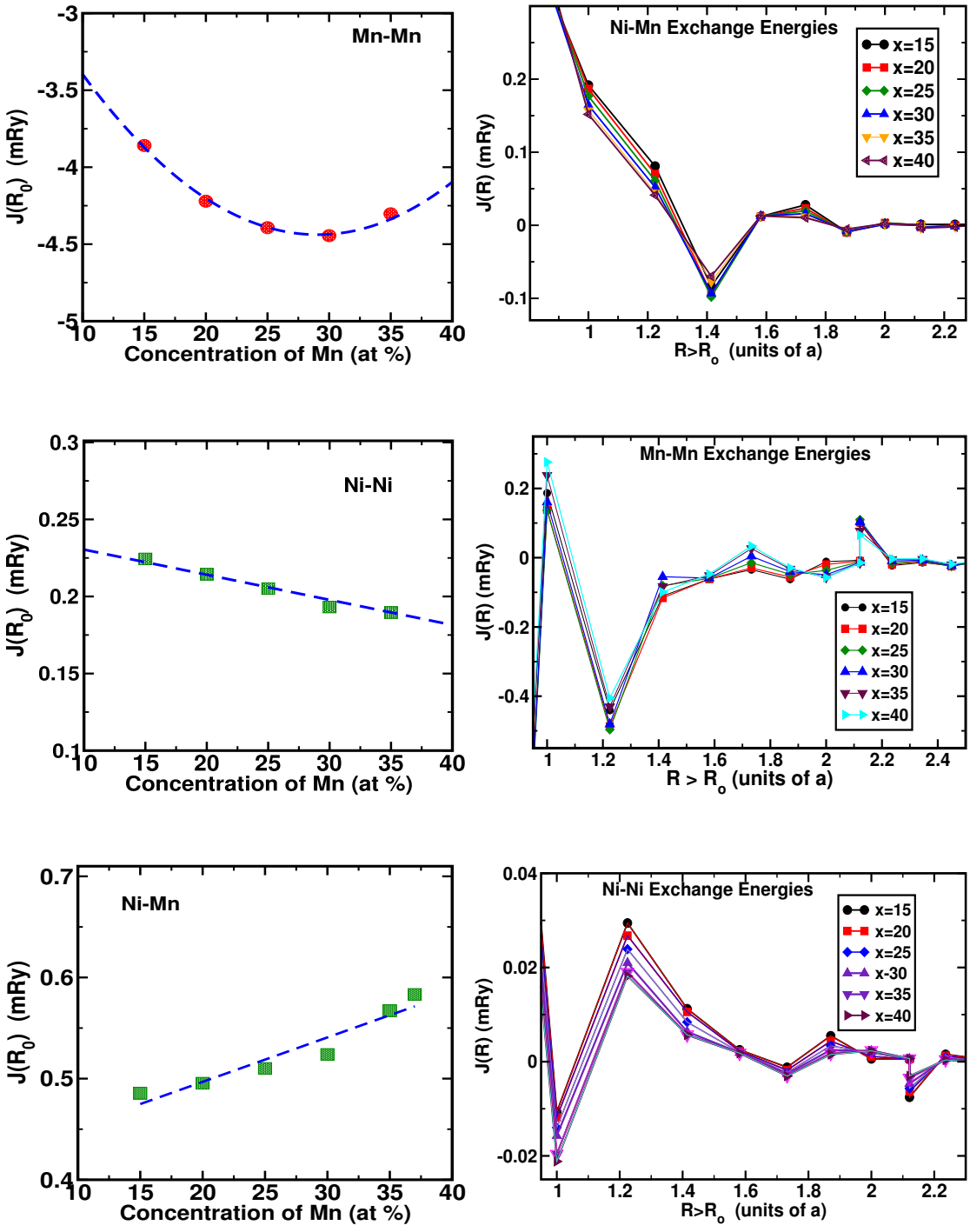

Figure 4.50: *EPE for Ni_xMn_{1-x} alloy. Left column : EPE for the nearest neighbor distances. It is seen that the Mn-Mn EPE is anti-ferromagnetic and most dominant; whereas, EPE for Mn-Ni and Ni-Ni are ferromagnetic but relatively weak. Right Column : EPE for second nearest neighbour and further distances. The oscillatory behavior shows the possibility of frustration.*

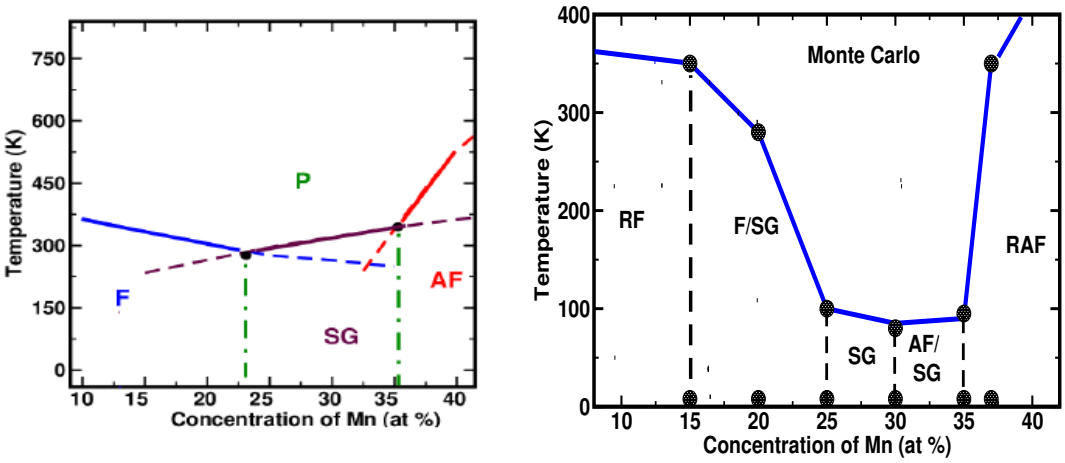

(a) (b)

Figure 4.51: *Magnetic phase diagram from present calculations and proposed phase diagram from Montecarlo simulations.*

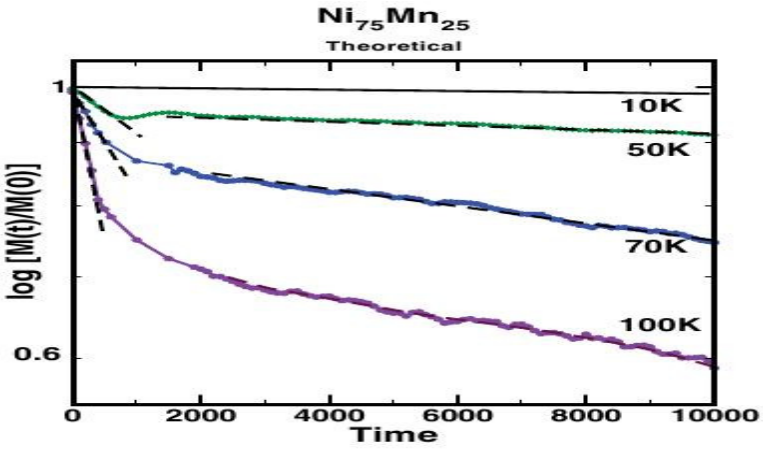

Figure 4.52: *LLG results for the time decay of magnetization for the $Ni_{75}Mn_{25}$ alloy at different temperatures which also shows anomalously slow relaxation as we approach and cross the glass-transition temperature below 100 K*

Carlo transition temperatures are now quite near to the experimental values.

Moreover, We have done the magnetic relaxation to conform the spin-glass behavior. Landau-Lifshitz-Ginzberg (LLG) formalism is directly used for the study of magnetization decay. This is an important tool to study the existence of the spin-glass phase (Mydosh, 1993), (Chaudhury & Mookerjee, 1984). The required magnetic pair energies i.e. $J^{Q,Q'}(R)$ used to calculate the time-dependent magnetic moment via a Landau-Lifshitz-Gilbert (LLG) equation of motion are either taken from experiment or from calculated theoretical values. We have used an atomistic approach as proposed by (Skubic, *et al.*, 2008). Skubic's approach, based on density functional theory starts with LLG equation. It allows us to carry out finite temperature calculations by including a

stochastic magnetic field ($\vec{b}_{\vec{R}}(t)$):

$$\frac{d\vec{m}^{Q}_{\vec{R}}}{dt} = -\gamma \vec{m}^{Q}_{\vec{R}} \times \left(\vec{B}^{Q}_{\vec{R}} + \vec{b}_{\vec{R}}(t) \right) - \frac{\gamma\alpha}{m} \left[\vec{m}^{Q}_{\vec{R}} \times \left\{ \vec{m}^{Q}_{\vec{R}} \times \left(\vec{B}^{Q}_{\vec{R}} + \vec{b}_{\vec{R}}(t) \right) \right\} \right] \tag{4.1}$$

where γ is the gyromagnetic ratio and the Weiss field is :

$$\vec{B}^{Q}_{vecR} = -\frac{\partial H}{\partial \vec{m}^{Q}_{\vec{R}}} = -\sum_{Q'} \sum_{\vec{R}' \in Q'} J^{QQ'}_{\vec{R}\vec{R}'} \ \vec{m}^{Q'}_{\vec{R}'} \tag{4.2}$$

The stochastic Gaussian white-noise field describing temperature fluctuations of the Weiss field is :

$$\left\langle b^{\mu}_{\vec{R}}(t) \right\rangle = 0 \quad < b^{\mu}_{\vec{R}}(t) b^{\nu}_{\vec{R}'}(t') >= 2D\delta_{\mu\nu}\delta_{\vec{R}\vec{R}'}\delta(t'-t) \quad D = \frac{\alpha}{1+\alpha}\frac{k_B T}{\gamma m}$$

where α is the damping parameter associated with D and temperature and m is the magnitude of the magnetic moment. These alloys often exhibit macroscopic magnetic anisotropy in experiments (Monod & Berthier, 1980). We shall, for the time being, ignore such anisotropy effects, and shall simply assume that some mechanism exists to provide magnetic damping. This will be parametrized by α. In the present case we are not attempting to obtain this parameter until we have identified the mechanism for damping. We shall empirically set $\alpha = 0.1$. Fig.(4.52) shows the behavior of $log[M(t)/M(0)]$ vs t at the composition $Ni_{75}Mn_{25}$ at the MCP. The linear fits at small and asymptotic times indicated decays are at two time scales: a fast decay initially, indicating a decay to a local minimum in the energy landscape. At long times the system slowly relaxes toward the global minimum. This has been done for both the experimental data and the LLG results. We note that across the temperature range they agree rather well, with exponential relaxations at high temperatures to an almost logarithmic relaxation at $10K$. This is a definite signature of the spin-glass phase.

4.6 Spin glass behaviour of disordered Pd-Mn, Pt-Mn and Ni-Mn alloys: non-collinear TB-LMTO-ASR Approach

The spin glass behavior of Pd-Mn, Pt-Mn and Ni-Mn are analyzed using non-collinear TB-LMTO-ASR technique. This is very powerful technique to deal with disordered binary alloys. The important equations for the calculation of electronic and magnetic properties based on non-collinear TB-LMTO is described in very short form. The important results and mean-field picture of reference systems are also presented within this section.

4.6.1 TB-LMTO-ASR in the non-collinear magnetism formalism

We have generalized the standard LSDA based electronic structure techniques to take non-collinear magnetism into account. Such a generalization of the tight-binding linear muffin-tin orbitals based augmented space recursion (TB-LMTO-ASR) method has been introduced by (Bergman, *et al.*, 2006) and (Ganguly, *et al.*, 2011). The technique has been described in great detail in the referenced papers. Here we shall introduce the main points of interest in our application. We begin by making the "rigid spin approximation". We shall associate a unique direction of magnetization with each atomic sphere labeled by $\vec{R}$. We shall call this direction the *local* quantization axis characterized, as described earlier, by two angles $\theta_{\vec{R}}$, $\phi_{\vec{R}}$ with respect to a set of suitably chosen global axes. The TB-LMTO Hamiltonian can be written in terms of local, potential parameters : $C^{\sigma}_{\vec{R}L}$ which describes the band centers, $\Delta^{\sigma}_{\vec{R}L}$ which determines the band widths and $o^{\sigma}_{\vec{R}L}$ which is orthogonality related and affects the band shape. In case spin-orbit interaction is important, there is a related fourth local potential parameter $\vec{v}_{RLL'}$. The crystal lattice is described by the sparse screened structure matrix $S_{\vec{R}L,\vec{R}'L'}$. The local potential parameters referred to the local quantization axes can be generically written as : $\Pi^{\sigma}_{\vec{R}L}$ where $\sigma = \uparrow, \downarrow$. Referred to the global axes these parameters transform to

$\Pi^{(1)}_{\vec{R}L} = (\Pi^{\uparrow}_{\vec{R}L} + \Pi^{\downarrow}_{\vec{R}L})/2$ and $\Pi^{(2)}_{\vec{R}L} = (\Pi^{\uparrow}_{\vec{R}L} - \Pi^{\downarrow}_{\vec{R}L})/2$.

We now turn to the treatment of disorder in the system. The augmented space formalism was introduced by (Mookerjee, 1973) as a methodology to obtain configuration averages of functions of a set of random variables directly described in chapter (4). Since there have been numerous and detailed descriptions of the methodology already (Mookerjee, 2003). Here we shall describe only the functional steps necessary to implement in our technique. For a random binary substitutional alloy, any local potential parameter $\Pi^{\sigma}_{\vec{R}L}$ is a random variable. In the augmented space formalism, we associate with any random variable $\Pi^{\sigma}_{\vec{R}L}$ an operator $M_{\vec{R}}$, whose eigenvalues are the values taken by it and whose spectral density is its probability density. The 'configuration space' of $\Pi^{\sigma}_{\vec{R}}$, $\Phi_{\vec{R}}$, is the space spanned by the eigenvectors of $M_{\vec{R}}$. For each random variable $\Pi^{\sigma}_{\vec{R}}$ we introduce an operator $M_{\vec{R}}$ in this way. The configuration space of the set of random variables is $\Phi = \prod^{\otimes} \Phi_{\vec{R}}$. The augmented space theorem (Mookerjee, 1973) states that the configuration average of any function $f(\{\Pi_{\vec{R}}\})$ may be written as :

$$\ll f(\{\Pi_{\vec{R}}\}) \gg = \langle\{\emptyset\}|\tilde{f}(\{\widetilde{M}_{\vec{R}}\})|\{\emptyset\}\rangle \tag{4.3}$$

where $\tilde{f}(\{\widetilde{M}_{\vec{R}}\})$ is the same operator function of the operators $\{\widetilde{M}_{\vec{R}}\}$ as $f(\{\Pi^{\sigma}_{\vec{R}}\})$ was of $\{\Pi^{\sigma}_{\vec{R}}\}$. Operationally we construct $\tilde{f}(\{\widetilde{M}_{\vec{R}}\})$ by replacing each $\Pi^{\sigma}_{\vec{R}}$ in $f(\{\Pi^{\sigma}_{\vec{R}}\})$ by the corresponding $\widetilde{M}_{\vec{R}}$. Here, $|\{\emptyset\}\rangle$ corresponds to the configuration without any fluc-

tuations about the 'mean configuration' or the vacuum in the space of configuration fluctuations. All tilded operators acts on the 'configuration space' Φ.

We now start from equation (4.3) and construct the Hamiltonian in *augmented space* $\Psi = \mathcal{H} \otimes \Phi$:

$$\widehat{h} = \sum_{RL} \widetilde{A}_{RL} \otimes P_{RL} + \sum_{RL,\vec{R}'L'} \left\{ \widetilde{B}^{(1)}_{RL,\vec{R}'L'} \otimes T_{RL,\vec{R}'L'} + \left(\widetilde{B}^{(2)}_{RL,\vec{R}'L'} \otimes T_{RL,\vec{R}'L'} \right) \sum_{\mu} e^{\mu}_{\vec{R}} e^{\mu}_{\vec{R}'} \right\} \quad (4.4)$$

$$\begin{aligned} \widehat{B}^{\mu} = & \sum_{RL} \left(\widetilde{D}_{RL} \otimes P_{RL} + \sum_{\vec{R}'} \widetilde{B}^{(3)}_{RL,\vec{R}'L'} \otimes T_{RL,\vec{R}'L'} \right) e^{\mu}_{\vec{R}} + \sum_{RL,\vec{R}'L'} \left\{ \left(\widetilde{B}^{(4)}_{RL,\vec{R}'L'} \otimes T_{RL,\vec{R}'L'} \right) e^{\mu}_{\vec{R}'} + \right. \\ & \left. \left(\widetilde{B}^{(2)}_{RL,\vec{R}'L'} \otimes T_{RL,\vec{R}'L'} \right) \sum_{\nu\xi} \varepsilon^{\mu\nu\xi} \; e^{\nu}_{\vec{R}} e^{\xi}_{\vec{R}'} \right\} \end{aligned} \quad (4.5)$$

where,

$$\begin{aligned} \widetilde{A}_{RL} &= \widetilde{C}^{(1)}_{RL} - \widetilde{E}_{\nu L} \quad ; \quad \widetilde{D}_{RL} = \widetilde{C}^{(2)}_{RL} \quad ; \quad \widetilde{B}^{(1)}_{RL\vec{R}'L'} = \widetilde{\Delta}^{(1)\ 1/2}_{RL} \otimes \tilde{S}_{RL\vec{R}'L'} \otimes \widetilde{\Delta}^{(1)\ 1/2}_{\vec{R}'L'} \\ \widetilde{B}^{(2)}_{RL\vec{R}'L'} &= \widetilde{\Delta}^{(2)\ 1/2}_{RL} \otimes \tilde{S}_{RL\vec{R}'L'} \otimes \widetilde{\Delta}^{(2)\ 1/2}_{\vec{R}'L'} \; ; \; \widetilde{B}^{(3)}_{RL\vec{R}'L'} = \widetilde{\Delta}^{(2)\ 1/2}_{RL} \otimes \tilde{S}_{RL\vec{R}'L'} \otimes \widetilde{\Delta}^{(1)\ 1/2}_{\vec{R}'L'} \\ \widetilde{B}^{(4)}_{RL\vec{R}'L'} &= \widetilde{\Delta}^{(1)\ 1/2}_{RL} \otimes \tilde{S}_{RL\vec{R}'L'} \otimes \widetilde{\Delta}^{(2)\ 1/2}_{\vec{R}'L'}. \end{aligned} \quad (4.6)$$

and ,

$P_{\vec{R}L}$ and $T_{\vec{R}L,\vec{R}'L'}$ are projection and transfer operators in $\mathcal{H}$. All hatted operators act on the full augmented space $\Psi = \Phi \otimes \mathcal{H}$. Thus,

$$\widehat{H}^{(0)} = \widehat{E}_{\nu} + \widehat{h} - \widehat{h} \otimes \widehat{o} \otimes \widehat{h}$$

Similarly, for the spin-orbit part :

$$\widehat{\Lambda}^{\pm} = \sum_{RL} \widetilde{v}^{\pm}_{L} \otimes P_{RL} \qquad \widehat{\Lambda}^{z} = \sum_{RL} \widetilde{v}^{z}_{L} \otimes P_{RL}.$$

So that the full augmented space Hamiltonian becomes :

$$\widehat{\mathbf{H}} = \widehat{H}^{(0)} \mathbf{I} + \left(\vec{\widehat{B}} + \vec{\widehat{\Lambda}} \right) \cdot \vec{\mathbf{S}} \quad (4.7)$$

The augmented space theorem then gives the averaged Green function as :

$$\ll \mathbf{G}_{RL,\vec{R}'L'}(E) \gg = \langle RL\{\emptyset\}| \; \widehat{\mathbf{G}}(E) \; |\vec{R}'L'\{\emptyset\}\rangle$$

where

$$\widehat{\mathbf{G}}(E) = \left(E\hat{\mathbf{I}} - \widehat{\mathbf{H}} \right)^{-1} \in \Psi$$

and $|RL\{\emptyset\}\rangle = |RL\rangle \otimes |\{\emptyset\}\rangle$ is a particular state in augmented space Ψ. The averaged projected and magnetic density of states are :

$$\begin{aligned} \ll n_{\vec{R}L}(E) \gg &= -\frac{1}{\pi}\Im m \mathrm{Tr}_\alpha \left\{ \widehat{\mathbf{G}}_{\vec{R}L\{\emptyset\},RL\{\emptyset\}}(E+i0) \right\} \\ \ll \vec{m}_{\vec{R}L}(E) \gg &= -\frac{1}{\pi}\Im m \ \mathrm{Tr}_\alpha \left\{ \vec{\mathbf{S}} \ \widehat{\mathbf{G}}_{\vec{R}L\{\emptyset\},RL\{\emptyset\}}(E+i0) \right\} \end{aligned}$$

One of the useful methods for the calculation of the Green function in systems where lattice translation symmetry broken is the recursion method proposed by Haydock,s group (Haydock, *et al.*, 1972). We obtain the averaged Green function as a continued fraction by the recursion method in full augmented space, which is one of the approximation related to the *termination* of the continued fraction. Haydock and coworkers (Haydock, 1980), (Beer & Pettifor, 1984) have described various analyticity preserving terminators. Unlike mean-field theories such as the coherent potential approximation (CPA) and its cluster generalizations, these approximations and errors can also be easily controlled (Haydock, 1980) within ASR.

In order to calculate a generalized non-collinear magnetization density, we also need to calculate the non-diagonal elements of the Green function in spinor space (Bergman, 2006), (Frota-Pessoa, 1992). At this point we carry out three recursions with local quantization axis rotated in the x,y or z directions by SU(2) rotation matrices.

If we do a rigid moment approximation within an atomic sphere, then we can define a local spin-axis in which $\mathbf{S}_z$ is diagonal. We can apply unitary SU(2) rotation operators $\mathcal{U}_x$, $\mathcal{U}_y$ and $\mathcal{U}_z = I$ which diagonalize $\mathbf{S}_x$ and $\mathbf{S}_y$ and $\mathbf{S}_z$. Thus,

$$\begin{aligned} \ll m^\mu_{\vec{R}L}(E) \gg &= -\frac{1}{\pi}\Im m \ \mathrm{Tr} \left\{ \left(\mathcal{U}_\mu \mathbf{S}_\mu \mathcal{U}_\mu^\dagger\right) \ \left(\mathcal{U}_\mu \mathbf{G}_{\vec{R}L\{\emptyset\},RL\{\emptyset\}}(E) \mathcal{U}_\mu^\dagger\right) \right\} \\ &= -\frac{1}{\pi}\Im m \ \mathrm{Tr} \left\{ \mathbf{S}'_\mu \ \mathbf{G}'_{\vec{R}L\{\emptyset\},RL\{\emptyset\}}(E) \right\} \end{aligned}$$

and

$$\ll m^\mu_{\vec{R}} \gg = \sum_L \int_{-\infty}^{E_F} dE \ll m^\mu_{\vec{R}L}(E) \gg$$

Since $\mathbf{S}'_\mu$ are diagonal in spinor space we need to calculate only the diagonal elements of $\mathbf{G}'_{\vec{R}L\{\emptyset\},RL\{\emptyset\}}$. This requires two recursions per direction, so six recursions in all (Ganguly, *et al.*, 2011).

4.6.2 Density of states and local magnetic moment

As a test case we have examined the possible stable electronic and magnetic structures of $Pt_{75}Mn_{25}$ alloys. We have looked at the component and spin projected densities of

Table 4.8: *Comparison of energy difference between different moment configurations at two different compositions :x=0.25 and x=0.5 for $Pt_{1-x}Mn_x$. In the former 1Q phase is stable, while in the latter the stable phase is 3Q.*

Type	x=0.25	x=0.5
	ΔE mRy/atom	ΔE mRy/atom
Ferro disordered	5	7.6
1Q disordered	0	1.41
2Q disordered	1.65	1.68
3Q disordered	1.78	0
Pt_3Mn ordered	6.5	8.0

states (PDOS) for 1Q antiferromagnetic disordered alloy, the ferromagnetic disordered alloy, the ordered compound Pt_3Mn and the 2Q and 3Q antiferromagnetic disordered alloys. The corresponding PDOS are shown in Fig.(4.53). The PDOS structures are different in the different states, giving rise to different local moments. Table (4.8) shows that the 1Q antiferromagnetic state is stable at this compositions.

The first observation is that the energy differences between the 1Q, 2Q and 3Q structures are almost at the limits of accuracy of our methodology. Although we make the statement that at x=0.25 the 1Q anti-ferromagnetic and at x=0.5 the 3Q antiferromagnetic states are the most stable, our judgment has to be open as the differences are too small for comfort. The energy differences between the 1Q and the disordered ferromagnet and the ordered compounds are also small, particularly at x=0.25. There is, therefore a possibility that during the process of alloy formation from high temperatures,

these phases are precipitated in the 1Q background. This could be the explanation of the experimental ferromagnetic signatures in this composition range. At x=0.50 the energy difference between the 3Q and the ferromagnetic and ordered L10 structures are larger. So probability of precipitation of the ferromagnetic phase becomes less. Experimental data in this composition is eagerly awaited.

Figs. (4.49, 4.56 and 4.57) compare the PDOS for $Ni_{1-x}Mn_x$, $Pt_{1-x}Mn_x$ and $Pd_{1-x}Mn_x$ alloys for selected the concentration required for our study. The PDOS shapes for all three alloys are overall similar. If we look more carefully, for $Ni_{1-x}Mn_x$ for the 25% composition it is the spin-glass state that is stable, while for the 1% composition it is the ferromagnetic one. For $Ni_{1-x}Mn_x$, the Ni bands are relatively narrow lying between 0.5 to 0.1 Ry below the Fermi level, and do not overlap the Mn peaks. On the other hand, for both $Pd_{1-x}Mn_x$ and $Pt_{1-x}Mn_x$, the Pd and Pt bands are much wider and

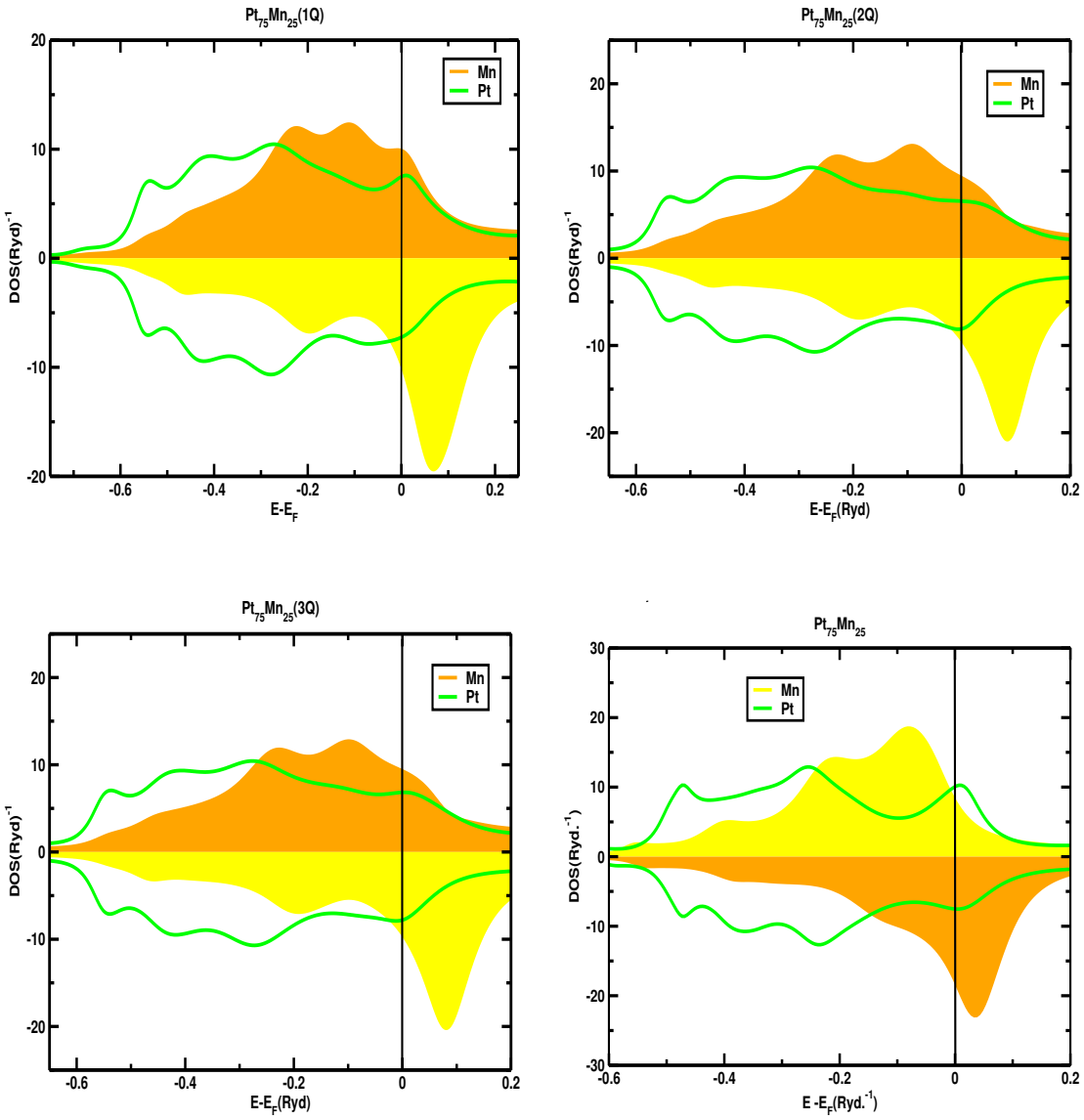

Figure 4.53: *PDOS of 1Q, 2Q and 3Q antiferromagnetic and ferromagnetic $Pt_{75}Mn_{25}$ disordered alloy, The PDOS structures are different in the different states, giving rise to different moments. The 1Q antiferromagnetic state turns out to have the lowest energy at this composition.*

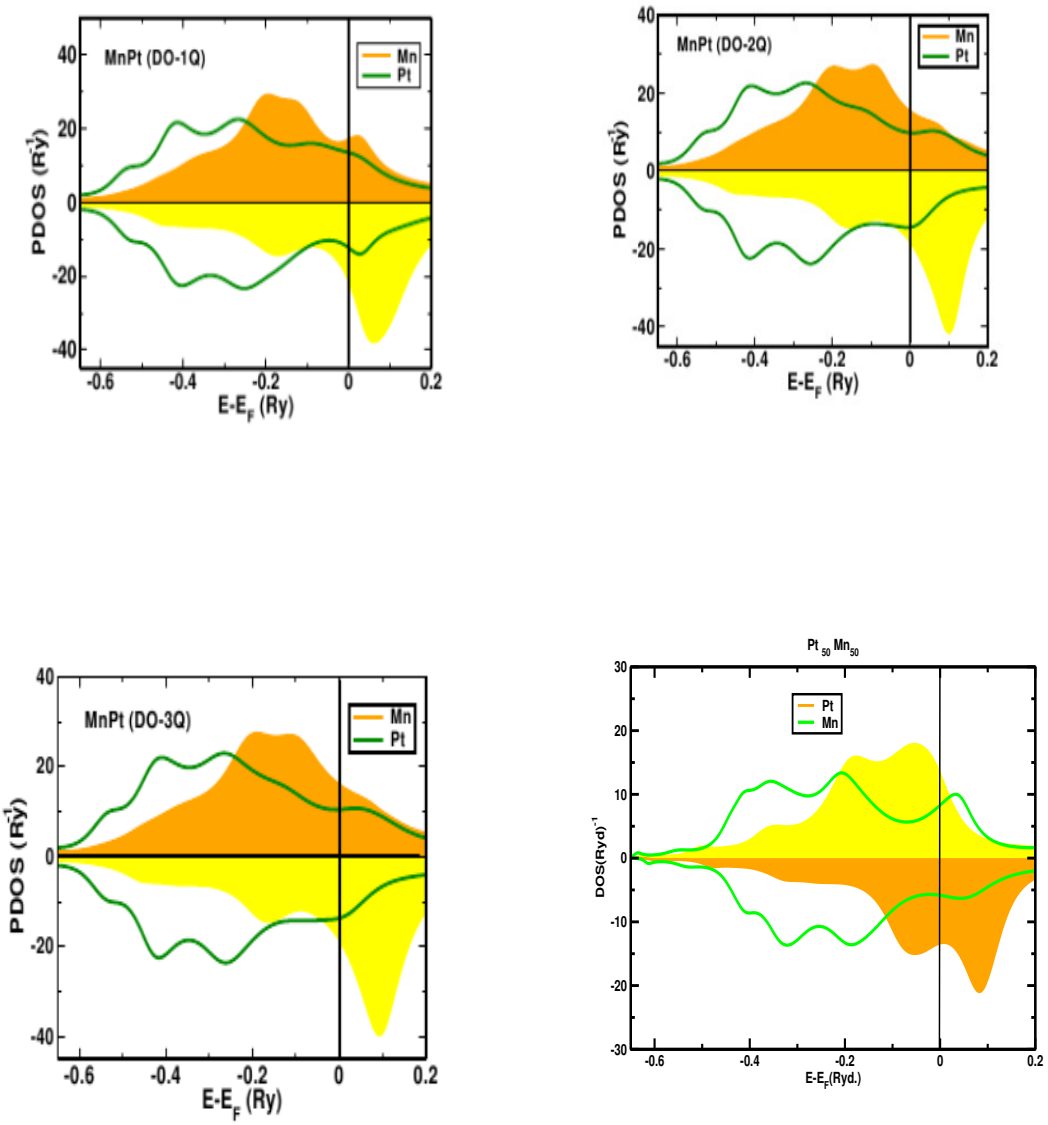

Figure 4.54: *PDOS of 1Q, 2Q and 3Q antiferromagnetic and ferromagnetic $Pt_{50}Mn_{50}$ disordered alloy. The PDOS structures are different in the different states, giving rise to different moments. The 3Q antiferromagnetic state turns out to have the lowest energy at this composition.*

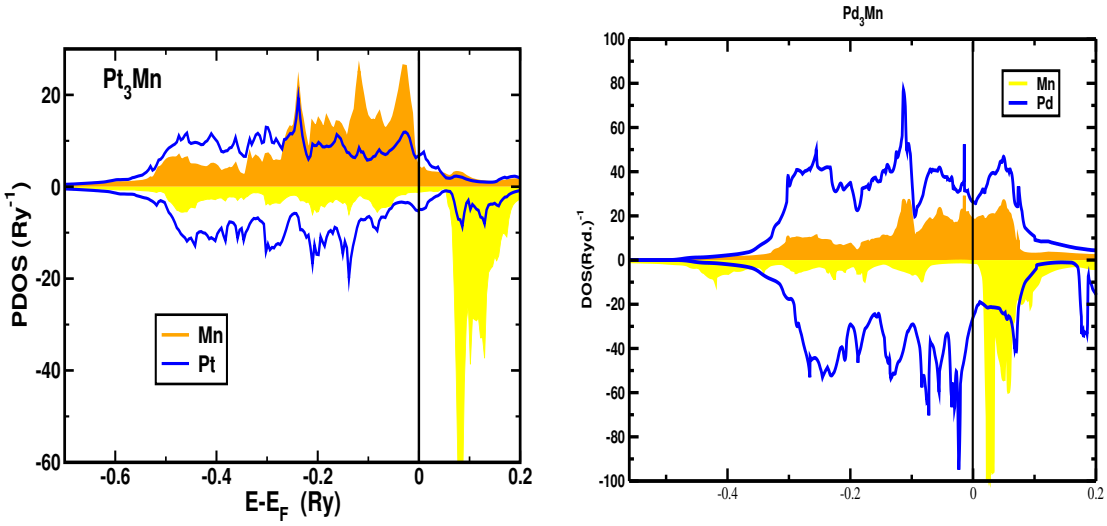

Figure 4.55: *PDOS of the ordered compound Pt_3Mn and Pd_3Mn.*

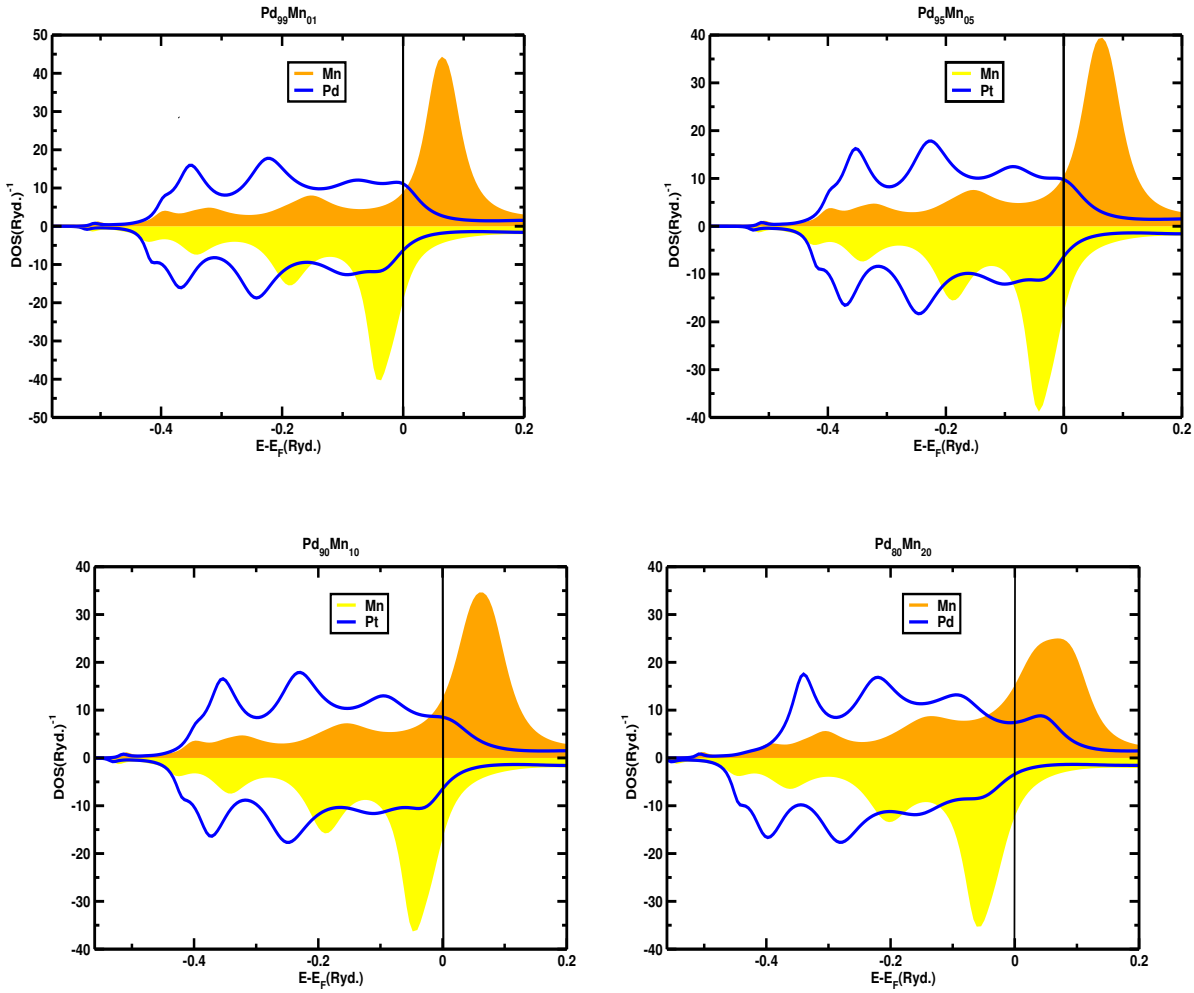

Figure 4.56: *(Color Online) Spin-resolved partial DOS for alloys $Pd_{1-x}Mn_x$.*

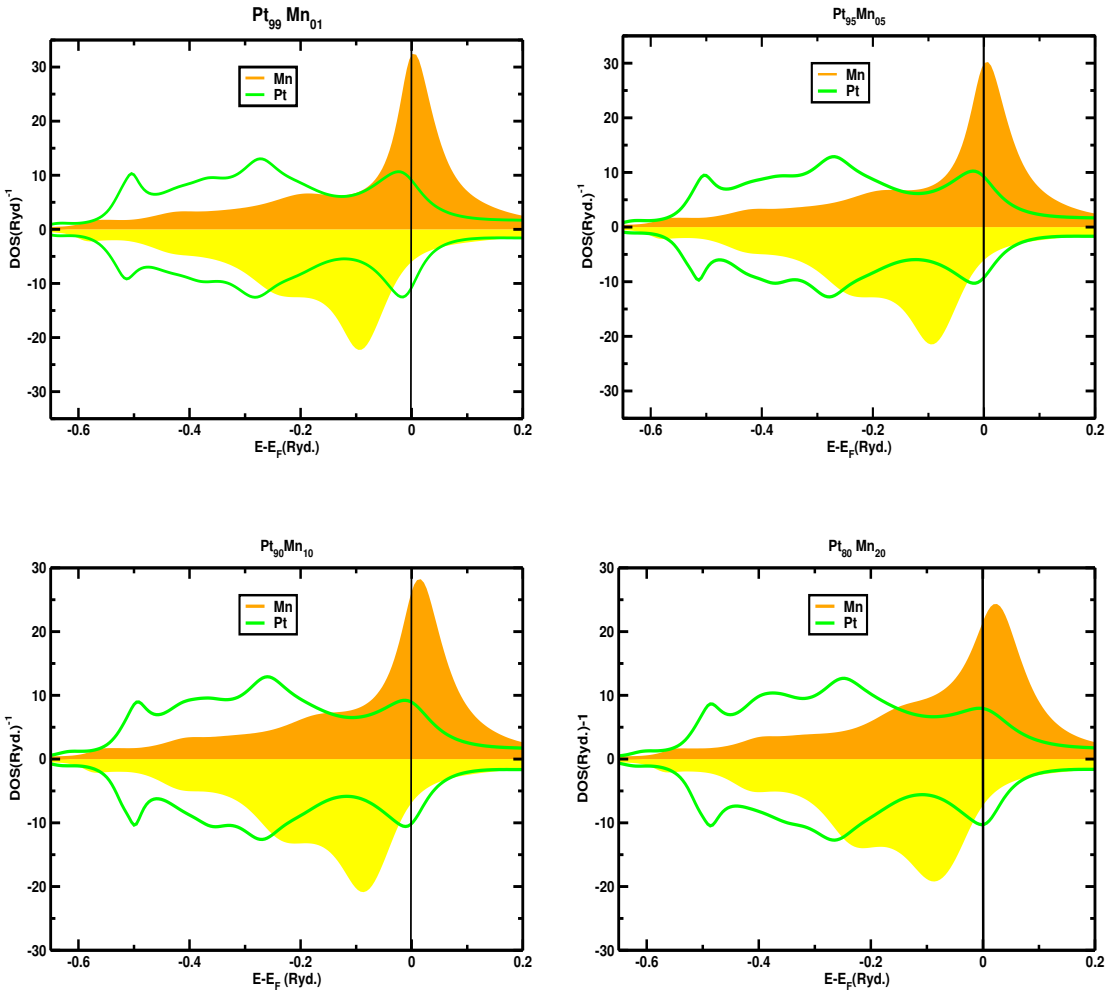

Figure 4.57: *(Color Online) Spin-resolved partial DOS for alloys* $Pt_{1-x}Mn_x$.

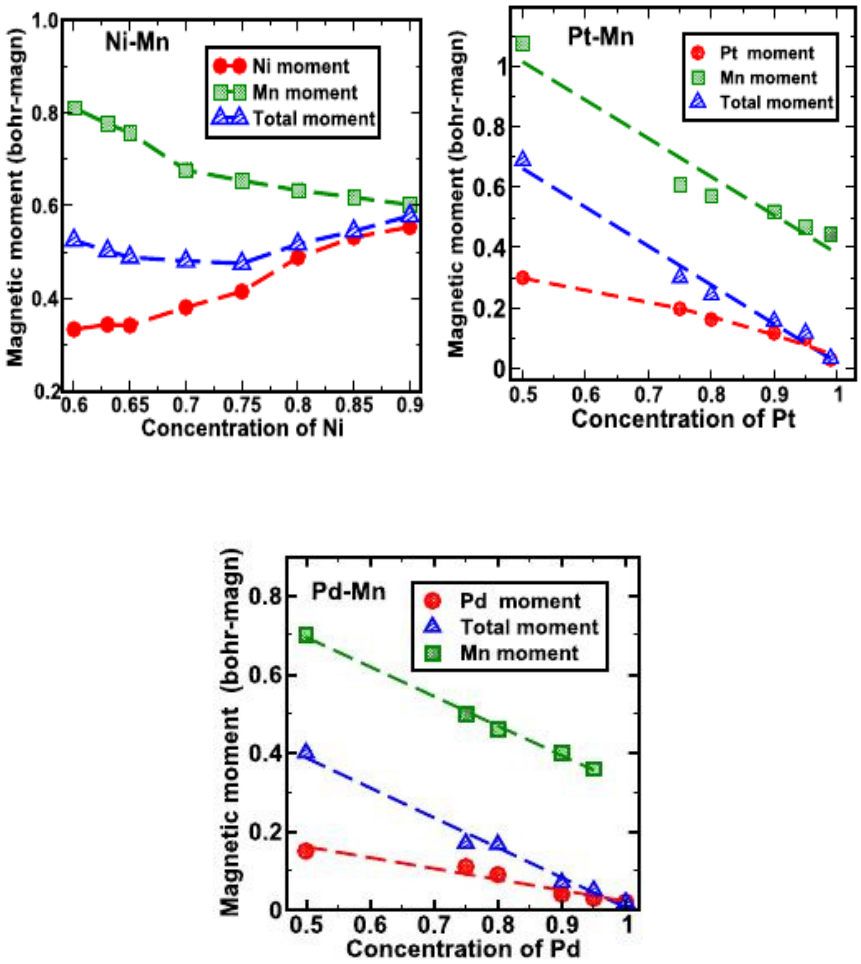

Figure 4.58: *Local magnetic moments in* $Ni_{1-x}Mn_x$,$Pd_{1-x}Mn_x$ *and* $Pt_{1-x}Mn_x$ *as functions of composition. While* $Pd_{1-x}Mn_x$ *and* $Pt_{1-x}Mn_x$ *behave similarly, with Mn polarizing Pt and Pd,* $Ni_{1-x}Mn_x$ *has a different trajectory. Ni moment is fragile and collapses with increasing dilution.*

overlap the Mn peaks considerably. In all such alloys the 1Q anti-ferromagnetic phase found to be most stable.

Fig.(4.58) shows the variation of the local and total magnetic moments per atom with composition. It is clear that qualitatively $Pd_{1-x}Mn_x$ and $Pt_{1-x}Mn_x$ behave in a similar manner, while $Ni_{1-x}Mn_x$ has a distinctly different behaviour. In $Ni_{1-x}Mn_x$, Ni is a ferromagnetic component with a fragile moment. As the Ni concentration decreases and the probability of Ni atoms being surrounded by Mn increases and the fragile Ni moment collapses. The moment on the Mn atom also decreases with Ni concentration increasing, but saturates at $0.3\mu_B$. In $Pd_{1-x}Mn_x$ and $Pt_{1-x}Mn_x$, the moments on the Mn atoms do decrease with increasing Pd and Pt concentrations. While the presence of Mn polarizes the Pd and Pt, so that they have induced magnetic moments. These are rather small, but not insignificant.

4.6.3 Magnetic ordering in the alloys

In order to study the magnetic phase diagram of the alloys, we should look for an effective Heisenberg model which describes the itinerant electron model we have already discussed. Such an effective model must be built up from our local spin density functional picture.(Oguchi, *et al.*, 1983, 1984, 1960) presented a calculation of the effective exchange parameters. (Lichtenstein, *et al.*, 2001) generalized this approach and derived a rigorous expression for the exchange coupling.

We have calculated the exchange energies using the Lichtenstein formula :

$$J^{\lambda\lambda'}(|\vec{R}-\vec{R}'|) = -\frac{1}{4\pi}\Im m \int_{-\infty}^{E_F} \sum_{LL'} \left\{ \delta^{\lambda}_{\vec{R}L}(E)\ G^{\lambda\uparrow\lambda\uparrow}_{\vec{R}L,\vec{R}'L'}(E)\delta^{\lambda'}_{\vec{R}'L'}(E)\ G^{\lambda'\downarrow\lambda'\downarrow}_{\vec{R}'L',\vec{R}L}(E) \right\}$$

where $\delta^{\lambda}_{\vec{R}L}(E) = P^{\lambda\uparrow}_{\vec{R}L}(E) - P^{\lambda\downarrow}_{\vec{R}L}(E)$ and $P^{\lambda\sigma}_{\vec{R}L}(E)$ is the LMTO 'potential' function $(E - C^{\lambda\sigma}_{\vec{R}L})/\Delta^{\lambda\sigma}_{\vec{R}L}$. This maps the itinerant magnetic problem onto a classical Heisenberg model :

$$H = -\frac{1}{2} \sum_{\lambda\lambda'=A,B} \sum_{\vec{R}\in\lambda} \sum_{\vec{R}'\in\lambda'} J^{\lambda\lambda'}(|\vec{R}-\vec{R}'|)\ \vec{\sigma}^{\lambda}_{\vec{R}} \cdot \vec{\sigma}^{\lambda'}_{\vec{R}'} \tag{4.8}$$

where $\vec{\sigma}^{\lambda}_{\vec{R}}$ is the familiar Heisenberg spin variable associated with an atom of the type Q. Figs. (4.59 and 4.60) show the exchange energies for $Pd_{1-x}Mn_x$ and $Pt_{1-x}Mn_x$ respectively. For both, the top left panels of the two figures show that all exchange energies are dominated by the Mn-Mn exchange energies $J^{\mathrm{MnMn}}(|\vec{R}-\vec{R}'|)$. The figures also show the behaviour of the exchange energies as functions of distance $(|\vec{R}-\vec{R}'|)$ for different compositions of the alloys. The bottom panels show the much smaller Pd-Mn/Pt-Mn and Pd-Pd/Pt-Pt exchange energies. The Pd-Pd/Pt-Pt exchange energies are negligibly small. This is consistent with the fact that the Pd/Pt partial DOS are hardly exchange split and carry negligible moment. At all compositions the variation of J^{MnMn} with distance exhibits exponentially decaying oscillatory (RKKY-like) behaviour characteristic in disordered alloys. Such an oscillatory behaviour leads to the possibility of frustrated Mn-edged plaquettes on the lattice. This frustration is essential for the occurrence of the spin-glass phase.

Fig.(4.59(a)) and Fig.(4.60(a)) show that at low Mn compositions the predominant nearest neighbour contribution to the transition temperature $ZJ^{\mathrm{MnMn}}(R_0)$ (where Z is the nearest neighbour coordination and R_0 the nearest neighbour distance) is anti-ferromagnetic and becomes more so as the concentration of Mn increases. However there is a saturation and a turn-round around 40-50% Mn concentration. Experiments show increase of T_N till 50% concentration of Mn followed by a downturn (Wasserman, 1982). We analyze the fluctuations in the far neighbour pair energies with distance by studying

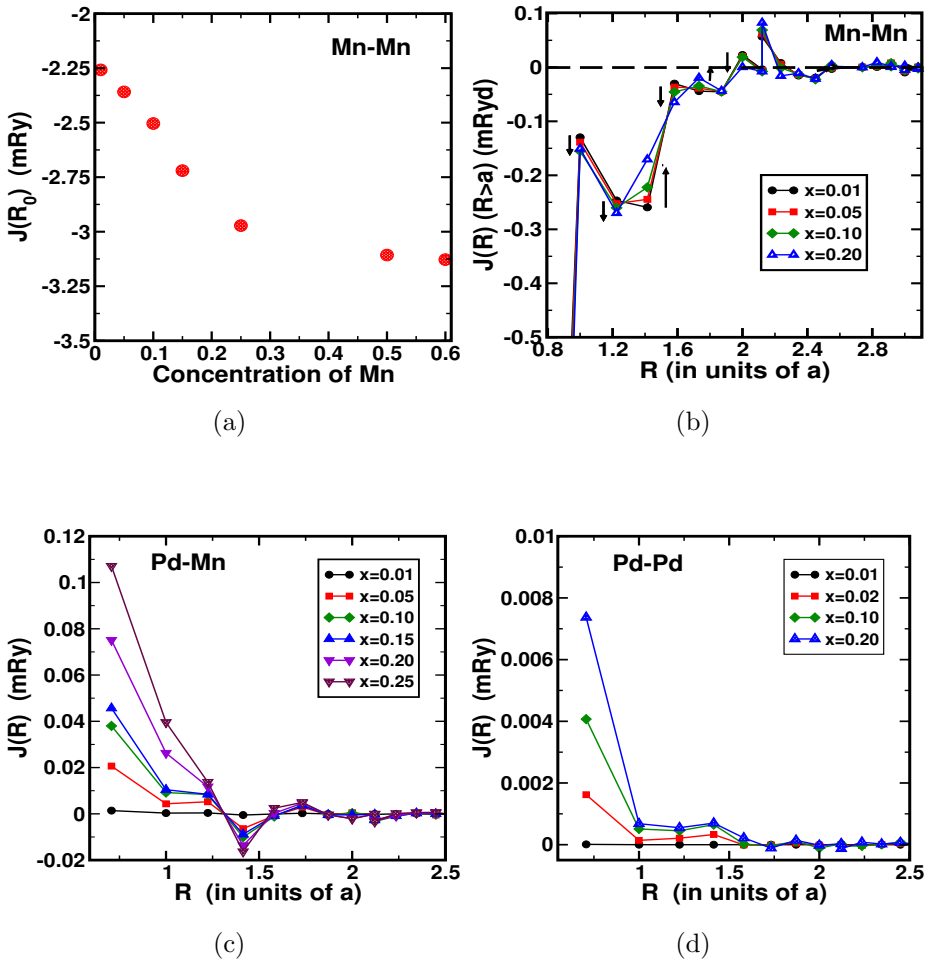

Figure 4.59: *Pair exchange energies for* $\mathrm{Pd}_{1-x}\mathrm{Mn}_x$ *alloys for different compositions as functions of distance. This behaviour gives us information about the possibility of frustration in the system. (a) The nearest neighbour* (R_0) *dominant Mn-Mn exchange energies as a function of composition (b) the Mn-Mn exchange energy as a function of lattice distance* $R > R_0$*. (c) Pd-Mn and (d) Pd-Pd exchange energies as functions of lattice distance R.*

the spatial moments M_1, M_2 and M_3 of J(R). In our case, the dominant contribution to these moments comes from the second to fourth nearest neighbor exchange energies. The moment M_1 measures the average contribution of the far-neighbours. This contribution is very slowly varying and still negative till 40% Mn then sharply becomes less negative. However, we note that contributions from the far-neighbours is completely dominated by the nearest neighbour contribution. We note that M_3 become less negative as Mn concentration increases. This indicates that the asymmetry of the further neighbour exchange energies towards negative values decreases with Mn concentration. Negative exchange leads to possibility of frustration, so the tendency of M_3 being more negative in the dilute Mn regime indicates a possibility of spin-glass phase at these compositions. Finally the decreasing M_2 indicates that with increasing Mn concentration, the fluctuations of the exchange energy with distance about its mean also decreases. At higher concentrations the net effect of these further neighbour energies becomes negligible. This detailed analysis of the behaviour of the exchange energies with distance and composition clearly shows that the earlier assertion that because of the ferromagnetic second nearest neighbor exchange energies, some second-neighbour ferromagnetic clusters in a disordered background was the origin of the ferromagnetic signatures in some composition ranges does not seem plausible. This 'ferromagnetism' of 'unknown origin' most probably arose from ordered Pt_3Mn clusters precipitated in the disordered background because of the way in which the samples were prepared. More careful experiments with annealing and homogenization need to be carried out to confirm this or otherwise.

Behaviour of $Ni_{1-x}Mn_x$ is rather different. $Ni_{1-x}Mn_x$ has been studied previously and described more detail in previous chapter.and we quote results from that work (Pal, *et al.*, 2012), Whereas Pt and Pd are themselves non-magnetic and usually attain induced magnetic moments on alloying, Ni has a fragile magnetic moment of its own. This moment is fragile, since if Ni gets surrounded by non-magnetic atoms on alloying, it tends to lose its magnetism altogether. Fig.(4.50) shows the exchange energies for $Ni_{1-x}Mn_x$ as functions of lattice distance R. As expected the Mn-Mn nearest neighbour exchange is negative leading to a tendency towards anti-ferromagnetism. As the concentration of Mn increases, as in the other two alloys the Mn-Mn nearest neighbour exchange becomes more negative. There is a sharp downturn around 40% Mn. The signatures of this downturn, though less sharp, is also seen in both $Pd_{1-x}Mn_x$ and $Pt_{1-x}Mn_x$. The positive second near neighbour exchange is also seen in $Pt_{1-x}Mn_x$, and quantitatively different from $Pd_{1-x}Mn_x$. The Ni-Ni nearest neighbour exchange decreases as the concentration of Mn increases. This is a signature of loss of magnetism by Ni, who magnetism is fragile. Now Ni-Mn exchange is no longer negligible. In fact Mn concentration boosts the Ni-Mn exchange coupling. In $Ni_{1-x}Mn_x$, because of the established ferromagnetic

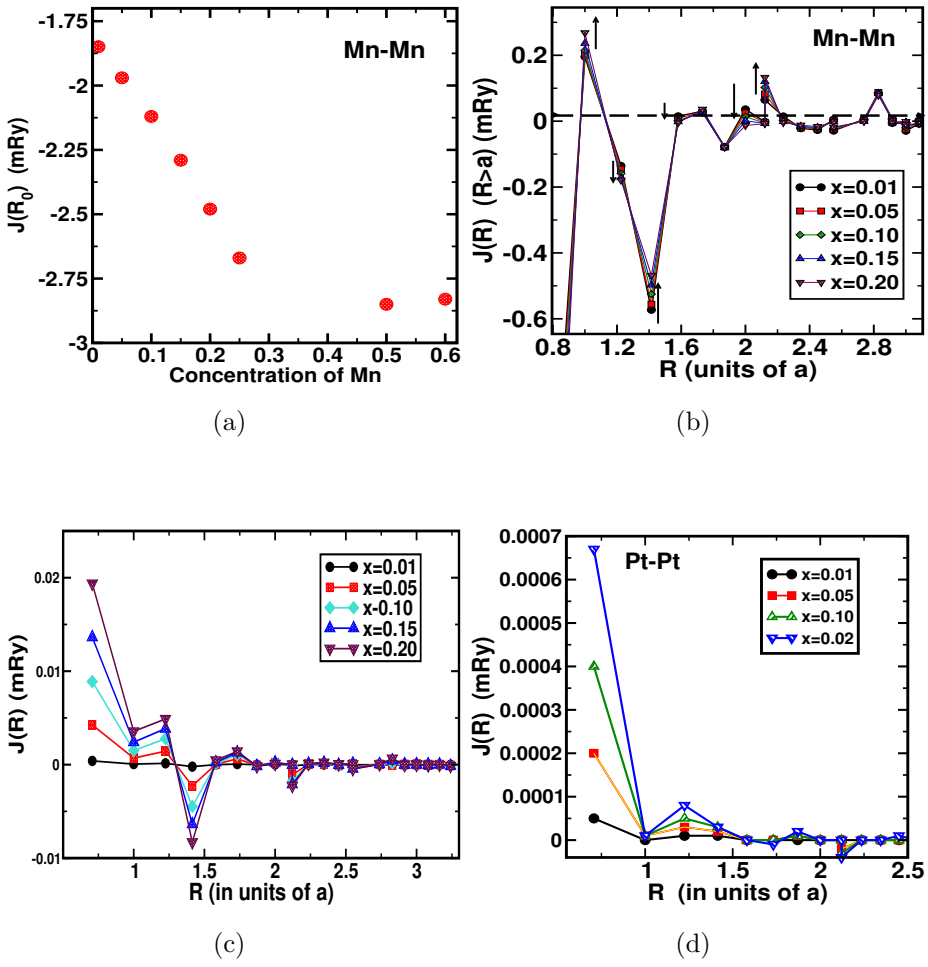

Figure 4.60: *Pair exchange energies for* $Pt_{1-x}Mn_x$ *alloys for different compositions as functions of distance. This behaviour gives us information about the possibility of frustration in the system. (a) The nearest neighbour* (R_0) *dominant Mn-Mn exchange energies as a function of composition (b) the Mn-Mn exchange energy as a function of lattice distance* $R > R_0$*. (c) The Pt-Mn and (d) Pt-Pt exchange energies as functions of lattice distance R.*

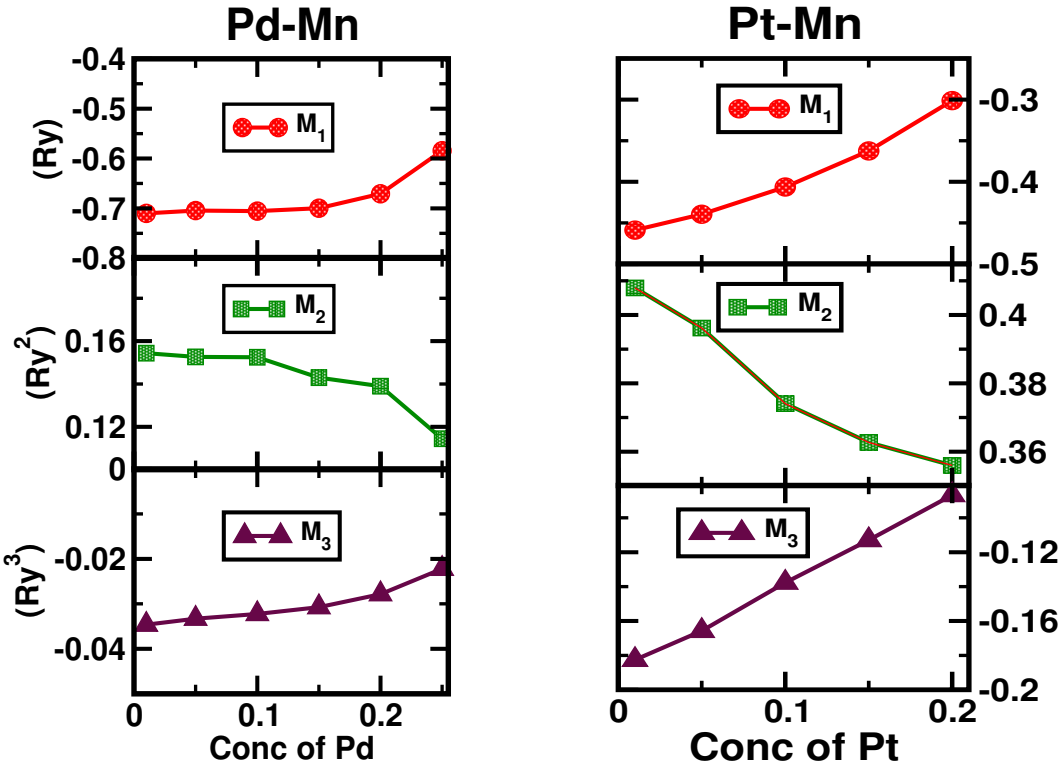

(a) (b)

Figure 4.61: *Spatial Moments of $J(R)$ for $R > R_0$ for $Pd_{1-x}Mn_x$ (a) and $Pt_{1-x}Mn_x$ (b). These moments give some idea of the fluctuations of $J(R)$ as functions of R.*

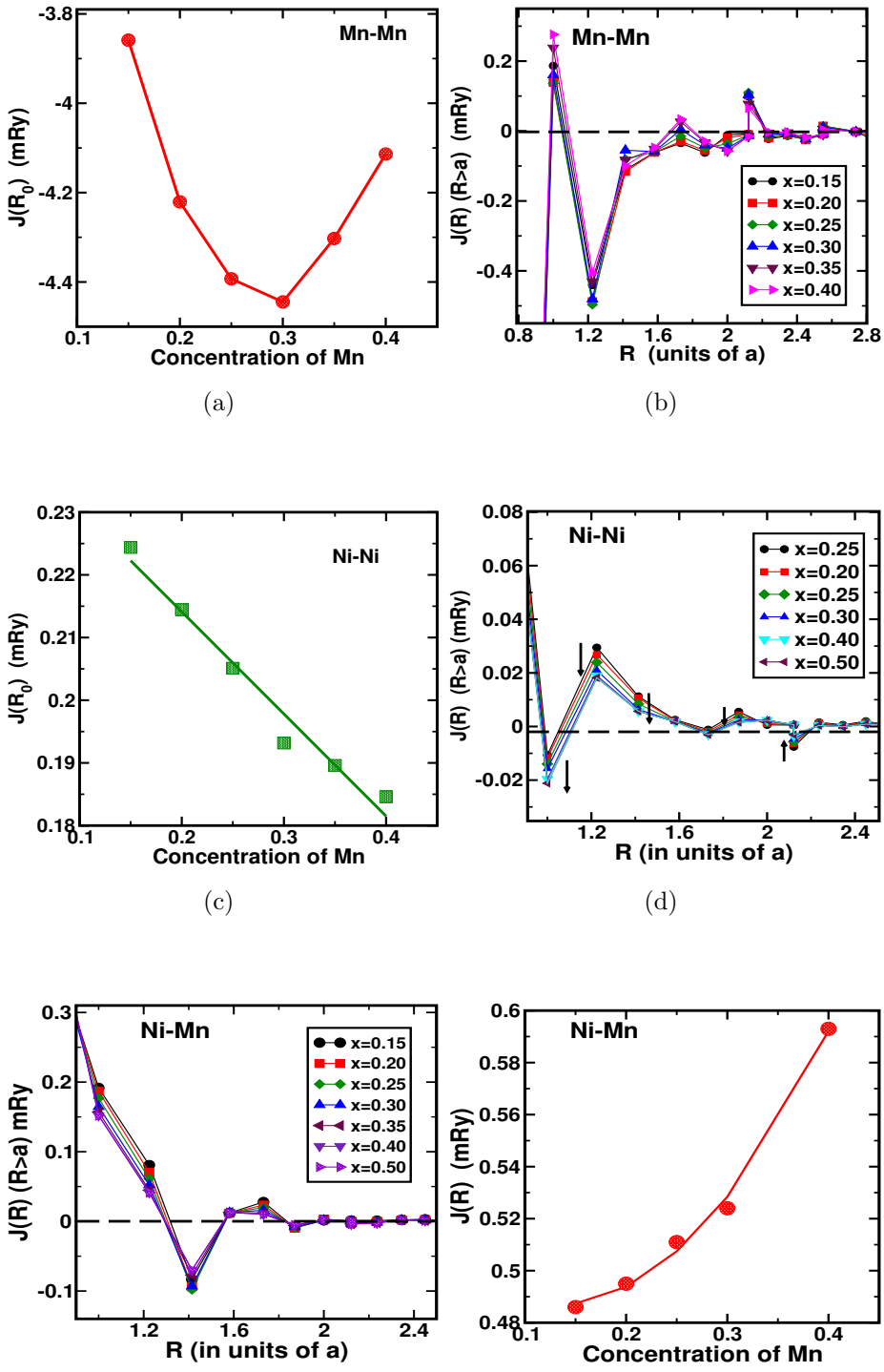

Figure 4.62: *Pair exchange energies for $Ni_{1-x}Mn_x$ alloys of different compositions as functions of distance. This behaviour gives us information about the possibility of frustration in the system. (a) the nearest neighbour (R_0) dominant Mn-Mn exchange energies as a function of composition; (b) the Mn-Mn exchange energy as a function of lattice distance$R > R_0$; (c) Ni-Ni nearest neighbour exchange; (d) Ni-Ni exchange as a function of the distance $R > R_0$; (e, f)bottom: the nearest neighbour Ni-Mn exchange and Ni-Mn exchange as a function of the distance $R > R_0$.*

Ni-Ni exchange, there is a transition from the antiferromagnetic phase. The reason for noting traces of ferromagnetism in $Pt_{1-x}Mn_x$ is, however, as discussed earlier, quite different.

4.6.4 Mean-field analysis of the magnetic phases

In ordered to analyze the magnetic phases the generalized perturbation expansion of the energy calculated from the previous section map to an effective Heisenberg model (equation (4.8)). For our alloy the dominant exchange coupling is negative and it is energetically favourable for nearest neighbour spins to anti-align. For the 1Q phase, the underlying lattice structure is bi-partite and can be separated into two inter-penetrating lattices labeled I and II. We rewrite the Hamiltonian as follows : whenever $\vec{R} \in$ I, $\vec{s}^{\lambda}_{\vec{R}} = \vec{\sigma}^{\lambda}_{\vec{R}}$, on the other hand if $\vec{R} \in$ II, $\vec{s}^{\lambda}_{\vec{R}} = -\vec{\sigma}^{\lambda}_{\vec{R}}$. Similarly if $\vec{R}$ and $\vec{R}'$ lie in different sub-lattices $\widehat{J}(|\vec{R} - \vec{R}'|) = -J(|\vec{R} - \vec{R}'|)$ otherwise they are the same. With this transformation we can rewrite the random Hamiltonian as follows :

$$H = -\frac{1}{2} \sum_{\lambda\lambda'=A,B} \sum_{\vec{R}\in\lambda} \sum_{\vec{R}'\in\lambda'} \widehat{J}^{\lambda\lambda'}(|\vec{R} - \vec{R}'|)\ \vec{s}^{\lambda}_{\vec{R}} \cdot \vec{s}^{\lambda'}_{\vec{R}'} \tag{4.9}$$

$\vec{s}^{\lambda}_{\vec{R}}$ are the local *staggered* magnetization order parameters and $\widehat{J}^{\lambda\lambda'}(|\vec{R} - \vec{R}'|)$ are the staggered exchange couplings.

The Free energy in the mean-field approximation is given by :

$$F = \frac{1}{2} \sum_{\lambda\lambda'=A,B} \sum_{\vec{R}\in\lambda} \sum_{\vec{R}'\in\lambda'} \widehat{J}^{\lambda\lambda'}(|\vec{R} - \vec{R}'|)\ \vec{m}^{\lambda}_{\vec{R}} \cdot \vec{m}^{\lambda'}_{\vec{R}'} - (1/\beta) \sum_{\lambda=A,B} \sum_{\vec{R}\in\lambda} \ln \mathrm{L}(\beta h^{\lambda}_{\vec{R}})$$

$\vec{m}^{\lambda}_{\vec{R}}$ is the thermal average $< \vec{s}^{\lambda}_{\vec{R}} >$, L(x) is the Langevin function and the *local random* staggered 'Weiss' field is given by :

$$\vec{h}^{\lambda}_{\vec{R}} = \sum_{\lambda'=A,B} \sum_{\vec{R}'} \widehat{J}^{\lambda\lambda'}(|\vec{R} - \vec{R}'|)\ \vec{m}^{\lambda'}_{\vec{R}'} \quad \text{and} \quad h^{\lambda}_{\vec{R}} = |\vec{h}^{\lambda}_{\vec{R}}| \tag{4.10}$$

Minimizing with respect to the local random order parameters we obtain a relationship between them and the local staggered 'Weiss fields' :

$$\vec{m}^{\lambda}_{\vec{R}} = (\vec{m}^{\lambda}_{\vec{R}}/m^{\lambda}_{\vec{R}}) \left[\frac{1}{\mathrm{L}(\beta h^{\lambda}_{\vec{R}})} \frac{\partial \mathrm{L}(\beta h^{\lambda}_{\vec{R}})}{\partial h^{\lambda}_{\vec{R}}} \right] = \vec{F}^{\lambda}_{\vec{R}}(\vec{h}^{\lambda}_{\vec{R}}) \tag{4.11}$$

In a random alloy the staggered Weiss fields at different sites are themselves random. We now proceed to calculate the probability distribution of these staggered Weiss fields using the Radon transform :

$$Pr(\{h_{\vec{R}}^{\lambda\mu}\}) = \sum_{\mathcal{C}} \mathcal{P}(\mathcal{C}) \prod_{\mu=x,y,z} \delta\left(\nu_{\vec{R}}^{\lambda\mu} - F_{\vec{R}}^{\lambda\mu}(\vec{h}_{\vec{R}}^{\lambda})\right)$$

where a *configuration* $\mathcal{C}$ is one in which the site $\vec{R}$ is occupied by an atom λ. Of the remaining $N-1$ sites, $N_1 - 1$ are occupied by λ randomly and $N - N_1$ by λ'. In the thermodynamic limit : $N \to \infty$, $N_1/N \to x_\lambda$ and $N_2/N \to x_{\lambda'}$, the concentration of the components.

We now follow the arguments of (Mookerjee & Roy, 1983), replace delta functions by their configuration averages and obtain in the thermodynamic limit :

$$Pr(\{h_{\vec{R}}^{\lambda\mu}\}) = \frac{1}{2\pi} \int d\vec{k} \exp\left[i\vec{k} \cdot \vec{h}_{\vec{R}}^{\lambda} - \sum_{\lambda} x_\lambda F^\lambda(\vec{k})\right]$$

where :

$$F^\lambda(\vec{k}) = \sum_{\vec{R}'} \int d\vec{h}_{\vec{R}'}^{\lambda} Pr(\{h_{\vec{R}'}^{\lambda\mu}\}) \left[1 - \exp\left(-i\widehat{J}^{\lambda\lambda'}(|\vec{R} - \vec{R}'|)\vec{k} \cdot \vec{F}_{\vec{R}}^{\lambda}(\{h_{\vec{R}'}^{\lambda'}\})\right)\right]$$

This is a complicated non-linear integral equation. However, in case the scaled moments $\tilde{M}_n = \sum_R \left(\widehat{J}^{\lambda\lambda'}(R)/\widehat{J}^{\lambda\lambda'}(R_0)\right)^n$ decrease rapidly with n, we can expand the exponential in the definition of F_1 and F_2 and neglect all $\tilde{M}_n \geq 3$. The probability densities then turn out to be Gaussian with negligible asymmetry and kurtosis.

$$Pr(\{h_{\vec{R}}^{\lambda\mu}\}) = P_0 \exp\left[-(h_{\vec{R}}^{\lambda\mu} - J0^{\lambda\mu})(2K1_{\mu\nu}^{\lambda})^{-1}(h_{\vec{R}}^{\lambda\nu} - J0^{\lambda\nu})\right] \tag{4.12}$$

where,

$$\begin{aligned} m_\mu^\lambda &= \int s_{\vec{R}}^{\lambda\mu}(\{h_{\vec{R}}^{\lambda\mu}\})\ Pr(\{h_{\vec{R}}^{\lambda\mu}\})\ \Pi dh_{\vec{R}}^{\lambda\mu} \\ q_{\mu\nu}^\lambda &= \int s_{\vec{R}}^{\lambda\mu}(\{h_{\vec{R}}^{\lambda\mu}\}) s_{\vec{R}}^{\lambda\mu}(\{h_{\vec{R}}^{\lambda\nu}\})\ Pr(\{h_{\vec{R}}^{\lambda\mu}\})\ \Pi dh_{\vec{R}}^{\lambda\mu} \end{aligned} \tag{4.13}$$

$$\begin{aligned} J0_\mu^\lambda &= x_\lambda m_\mu^\lambda \sum_{\vec{R}} \widehat{J}^{\lambda\lambda}(\vec{R}) + x_{\lambda'} m^{\lambda'} \sum_{\vec{R}} \widehat{J}^{\lambda\lambda'}(\vec{R}) \\ J1_{\mu\nu}^\lambda &= x_\lambda q_{\mu\nu}^\lambda \sum_{\vec{R}} \left(\widehat{J}^{\lambda\lambda}(\vec{R})\right)^2 + x_{\lambda'} q_{\mu\nu}^{\lambda'} \sum_{\vec{R}} \left(\widehat{J}^{\lambda\lambda'}(\vec{R})\right)^2 \end{aligned} \tag{4.14}$$

If U is a unitary matrix that diagonalizes $q_{\mu\nu}^\lambda$, i.e.

$$\sum\sum\ U_{\mu\xi}^T q_{\xi\chi}^\lambda U_{\chi\nu} = q_\mu^\lambda \delta_{\mu\nu}$$

and

$$K1_{\mu\nu}^\lambda = \sum\sum\ U_{\mu\xi}^T J1_{\xi\chi}^\lambda U_{\chi\nu} = q_\mu^\lambda \delta_{\mu\nu}$$

We use the equations (4.10), (4.11) and (4.12) to get the phases : The phase boundaries can be obtained by expanding equation(5.11) for small m^λ and q^λ (Mookerjee & Roy, 1983). The possible phases are charactrized by :

(i) $m_z = m_x = m_y = 0, q_\parallel = q_\perp = 0$ this is the random paramagnet.

(ii) $m_z = m_x = m_y = 0, q_\parallel = q_\perp \neq 0$ this is the spin glass phase.

(iii) $m_z = m, m_x = m_y = 0, q_\parallel \neq 0, q_\perp = 0$ this is the random antiferromagnet

(iv) $m_z = m, m_x = m_y = 0, q_\parallel \neq 0, q_\perp \neq 0$ this is the random mixed phase.

After using the above mentioned phase boundaries, we found the phase diagram follows qualitatively to experiment. Actually all the values of temperature are found to be higher than experiment which is expected in a simple mean-field approach because the actual transition temperatures are overestimated in mean field approach. Fig.(4.63(a)(b)(c)) show the mean field phase diagrams for the three alloys. As expected, the diagrams for PdMn and PtMn are qualitatively similar. In both cases, Pd and Pt carry a very small moment and the Pd-Pd and Pt-Pt exchange energies are negligible. The phase diagram follows the generic case of AuFe, with the spin-glass phase at low Mn concentrations and anti-ferromagnet for high Mn concentrations. For NiMn however, the phase diagram is different with random ferromagnet and antiferromagnet flanking either side (both Mn as impurity or Ni). The spin-glass phase stretches from 0.1 to 0.3 concentration of Mn. The NiMn phase diagram qualitatively agrees with experiment (Pal, *et al.*, 2012), while the other two also follows whatever experimental data are available and which we have talked about in the Introduction and literature review sections. If we compare our PtMn Phase diagram with the experimental results of (Wasserman, 1982) and (Kren, *et al.*, 1968), on which the low temperature spin-glass/cluster-glass regime stretches from 0 to 25% Mn concentration with a tri-critical point at 15% Mn and T=$50K$. Our findings show a low temperature spin-glass phase stretching from 0 to 20% Mn concentrations which is comparable to experiment. Our single-site mean-field approximation cannot study effect of clusters. The tri-critical point sits around 10% Mn concentration and T=$200K$. Such an over estimation of the tri-critical temperature is not unusual in a simple mean-field estimation. T_N at 40% Mn concentration was 800K experimentally (Wasserman, 1982) while our estimate is around $1000K$. In case of Pd-Mn SG phase stretches from 0.0 to 0.17 atomic concentration of Mn with tri-critical points around $200K$ around 7% atomic concentration of Mn. Though Our approximation is good for the analysis of spin glass systems, we encourage the reader/researcher to go beyond the mean field picture and spin dynamics analysis for the detail study of spin glass behavior

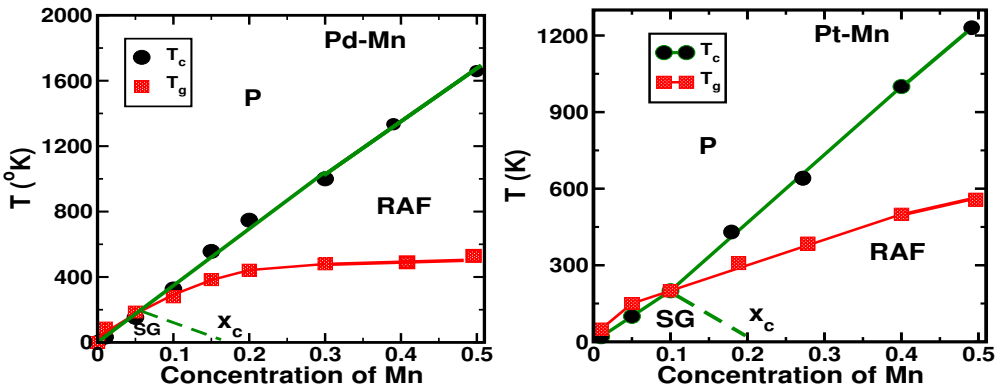

(a) (b)

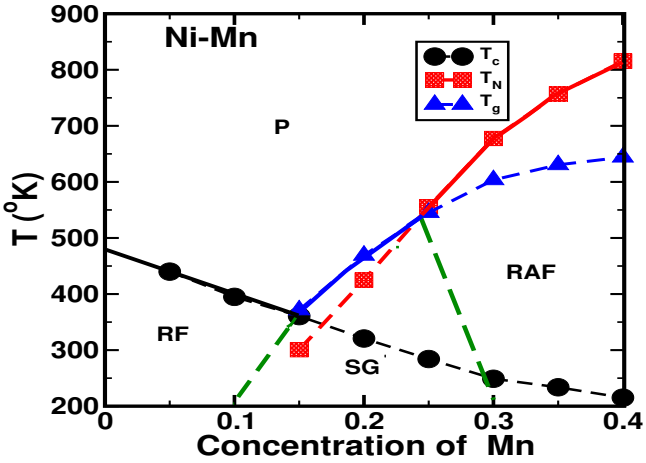

(c)

Figure 4.63: *The mean-field phase diagrams for (a)* $Pd_{1-x}Mn_x$ *and (b)* $Pt_{1-x}Mn_x$ *. The phase diagrams are very similar for both alloys with a spin-glass phase for low concentrations of Mn and anti-ferromagnets for high Mn concentrations. The mean field approach does not hold for very low concentrations of Mn. So the characteristic very low Mn concentration ferromagnetism in* $Pd_{1-x}Mn_x$ *(*$x < 0.02$*) does not show up in these figures.(c) mean-field phase diagrams for* $Ni_{1-x}Mn_x$ *.*

of systems. Finally, Our theoretical calculations show that there is spin glass behavior in PtMn/PdMn and NiMn systems as predicted by experiments.

CHAPTER 5

CONCLUSIONS AND RECOMMENDATIONS

We have studied the properties of pristine clusters, clusters with doping, adsorption and dissociation properties as well as bulk properties, as explained in previous chapter. The effective conclusions drawn from our study are presented follows.

5.1 Structural electronic and magnetic properties of Pd_n, $Pd_{n-1}Mn$ and $Pd_{n-2}Mn_2$ clusters

First, we study the structural, electronic and magnetic properties of pristine Pd_n clusters. The structural evolution, electronic and magnetic properties are also observed. The effect in structure, electronic and magnetic properties after doping the mono and bi-dop of Mn atoms and origin of magnetism are also studied. From the study, we found many interesting features regarding structural, electronic and magnetic properties of Pd_n (n=1-19), $Pd_{n-1}Mn$ and $Pd_{n-2}Mn_2$ up to 13 atom clusters which are summarized as follows :

(i) We found four types of structural growth patterns (i) fcc based (ii) octahedron based and (iii) icosahedron based and (iv) buckled bi-planer from the present study. Out of them the icosahedral structure found to be most stable for 13-atom atoms clusters. The higher clusters do not follows the exact trends. However, Pd_{19} bears fcc like structure. In the bi-doped 13 atom clusters, two Mn atom aligned anti-ferromagnetically in the icosahedral structure, while the buckled bi-planar has a ferrimagnetic Mn spin alignment. The latter, therefore has a higher total magnetic moment than the former.

(ii) The transition from two dimensional structures to three-dimensional is found between cluster sizes 4, 5 and 6 for pristine and mono-doped Pd, and between 5 and 6 for Pd_nMn_2.

(iii) The average binding energy/atom of the clusters increases with increasing the clusters size and tends towards the bulk cohesive energy.

(iv) The average binding energies of both icosahedral, octahedron and fcc based structures are comparable to that of closed packed "irregular" clusters at n = 13, indicating that transition from 'irregular' structures to the icosahedral and fcc-like structures could occur at smaller cluster sizes.

(v) The binding energy per atom and the average bond length of Pd-Pd and Pd-Mn clusters and Bader charges are interlinked with each other. In general binding energy increases with bond length monotonically.

(vi) The results of dissociation and second differences and the binding energy show that clusters of atoms 2, 8, 13, 18 in Pd_n are clearly found to be more stable than their neighborhoods. The magic number effect is effectively applicable in pristine Pd clusters. The results of HOMO-LUMO gap shows that Pd_nMn clusters are chemically more reactive than others.

(vii) Present calculations show that high symmetry, always does not guarantee success when used as a starting point criteria in the search of minimum energy configurations. It is better to carry out unconstrained optimization.

(viii) A trend of larger magnetic moments with increasing size were not followed but magnetic moment shows odd-even alternation The magnetic moment was found to be varies from $(4.58 - 9.64)\mu_B$ and $(2 - 12.52)\mu_B$ after doping Mn and Mn_2 on pristine Pd clusters respectively.

(ix) Overall clusters structure does not change after doping with one or two Mn atoms. The lowest-energy structure of $Pd_{n-1}Mn$ and $Pd_{n-2}Mn_2$ are also similar to that of Pd_n clusters. The magnetic moment of Mn decreases as clusters size increases. This is mainly due to transfer of charge from Mn to Pd and hybridization parameters. There is an intimate relationship between Pd-Pd and Pd-Mn bond lengths; alignment of up and down spin moments and hybridization according to which increasing and decreasing of net magnetic moments of the system occurs.

5.2 Adsorption and dissociation of N_2 and H_2 molecules on tantalum and niobium clusters

The dissociation of nitrogen is very much useful to synthesis the ammonia, which is one of the mostly used fertilizer in world and dissociation of hydrogen is interesting for the use of hydrogen fuel in future. We carried out the dissociation and /or adsorption of hydrogen and/or nitrogen molecules on small Ta_n and Nb_n (n = 2-7) clusters. We

used VASP code to evaluate the optimization energy, spin multiplicity and Bader charge analysis for charge transformation. We found interesting results from the present study which are concluded as follows,

(i) The binding energy per atom of Nb_nH_2, Nb_nN_2, Ta_nH_2 and Ta_nN_2 clusters follows the same trends of binding energy of pure Nb and Ta clusters. Binding energy increases towards the bulk as increases the cluster size.

(ii) Our finding show that H_2 and N_2 absorbed in molecular form with slightly higher H-H and N-N bond lengths by single Ta and Nb atoms. Beyond that H_2 and N_2 found to be dissociate on the small Nb_n and Ta_n clusters (n = 2-7) and it is also found that H_2 and N_2 prefer to adsorb on the edge site such that two hydrogen (or Nitrogen) atoms on the clusters were in two neighboring sites.

(iii) The charge transformation ratio is found to be constant for all the clusters system but amount of charge transformed from Nb-H and Ta-H are lesser than Nb-N and Ta-N, which also reflects from the charge density plot.

(iv) The Nb and Ta clusters can be used as a catalyst for the hydrogen storage purpose because hydrogen is found to be favor dissociative property.

(v) The Nb and Ta clusters can be used as catalysts for the reaction which requires dissociation of hydrogen and nitrogen as in the synthesis of ammonia.

5.3 Electronic and magnetic properties of different morphologies of 3d transition metal doped ZnO

There is lack of systematic study of sheet, nanotube and fullerene like structures in ZnO clusters and TM doped on it. We perform both PBE and HSE calculations in ordered to find out the magnetic behavior as well as band gap properties using VASP. In this study, we restrict up to 48 atoms clusters to perform the electronic and magnetic properties of pristine and doping effect of TMs in three morphologies. This is mainly due to computational cost and lack of experimental results. The main conclusions drawn from the present study is listed in item wise as follows,

(i) Present study showed that ZnO:Mn always favors the near dop AFM alignment in all three morphologies. In case of ZnO:X (X = Fe, Co, Ni), the AFM alignment favors for sheet and this alignment changes while moving sheet to fullerene like structure.

(ii) We observed from the symmetrical distribution of DOS by up and down spin in case of AFM and asymmetrical distribution of spin up and down near the fermi level in case of FM.

(iii) Due to the above reason we predict that ZnO:(Co, Mn) materials would not be the suitable candidates for spintronics. This result supports Spaldin's at which he reported that robust FM can't occur in Mn or Co doped ZnO.

(iv) In case of ZnO:Cu we found FM behavior in sheet and tube this may be due to hybridization between Cu-3d and O-2p electrons.

(v) Since, PBE always underestimate the band gap of metal oxides. We also performed hybrid functional (HSE06) for magnetism and band gap. The nature in magnetic moments does not change after the inclusion of HSE. We found the drastic change in band gap as we moved from PBE to HSE calculations.

(vi) From HSE calculations, we predict that ZnO based nanostructures and TM doped on it can be used for flat screen displays, field emission sources, gas, chemical and biological sensors and as ultraviolet light emitters and switches etc. as well as some of other applications like piezoelectric and spintronics devices. It is because doped TMs shows higher BE and ferromagnetic behaviour in most of the cases. The variation of band gap also plays an important role in above mentioned properties.

5.4 Magnetic ordering in Ni-rich NiMn alloys around the multi-critical point

The magnetic behaviour of Ni-rich Ni-Mn alloys are studied both experimentally as well theoretically. In ordered to performed the experiment we prepared six samples of $Ni_{1-x}Mn_x$ at different concentrations. The magnetic phase diagram also drawn after calculation of MM at various concentrations of Mn according to the sample. We found interesting results which are pointed out in figure as follows.

(i) We conclude from a detailed experimental magnetic study of several disordered $Ni_{1-x}Mn_x$ alloys that the spin-glass-like state in these alloys below T_{fg} has a spontaneous (FM) moment. This moment decreases slowly with rising temperature and merges smoothly with the spontaneous moment of the FM state at the multi-critical point (MCP) around 25 at.% Mn.

(ii) The existence of the re-entrant SG phase, a canonical SG phase, and the onset of an anti-ferromagnetic phase around 37 at % Mn is also conformed.

(iii) We found ferromagnetic LRO with re-entrant spin-glass (RSG)/ferro-spin-glass (FSG) phase for $x = 25$, an anti-ferromagnetic LRO around $x = 37$, and a gradual change from a canonical spin-glass state (which is nothing but a short-range anti-ferromagnet) to a long-range AF phase in the intermediate composition region.

(iv) A first-principles density functional based theory predicts magnetization, as a function of composition, in good agreement with experiment.

(v) The spin-glass transition is a dynamic freezing of spin degrees of freedom, we studied magnetization relaxation using a LLG formalism and observed that in the composition range where experiment observes spin-glassy behavior, we also see anomalously slow relaxation of magnetization to support such behavior.

5.5 Spin glass behavior of disordered Pt-Mn, Pd-Mn and Ni-Mn alloys: an augmented space recursion approach

We study the electronic and magnetic properties of $Pd_{1-x}Mn_x$, $Pt_{1-x}Mn_x$ and $Ni_{1-x}Mn_x$ using non-collinear form of TB-LMTO-ASR technique which is extremely use full for the calculation of electronic structure properties like CPA technique. This new package not only takes into account short-ranged ordering and local lattice relaxations. It can also study non-collinear magnetic phases and incorporate spin-orbit coupling. In its application this turned out to be eminently successful : giving us electronic, structural, statistical and magnetic properties of all three alloys. In each of these areas, our conclusion is that PtMn and PdMn belong to a similar behavioral class, while NiMn belongs to a different category. This is evident also in their phase diagrams which we have obtained via a mean-field theory. The over all conclusions are summarized as follows,

(i) We conclude that the magnetic moments changes i.e. found to be decrease as composition of Mn increase for the particular concentration ranges from 0.01- 0.25 % of Mn in PdMn and PtMn systems, which can clearly shown total up and down s-d moments from PDOS graphs.

(ii) The exchange interaction graph clearly indicates that there is RKKY types oscillation with respect to position co-ordinates and found to be ferromagnetic exchange interaction in case of Pt-Mn systems whereas anti-ferromagnetic interaction in case of Mn-Mn systems. From this we can easily analyze that there should be certain spin-glass phase obtained by competition of FM and AFM spins. Means it is easier to predict that there will be spin glass nature within this composition range. The pd-Pd and Pt-Pt has negligible role in exchange interactions.

(iii) We mapped our results of J_{ij} to ising model, present magnetic phase diagram for PtMn agrees qualitatively with experimental results of Wasserman, Auwärter and Kussmann and a Kren. Experimentally the low temperature spin-glass/cluster-glass regime stretches from 0 to 25% Mn concentration with a tri-critical point at 15% Mn and $T = 50K$. Our findings show a low temperature spin-glass phase stretching from 0 to 20% Mn concentrations which is comparable to experiment. Our single-site mean-field approximation cannot study effect of clusters. The tri-critical point sits around 10% Mn concentration and $T = 200K$. Such an over estimation of the tri-critical temperature is not unusual in a simple mean-field estimation. T_N at 40% Mn concentration was $800K$ experimentally while our estimate is around $1000K$. This indicates that the ferromagnetic properties comes from the unknown origin as experiment from 20% of Mn in PtMn system.

(iv) In case of $Pd_{1-x}Mn_x$, low temperature spin-glass/cluster-glass regime stretches from 0 to 17% Mn concentration with a tri-critical point at 8% Mn and $T = 150K$. slightly lower than $Pd_{1-x}Mn_x$.

(iv) The case of $Ni_{1-x}Mn_x$ is different from other two, on which random FM and AFM flaking eitherside(from both Mn as impurity or Ni). The spin-glass phase stretches from 10% to 30% of Mn. This phase is exactly resembles with experiment and Montecarlo techniques Two tri-critical points are found to be within$350K$ and $550K$.

To strengthen the research capability of university and nation on the important area of physics there should be encouragement and support from the government side, private sector as well as concern community to develop well equipped lab and research environment. So that we can perform complex calculations like spin glass systems, higher clusters and nanosystems to go more insight into their properties.

CHAPTER 6

SUMMARY

In the present thesis, we have studied and analyzed the structural, electronics and magnetic properties of pristine Pd_n clusters, clusters with doping effect, adsorption and dissociation behavior of hydrogen and nitrogen molecules on Ta_n and Nb_n clusters, Nanosystems (Pristine ZnO and TM doped on it) and disordered binary alloys. We used VASP for the first principles study of pristine clusters, clusters with doping effects and nanosystems and TBLMTO-ASR code for the analysis of disordered binary alloys. The major and important achievements from the present study are summarized in point wise as follows.

1. We have discussed structural, electronic and magnetic properties of pristine Pd_n clusters with $n \leq 19$ and the mono and bi-dop of Mn atom on Pd_n clusters up to $n = 13$ atoms. We have taken four types of structural configurations like Icosahedral, Buckle Bi-Planner, Hexagonal close-packed and cube-octahedral, as a base. All the other clusters $n \leq 13$ are the derivatives of them. We have optimized maximum possible structures and analyzed most stable one. The computational details and some theory related to calculate the binding energy and stability is given in Appendix-I. From the present study, we concluded that 13-atom Icosahedral structure are most favorable compare from all the cases and magnetic moment enhanced up to $12\mu_B$ after doping Mn on pristine Pd_n clusters. It is also observed that AFM Pd_nMn_2 favors the stable structure than FM Pd_nMn_2. For the analysis purpose, we have chosen randomly the different kinds of structures and picked most stable on for the calculation throught the study (see section (4.2.1)). From the study it is found that there is direct relationship between MM and bond length. in pristine as well as doped case. Pristine Pd_n clusters follows the magic numbers strictly.

2. We have discussed adsorption and dissociation of Hydrogen or nitrogen molecules on Ta_n and Nb_n (n = 1-7)clusters. The computational detail for the calculation of binding energy dissociation energy and spin gaps are explained in Appendix-I. In this case we have analyzed structural as well as chemical stability, which was done by the

study of charge transformation, binding and chemisorption energy as well as HOMO-LUMO gap analysis. From the present analysis it is observed that Ta and Nb clusters can be used as catalyst for the dissociation of hydrogen and nitrogen molecules which is necessary for the synthesis of ammonia. It is also concluded that Ta and Nb nanostructures may be used for the hydrogen storage materials. This will be the important task for future generation. We found hydrogen and nitrogen both dissociates on Ta_n and Nb_n (n = 2-7) clusters

3. We performed both PBE and HSE calculations in ordered to find out the magnetic behavior as well as band gap properties using VASP on ZnO nanosystems with different Morphologies The different morphologies are Nanosheet, Nanotube and Fullerene type structure in pristine case and after doping of TM elements (Mn, Fe, Co, Ni and Cu) on pristine ZnO. We restrict our problem up to 48 atoms clusters of different morphologies. Present study showed that ZnO:Mn always favors the near dop AFM alignment in all three morphologies. In case of ZnO:X(X=Fe, Co, Ni), the AFM alignment favors for sheet and this alignment changes while moving sheet to fullerene like structure. Same kinds of feature can be observed from the symmetrical distribution of DOS by up and down spin in case of AFM and asymmetrical distribution of spin up and down near the fermi level in case of FM. Due to the above reason we predict that ZnO:(Co, Mn) materials would not be the suitable candidates for spintronics. This result supports Spaldin's at which he reported that robust FM can't occur in Mn or Co doped ZnO. In case of ZnO:Cu we found FM behavior in sheet and tube this may be due to hybridization between Cu-3d and O-2p electrons. Since PBE always underestimate the band gap of metal oxides. We also performed hybrid functional (HSE06) for magnetism and band gap. The nature in magnetic moments does not change after the inclusion of HSE. We found the drastic change in band gap as we moved from PBE to HSE calculations. From HSE calculations, we predict that Zno based nanostructures and TM doped on it can be used for flat screen displays, field emission sources, gas, chemical and biological sensors, ultraviolet light emitters and switches etc. as well as some of other applications like piezoelectric and spintronics devices.

4. Next, we have discussed electronic and magnetic properties of disordered NiMn experimentally as well as theoretically. In this case we used ScASR code and used $Ni_{1-x}Mn_x$ at different concentrations like 15%, 20%, 25%. 30%, 35% and 37% of Mn by atom. For that we used lattice parameters $3.572A^0$, $3.583A^0$, $3.595A^0$, $3.615A^0$, $3.654A^0$ and $3.670A^0$ respectively which is obtained from XRD analysis. We have analyzed electronic as well as magnetic properties and compare theoretical and ex-

perimental work done by us. It is observed that our theoretical and experimental phase diagram exactly matched with phase diagram of Montecarlo calculations. This also indicates that present scASR code is extremely useful for the study electronic and magnetic properties of binary disordered alloys. Spin dynamics relaxation through LLG spin dynamic code also supports our experimental result.

5. We studied the electronic and magnetic behavior of disordered Pt-Mn, Pd-Mn and Ni-Mn alloys. For this, we used non-collinear version of TB-LMTO-ASR for the electronic and magnetic properties as well as LMTOGF based on CPA code for the exchange pair interaction. We found SG behaviors in all the three systems. Exchange coupling are found to be same for former two system i.e PM to AFM where as for the latter case it is found PM to FM up to 25% Mn and RAFM to PM around 37% Mn. The phase diagram are more or less comparable to experimental one or previously predicted results. This also provides the validity of non-collinear form of TB-LMTO-ASR code for the electronic and magnetic properties.

6. Though Our approximation(TB-LMTO-ASR) is good for the analysis of spin glass systems, we encourage the reader/researcher to go beyond the mean field picture and spin dynamics analysis for the detail study of spin glass behavior of systems. Finally Our theoretical calculations show that there is spin glass behavior in PtMn, PdMn and NiMn systems as predicted by experiments.

Finally, as mentioned in the quotation from acknowledgment that it is only the beginning. It opens new ideas and encourages us to do more in the field of electronic calculations. The work on density functional theory(DFT) and time dependent density functional theory (TDDFT) has to be extended using VASP, Wein2K, QE and LMTO-ASR for perovskite, Half-metallic, Superconducting and Semiconducting materials for electronic, magnetic and optical properties as well as hydrogen storage systems. Further, extension of TB-LMTO-ASR code for ternary alloys and oxide materials are equally challenging field for the new researchers.

REFERENCES

Abdul-Razzaq, W., & Kouvel, J. S. (1987). Magnetic phase diagram of disordered Ni-Mn near the multicritical point. *Phys. Rev. B* **35**, 1764.

Aguilera-Granja, F., Redriguez-lopez, J. L., Michaelian, K., & Berlanga-Ramirez, E. O., Vega, A. (2002). Structure and magnetism of small rhodium clusters. *Phy. Rev. B* **66**, 224410.

Ahmadi, T. S., Wang, J. L., Green, T. C., Henglein, A., & El-sayed M. A.(1996). Shape controlled synthesis of colloidal platinum nanoparticles. *Science* **272**, 1924.

Ahmed, F., Kumar, S., Arshil, N., Anwar, M. S., Koo, B. H. (2012). Morphological evolution between nanorods to nanosheets and room temperature ferromagnetism of Fe-doped ZnO nanostructures. *CrystEngComm* **14**(11), 4016.

Aitken, R. G., Cheung, T. D., Kouvel, J. S., & Hurdequint H. (1982). Transitions between spin-glass and ferromagnetic (or related) states in disordered Ni-Mn alloys. *J. Magn. Mag. Mater* **30**, L1.

Alonso J. A.(2000). Electronic and Atomic Structure, and Magnetism of Transition Metal Clusters. *Chem. Rev.* **100**, 637.

Andersen O. K. (1975). Linear methods in band theory. *Phys. Rev. B* **12**:3060.

Andersen, O. K., & Jepsen O. (1984). Explicit, First-Principles Tight-Binding Theory. *Phys. Rev. Lett* **53**, 2571

Andersen, O. K., & Kasowski, R. V.(1971). Electronic states as a linear combination of muffin-tin orbitals. *Phys. Rev. B* **4**(4), 1064 .

Anderson, P. W., Halperin, B. I., Varma C. M.(1972). Anomalous low-temperature thermal properties of glasses and spin glasses. *Philos. Mag.* **25**, 1-9.

Anisimov, V. I., Aryasetiawan, F., & Lichtenstein A. I. (1997). First-principles calculations of the electronic structure and spectra of strongly correlated systems: the LDA+U method. *J. Phys.: Condens. Matter* **9**, 767.

Anisimov, V. I., Zaanen, J., & Andersen, O. K. (1991). Band theory and Mott insulators: Hubbard U instead of Stoner I. *Phys. Rev. B* **44**, 943.

Antropov, V. P., Harmon, B. N., & Smirnov A. N.(1999). Aspects of spin dynamics and magnetic interactions. *J. Magn. Magn Mater.* **200**, 148.

Ashcroft, N .W., & Mermin, N. D.(1976). *Solid State Physics*. Harcourt College Publishers.

Banerjee, R., & Mookerjee, A. (2010). Augmented space recursion code and application in simple binary metallic alloy. *Int. J. Mod. Phys. C* **21**(2), 205.

Bansmann, J., Baker, S. H., Binns, C., Blackman, J. A., Bucher, J. P., Dorantes-D avila J., Dupuis, V., Favre, L., Kechrakos, D., Kleibert, A., Meiwes-Broer, K. H., Pastor, G. M., Perez, A., Toulemonde, O., Trohidou, K. N., Tuaillon, J., Xie, Y. (2005). Magnetic and structural properties of isolated and assembled clusters. *Surface science Rep.* **56**, 189.

Becke A. D. (1988). Density-functional exchange-energy approximation with correct asymptotic behavior. *Phys. Rev. A* **38**, 3098.

Becke A. D. (1993). A new mixing of HartreeFock and local density functional theories. *J. Chem. Phys.* **98**, 1372.

Becke A. D. (1993). Density-functional thermochemistry.III.The role of exact exchange. *J. Chem. Phys.* **98**(7), 5648.

Beer, N., & Pettifor, D. (1984). *The Electronic structure of complex systems* New York, Plenum Press.

Bergman A., Nordström, L., Klautau, A. B., Frota-Pessoa, S., & Eriksson, O.(2006). Magnetic interactions of Mn clusters supported on Cu. *Phys. Rev. B* **73**, 174434.

Bertolus M., Brenner, V., & Millie, P.(2001). Are lithium hydride clusters purely ionic? Study using model potentials and density-functional theory. *J. Chem. Phys.* **115**, 4070.

Binder, K. & Yong A. P. (1986). Spin Glasses:Experimental facts, theoretical concepts and open questions. *Rev. Mod. Phys.* **58**(4), 801.

Blöchl P. E. (1994). Projector augmented-wave method, *Phys. Rev. B* **50**, 17953.

Blonski, P., & Hafner, J. (2011). Magneto-structural properties and magnetic anisotropy of small transition-metal clusters: a first-principles study. *J. Phys.: Codens. Matter* **23**, 136001.

Boerstoel, B. M., Zwart, J. J., & Hansen, J. (1972). The specific heat of dilute palladium manganese alloys; Critical behaviour and magnetic-field dependence. *Physica* **57**(3), 397.

Bolzoni, F., & Cabassi, R. (2004). Review of singular point detection techniques.

Physica B **346-347**, 524.

Born M., & Oppenheimer, J. R. (1927). Zur Quanten theorie der Meleken. *Ann. Physik* **84**, 457.

Brack M. (1995). The Physics Of Simple Metal Clusters, *Rev. Mod. Phys.* **65**(3), 77.

Bullett D. (1980). *Solid State Physics*, New York, Academicy Press.

Cabria, I., Lopez, M. J., & Alonso, J. A.(2006). Density functional study of molecular hydrogen coverage on carbon nanotubes. *Computational Material Science* **35**, 238.

Carr Jr. W. J. (1952). Intrinsic Magnetization in Alloys.*Phys. Rev.* **85**, 590.

Ceperley, D. M. & Alder. B. J.(1980). Ground State of the Electron Gas by a Stochastic Method. *Phys. Rev. Lett.* **45**, 566.

Chang, C. M.,& Chou M. Y.(2004). Alternative Low-Symmetry Structure for 13-atom Metal Clusters. *Phys. Rev. Lett.* **93**, 133401.

Chaudhury, D. & Mookerjee, A.(1984). Dynamical mean field theory of realistic spin glasses beyond the independent mode approximation. *J. Phys.: Condens. Matter* **17**, 5049.

Chowdhury, D. & Mookerjee, A. (1984). Mean-field theories of spin glasses. *Physics Reports* **114**(1), 1.

Cheng, X. M., & Chien C. L.(2003). Magnetic properties of epitaxial Mn-doped ZnO thin films. *J. Appl. Phys.* **93**, 7876.

Cleri, F., & Rosato, V.(1993). Tight-binding potentials for transition metals and alloys. *Phys. Rev. B* **48**, 22.

Coles, B. R., Jamieson, H., Taylor, R. H., & Tari, A.(1975). Limited ferromagnetism and other magnetic properties of Pd-Mn alloys. *J. Phys. F : Metal Phys* **5**, 565.

Coles, B. R., Sarkissian, B. V. & Taylor, R. H. (1978). The role of finite magnetic clusters in Au-Fe alloys near the percolation concentration. *Philos. Mag. B* **37**, 489.

Condon, E. U. & Shortley, G. (1935). *The theory of atomic Spectra* , Cambridge, Cambridge University Press.

Connolly, J. W. D., & Williams, A. R.(1983). Density-functional theory applied to phase transformations in transition-metal alloys.*Phys. Rev. B* **27**, 5169.

Cox H., Johnston, R, L., & Murrell, J.(1990). Empirical potentials for modeling solids, surfaces, and clusters. *J. Solid State Chem.* **145**, 571.

Dai, J., Meng C. C., & Li, Q. (2013). First-principles study on the magnetism of Mn and Co co-doped ZnO. *Physica B* **409**, 5.

Datta S., Kabir M., & Saha-Dasgupta T. (2012). Effects of shape and composition on the properties of CdS nanocrystals. *Phys. Rev. B* **86**, 115307.

de Heer, W. A.(1995). The Physics Of Simple Metal Clusters:experimental aspects and simple models.*Rev. Mod. Phys.* **65**(3), 611.

De, Pater, C. J., van Dijk C. & Nieuwenhuys G. J. (1975), Neutron small-angle scattering from palladium alloys. *J. Phys. F : Metal Phys* **5**, L58.

Dietl, T., Ohno, H., Matsukura, F., Gilbert, F. & Ferrand, D. (2000). Zener Model Description of Ferromagnetism in Zinc-Blende Magnetic Semiconductors. *Science* **287**(54-55), 10191022.

Ducastelle, F., & Gautier F. (1978). Generalized perturbation theory in disordered transitional alloys: Applications to the calculation of ordering energies. *J. Phys. F: Met.Phys.* **6**, 2039.

Edward, S. F. & Anderson P. W.(1975). Theory of spin glasses. *J. Phys. F: Met. Phys.* **5**, 965.

Efremenko, I. & Sheintuch, M.(1998). Quantum chemical study of small palladium clusters. *Surf. Sci.* **414**, 148 .

Ehrenreich, H & Schwartz, L. (1982). *Solid State Physics*, Seitz, F, and Turmbul D. Ed., New York, Academic Press.

Ernzerhof, M., Perdew, J. P., & Burke K. (1996). Coupling-Constant Dependence of Atomization Energies. *Int. J. Quantum Chem.* **64**, 285.

Ernzerhof M., & Scuseria, G. E. (1999). Assessment of the Perdew Burke Ernzerhof exchange correlation functional. *J. Chem. Phys.* **110**, 5029.

Faulker, J. S.(1982). The modern theory of alloys: Progress in Materials. *Science* **27**, 1.

Fermi E. (1928). A statistical method for the determination of some atomic properties and the application of this method to the theory of the periodic system of elements. *Z. Physics* **48**, 73.

Fischer, K. H. & Hertz, J. A. (1993). *Spin Glasses*. Cambridge University Press .

Fock V.(1930). Naherungs method Zur Losung des Quanten-mechanischen Mehrkorper Probleme. *Z. Phys.* **61**, 126.

Forrando R., Jellineck J., & Johnston, R. L.(2006). Nanoalloys: From Theory to Applications of Alloy Clusters and Nanoparticles. *Chem. Rev.* **108**(3), 845.

Frota-Pessoa S. (1992). First-principles real-space linear-muffin-tin-orbital calculations of 3d impurities in Cu. *Phys. Rev. B* **46**, 14570.

Fukumura T., Jin Z., Kawasaki M., Shono T., Hasegawa T., Koshihara S. and Koinuma H. (2001). Magnetic properties of Mn-doped ZnO. *Appl. Phys. Lett.* **78**, 958.

Futschek T., Marsman M., Hafner J. (2005). Structural and magnetic isomers of small Pd and Rh clusters: an ab initio density functional study. *J. Phys.: condens. Matter* **17**, 5927.

Gabay, M. & Toulouse, G. (1981). Coexistence of Spin-Glass and Ferromagnetic Orderings. *Phys. Rev. Lett.* **47**, 201.

Ganguly, S., Costa, M., Klautau, A. B., Bergman, A., Sanyal, B., Mookerjee, A., & Eriksson O.(2011). Augmented space recursion formulation of the study of disordered alloys with noncollinear magnetism and spin-orbit coupling: Application to MnPt and Mn_3Rh. *Phys. Rev. B* **83**, 094407.

Garcia-Rodeja, J., Rey, C., Gallego, L. J., & Alonso, J. A. (1994). Molecular-dynamics study of the structures, binding energies, and melting of clusters of fcc transition and noble metals using the Voter and Chen version of the embedded-atom model. *Phys. Rev. B* **49**, 8495.

Gardeniers, J. G. E., Rittersma, Z. M., & Burger, G. J. (1998). Preferred orientation and piezoelectricity in sputtered ZnO films. *J. Appl. Phys.* **83**, 7844.

Ghosh, M., Seshadri, R. & Rao, C. N. R.(2004). A solvothermal route to ZnO and Mn doped ZnO nanoparticles using the Cupferron complex as the precursor. *J. Nanosci. Nanotechnol.* **4**, 136140.

Gonis, A., Zhang, X. G., Freeman, A. J., Turchi, P., Stocks, G. M., & Nicholsen D. M. (1987). Configurational energies and effective cluster interactions in substitutionally disordered binary alloys. *Phys. Rev. B* **36**(9), 4630.

Gonzales, A. C. & Parra, R. E. (1995). Ferromagnetic critical temperatures in dilute PdMn alloys. *J. Magn. Mag. Mater* **149**(3), 341.

Gopal, P. & Spaldin, N. A. (2006). Magnetic interactions in transition-metal-doped ZnO: An ab initio study. *Phys. Rev. B* **74**, 094418.

Grushow, A., & Ervin, K. M. (1997).Ligand and metal binding energies in platinum carbonyl cluster anions: Collision-induced dissociation of Pt_m^- and $Pt_mCO_n^-$. *J. Chem. Phys.***106**, 9580.

Gu, G., Xiang, G., Luo, J., Ren, H., Lan, Mu, He, D., & Zhang, Xi (2012). Magnetism in transition-metal-doped ZnO: A first-principles study. *J. Appl. Phys.* **112**, 023913.

Guo, H., Zhao, Yu, Lu, N., Kan, E., Zeng, X. C., Wu, X., Yang, J. (2012). Tunable Magnetism in a Nonmetal-Substituted ZnO Monolayer: A First-Principles Study. *J. Phys. Chem. C* **116**, 11336.

Hahn, R & Kneller, E. (1958). Magnetic Properties and Order Structure of Nickel-Manganese Alloys. I. Quasi Paramagnetism of Partially Ordered Nickel-Manganese Alloys. *Z. Metallk.* **49**, 426.

Hartree D. R. (1928). The wave mechanics of an atom with non coulombic central field (Part I, II, III). *Proc. Cambridge Phil. Soc.***24**(89), 111.

Hauser, J. J. & Bernardini, J. E. (1984). Structure-sensitive magnetic properties of Ni-Mn alloys. *Phys. Rev. B* **30**, 3803.

Haydock, R., Heine, V., & Kelly, M. J. (1972). Electronic structure based on the local atomic environment for tight-binding bands. *J. Phys. C: Solid State Physics* **5**, 2845.

Haydock R. (1980). *Solid State Physics* **35**, New York, Academic Press.

Haydock, R., Heine, V. & Kelly, M. J. (1972). Electronic structure based on the local atomic environment for tight-binding bands. *J. Phys. C : Solid State Phys* **5**, 2845.

Haydock R., Heine, V., & Kelly, M. J. (1975). Electronic structure based on the local atomic environment for tight-binding bands:II. *J. Phys. C: Solid State Phys.* **8**, 2591.

Henderson Thomas M, Izmaylov Artur F., Scuseria Gustavo E., & Savin A. (2008). Assessment of a Middle-Range Hybrid Functional. *J. Chem. Theory Comput.* **4**, 1254.

Henry C. R. (1998). Surface studies of supported model catalysts. *Surf. Sci. Rep.* **31**, 235.

Henwood D. and Carey J. D. (2007). Ab initio investigation of molecular hydrogen physisorption on graphene and carbon nanotubes. *Phy. Rev. B* **75**, 245413.

Heyd, J., Scuseria, G. & Ernzerhof M. (2006). Hybrid functionals based on a screened

Coulomb potential. *J. Chem. Phys.* **124**(21), 219906.

Ho, S. C., Maartence I., & Williams G. (1981). AC susceptibility and resistivity of the ferromagnetic phase of PdMn. *J. Phys. F : Metal Phys* **11**, 699

Ho, S. C., Maartence, I., & Williams G.(1981). Mixed ordering in PdMn Alloys. *J. Phys. F : Metal Phys* **11**, 1107.

Hohenberg, P., & Kohn, W. (1964). Inhomogeneous Electron Gas. *Phy. Rev.* **136**, B864.

Huang, S. P., Xu, H., Bellow I., & Zhang, R. Q. (2010). Surface Passivisation-Induced strong ferromagnetism of Zinc- Oxide Nano wires. *Chem. Eur. J.* **16**, 13072.

Huang, D., Zhao, Y. Z., Chen, D. H. & Shao, Y. Z. (2008). Magnetism and clustering in Cu doped ZnO. Appl. *Phys. Lett.* **92**, 182509.

Huang, X., Jain, P. K., El-Sayed, I. H., & El-sayed M. A. (2007). Gold nanoparticles: interesting optical properties and recent applications in cancer diagnostics and therapy.*Nanomedicine* **2**, 681.

Huynh, W. U., Dittmer, J. J. & Alivisatos, A. P. (2002). Hybrid Nanorod-Polymer Solar Cells. *Science* **295**, 2425.

Jena, A. P., Rahaman, M. & Mookerjee, A. (2011). Study of disorder-order transitions in Fe_xAl_{1-x} binary alloys using the augmented space recursion based orbital peeling technique. *Physica B: Condens Matter* **406**(20), 3810.

Jeon, S. H., Park, B. H., Lee, J., Han, S. (2006). First-principles modeling of resistance switching in perovskite oxide material. *Appl. Phys. Lett.* 89, 042904.

Jiang, A., Tyson, T. A., & Axe L. (2005). The structure of small Ta clusters. *J. Phys: Condensed matter* **17**, 6111.

Jing, C., Yang, Y., Cao, S. X., & Zhang, J. C. (2006). Electronic Structure and magnetism of $Mn_{1-x}Pd_x$ alloys. *Mod. Phys. Lett. B* **20**, 305.

Jollet, F., Jomard, G., Amadon, B., Crocombette, J. P., & Torumba D. (2009). Hybrid functional for correlated electrons in the projector augmented-wave formalism: Study of multiple minima for actinide oxides. *Phys. Rev. B* **80**:235109.

Josheph, D. Paul, & Venkateswaran C. (2011). Bandgap Engineering in ZnO By Doping with 3d Transition Metal Ions. *Journal of Atomic, Molecular and Optical Physics*, 270540.

Jules, J. L., & Lombardi J. R. (2003). Transition Metal Dimer Internuclear Distances from Measured Force Constants. *J. Phys. Chem. A* **107**, 1268.

Jung, S. W., An, S. J., Yi G. C., Jung, C. U., Lee J. & Cho, S. (2002). Ferromagnetic properties of ZnMnO epitaxial thin films. *Appl. Phys. Lett.* **80**(24), 4561.

Kastner, J., Wasserman, E. F., Matho, K., & Tholence J. L. (1978). Low-temperature resistivity of dilute PtMn alloys. *J. Phys. F : Metal Phys. 8*, 103.

Kane, M. H., Shalini, K., Summers, C. J., Varatharajan, R., Nause, J., Vestal C. R., Zhang, Z. J., & Ferguson, I. T. (2005). Magnetic properties of bulk $Zn_{1-x}Mn_xO$ and $Zn_{1-x}Co_xO$ single crystals. *Journal of Applied Physics* **97**, 023906.

Kaneyoshi T. (1976). Effective-field theory of the spin glass. *J. Phys. C* **9**, L289.

Kaneyoshi T. (1981). Spin-glass ordering temperature beyond its mean-field value. *Phys. Rev. B* **24**, 2693.

Kaphle, G. C., Ganguly, S., Banerjee, R., Banerjee, R., Khanal, R., Adhikari, C. M., Adhikari, N. P. & Mookerjee, A. (2012). A study of magnetism in disordered Pt-Mn, Pd-Mn and Ni-Mn alloys: an augmented space recursion approach. *J. Phys.: Condens. Matter* **24**, 295501.

Karabacak, M., Ozcelik, S., Guvenc, Z. B. (2002). Structures and energetics Of Pd_n(n=220) clusters using an embedded-atom model potential. *Surface Science* **(507-510)**, 636.

Karolewski M. A. (2001), Tight-binding potentials for sputtering simulations with fcc and bcc metals. *RADIAT EFF* **153**(3), 239.

Kasuya T. (19560). Electrical resistance of ferromagnetic metals. *Prog. Theor. Phys. 16*, 45.

Kato, T. & Saita, T. (2011). The ferromagnetic-spin glass transition in PdMn alloys: symmetry breaking of ferromagnetism and spin glass studied by a multi-canonical method. *J. Phys. Condens Matter* **23**, 106001.

Keeyung Lee (1998). Possible magnetism in small palladium clusters. *Phys. Rev. B* **58**(5), 2391.

Kim, C., Kim, S. J., Lee, Y. & Kim Y.(2000). *Bull. Korean. Chem. Soc.* **21**, 5.

Kim, K. J. & Park, Y. R. (2004). Optical investigation of ZnFeO films grown on AlO by radio-frequency sputtering. *Journal of Applied Physics* **96**, 4150.

Kimishima, Y., Kobayashi, M., Seto, R. & Miyako, Y. (1977). Specific Heat of Spin

Glass in PtMn Dilute Alloys. *J. Phys. Soc.* (Japan) **43**, 1577.

Kittel C. (2005).*Introduction to Solid state physics.* John Wiley & Sons, 8th edition.

Kleiman, R. N., Maartence, I. & Williams, G (1982). Ac susceptibility of AuFe near the percolation limit. *Phys. Rev. B* **26**, 5241.

Klimov, V. I., Mikhailovsky, A. A., Xu, S., Malko, A., Hollingworth, J. A., Leatherdale C. A., Eisler, H. J., & Bawendi, M. G. (2000). Optical gain and stimulated emission in nanocrystal quantum dots. *Science* **290**, 314.

Knickelbein M. B. (2004). Magnetic ordering in manganese clusters. *Phys. Rev. B* **70**, 014424.

Knickelbein M. B. (2004). Spin relaxation in isolated molecules and clusters: The interpretation of Stern-Gerlach experiments. *J. Chem. Phys.* **121**(10), 5281.

Kohn, W. & Sham, L. J. (1965). Self-Consistent Equations Including Exchange and Correlation Effects. *Phys. Rev.* **140**, A1133.

Korringa J. (1994). Early history of multiple scattering theory for ordered systems. *Phys. Rep.* **238**(6), 341.

Kouvel, J. S. & Graham, C. D. (1959). Exchange anisotropy in disordered nickel-manganese alloys. *J. Phys. Chem. Solids* **11**, 220.

Kouvel, J. S., Abdul-Razzaq, W. & Ziq, Kh. (1987). Magnetic phase diagram of disordered Ni-Mn near the multicritical point. *Phys. Rev. B* **35**, 1764.

Kreibig (1970). Kramers Koning Analysis of the optical properties of small silver particles. *Z. Phys.* **234**, 307.

Kren, E., Kadar, G., Pal, L., Solyom, J., Szabo, P. & Tarnoczi, T. (1968). Magnetic structure and exchange interactions in the Mn-Pt systems. *Phys. Rev.* **171**, 574.

Kresse, G. & Hafner, J. (1993). Ab initio molecular dynamics for liquid metals. *Phys. Rev. B* **47**, 558.

Kresse, G. & Hafner, J. (1996). Efficient iterative schemes for ab initio total-energy calculations using a plane-wave basis set. *Phys. Rev. B* **54**, 11169.

Kumar V. (2006). Recent theoretical progress on electronic and structural properties of clusters: Permanent electric dipoles, magnetism, novel caged structures, and their assemblies. *Comput. Mater. Sci.* **35**, 375.

Kumar, V. & Kawazoe, Y. (2002). Icosahedral growth, magnetic behavior and

adsorbate induced metal-non-metal transition in palladium clusters. *Phys. Rev. B* **66**, 144413.

Lany, S. & Zunger A. (2007). Dopability, Intrinsic Conductivity and Nonstoichiometry of Transparent Conducting Oxides. *Phys. Rev. Lett.* **98**, 045501.

Lawes, G., Ramirez, A. P., Risbud, A. S. & Ram S. (2005). Absence of ferromagnetism in Co and Mn substituted polycrystalline ZnO. *Phys. Rev. B* **71**, 045201.

Lee, C., Yang, W., & Par, R. G. (1998). Development of the Colle-Salvetti correlation energy formula into a functional of the electron density. *Phys. Rev. B* **37**. 785.

Lee, E. C., & Chang, K. (2004). Ferromagnetic versus anti-ferromagnetic interaction in Co-doped ZnO. *Phys. Rev. B* **69**, 085205.

Lee K. (1998). Possible magnetism in small palladium clusters. *Phys. Rev B* **58**, 2391.

Levy M. (1979). Universional variational functionals of electron densities, First-order density matrices and natural spin orbitals and solution of the v-representability problem. *Proc. Natl. Acad. Sci.*, USA **76**, 6062.

Liao, L., Li, J. C., Wang, D. F., Liu, C., Liu, C. S., Fu, Q. & Fan, L. X. (2005). Field emission property improvement of ZnO nanowires coated with amorphous carbon and carbon nitride films. *Nanotechnology* **16**, 985.

Lichtenstein A. I., Katsnelson M. I. and Kotlier G. (2001). Finite temperature magnetism of transition metals: ab-initio dynamical mean field theory. *Phy. Rev. Lett.* **87**, 067205.

Lichtenstein, A. I., Katsnelson, M. I., Antropov, V., & Gubanov, V. A. (1987). Local spin density functional approach to the theory of exchange interactions in ferromagnetic metals and alloys. *J. Mag. Magn. Mater.* **67**, 65.

Lieb E. H.(1982). Density functionals for Coulomb systems. *Int. J. Quantum Chem* **24**, 243.

Limpijumnong, S., Li X., Wei, S., & Zhang, S. B. (2005). Substitutional diatomic molecules NO, NC, CO, N_2, and O_2: Their vibrational frequencies and effects on p doping of ZnO. *Applied Physical Letters* **86**, 211910.

Loucks T. L. (1967). *Augmented Plane Wave Methods.* New York, Benjamin.

Luchini M. U. and Nex C. M. M. (1987). A new procedure for appending terminators in the recursion method. *Journal of Physics C: Solid State Physics* **20**, 3125.

Luo, C., Zhou, C,, Wu, J., Dhilip Kumar, T. J., Balakrishan, N. R. C., & Cheng H.(2007). First Principles Study of Small Palladium Cluster Growth and Isomerization. *International Journal of Quantum Chemistry* **107**, 1632.

Maartence, I., & Williams, G. (1978). AC susceptibility of the ferromagnetic phase of the AuFe system. *Phys. Rev. B* **17**, 377.

Maiti, U. N., Ghosh, P. K., Nandy, S., & Chattopadhyay, K. K. (2007). Effect of Mn doping on the optical and structural properties of ZnO nano/micro-fibrous thin film synthesized by solgel technique. *Physica B* **387**, 103.

Majumdar, A. K., & Blanckenhagen, P. V. (1984). Magnetic phase diagram of $Fe80 - xNi_xCr_{20}$ $(10 \leq x \leq 30)$ alloys. *Phys. Rev. B* **29**, 4079.

Marsman, M., Paier J., Stroppa, A. & Kresse G. (2008). Hybrid functionals applied to extended systems. *J. Phys.: Condens. Matter* **20**, 064201.

Mie G. (1908). Contributions to the optics of turbid media, particularly of colloidal metal solutions . *Ann. Phys.*(Leipzig) **25**, 377.

Monod, P., & Berthier, Y. (1980). Zero field electron spin resonance of CuMn in the spin glass state. *J. Magn. Magn. Mater.* **15**, 149.

Mookerjee, A., & Prasad, R. (1993). Generalized augmented-space theorem for correlated disorder and the cluster-coherent-potential approximation. *Phys. Rev.B* **48**, 17724.

Mookerjee A. (1973). A new formalism for the study of configuration-averaged properties of disordered systems. *J. Phys. C: Solid state Physics* **6**, L205.

Mookerjee A. (1973). Averaged density of states in disordered systems. *J. Phys. C : Solid State Phys* **6**, 1340.

Mookerjee A. (1980). A mean-field,effective medium theory of random magnetic alloys II the random Heisenberg model. *Pramana* **14**, 11.

Mookerjee A. (2003). *Electronic structure of alloys, surfaces and clusters.* Eds. A. Mookerjee and D. D. Sharma, U. K., Tyalor-Francis.

Mookerjee, A. & Roy S. B. (1983). A mean-field, effective medium theory of random binary alloys III. The Ising model with competitive interactions. *Pramana* **21**, 171.

Mookerjee A. (2003). *Electronic structure of clusters, surfaces and disordered materials* Eds.A. Mookerjee and D. D. Sharma, U.K., Taylor-Francis

Morse M. D. (1986). Clusters of TM atoms. *Chem. Rev.* **86**(6), 1049.

Moruzzi, V. L., & Marcus, P. M. (1989). Magnetism in fcc rhodium and palladium. *Phys. Rev. B***39**, 471.

Moseler, M., Hakkinen, H., Barnet, R. N., & Landmann Uzi.(2002). Structure and Magnetism of Neutral and Anionic Palladium Clusters. *Phys. Rev. Lett.* **86**, 2545.

Moze, O, Hicks, T. J., & Blanckenhagen, P. V. (1984). The variation of sub-lattice moment with composition for antiferromagnetic nickel-manganese alloys. *J. Magn. Magn. Mater* **42**, 103.

Mulder, C. A. M., van Duyneveldt, A. J., & Mydosh, J. A. (1981). Susceptibility of the CuMn spin-glass: Frequency and field dependences. *Phys. Rev. B* **23**, 1384.

Mulder, C.A.M., van Duyneveldt, A. J., van der Linden, H. W. M., Verbeek, B. H., van Dongen, J. C. M., Nieuwenhuys, G. J., & Mydosh J. A. (1981). The frequency dependence of the ac susceptibility of the PdMn spin glass. *Phys. Lett.* **83A**(2), 74.

Murugadoss G. (2012). Synthesis and Characterization of Transition Metals Doped ZnO Nanorods, *J. Mat. Sci. Technol.* **28**(7), 587.

Mydosh J. A. (1993). *Spin Glass:An Experimental Introduction.*, U. K., Taylor and Francis.

Nieuwenhuys, G. J., & Verbeek, B. H. (1977). On the magnetic ordering in palladium manganese dilute alloys. *J. Phys. F : Metal Phys* **7**, 1497.

Nigam, S., Majumder, C., & Kulshrestha, S. K. (2007). Geometry and electronic and magnetic properties of MPd_{12} clusters (M=Ti, V, Cr, Mn, Fe, Co, Ni, Cu, Zn, and Pd) from first principles. *Phys. Rev. B* **76**, 195430.

Norton, D. P., Pearton, S. J., Hebard, A. F., Theodoropoulou, N., Boatner, L. A., & Wilson R. G. (2003). Ferromagnetism in Mn-implanted ZnO: Sn single crystals. *Appl. Phys. Lett.* **82**, 239.

Oguchi T., Terakura, K., & Hamada, H. (1993). Magnetism of iron above the Curie temperature. *J. Phys. F : Metal Phys* **13**, 145.

Oguchi, T., Terakura, K., & Williams, A. R. (1983). Band theory of the magnetic interaction in MnO, MnS, and NiO. *Phys. Rev. B* **28**, 6443.

Oguchi, T., Terakura, K., & Williams, A. R. (1984). Transitionmetal monoxides: Itinerant versus localized picture of superexchange. *J. Appl. Phys.* **55**, 2318.

Oswald, A., Zeller, R., & Dederiches P. H. (1986). Giant moments in palladium.

Phys. Rev. Lett. **56**(13), 1419.

Ohno H. (1998). Making Nonmagnetic Semiconductors Ferromagnetic. *Science* **281**, 951.

Ozgur U., Alivov, Ya., I, Liu, C., Teke, A., Reshchikev, M. A., Dogan, S., Avrutin, V., Cho, S. J., & Morko, C. H. (2005). A comprehensive review of ZnO materials and devices. *J. Appl. Phys.* **98**, 041301.

Pal, P, Banerjee, R., Banerjee, R., Mookerjee A. , Kaphle, G. C., Sanyal, B., Hellsvik, J., Eriksson, o., Mitra, p., Majumdar, A. K., & Nigam, A. K. (2012). Magnetic ordering in Ni-rich NiMn alloys around the multicritical point: Experiment and theory. *Phys. Rev. B* **85**, 174405.

Park, S. Y., Kim, B. J., Kim, K., Kang, M. S., Lim, K. H., Lee, T. I., Myoung, J. M., Baik, H. K., Cho, J. H., & Kim, Y. S. (2012). Low Temperature, Solution Processed and Alkali Metal Doped ZnO for High Performance Thin Film Transistors. *Adv. Mater.* **24**, 834.

Park, S., Lee, B., Jeon, S. H, & Han, S. (2011). Hybrid functional study on structural and electronic properties of oxides. *Current Applied Physics* **11**, S337.

Parra, R. E., & Gonzales, A. C. (1992). Atomic short range order and anti-ferromagnetism in PdMn alloys. *J. Magn. Mag. Mater* **104**, 2017.

Pedersen, J., Bjϕrnholm, Borggreen, J., Hansen, K., Martin, T. P., & Rasmussen, H. D., (1991). Observation of quantum supershells in clusters of sodium atoms. *Nature* **353**, 733.

Perdew, J. P. & Wang Y. (1992). Accurate and simple analytic representation of the electron-gas correlation energy.*Phys. Rev. B* **45**,13244.

Perdew J. P. (1986). Density-functional approximation for the correlation energy of the inhomogeneous electron gas. *Phys. Rev. B* **34**,7406 .

Perdew, J. P., Burke, K., & Ernzerhof, M. (1996). Generalized Gradient Approximation Made Simple. *Phys. Rev. Lett.* **77**, 3865.

Perdew, J. P., Ernzerhof, M., & Burke, K (1996). Rationale for mixing exact exchange with density functional approximations. *J. Chem. Phys.* **105**, 9982.

Philips, J. C., & Kleinman, L (1959). New Method for Calculating Wave Functions in Crystals and Molecules. *Phys. Rev.* **116**, 287.

Plefka T. (1976). Internal field distribution for spin glasses. *J. Phys. F* **6**, L327.

Pokrovski, B. I., & Khachaturyan, A. G. (1986). The concentration wave approach to the pair wise interaction model for predicting the crystal structures of ceramics, I. *Journal of Solid State Chemistry* **61**, 137.

Prasad R. (1995). *Method of Electronic Structure Calculations*. Eds. Andersen O. K., Kumar V.,& Mookerjee A. Singapore, World-Scientific.

Rao, C. N. R., & Deepak, P. L. (2005). Absence of ferromagnetism in Mn- and Co-doped ZnO. *J. Mater. Chem.* **15**, 573.

Rayleigh L. (1892). On the influence of obstacles arranged in rectangular order upon the properties of the medium. *Phil. Mag.* **34**, 481.

Reddy B. V., Nayak, S. K., Khanna, S. N., Rao, B. K. & Jena, P. (1999). Electronic structure and magnetism of Rh_n (n=2-13) clusters. *Phys. Rev. B* **59**, 5214.

Rey C., Gallego L. J., Garcia-Rodeja J., Alonso, J. A., & Iniguez, M. P. (1993). Molecular dynamics study of the binding energy and melting of- transition-metal clusters. *Phys. Rev. B: Condens Matter* **48**(11), 8253.

Rogan, J., Gracia, G., Ramirez, M., Murioz, V., Valdivia, J. A., Andrade, X., Ramirez, R. & Kiwi, M. (2008). The structure and properties of small Pd clusters. *Nanotechnology* **19**, 205701.

Ruderman, M. A. & Kittel, C. (1954). Indirect Exchange Coupling of Nuclear Magnetic Moments by Conduction Electrons. *Phys. rev.* **96**, 99.

Sacli, O. A., Emerson, D. J., & Brewer, D. F. (1974). Ferromagnetic and anti-ferromagnetic ordering in platinum-manganese alloys: Low-temperature specific heat. *J. Low Temp. Phys.* **17**, 425.

Sakuma A. (2000). First-Principles Study on the Non-Collinear Magnetic Structures of Disordered Alloys. *J. Phys. Soc.*, (Japan) **69**, 3072.

Samanta, K., Bhattacharya, P., & Katiyar, R. S. (2006). Raman scattering studies in dilute magnetic semiconductor $Zn_{1-x}Co_xO$. *Phys. Rev. B* **73**(24), 245213.

Sarachik, M. P. & Shaltiel, D. (1967). Low Temperature Resistivity and the Sign of the Exchange Integral. *J. Appl. Phys.* **38**, 1155.

Sarkissian, B. V. B., & Taylor R. H. (1974). Electrical resistivity of Pt-Mn alloys. *J. Phys. F : Metal Phys* **4**, 243.

Sato, K., Bergqvist, L., Kundrnovsky, J., Dederichs, P. H., Errikson, O., Turek, I., Sanyal, B., Bouzerar, G., Katayama-Yosida, H., Dinh, V. A., Fukosima, T., Kizaki,

H., & Zeller, R. (2010). First-principles theory of dilute magnetic semiconductors. *Rev. Mod. Phys.* **82**, 1633.

Sato, K. & Katayama-Yoshida, H. (2000). First principles materials design for semiconductor spintronics. *Jpn. J. Appl. Phys.* **39**, L555.

Senoussi, S., Hamzic, A. & Campbell, I. A. (1980). New information on the spin-glass state of AuFe from transport measurements. *J. Phys. F : Metal Phys :Metal Physics* **29**, 1223 .

Sernelius, B. E., Berggren, K. F., Jin, Z. C., Hamberg, I. & Granqvist, C. G. (1988). Bandgap tailoring of ZnO by means of heavy Al doping. *Phys. Rev. B* **37**, 10244

Sharma, P., Gupta, A., Rao, K. V., Owens, F. Z., Sharma, R., Ahuja, R., Guillen, J. M. O., Johnson, B. & Gehring, G. A. (2003). Ferromagnetism above room temperature in bulk and transparent thin films of Mn-doped ZnO. *Nat. Mater.* **2**, 673.

Shen, N. F., Wang, J. L., & Zhu, L. Y. (2008). Ab initio study of magnetic properties of bimetallic $Co_{n-1}Mn$ and $Co_{n-1}V$ clusters. *Chem. Phys. Lett.* **467**, 114.

Shinhora, T., Sato, T. & Taniyama, T. (2003). Surface Ferromagnetism of Pd Fine Particles. *Phys. Rev. Lett.* **91**, 197201.

Shun-Ping, S., Yi-Ping, C., Al-Ping, Z., Yang, L., & xing-Xing, J. (2011). Geometries, stabilities and electronic properties of small Nb-doped gallium clusters: A density functional theory study. *Physica B* **406**, 3544.

Sirbuly, D. J., Law, M., Yan, H. Q., & Yang, P. D. (2005). Semiconductor nanowires for sub wavelength photonics integration. *J. Phys. Chem. B* **109**, 15190.

Skriver (1984). *The LMTO METHOD. Springer*, Berlin, Verlag.

Skubic, B., Hellsvik J., Nordstr´om, L., & Eriksson O. (2008). A method for atomistic spin dynamics simulations: implementation and examples. *J. Phys.:Condens. Matter* **20**, 315203.

Slater, J. C. & Koster, G. F. (1954). Simplified LCAO Method for the Periodic Potential Problem. *Phys. Rev.* **94**, 1498.

Slater J. C. (1937). Wave function in periodic potentials. *Phys. Rev.* **51**, 846.

Soven P. (1970). Application of the Coherent Potential Approximation to a System of Muffin-Tin Potentials. *Phys. Rev. B* **2**, 4715.

Sun, X., Du, J, Zhang, P., & Jiang, G. (2010). A Systemic DFT Study on Several 5d-Electron Element Dimers: Hf_2, Ta_2, Re_2, W_2, and Hg_2. *J. Clus. Sci.* **21**,

619.

Sutton, A. P., & Chen, J. (1990). Long range Finnis-Sinclair potentials. *Philos. Mag. Lett.* **61**, 139.

T. Oguchi (1960). Theory of Spin-Wave Interactions in Ferro- and Anti-ferromagnetism. *Phys. Rev.* **117**(1), 117 .

Thomson, J. O. & Thompson, J. R.(1979), Very low temperature magnetization of two dilute PdMn alloys, *J. Appl Phys.* **50**, 7364 .

Thota, S., Dutta, T. & Kumar, J. (2006). On the solgel synthesis and thermal, structural, and magnetic studies of transition metal (Ni, Co, Mn) containing ZnO powders. *J. Phys: Condens. Matter* **18**, 2473.

Thouless, D. J., Anderson, P. W., & Palmer (1977). Solution of solvable model of a spin glass. *Philos. Mag.* **35**, 593.

Tiwari, A., Jin, C., Kvit, A., Kumar, D., Muth, J. F., & Narayan, J. (2002). Structural, optical and magnetic properties of diluted magnetic semiconducting $Zn_{1-x}Mn_xO$ films. *Solid state Commun.* **121**(6), 371.

Tsunoda, Y., Hiruma, N., Robertson, J. L., & Cable, J. W. (1997). Spin-density-wave clusters in PdMn spin-glass alloys. *Phys. Rev. B* **56**, 11051.

Turchi, P. E., Stocks, G. M., Buttler, W. H., Nicholson, D. M.,& Goins A. (1988). First principles study of ordering properties of substitutional alloys using the generalized perturbation method. *Phys. Rev. B* **37**, 5982.

Vanderbilt D. (1985). Soft self-consistent pseudo-potentials in a generalized eigenvalue formalism. *Phys. Rev. B* **41**,7892.

Venkataramanan, N. S., Khazaei M., Sahara, R., Mizuseki, H., & Kawazoe, Y. (2010). Titanium Doped Nickel Clusters $TiNi_n$ (n = 1-12): Geometry, Electronic, Magnetic and Hydrogen Adsorption Properties. *J. Phys. Chem. A* **114**, 5049.

Verbeek, B. H., & Mydosh, J. A. (1978). Spin glass freezing above the ferromagnetic percolation limit in AuFe alloys. *J. Phys. F.* **8**, L109 .

Verbeek, B. H., Nieuwenhuys, G. J., Mydosh, J. A., van Dijk, C., & Rainford, B. D. (1980). Inhomogeneous ferromagnetic ordering in PdFe and PdMn alloys studied via small-angle neutron scattering. *Phys. Rev. B* **22**, 5426.

Walter, E., Murray, B. J., Favier, F., Kaltenpoth, G., Grunze, M., & Penner, R. M. (2002). Noble and Coinage Metal Nanowires by Electrochemical Step Edge

Decoration. *J. Physics. Chem. B* **106**, 11407.

Wang, Q. & Jena, P. (2004). First-principles study of magnetism in (1 $1\bar{2}0$) $Zn_{1x}Mn_xO$ thin film. *Appl. Phys. Lett.* **84**(21), 4170.

Wang Z. L. (2004). Zinc oxide nanostructures: growth, properties and applications. *J. Phys. cond. Matter* **16**, R829.

Weizner, E. & Seitz, F. (1934). On the constitution of metalic sodium II. *Phys. Rev.* **46**, 509.

Williams, G. & Loram, J. W. (1969). Electron-magnon scattering in dilute PdMn at low temperatures. *Solid State Commun.* **7**, 1261.

Wojcik, A., Kopalko, K., Godlewski, M., Lusakowska, E., Paszkowicz, W., Dybko, K., Domagala, J., Szczerbakow, A. & Kaminska, E. (2004). Mono-crystalline and Polycrystalline ZnO and ZnMnO Films Grown by Atomic Layer Epitaxy-Growth and Characterization. *Acta Physica Polonica A* **105**, 667.

Xu, X., Yin, S., Moro, R, & de Heer, W. A. (2005). Magnetic Moments and Adiabatic Magnetization of Free Cobalt Clusters. *Phys. Rev. Lett.* **95**, 237209.

Yadav, M. K., & Mookerjee, A. (2010). Nitrogen absorption and dissociation on small Tantalum clusters. *Physica B* **405**, 3940.

Yasida K. (1957). Magnetic properties of Cu-Mn alloys. *Phys. Rev.* **106**, 893.

Yin. S. F., Xu. B. Q., Zhou, X. P., & Au, C. T.(2004). A mini-review on ammonia decomposition catalysts for on-site generation of hydrogen for fuel cell applications. *Appl. Catal. A: Gen.*, 277.

Yuewen, Mu, Yan, Han, Jinlan, Wang, Jian-guo, Wan & Guanghou, Wang (2011). Structures and magnetic properties of Pd_n clusters (n=3-19) doped by Mn atoms. *Phys. Rev. A* **84**, 053201.

Zhan, H. L., Tian, D. X., & Zhao, J. J. (2008). Structural evolution of medium-sized Pd_n (n=15-25) clusters from density functional theory, *J. Chem. Phys.* **129**, 114302.

Zhang, J., Xu, H., Jin, X., Ge, Q., & Li, W.(2005). Characterizations and activities of the nano-sized Ni/Al_2O_3 and Ni/$LaAl_2O_3$ catalysts for NH_3 decomposition. *Appl. Catl. A: Gen.* **290**, 87.

APPENDIX-I

Computational Method and theoretical detail for binding energy and stability

The energetics and geometry optimization calculations have been carried out using density functional theory and plane basis set for the expansion of wave functions through code used in Vienna ab initio simulation package(VASP). The spin states and magnetic moments were determined based on the calculated energy of spin up ans spin down orbitals. We have used the projector augmented wave technique (PAW) (Perdew, *et al.*, 1996),
(Perdew & Wang, 1992) which is extensively used for the study of electronic properties of transition and noble metals, possibly better than the proposed ultra-soft pseudopotentials. We have treated the 4s and 4d states of Pd as valence states in order to take into account of the contribution of semi-core states to electronic structure. The exchange correlation energy has been calculated using the Perdew, Burke, Ernzerhof (PBE) (Perdew, *et al.*, 1996) functional. The size of the super-cell was taken to be large enough (cube of sides $16A^o$) to avoid spurious interaction between images. Gamma point calculations have been performed with the plane wave cut-off energy of 400 eV. Geometries of our clusters have been optimized using the conjugate gradient algorithm and convergence was achieved till the Hellman-Feynman force on each ion was ≤ 0.01 eV/A and energy is converged to an accuracy of 0.001 eV. In order to check the reliability of Pseudo potential used in the present work, test calculation were performed for Ta-Ta, Nb-Nb, N-N and H-H dimers where binding energies are well agreed with other theoretical works and bond-length calculation found to be fair agreement with experiment.

The average binding energy of the clusters was calculated using the formula,

$$B.E. = \Delta E_n = \frac{nE(Z) - E(Z_n)}{n}, n = 2, 3, ... \tag{6.1}$$

where, $E(Z)$= atomic energy of Z and $E(Z_n)$ = atomic energy of Z_n clusters.

Z= Pd, Nb or Ta atoms

Similarly, the average binding energy of the clusters after doping hydrogen and nitrogen will be obtained as,

$$E_b(Z_nX_2) = \frac{nE(Z) + 2E(X) - E(Z_nX_2)}{n+2}, n = 1, 2, 3, ... \tag{6.2}$$

where X= Mn, N or H and other symbol have their usual meanings.

The chemisorption energy, which is the energy to form the hydride and nitride species from Z_n clusters with H_2 and N_2 was evaluated as

$$\Delta E_{CE} = E(Z_n) + E(X_2) - E(Z_nX_2), n = 1, 2, 3, ... \tag{6.3}$$

where X = Mn, N or H

Z= Pd, Nb or Ta and E_{CE} = Chemisorption Energy of system under study.

The magnitude of first differences measure the relative stability of clusters against the loss of one of its constituents atoms, which is called the dissociation energy can be calculated using ,

$$\Delta_1 E = E_{n+1} - E_n, \tag{6.4}$$

where the symbol have there usual meanings. The second differences of total energy give the enhanced stability of clusters relative to its heavier and lighter neighbors, which can be calculated using the formula as,

$$\Delta_2 E = E_{n+1} + E_{n-1} - 2E_n \tag{6.5}$$

The value of Δ_1 and Δ_2 have local structures, generally decreases slowly as co-ordination increases with the size of clusters.

In order to get the knowledge of chemical and magnetic stability of any clusters we have to analyze the spin gaps, which is calculated using the equations,

$$\delta_1 = -[\epsilon_{HOMO}^{majority} - \epsilon_{LUMO}^{minority}] \tag{6.6}$$

$$\delta_2 = -[\epsilon_{HOMO}^{minority} - \epsilon_{LUMO}^{majority}] \tag{6.7}$$

The clusters is said to be stable if both the spin gaps are positive i.e. the lowest unoccupied molecular orbitals (LUMO) of majority spin lies above the highest occupied molecular orbital(HUMO) of minority spin and vice versa.

The Table (6.1) summarizes all the important characteristics of the pristine, mono- and bi-doped Pd clusters for easy reference. on which the ICO, BBP, HCP and CUB represent Icosahedral, Buckle Bi-Planner, Hexagonal closed Pack and Cube-Octahedral structures respectively.

Table 6.1: *Summarizes the characteristics of pristene Pd clusters and Pd clusters mono- and bi-doped with Mn.*

Pristene Pd Clusters											
Cluster size	Binding Eng.(eV)	Mag.Mom. (μ_B)	spin-gap		Avg. bond length (r A)	Cluster size	Binding Eng.(eV)	Mag.Mom. (μ_B)	spin-gap		Avg. bond length (r A)
			δ_1(eV)	δ_2(eV)					δ_1(eV)	δ_2(eV)	
Pd_2	0.645	1.21	2.134	0.364	2.48	Pd_7	1.974	0.00	0.199	0.197	2.68
...	...	...	...	...	...	Pd_8	1.998	5.01	1.155	0.151	2.67
Pd_{31L}	0.859	1.85	0.283	0.148	2.42	Pd_9	2.079	1.88	0.242	0.205	2.70
Pd_{31T}	1.260	0.00	0.283	0.282	2.47	Pd_{10}	2.158	1.90	0.119	0.239	2.71
Pd_4	1.489	0.00	0.323	0.283	2.47	Pd_{11}	2.211	5.38	0.340	0.345	2.70
Pd_5	1.798	1.94	0.745	0.068	2.64	Pd_{12} (CUB)	2.228	3.82	0.355	0.355	2.69
Pd_6	1.882	3.14	1.655	0.034	2.66	Pd_{13} (ICO)	2.312	6.87	1.592	0.1999	2.73
Pd_nMn Clusters											
Pd_1Mn	1.308	4.61	1.676	1.887	2.26	Pd_9Mn	2.325	1.99	0.119	0.411	2.66
Pd_2Mn	1.707	4.60	1.207	1.513	2.46	$Pd_{10}Mn$	2.377	1.12	0.144	0.465	2.71
Pd_3Mn	1.829	4.58	0.659	0.681	2.47	$Pd_{11}Mn$	2.348	4.62	0.183	0.132	2.72
Pd_4Mn	2.042	4.59	0.536	0.511	2.64	$Pd_{12}Mn$ (CUB)	2.457	9.61	1.568	0.218	2.72
Pd_5Mn	2.120	4.59	0.343	0.549	2.66	$Pd_{12}Mn$ (HCP)	2.371	7.00	0.338	0.031	2.71
Pd_6Mn	2.139	6.03	0.207	0.111	2.70	$Pd_{12}Mn$ (ICO)	2.506	9.64	1.568	0.218	2.69
Pd_7Mn	2.233	6.37	0.404	0.191	2.67	$Pd_{12}Mn$ (BBP)	2.440	3.66	0.035	0.802	2.73
Pd_8Mn	2.281	6.57	0.253	0.100	2.68						
Pd_nMn_2 Clusters											
Pd_1Mn_2	1.443	8.74	0.769	1.019	2.49	Pd_8Mn_2	2.443	9.35	0.125	0.231	2.68
Pd_2Mn_2	1.880	10.00	0.228	1.425	2.51	Pd_9Mn_2	2.462	11.01	0.253	0.125	2.66
Pd_3Mn_2	2.059	.10.00	0.474	1.097	2.47	$Pd_{10}Mn_2$	2.538	12.52	1.453	0.185	2.71
Pd_4Mn_2	2.226	9.03	0.312	0.312	2.64	$Pd_{11}Mn_2$ (CUB)	2.561	1.47	0.134	0.089	2.67
Pd_5Mn_2	2.303	10.2	0.674	0.441	2.66	$Pd_{11}Mn_2$ (HCP)	2.477	5.55	0.108	1.062	2.71
Pd_6Mn_2	2.326	9.27	0.159	0.333	2.70	$Pd_{11}Mn_2$ (ICO)	2.593	2.00	1.568	0.2184	2.69
Pd_7Mn_2	2.348	10.71	0.452	0.149	2.67	$Pd_{11}Mn_2$ (BBP)	2.579	2.71	0.429	0.517	2.72

APPENDIX-II

Brief explanation of probability distribution function

We shall briefly repeat the arguments of the work by (Mookerjee & Roy, 1993) to obtain the probability distribution of the local Weiss fields. We shall begin from equation (4.10). It is clear that the local staggered Weiss fields are disordered in the present problem. Therefore the Weiss fields are also random. We proceed to find the probability distribution of the Weiss field. Mookerjee and Roy do this using the Radon transform

$$Pr(h^Q_{\vec{R},x}; h^Q_{\vec{R},y}; h^Q_{\vec{R},z}) = \ll \delta \left(h^Q_{\vec{R},\mu} - \sum_{Q',R'} J^{Q,Q'}(|\vec{R} - \vec{R'}|)\sigma^{Q'}_{\vec{R'},\mu} \right) \gg$$

The site $\vec{R}$ is definitely occupied by a Q type of atom, while the sites R' are randomly occupied by N_1 A and N_2 B atoms. A particular configuration C is a random distribution of N_1 A and N_2 B atoms over $N = N_1 + N_2 + 1$ sites. The averaging mentioned above is over these random configurations. P(C) is the probability of one configuration. We now incorporate (11) into the equation and write the delta function as an exponential integral

$$\begin{aligned} Pr(h^Q_{\vec{R},x}; h^Q_{\vec{R},y}; h^Q_{\vec{R},z}) \quad &= \tfrac{1}{8\pi^3} \int\int\int d\vec{k} exp\left(i\vec{k}.\vec{h}^Q_{\vec{R}}\right) \sum_C P(C) \ldots \\ &\prod_\mu \prod_{Q'} \int \delta h^{Q'}_{\vec{R'},\mu} \delta \left(h^{Q'}_{\vec{R'},\mu} - \textstyle\sum_{\vec{R'}} J^{Q,Q'}(|\vec{R} - \vec{R'}|) m^Q_{\vec{R'},\mu} \right) \\ &xexp\left(-ik_\mu \textstyle\sum_{\vec{R'}} J^{Q,Q'}(|\vec{R} - \vec{R'}|) F^{Q'}_{\vec{R'},\mu} \right) \end{aligned}$$

As it stands this integral equation is still intractable. At this point we introduce the approximation discussed by Klein [46]. It entails replacement of the delta functions by their configuration averages. It is explicit from the equation above that the distribution of $h^Q_{\vec{R},\mu}$ involves the $h^{Q'}_{\vec{R'},\mu}$ at all other sites. Our approximation replaces the contributions of these other random variables by a configuration averaged effective contribution. In this sense this approximation is an effective medium approximation. Since the configu-

ration averages of the delta functions are the probability densities themselves,

$$\begin{aligned} Pr(h^Q_{\vec{R},x}; h^Q_{\vec{R},y}; h^Q_{\vec{R},z}) &= \tfrac{1}{8\pi^3} \int\int\int d\vec{k} exp\left(i\vec{k}.\vec{h}^Q_{\vec{R}}\right) \sum_C P(C) \ldots \\ & \prod_\mu \prod_{Q'} \int \delta h^{Q'}_{\vec{R}',\mu} dh^{Q'}_{\vec{R}',\mu} Pr(h^{Q'}_{\vec{R}',\mu}) \\ & \underline{r} exp\left(-ik_\mu \textstyle\sum_{\vec{R}'} J^{Q,Q'}(|\vec{R}-\vec{R}'|) F^{Q'}_{\vec{R'},\mu}\right) \end{aligned}$$

We now note that all configurations, i.e. distributions of N_1 A atoms and N_2 B atoms, are equally probable in homogeneous disorder. Thus, after a little algebra we get

$$\begin{aligned} Pr(h^Q_{\vec{R},x}; h^Q_{\vec{R},y}; h^Q_{\vec{R},z}) &= \tfrac{1}{8\pi^3} \int d\vec{k} exp\left(i\vec{k}.\vec{h}^Q_{\vec{R}}\right) \\ & \underline{r}(1-G_1/N)^{N_1}(1-G_2/N)^{N_2}. \end{aligned}$$

where,

$$G_1 = \sum_R \int \vec{h}^Q_{\vec{R}} \left[1 - exp\{-i\vec{k} \cdot J^{Q,Q}(\vec{R}) \vec{F}^Q_{\vec{R}}\}\right] \tag{6.8}$$

$$G_2 = \sum_R \int \vec{h}^{Q'}_{\vec{R}} \left[1 - exp\{-i\vec{k} \cdot J^{Q,Q'}(\vec{R}) \vec{F}^{Q'}_{\vec{R}}\}\right] \tag{6.9}$$

In the thermodynamic limit the factors $(1-G_1/N)^{N_1}$ tend to $exp(-G_1)$. Mookerjee and Roy [42] showed that if we now expand the exponential factors and if the scaled moments $I_n = \sum_R \{J(R)/J(R_0)\}$ decrease rapidly with n, then we can simplify the integrals in the expression for the probability density to get

$$Pr(h^Q_x, h^Q_y, h^Q_z) = P_0 exp\left[\sum \left(h^Q_\mu - I^Q_{1\mu}\right)\left(K^Q_{\mu\nu}\right)\left(h^Q_\nu - h^Q_{1\nu}\right)\right] \tag{6.10}$$

Note that we have dropped the $\vec{R}$ index, as the distribution is independent of site for homogeneous disorder.P_0 is the normalizing factor.

$$I^Q_{1\mu} = \sum_{Q'} x^{Q'} I_1^{QQ'} m^{Q'}_\mu \tag{6.11}$$

where $I_1^{QQ'}$ is the first scaled moment of $J^{QQ'}(\vec{R})$. If we diagonalize $K^Q_{\mu\nu}$ using a unitary transformation then the diagonal terms are

$$I^Q_{2\mu} = \sum_{Q'} x^{Q'} I_2^{QQ'} q^{Q'}_\mu \tag{6.12}$$

where $I_2^{QQ'}$ is the second scaled moment of $J^{QQ'}(\vec{R})$.

APPENDIX-III

Publications

A. International Peer-Reviewed Journals

1. **A study of magnetism in disordered PtMn, PdMn and NiMn alloys: an augmented space recursion approach.**
   G. C. Kaphle, S. Ganguly, R. Banerjee, R. Banerjee, R. Khanal, C. M. Adhikari, N. P. Adhikari and A. Mookerjee
   J. Phys.: Condens. Matter **24**, 295501 (2012).

2. **Magnetic ordering in Ni-rich NiMn alloys around the multicritical point: Experiment and theory.**
   P. Pal, R. Banerjee, R. Banerjee, A. Mookerjee, G. C. Kaphle, B. Sanyal, J. Hellsvik, O. Eriksson, P. Mitra, A. K. Majumdar and A. K. Nigam
   Phys. Rev. B **85**, 174405 (2012).

3. **Adsorption and dissociation of Nitrogen and Hydrogen molecules on Palladium(Pd) and Platinum(Pt) clusters.**
   G. C. Kaphle, N. P. Adhikari and A. Mookerjee
   Accepted in Quantum matter

4. **Electronic Structures and Magnetic properties of $NiAl$ and Ni_3Al.**
   S. Lamichhane, G. C. Kaphle and N. P. Adhikari
   Accepted in Quantum matter

5. **Structural, electronic and magnetic properties of Pd_n, Pd_nMn and Pd_nMn_2 clusters.**
   G. C. Kaphle, N. P. Adhikari and A. Mookerjee
   Manuscript Submitted to Physica B

6. **Adsorption and dissociation of Nitrogen and Hydrogen molecules on Tantalum(Ta) and Niobium(Nb) clusters.**
   G. C. Kaphle, N. P. Adhikari and A. Mookerjee
   Manuscript Submitted to Physica B.

7. **Study of magnetic engineering and bandgap engineering of ZnO nanosystems at different morphologies.**
   G. C. Kaphle, S. Datta, N. P. Adhikari and A. Mookerjee
   Manuscript Ready for submission

B. National Peer-Reviewed Journals

1. **Study of Structural, Electronic and Magnetic Properties of Pd_n(n=2-19) clusters.**
   G. C. Kaphle, N. P. Adhikari and A. Mookerjee
   Journal of Nepal Chemical Society, **32**(1), 77-88 (2014).

2. **Study of Electronic and Magnetic Properties of CuPd, CuPt, Cu_3Pd and Cu_3Pt: Tight Binding Linear Muffin-tin Orbitals Approach.**
   S. Dahal, G. P. Kafle, G. C. Kaphle and N. P. Adhikari
   Journal of Institute of Science and Technology, **19**(1), 137-144 (2014).

3. **Electronic structure and Magnetic Properties of bulk elements (Fe and Pd) and Ordered Binary Alloys (FePd and Fe_3Pd):TB-LMTO-ASA Approach.**
   S. Pandey, G. C. Kaphle and N. P. Adhikari
   BIBECHANA 11(1), 66-76 (2014).